

MEMOIRE DE DOCTORAT DE

L'ECOLE CENTRALE DE NANTES

ECOLE DOCTORALE N° 602

Sciences de l'Ingénierie et des Systèmes

Spécialité : Mécanique des Solides, des Matériaux, des
Structures et des Surfaces

Par

François MAHÉ

Statistical mechanical framework for discontinuous composites: application to the modeling of flow in SMC compression molding

Projet de recherche doctoral présenté et soutenu à l'Ecole Centrale de Nantes, le 24 janvier 2023
Unité de recherche : UMR 6183, Institut de Recherche en Génie Civil et Mécanique (GeM)

Rapporteurs avant soutenance :

Luise KÄRGER	Professor, Karlsruher Institut für Technologie, Allemagne
Laurent ORGEAS	Directeur de recherche CNRS, Université Grenoble Alpes

Composition du Jury :

Président :	Laurent ORGEAS	Directeur de recherche CNRS, Université Grenoble Alpes
Examineurs :	Luise KÄRGER	Professor, Karlsruher Institut für Technologie, Allemagne
	Laurent ORGEAS	Directeur de recherche CNRS, Université Grenoble Alpes
	Charles L. TUCKER, III	Professor Emeritus, University of Illinois, États-Unis
Directeur de recherches doctorales :	Christophe BINETRUY	Professeur des universités, École Centrale de Nantes
Co-dir. de recherches doctorales :	Suresh ADVANI	Professor, University of Delaware, États-Unis
Co-enc.de recherches doctorales :	Julien FÉREC	Professeur des universités, Université Bretagne-Sud

Invité

Benedikt ECK CAE Team Leader, FORVIA, Saint-Malo

A mon Grand-Père...

Remerciements :

Je tiens avant tout à exprimer ma profonde gratitude envers mon directeur de thèse, Christophe Binetruy, pour m'avoir offert cette opportunité et pour son accompagnement exceptionnel tout au long de ce travail. Je mesure à quel point cette thèse n'aurait pas pu aboutir sans son encadrement sans faille et je lui suis très reconnaissant pour son immense soutien, ainsi que pour ses qualités humaines, pédagogiques et scientifiques remarquables. J'ai énormément appris grâce à lui, tant sur le plan professionnel que personnel.

Je souhaiterais également remercier chaleureusement mes co-directeurs de thèse, Suresh Advani et Julien Férec, pour leur grande implication, leurs conseils avisés et leur franchise. L'encadrement de grande qualité qu'ils m'ont accordé, malgré la distance et les fuseaux horaires, a été un vrai moteur pour moi et je suis honoré d'avoir travaillé avec eux.

Je tiens également à exprimer ma gratitude envers les rapporteurs de cette thèse, Luise Kärgner, Laurent Orgéas et Charles L. Tucker III, pour leur examen minutieux de mon travail et leurs remarques constructives qui ont permis d'améliorer considérablement cette thèse.

J'associe à ces remerciements Chung-Hae Park et Sébastien Comas-Cardona pour avoir suivi l'évolution de mon travail chaque année, ainsi pour leurs précieux conseils et leur grande gentillesse.

J'adresse de sincères remerciements à l'entreprise Forvia pour avoir soutenu cette thèse, et particulièrement à Benedikt Eck, pour son aide, son ouverture d'esprit et sa confiance. Ses grandes compétences techniques et scientifiques ont beaucoup apporté à ce travail, en permettant d'aborder des questions théoriques et fondamentales dans un contexte industriel exigeant. Je le remercie pour tout cela.

Un grand merci à tout le reste de l'équipe du GeM du bâtiment T, pour la formidable ambiance que j'ai pu découvrir pendant mes études d'ingénieur et qui m'a donné envie de poursuivre en thèse. Merci notamment à Bertrand Huneau, Erwan Verron, Michel Coret, Adrien Leygue et Sébastien Comas-Cardona pour leur grande disponibilité et l'engagement dont ils font preuve pour permettre à tous les doctorant.e.s de s'épanouir pendant leur thèse et qui m'auront beaucoup apporté personnellement.

Pour finir, je voudrais exprimer toute ma gratitude envers mes amis et ma famille qui m'auront accompagné et encouragé pendant ces années malgré les difficultés. Une pensée particulière pour les cafés avec Buzz et Julien, ainsi que pour Simone, formidable collègue de bureau, avec qui j'aurai beaucoup partagé. Enfin, un immense merci à Lucie, qui de par son soutien et son amour, aura participé activement à cette thèse.

Merci à tous pour votre soutien et votre contribution à la réussite de ce travail.

Statistical mechanical framework for discontinuous composites: application to the modeling of flow in SMC compression molding

Abstract:

Sheet Molding Compounds (SMC) are composite materials made of chopped fiber bundles and a thermosetting resin. They are processed by compression molding and are known to exhibit complex rheological behaviors, difficult to model and coupled to the evolution of the fibrous reinforcement.

Tomographic observations, on a series of short shots of different SMC materials, highlight several transformation mechanisms of the fibrous network according to its characteristics. They reveal the involvement of contacts and friction forces between fiber bundles in the compression deformation of SMC materials. These internal mechanisms are generally neglected in current modeling approaches.

A new framework of statistical mechanics is developed to model the behavior of discontinuous and random fibrous media. A mesostructure generator is implemented to study the contact forces in a fibrous stack. At the macroscopic scale, the behavior of the mesostructure is described analytically by a probabilistic approach, in agreement with the results of numerical simulations.

This framework applied to the flow of SMC materials leads to a mixed fluid/friction model, governed by probabilistic contact forces within the fibrous reinforcement. An experimental characterization protocol is proposed to identify the rheological parameters of this model and applied to different types of SMC materials.

Keywords: SMC, process modeling, composite, statistical mechanics, characterization, simulation

Un cadre de mécanique statistique pour les composites discontinus : application à la modélisation de l'écoulement du moulage par compression de matériaux SMC

Résumé :

Les Sheet Molding Compounds (SMC) sont des matériaux composites formés de mèches de fibres coupées et d'une résine thermodurcissable. Ils sont mis en forme par moulage par compression et sont connus pour présenter des comportements rhéologiques complexes, difficiles à modéliser et dépendant de l'évolution du renfort fibreux.

Des observations tomographiques, sur une série d'incomplets pour différents matériaux SMC, met en évidence plusieurs mécanismes de transformation du renfort fibreux en fonction de ses caractéristiques. Ces constats soulignent l'implication des contacts et de la friction entre mèches dans la déformation de ces matériaux, mécanismes internes généralement négligés dans les approches de modélisation actuelles.

Un nouveau cadre de mécanique statistique est développé pour modéliser le comportement de milieux fibreux discontinus et aléatoires. Un générateur de mésostructures est implémenté pour étudier les forces de contacts dans un empilement fibreux. A l'échelle macroscopique, le comportement de la mésostructure est décrit analytiquement par une approche probabiliste, en accord avec les résultats des simulations numériques.

Dans le cas de l'écoulement des SMC, cette démarche mène à la formulation d'un modèle de comportement mixte fluide/solide, régi par la distribution des forces de contact à l'intérieur du renfort fibreux. Un protocole expérimental d'identification de ce modèle est développé et appliqué à différents types de matériaux SMC.

Mots-clés : SMC, procédé, composite, mécanique statistique, caractérisation, simulation

Contents

1. Introduction	1
1.1 Sheet Molding Compounds	1
1.2 Models for the compression molding process	5
1.3 Summary of thesis content	11
Bibliography.....	13
 2. Geometrical analysis of the discontinuous mesostructures of SMC materials	 17
2.1 Introduction.....	18
2.2 Investigation on the effect of the manufacturing parameters of SMC materials on the deformation of their mesostructures during the compression molding process.	19
2.2.1 Motivations.....	19
2.2.2 Custom-designed SMC materials	19
2.2.3 Compression molding using an industrial hydraulic press	21
2.2.4 Observation by tomography of mesostructures and orientation analysis	22
2.2.5 Discussion about the deformation mechanisms of SMC mesostructures	28
2.3 Geometric descriptors of fiber bundle stack mesostructures	31
2.3.1 Introduction.....	31
2.3.2 Definition and assumptions.....	31
2.3.3 Mathematical derivation of the stack	32
2.3.3.1 Introduction to integral geometry	32
2.3.3.2 Application to random stacks of in-plane fibers	34
2.3.3.3 Generalization to arbitrary planar orientation distributions	36
2.3.3.4 Application to random stacks of planar objects	37
2.3.3.5 Generalization to volume objects.....	40
2.3.4 Summary	43

2.4	Implementation of a mesostructure generator and numerical validations	44
2.4.1	●bjectives	44
2.4.2	Implementation.....	44
2.4.3	Method	48
2.4.4	Results	48
2.4.5	Analysis and discussion.....	53
2.4.6	Summary about the description of random stacks.....	53
2.5	Conclusion	54
	Appendices.....	55
2.A.	Incomplete parts molded in the industrial hydraulic press	55
2.B.	Qualitative observations of the flow patterns and the compressed SMC material.....	62
2.C.	Tomography images of the SMC materials	67
2.D.	Orientation analysis of the SMC mesostructures	71
	Bibliography.....	77
3.	A statistical framework to characterize discontinuous fibrous media	79
3.1	Introduction.....	80
3.2	Microscopic scale	80
3.3	Mesoscopic scale	85
3.3.1	Introduction.....	85
3.3.2	Finite element formulation of a fibrous stack	85
3.3.3	Algorithm to solve for the deformation and contact forces.....	93
3.4	Compaction of fibrous mesostructures	93
3.4.1	Introduction.....	93
3.4.2	Theory and method	93
3.4.2.1	Statistical description and constitutive model of contact forces	93
3.4.2.2	Finite element formulation	98

3.4.2.3	Simulations	99
3.4.3	Results	101
3.4.4	Discussions	106
3.4.4.1	Comparison of the numerical results with the analytical model	106
3.4.4.2	Application to SMC mesostructures	107
3.5	Conclusions	108
Appendices		110
3.A.	Derivation of beam equations and finite element formulations	110
3.B.	Statistical framework	122
Bibliography		138
4.	Development and characterization of a new rheological model for SMC materials	139
4.1	Introduction	140
4.2	Compression tests and internal friction mechanisms	141
4.2.1	Objectives	141
4.2.2	Preparation of the samples	141
4.2.3	Experimental protocol	142
4.2.4	Results	144
4.2.5	Analysis and discussion	145
4.2.5.1	Initial friction effect	145
4.2.5.2	Comments on the rheological behavior observed during the squeeze-flow	146
4.2.6	Conclusion	147
4.3	Characterization of SMC material parameters during compression molding	147
4.3.1	Objectives	147
4.3.2	Industrial SMC materials	148
4.3.3	Description of the experimental setup	150
4.3.4	Experimental protocol	151

4.3.5	Methods	153
4.3.5.1	Geometrical dimensions of the SMC samples	153
4.3.5.2	SMC rheological model	155
4.3.6	Results	157
4.3.7	Analysis and discussions	165
4.3.7.1	Description of the experimental curves	165
4.3.7.2	Identification of the mechanical behaviors	166
4.3.7.3	Discussion about the rheological model	170
4.3.8	Conclusion	173
4.4	General conclusions	174
	Appendices	175
4.A.	Comparison of compression curves for different parameters of SMC formulations and compression molding process	175
4.B.	Derivation of the compression stress formula	177
4.C.	Phase averages and averaging theorem	183
	Bibliography	187
5.	Conclusions and overview on the statistical SMC model	191
5.1	Summary, conclusions and contributions	191
5.2	Discussion about the statistical model	194
5.3	Future work and perspectives	199
	Bibliography	201
	Appendix I: Numerical generator of compacted fibrous mesostructures	203

Chapter 1

Introduction

Table of contents

1.1	Sheet Molding Compounds	1
1.2	Models for the compression molding process	5
1.3	Summary of thesis content	11
	Bibliography	13

1.1 Sheet Molding Compounds

Sheet Molding Compounds (SMC) are composite materials made of chopped fiber bundles and thermoset resin processed by compression molding (Orgéas & Dumont, 2011). The semifinished uncured material, which already combines the fibers and the reactive resin, is produced in advance in large quantities and stored in the form of rolls. To produce a part, plies are cut from the rolls and stacked into a heated mold. The mold is closed to apply heat and pressure on the SMC charge. The material flows and fills the mold cavity, before curing to form a solid part (see Figure 1.1).



Figure 1.1: SMC automotive part (Faurecia).

Unlike continuous fiber-reinforced composites, which must be precisely placed over the entire mold surface, SMC materials can be placed to cover a partial fraction of the mold, typically 30%-80% of the mold surface. Combined with the short compression cycle of a few seconds and

the curing time of a few minutes, it allows for high rates of production. This makes the process advantageous for high volume production of thin parts with a shell geometry. It represents one of the main composite manufacturing processes in terms of volume produced (first process in France with 35% of the production of composites in 2014 (Marzano & Celle, 2014)).

The produced parts are light, they have good mechanical properties, particularly with regard to damages and corrosion. Most of the industrial applications of SMC materials are in the transport and the energy sector, from non-structural to semi-structural components, depending on the formulation and the properties of the SMC material.

SMC materials are manufactured from fiber rovings, generally glass or carbon fibers, which are chopped at a given length and land on a moving film of polymer resin (see Figure 1.2). The polymer is an uncured thermoset resin, often an unsaturated polyester, but it can be vinyl ester or epoxy-based resin as well. The resin is mixed with different additives to adjust its viscosities and its physico-chemical properties during the manufacturing and the molding process. A typical formulation of a SMC resin paste contains (Sawallisch, 1984):

- Mineral fillers (40%_{wt.}-65%_{wt.}): mineral powder, mostly calcium carbonates (CaCO_3). They are used to control the viscous behavior of the material during the process, increasing its viscosity to improve the processability of the material (Seymour, 1976). They can also improve the mechanical properties of the parts and the quality of the surface, reducing the matrix shrinkage (Lautenschläger, et al., 2018). In carbon SMC materials, usually there are no fillers.
- Fibrous reinforcement (10%_{wt.}-65%_{wt.}): chopped fiber bundles to ensure the mechanical performances of the material (see Figure 1.3). Traditionally, the reinforcement is made of glass fibers, but the use carbon fibers is rapidly increasing for structural applications, and new materials with plant-based or basalt fibers are in development (Van Voorn, et al., 2001), (Asadi, et al., 2017).

The fibers are arranged in fiber bundles, containing several hundreds of fibers. The typical fiber length varies from 12mm to 50mm (0.5 inch to 2 inches), most of the applications use fiber length of 25mm (1 inch). The fiber bundle width is around 0.5mm to 1mm for glass fibers and up to 5mm for carbon fibers. The fiber volume in a bundle is about 65% (Orgéas & Dumont, 2011), (Endruweit, et al., 2013).

The fibers are coated by a sizing polymer to improve the cohesion of the fiber bundles, protect them from abrasion and increase the chemical compatibility with the resin matrix (Larson & Drzal, 1994), (Drown, et al., 1991).

- Polymer resin + reactive monomers (25%_{wt.}-35%_{wt.}): unsaturated polyester for most of the applications, vinyl ester or epoxy depending on the required properties and costs. It is often called the SMC paste. It forms the continuous matrix phase of the SMC material and ensures the deformation and flow of the material during the compression molding process, transporting the fiber bundles everywhere within the mold. The monomers are blended with a reactive solvent, commonly styrene for unsaturated polyester resins, to react with the polymer resin during its curing.

The viscosity of the paste must be high during the compression process to enable the processability of the material, and low during the manufacturing of SMC to immerse the fibrous reinforcement. This control of the viscosity is allowed by the use of several additives and the maturation step which follows the manufacturing process

Some bio-sourced resins are in development (Lu, et al., 2005) to obtain more sustainable materials.

- Low-profile additives (2%_{wt.}-5%_{wt.}): thermoplastic particles to improve the quality of surface finish and reduce the shrinkage of unsaturated polyester resins (Pattison, et al., 1974).
- Thickening agents (0.5%_{wt.}-3%_{wt.}): metal oxides or hydroxides additives to increase the viscosity of the paste after the maturation.
- Initiator and inhibitors (0.5%_{wt.}): chemical additives to control the curing reaction of the thermoset resin.
- Release agent to improve the demolding.
- Pigments to modify the color of the material, usually light (called “natural”) or black.
- Fire retardants, as aluminum hydroxide ($\text{Al}(\text{OH})_3$), to release water if the material is burned and reduce the flame spread.

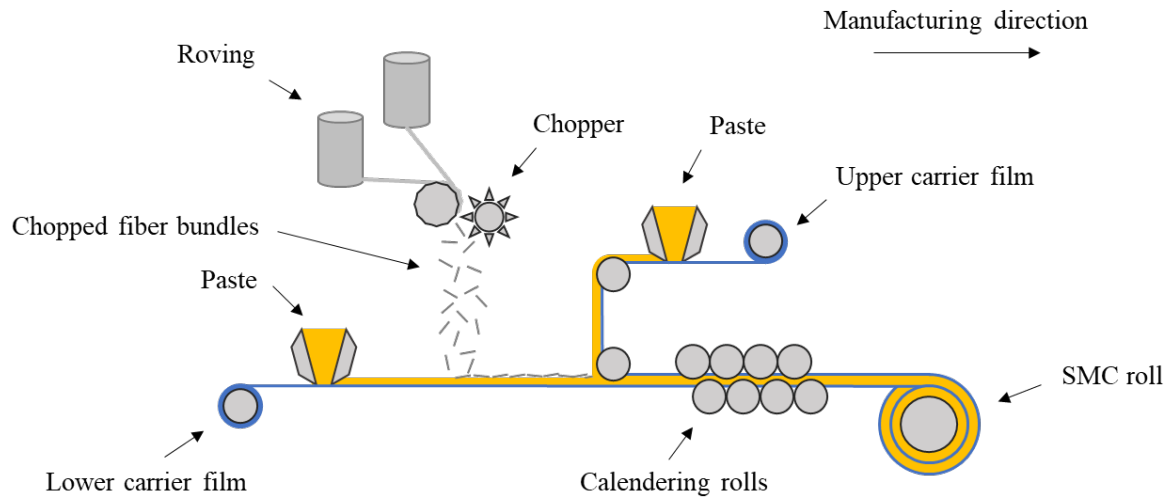


Figure 1.2: Schematic representation of the manufacturing process of an SMC material.

The chopped fiber bundles form a mat structure, whose discontinuous structure contributes significantly to the flow of the SMC material under applied pressure, needed to mold. The landing of the fiber rovings during the manufacturing process generates random in-plane distribution of the fiber bundle orientations, although small anisotropies induced by the moving resin film can be observed, with a slight alignment in the manufacturing direction (see Figure 1.1).

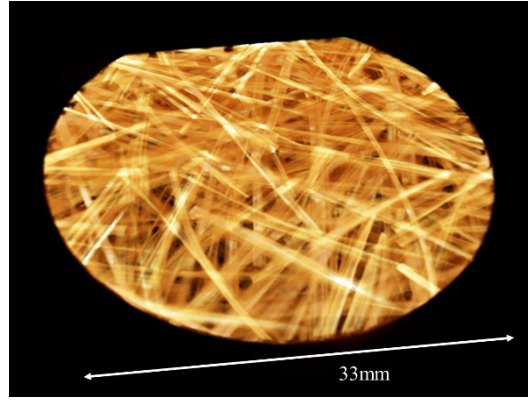


Figure 1.3: SMC fibrous mesostructure observed by X-ray tomography with visible fiber bundles.

After depositing the fiber bundles between two uncured resin films, the compound is compacted between calendaring rolls. The aim is to increase the impregnation of the resin inside the fibrous reinforcement and control the final concentration of the fiber bundles in the SMC material.

The semifinished material is stored in rolls, sandwiched between two polyethylene carrier films to prevent the sheets of SMC from sticking together, but also to reduce the release of the styrene solvent which would impact the rheological and curing properties of the resin.

After the manufacturing process, the SMC material is stored for several days in a dedicated area for the maturation step, with temperature and humidity controls, to allow the thickening of the paste and significant increase of its viscosity (from $\sim 10\text{Pa.s}$ to $\sim 100\text{kPa.s}$) (see Figure 1.4).

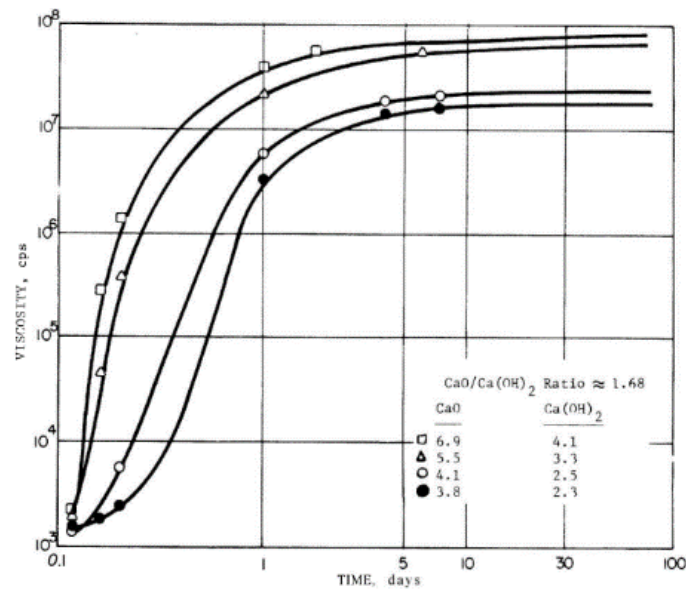


Figure 1.4: Evolution of the viscosity of a SMC material during the maturation step (Engineering design handbook, Short fiber plastic base composites, 1975).

In the compression molding process, pieces of SMC sheets are cut from the SMC rolls and stacked together to form a charge, which is placed into a heated mold. The molding temperature depends on the material, but is usually in the range $140^\circ\text{--}155^\circ\text{C}$. The temperature

of the two mold platens can be different. The shape of the SMC charges, their placement and the initial covered area of the mold are important factors to control the process and optimize the mechanical performances of the produced parts. The compression machine is a hydraulic press of several hundred tons, able to apply high compression rates and pressures on the material. Usual compression velocities in industrial processes are in between 0.5mm/s to 10mm/s. The high pressure applied combined with the heating of the resin (it reduces the viscosity of the paste between $\sim 100\text{Pa}\cdot\text{s}$ to $\sim 1000\text{Pa}\cdot\text{s}$ during the molding process) (Lee, et al., 1981), induce the flow of the SMC material. The significant viscous drag forces applied by the paste on the fibrous reinforcement allows one to transport the fiber bundles everywhere within the mold. At the end of the compression, the part is held in the mold for 60s to 300s to ensure the curing of the resin is complete. Then, the mold is opened to release and demold the part.

During the compression molding process, the SMC material is highly deformed to fill the mold, which is known to induce large movements and re-orientation of the fibrous reinforcement and could lead to many defects. The processing conditions, the initial charge in the mold and the material properties are all factors influencing the properties of the final part. Main defects for SMC parts can be welding lines if the position of the initial charges is not suitable, incomplete filling patterns or heterogenous distribution of the matter if the compression parameters do not match the material requirements. The geometry of the mold can also generate defects, one of the most well-known issues is the filling of the ribs, which can generate sink marks and a possible lack of fibers within the ribs (Smith & Suh, 1979).

At the mesoscale, the fibrous reinforcement is deformed according to complex transformations (Le, et al., 2008), inducing anisotropy of the flow (Dumont, et al., 2003) with significant consequences on the final mechanical properties of the parts (Chen & Tucker III, 1984), because the fibrous reinforcement provides most of the mechanical performance.

In order to control the quality and the repeatability of the molding process, the mold filling patterns and the evolution of the fibrous reinforcement induced by the flow of compression are major needs for the industries using SMC materials. A fundamental understanding of the mechanical and rheological behaviors is required as input for numerical tools that simulate the compression molding process and predict the properties of the parts produced. However, the multiplicity of material and processing parameters, the different physical coupling effects occurring the flow, and the random nature of SMC materials make this task difficult, leading to the development of numerous models to represent the compression molding process of SMC materials.

1.2 Models for the compression molding process

The first developments of SMC molding technology and materials dates back to the 1970s and were initially driven by the first technical applications, as the Chrysler air deflector (Currier, 1972). The rheological behavior of these new materials was first investigated by several rheometric experiments initially developed for plastic materials (Burns, 1982). First observations of the flow patterns indicate different flow behaviors, with a dependence on the fiber aspect ratio: pseudoplastic or plug-flow for high aspect ratios, Newtonian or parabolic profiles of flow for low aspect ratio (see Figure 1.5). The effect of fibrous reinforcement on the material rheology was initially neglected.

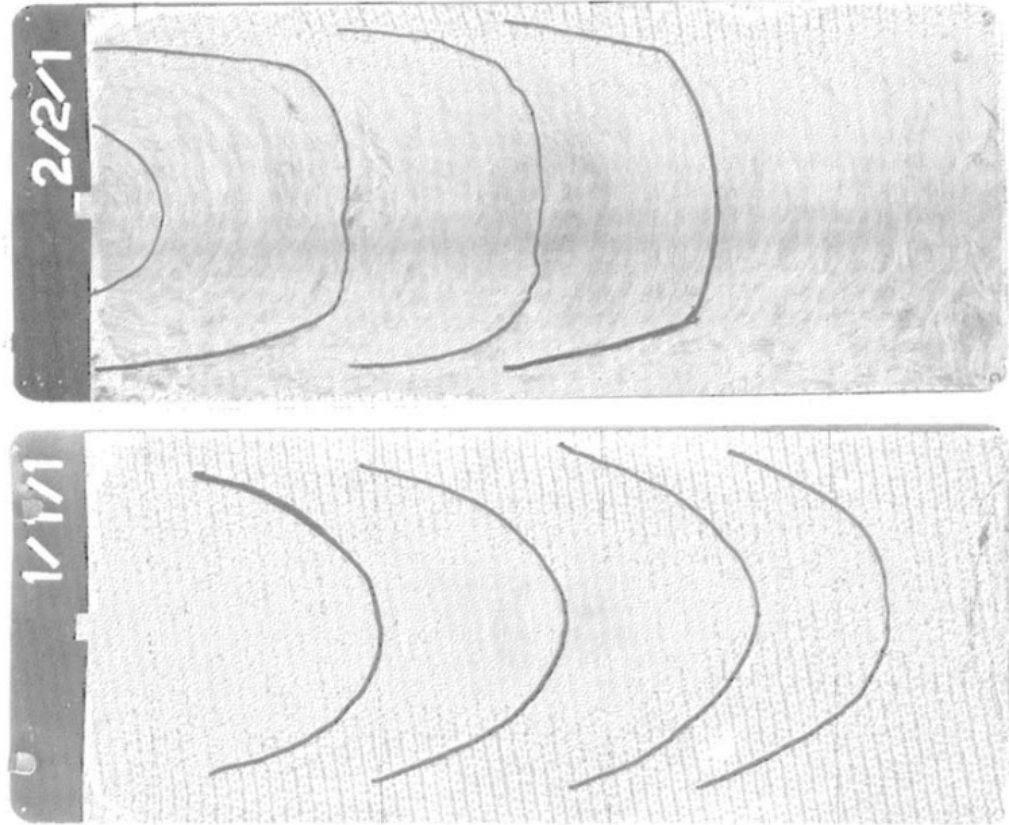


Figure 1.5: Plug-flow (top) and parabolic (bottom) flow profiles of SMC materials determined by X-ray observations (Burns, 1982).

One of the first detailed analyses of the rheology of SMC materials has been done by (Lee, et al., 1981). The authors used different rheometer systems with temperature control to characterize SMC materials from a general Carreau viscosity model. They conclude about the non-linear viscous behavior of SMC materials (unsaturated polyester resin and glass fibers), with decreasing viscosities at high shear rates and with increasing temperatures. They also noticed that the paste has a Newtonian behavior at low to medium shear rates (see Figure 1.6). At high shear rates, the SMC behavior tends for all the temperature toward a similar behavior, designated as “Melt fracture”, which is typical of irregular wall sliding in polymers (Benbow & Lamb, 1963). The increase in (extensional) viscosity with fiber length was established. The rheological parameters follow an Arrhenius law for the dependance in the temperature.

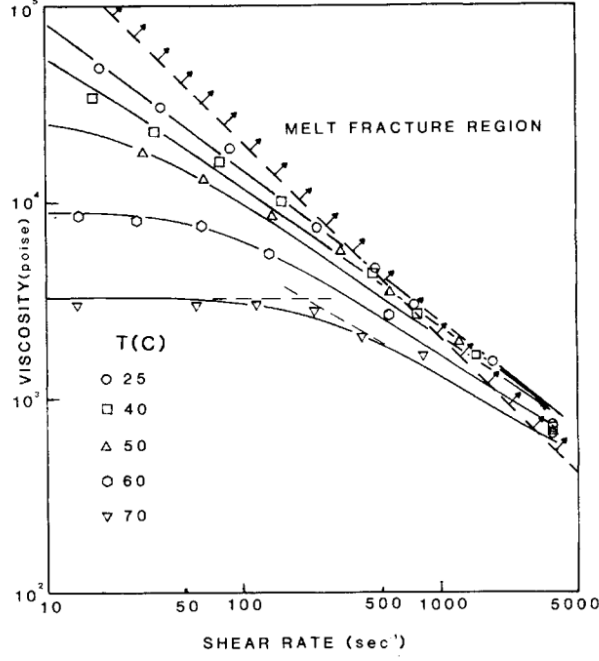


Figure 1.6: Steady shear viscosities of SMC materials as function of shear rate and temperature (Lee, et al., 1981).

During the 1980s, different models emerged to describe the rheology of SMC materials and lead to two different approaches of the rheological kinematics of SMC materials. On one hand, some authors assumed slip boundary conditions and a plug-flow kinematics, motivated by the assumption that the fibrous reinforcement resists the viscous shear forces of the flow (Barone & Caulk, 1985). On the other hand, models are proposed based on a generalized fluid behavior as a Hele-Shaw model with no-slip boundary conditions (Tucker III & Folgar, 1983). These two approaches have been discussed in the literature, and confirmed experimentally by them. Each of them can be assimilated to a flow pattern observed in Figure 1.5, which shows the complexity of SMC rheology. Other models combined different behaviors to reproduce the observations of flow patterns. (Silva-Nieto, et al., 1981) proposed a description using an elasto-visco-plastic model with a non-linear fluid viscosity. (Castro & Griffith, 1989) reused the model of (Barone & Caulk, 1985), adding friction boundary conditions to predict correctly the molding forces. In (Barone & Caulk, 1986), the authors investigated different friction models to describe the boundary conditions along the mold and concluded about the validity of the hydrodynamic model proportional to the compression velocity. The authors also insisted on the non-fluid character of the SMC materials which must be considered in the rheological models.

All these models consider the SMC materials as continuous and isotropic materials, neglecting the effects induced by the presence of the fibrous reinforcement. The description of the orientations of a population of fiber bundles within a flow has been formulated by (Folgar & Tucker III, 1984). The orientations are described by the use of an orientation distribution function $\psi(\vec{u})$ giving the probability to observe a fiber bundle in the direction \vec{u} , or by symmetry, in the direction $-\vec{u}$.

As it is a probability distribution, the function ψ must verify the normalization condition $\oint \psi(\vec{u}) d\vec{u} = 1$. Considering the conservation of distribution, the evolution of ψ is given by:

$$\frac{d\psi}{dt} = -\frac{\partial}{\partial \vec{u}}(\psi \dot{\vec{u}}) \quad (1.1)$$

The evolution of the fiber orientations within a flow has been initially derived by (Jeffery, 1922). The orientation of a fiber is identified by its unit direction vector \vec{u} . Consider the gradient tensor of the transformation $\mathbb{F} = \frac{\partial \vec{x}}{\partial \vec{X}}$ applied on the fiber. Then, the transformation of an arbitrary small vector \vec{X} is:

$$\vec{x} = \mathbb{F} \cdot \vec{X} \quad (1.2)$$

The time derivation of Eq. (1.2) gives:

$$\dot{\vec{x}} = \underbrace{\dot{\mathbb{F}} \cdot \mathbb{F}^{-1}}_{\mathbb{L}} \cdot \vec{x} \quad (1.3)$$

where \mathbb{L} is the velocity gradient field resulting from the transformation. Now, replacing \vec{x} by the unit vector $\vec{u} = \frac{\vec{x}}{\|\vec{x}\|}$ in Eq. (1.3) leads to Jeffery equation:

$$\dot{\vec{u}} = \mathbb{L} \cdot \vec{u} - (\vec{u} \cdot \mathbb{L} \cdot \vec{u})\vec{u} \quad (1.4)$$

where the second term of the right-hand side corrects the elongation to conserve the unit norm of the vector \vec{u} .

Considering that the fibers are rigid and small compared to typical variation lengths of the flow, and that the fluid is sufficiently viscous to neglect the inertial and other forces applied on the fibers, the velocity gradient \mathbb{L} can be associated the velocity gradient of the flow $\nabla \vec{v}$.

(Folgar & Tucker III, 1984) completed Jeffery's model to incorporate the interactions between the fibers and proposed a diffusion model to represent the disturbances induced by the fibers in semi-diluted suspensions. This model is of the form:

$$\dot{\vec{u}} = \mathbb{L} \cdot \vec{u} - (\vec{u} \cdot \mathbb{L} \cdot \vec{u})\vec{u} - \frac{C_I \dot{\gamma}}{\psi(\vec{u})} \frac{\partial \psi}{\partial \vec{u}} \quad (1.5)$$

where $\dot{\gamma}$ is the shear rate of the flow and C_I is an empirical parameter which must be measured experimentally. The usual values of C_I are in between, 0 to 0.1 in this phenomenological model.

This model is a powerful representation as it can represent any type of orientation distribution. However, the resolution of Eq. (1.1) is generally complex and requires a discretization of the orientation space for each location in the flow domain. A more compact descriptor of the orientation field has been proposed later by (Advani & Tucker III, The use of tensors to describe and predict fiber orientation in short fiber composites., 1987). The second statistical moment of the orientation distribution function defines the second order orientation tensor:

$$\mathbb{A}^{(2)} = \oint (\vec{u} \otimes \vec{u}) \psi(\vec{u}) d\vec{u} \quad (1.6)$$

This is a symmetric tensor whose eigenvalues and eigenvectors can be used to characterize the alignment of the fiber bundles and the principal directions of the fiber bundle population. According to Eq. (1.5), the time derivative of the orientation tensor is:

$$\dot{\mathbb{A}}^{(2)} = \mathbb{L} \cdot \mathbb{A}^{(2)} + \mathbb{A}^{(2)} \cdot \mathbb{L}^T - 2\mathbb{L} : \mathbb{A}^{(4)} + C_I \dot{\gamma} (\mathbb{I} - \dim \cdot \mathbb{A}^{(2)}) \quad (1.7)$$

where $\dim = 3$ in 3D, and 2 in 2D. The tensor \mathbb{I} designates the identity tensor of the corresponding dimension. The calculation of the evolution of the second order orientation tensor involves the fourth order orientation tensor:

$$\mathbb{A}^{(4)} = \oint (\vec{u} \otimes \vec{u} \otimes \vec{u} \otimes \vec{u}) \psi(\vec{u}) d\vec{u} \quad (1.8)$$

which contain higher order information about the orientation distribution function than $\mathbb{A}^{(2)}$. In particular, the trace of $\mathbb{A}^{(4)}$ with respect to any couple of its indices is equal to $\mathbb{A}^{(2)}$. Thus, the resolution of Eq. (1.7) requires a closure approximation for $\mathbb{A}^{(4)}$ as a function of $\mathbb{A}^{(2)}$.

Various closure approximations have been proposed and discussed in the literature. The simplest one is the quadratic closure $\mathbb{A}^{(4)} = \mathbb{A}^{(2)} \otimes \mathbb{A}^{(2)}$, which is correct for aligned fibers but not valid for random distributions, as it is the case in SMC materials. The second common closure approximation is the linear approximation, given by:

$$\begin{aligned} \mathbb{A}^{(4)} = \mathbb{A}_{ijkl} = & -\frac{1}{35} (\delta_{ij}\delta_{kl} + \delta_{ik}\delta_{jl} + \delta_{il}\delta_{jk}) \\ & + \frac{1}{7} (\mathbb{A}_{ij}\delta_{kl} + \mathbb{A}_{ik}\delta_{jl} + \mathbb{A}_{il}\delta_{jk} + \mathbb{A}_{kl}\delta_{ij} + \mathbb{A}_{jl}\delta_{ik} + \mathbb{A}_{jk}\delta_{il}) \end{aligned} \quad (1.9)$$

which is suitable for random distributions, and not for aligned distributions. These two closures can be combined linearly to defined the hybrid closure.

More complex closure methods have been proposed by the following. The hybrid closure has been improved with a transition parameter between the quadratic and linear closures which is a linear function of $\det(\mathbb{A}^{(2)})$ (Advani & Tucker III, 1990). The orthotropic fitted closures were based on the interpolation using the eigenvalues of $\mathbb{A}^{(2)}$ and specific solution of the orientation tensors (Cintra Jr & Tucker III, 1995), (Chung & Kwon, 2001). Similar methods, called the natural closure approximations, were based on the invariants of the orientation tensor and analytical solutions of the probability distribution (Verleye, 1999), (Chung & Kwon, 2002).

The presented models capture, at least partially, the evolution of the fiber orientations within the flow. Thereafter, rheological models coupled with the orientation distribution have been proposed, generally based on an additional viscosity expressed linearly with respect to the second and the fourth orientation tensors (Hinch & Leal, 1972), (Dinh & Armstrong, 1984), (Lipscomb II, et al., 1988).

The complexity of the developed model makes it difficult to identify the parameter, especially for SMC materials which are subject experimentally to multiple physical couplings. Another limitation of the model to be applied in the case of SMC materials is their basic kinematic assumption of dilute media, which is not consistent with real SMC entangled mesostructures (see Figure 1.3). Also, most of these models were developed with individual fiber filaments in

mind whereas the SMC materials considered here are mainly present in the form of fiber bundles with some filamentization.

In SMC materials, it has been shown that the orientations of fiber bundles are not accurately predicted by the current orientation models (Oter-Carbonell, 2018). Experimental measurements highlighted the low reorientation of the fibers due to the contact interaction within the fibrous network. To capture the slow kinematics, a variant of the Eq. (1.7) was presented in (Wang, et al., 2008) multiplying the symmetric part of the velocity gradient (the shear rate) by a constant strain reduction factor $0 \leq \kappa \leq 1$:

$$\dot{\mathbb{A}}^{(2)} = \mathbb{W} \cdot \mathbb{A}^{(2)} - \mathbb{A}^{(2)} \cdot \mathbb{W} + \kappa \left(\mathbb{D} \cdot \mathbb{A}^{(2)} + \mathbb{A}^{(2)} \cdot \mathbb{D} - 2\mathbb{D} : \mathbb{A}^{(4)} + C_I \dot{\gamma} (\mathbb{I} - \text{dim} \cdot \mathbb{A}^{(2)}) \right) \quad (1.10)$$

where $\mathbb{W} = \frac{\mathbb{L} - \mathbb{L}^T}{2}$ is the skew symmetric part of the velocity gradient (also called the vorticity), and $\mathbb{D} = \frac{\mathbb{L} + \mathbb{L}^T}{2}$ is the strain rate. This method, which is equivalent to modifying the applied velocity gradient, assuming a local relative motion between the fibers and the flow of resin, is called the Strain Reduced Factor (SRF) model. However, this model is not objective. An improved model has then been developed in (Wang, et al., 2008) to apply the reduced strain rate on the eigenvalues of the orientation tensor. The authors called this method the Reduced Strain Closure (RSC) model, which is given by:

$$\begin{aligned} \dot{\mathbb{A}}^{(2)} = \mathbb{W} \cdot \mathbb{A}^{(2)} - \mathbb{A}^{(2)} \cdot \mathbb{W} + \mathbb{D} \cdot \mathbb{A}^{(2)} + \mathbb{A}^{(2)} \cdot \mathbb{D} - 2 \left(\mathbb{A}^{(4)} + (1 - \kappa)(\mathbb{N} - \mathbb{M} : \mathbb{A}^{(4)}) \right) : \mathbb{D} \\ + \kappa C_I \dot{\gamma} (\mathbb{I} - \text{dim} \cdot \mathbb{A}^{(2)}) \end{aligned} \quad (1.11)$$

where $\mathbb{N} = \sum_I A_I (\vec{e}_I \otimes \vec{e}_I \otimes \vec{e}_I \otimes \vec{e}_I)$, $\mathbb{M} = \sum_I (\vec{e}_I \otimes \vec{e}_I \otimes \vec{e}_I \otimes \vec{e}_I)$ with the diagonalization of $\mathbb{A}^{(2)}$ written as $\mathbb{A}^{(2)} \sim \sum_I A_I (\vec{e}_I \otimes \vec{e}_I)$.

Other approaches began to model the mechanical interactions which can occur between two rod-like particles in contact (Férec, et al., 2015), (Natale, et al., 2016), (Férec, et al., 217), but were applied on semi-dilute suspensions of short fibers.

Some works studied also the effect of the different parameters of the fibrous reinforcement on the rheology and the evolution of SMC materials during the compression process (Merhi, et al., 2005), (Kardos, et al., 2020).

Regarding the different models which have been proposed in the literature, the rheology of SMC materials have generally been studied from the point of view of fluid, even if some authors have highlighted the limits of this approach. Faced with the increase of structural application needed for the industry and enhancement of the mechanical performances, SMC materials with high fiber contents in the form of fiber bundles or long fiber bundles are the constituents of the High-Performance SMC (HP-SMC) materials. For this class of materials, the mechanical behavior of the very entangled fibrous mesostructure cannot be ignored during the molding process. To the best of our knowledge, there are few studies which model the effect of the compacted fibrous reinforcement. (Toll S. , 1993) and (Toll & Månson, 1994) developed a new approach to described the contacts and the friction forces between a concentrated population of fibers. (Schommer, 2018) and (Romanenko, et al., 2022) proposed the use of the solid continuum mechanics to model some carbon SMC materials. To the best of our knowledge, there is no complete model formulated in the literature to link the mechanical response of the fibrous reinforcement to the rheological behavior of the SMC materials. Moreover, the random

nature of SMC materials is generally limited to the description of the orientation distribution of the fiber bundles and their rheological behavior is only addressed by mean field descriptions, giving few information about its inherent variability.

The present work was carried out in the frame of Faurecia Chair at Centrale Nantes. The study was motivated by improving the understanding of the SMC compression molding process and aims to explain difficulties in HP-SMC molding and mechanical heterogeneities encountered in industrial productions. In particular, some observations made by (Oter-Carbonell, 2018), (Hohberg, et al., 2017) confirmed industrial findings about very irregular flow front patterns on incomplete molded parts, highlighting complex rheological behaviors which can lead to different evolution of the materials that current models cannot predict (see Figure 1.7).



Figure 1.7: Irregular flow front observed by (Oter-Carbonell, 2018).

1.3 Summary of thesis content

In this work, a new model is developed to describe the deformation of SMC materials during the compression molding process. The proposed approach aims to improve the current descriptions to take into account the presence of the fibrous reinforcement and its evolving mechanical behavior within the flow during the compression stage of the process.

In **Chapter 2**, SMC materials with different reinforcement parameters are molded under an industrial press to make short shots. The macroscopic flow patterns are observed and described to highlight the complex deformation behavior mentioned in the literature. This analysis is completed by a series of X-ray tomography observations of the SMC mesostructures for the selected different materials. Then, a kinematic description based on a mathematical model of random stacks of fiber bundles is developed to represent the different observed mesostructures. This analytical description is validated with an implementation of a numerical generator of realistic mesostructures of SMC materials.

In **Chapter 3**, the developed kinematic model is used to build a framework of statistical mechanics to obtain the macroscopic behavior of the fibrous reinforcement under compression loadings by a multi-scale approach. The microscopic behavior of the fiber bundles is represented by a beam formulation which is then used to develop a mesoscopic model with a finite element method. The generator algorithm of the kinematic model in Chapter 2 is employed to solve for the mechanical compression of the fibrous stack by a fast iterative method based on the beam

model. Then, a statistical framework is developed to obtain the average behavior of the fibrous reinforcement, as well as the statistical distribution of contact forces inside the fibrous network. The analytical model is confirmed with numerical simulations of compacted mesostructures.

In **Chapter 4**, the mechanical model of the SMC mesostructures is used in conjunction with a friction model to represent the internal resistance forces due to the fibrous reinforcement, opposed to the flow. Two types of rheological experiments are conducted using various types of SMC materials to validate the model and identify the material parameters of the model.

In **Chapter 5**, the main conclusions and contributions are summarized, and the future work using the statistical distribution of contact forces within the fibrous reinforcement are discussed.

Bibliography

- [1] Advani, S. G., & Tucker III, C. L. (1987). The use of tensors to describe and predict fiber orientation in short fiber composites. *Journal of rheology*, 31(8), 751-784.
- [2] Advani, S. G., & Tucker III, C. L. (1990). Closure approximations for three-dimensional structure tensors. *Journal of Rheology*, 34(3), 367-386.
- [3] Asadi, A., Baaij, F., Mainka, H., Rademacher, M., Thompson, J., & Kalaitzidou, K. (2017). Basalt fibers as a sustainable and cost-effective alternative to glass fibers in sheet molding compound (SMC). *Composites Part B: Engineering*, 123, 210-218.
- [4] Barone, M. R., & Caulk, D. A. (1985). Kinematics of flow in sheet molding compounds. *Polymer composites*, 6(2), 105-109.
- [5] Barone, M. R., & Caulk, D. A. (1986). A model for the flow of a chopped fiber reinforced polymer compound in compression molding. *Journal of Applied Mechanics*, 53(2), 361-371.
- [6] Benbow, J. J., & Lamb, P. (1963). New aspects of melt fracture. *Polymer Engineering & Science*, 3(1), 7-17.
- [7] Burns, R. (1982). *Polyester molding compounds (Vol. 2)*. CRC Press.
- [8] Castro, J. M., & Griffith, R. M. (1989). Sheet molding compound compression-molding flow. *Polymer Engineering & Science*, 29(10), 632-638.
- [9] Chen, C. Y., & Tucker III, C. L. (1984). Mechanical property predictions for short fiber/brittle matrix composites. *Journal of reinforced plastics and composites*, 3(2), 120-129.
- [10] Chung, D. H., & Kwon, T. H. (2001). Improved model of orthotropic closure approximation for flow induced fiber orientation. *Polymer composites*, 22(5), 636-649.
- [11] Chung, D. H., & Kwon, T. H. (2002). Invariant-based optimal fitting closure approximation for the numerical prediction of flow-induced fiber orientation. *Journal of rheology*, 46(1), 169-194.
- [12] Cintra Jr, J. S., & Tucker III, C. L. (1995). Orthotropic closure approximations for flow-induced fiber orientation. *Journal of Rheology*, 39(6), 1095-1122.
- [13] Currier, G. J. (1972). Development of the First Sheet Molding Compound (SMC) Body Component: The Chrysler Station Wagon Air Deflector (No. 720493). *SAE Technical Paper*.
- [14] Dinh, S. M., & Armstrong, R. C. (1984). A rheological equation of state for semiconcentrated fiber suspensions. *Journal of Rheology*, 28(3), 207-227.
- [15] Drown, E. K., Al Moussawi, H., & Drzal, L. T. (1991). Glass fiber'sizings' and their role in fiber-matrix adhesion. *Journal of adhesion science and technology*, 5(10), 865-881.

- [16] Dumont, P., Orgéas, L., Le Corre, S., & Favier, D. (2003). Anisotropic viscous behavior of sheet molding compounds (SMC) during compression molding. *International Journal of Plasticity*, 19(5), 625-646.
- [17] Endruweit, A., Gommer, F., & Long, A. C. (2013). Stochastic analysis of fibre volume fraction and permeability in fibre bundles with random filament arrangement. *Composites Part A: Applied Science and Manufacturing*, 49, 109-118.
- [18] *Engineering design handbook, Short fiber plastic base composites*. (1975). Department of the army, Headquarters United States Army material command.
- [19] Férec, J., Bertevas, E., Khoo, B. C., Ausias, G., & Phan-Thien, N. (217). A rheological constitutive model for semiconcentrated rod suspensions in Bingham fluids. *Physics of Fluids*, 29(7), 073103.
- [20] Férec, J., Perrot, A., & Ausias, G. (2015). Toward modeling anisotropic yield stress and consistency induced by fiber in fiber-reinforced viscoplastic fluids. *Journal of Non-Newtonian Fluid Mechanics*, 220, 69-76.
- [21] Folgar, F., & Tucker III, C. L. (1984). Orientation behavior of fibers in concentrated suspensions. *Journal of reinforced plastics and composites*, 3(2), 98-119.
- [22] Hinch, E. J., & Leal, L. G. (1972). The effect of Brownian motion on the rheological properties of a suspension of non-spherical particles. *Journal of Fluid Mechanics*, 52(4), 683-712.
- [23] Hohberg, M., Kärger, L., Henning, F., & Hrymak, A. (2017). Rheological measurements and rheological shell model Considering the compressible behavior of long fiber reinforced sheet molding compound (SMC). *Composites Part A: Applied Science and Manufacturing*, 95, 110-117.
- [24] Jeffery, G. B. (1922). The motion of ellipsoidal particles immersed in a viscous fluid. *Proceedings of the Royal Society of London. Series A, Containing papers of a mathematical and physical character*, 102(715), 161-179.
- [25] Kardos, M., Körner, E., Penumadu, D., & Modler, N. (2020). The influence of fiber volume fraction and fiber length on the evolution of pore content and the paintability of sheet molding compounds. *Composites Part B: Engineering*, 185, 107760.
- [26] Larson, B. K., & Drzal, L. T. (1994). Glass fibre sizing/matrix interphase formation in liquid composite moulding: effects on fibre/matrix adhesion and mechanical properties. *Composites*, 25(7), 711-721.
- [27] Lautenschläger, M. I., Mayer, L., Gebauer, J., Weidenmann, K. A., Henning, F., & Elsner, P. (2018). Comparison of filler-dependent mechanical properties of jute fiber reinforced sheet and bulk molding compound. *Composite Structures*, 203, 960-967.
- [28] Le, T. H., Dumont, P. J., Orgéas, L., Favier, D., Salvo, L., & Boller, E. (2008). X-ray phase contrast microtomography for the analysis of the fibrous microstructure of SMC composites. *Composites Part A: Applied Science and Manufacturing*, 39(1), 91-103.
- [29] Lee, L. J., Marker, L. F., & Griffith, R. M. (1981). The rheology and mold flow of polyester sheet molding compound. *Polymer Composites*, 2(4), 209-218.

- [30] Lipscomb II, G. G., Denn, M. M., Hur, D. U., & Boger, D. V. (1988). The flow of fiber suspensions in complex geometries. *Journal of Non-Newtonian Fluid Mechanics*, 26(3), 297-325.
- [31] Lu, J., Khot, S., & Wool, R. P. (2005). New sheet molding compound resins from soybean oil. I. Synthesis and characterization. *Polymer*, 46(1), 71-80.
- [32] Mahé, F., Binetruy, C., Advani, S., Férec, J., & Eck, B. (2021). A multi-scale statistical description of stacks of non-cohesive thin particles. *Powder Technology*, 399, 116988.
- [33] Marzano, M., & Celle, P. (2014). *Les matériaux composites*. Retrieved from Educauto: http://www.educauto.org/files/file_fields/2015/04/01/dossier_peda_materiaux_composites_1.pdf
- [34] Merhi, D., Comte, E., Michaud, V., & Månson, J. A. (2005). Correlation between sizing formulation and compressive behavior of concentrated glass bundle suspensions. *Polymer composites*, 26(3), 370-376.
- [35] Natale, G., Ausias, G., Férec, J., Heuzey, M. C., & Carreau, P. J. (2016). Modeling interactions in carbon nanotube suspensions: Transient shear flow. *Journal of Rheology*, 60(6), 1069-1083.
- [36] Orgéas, L., & Dumont, P. J. (2011). Sheet molding compounds. *Wiley encyclopedia of composites*, 1-36.
- [37] Oter-Carbonell, L. (2018). *Process-induced microstructure in industrial SMC compression: quantitative descriptive analysis and predictability of a state-of-the-art numerical model*. École centrale de Nantes.
- [38] Pattison, V. A., Hindersinn, R. R., & Schwartz, W. T. (1974). Mechanism of low profile behavior in unsaturated polyester systems. *Journal of Applied Polymer Science*, 18(9), 2763-2771.
- [39] Romanenko, V., Duhovic, M., Schommer, D., Hausmann, J., & Eschl, J. (2022). Advanced process simulation of compression molded carbon fiber sheet molding compound (C-SMC) parts in automotive series applications. *Composites Part A: Applied Science and Manufacturing*, 106924.
- [40] Sawallisch, K. (1984). Compounding of sheet molding compound. *Polymer-Plastics Technology and Engineering*, 23(1), 1-36.
- [41] Schommer, D. D. (2018). Development of a solid mechanics based material model describing the behavior of SMC materials. *14th International Conference on Flow Processes in Composite Materials*, 30, pp. 01-06. Lulea, Sweden.
- [42] Seymour, R. B. (1976). The role of fillers and reinforcements in plastics technology. *Polymer-Plastics Technology and Engineering*, 7(1), 49-79.
- [43] Silva-Nieto, R. J., Fisher, B. C., & Birley, A. W. (1981). Rheological characterization of unsaturated polyester resin sheet molding compound. *Polymer Engineering & Science*, 21(8), 21(8), 499-506.
- [44] Smith, K. L., & Suh, N. P. (1979). An approach towards the reduction of sink marks in sheet molding compound. *Polymer Engineering & Science*, 19(12), 829-834.

- [45] Toll, S. (1993). Note: On the tube model for fiber suspensions. *Journal of Rheology*, 37(1), 123-125.
- [46] Toll, S., & Månson, J. A. (1994). Dynamics of a planar concentrated fiber suspension with non-hydrodynamic interaction. *Journal of Rheology*, 38(4), 985-997.
- [47] Tucker III, C. L., & Folgar, F. (1983). A model of compression mold filling. *Polymer Engineering & Science*, 23(2), 69-73.
- [48] Van Voorn, B., Smit, H. H., Sinke, R. J., & De Klerk, B. (2001). Natural fibre reinforced sheet moulding compound. *Composites part A: Applied science and manufacturing*, 32(9), 1271-1279.
- [49] Verleye, V. (1999). Modelling the flow of fiber suspensions in narrow gaps. *Rheology series*, 8, 1347-1398.
- [50] Wang, J., O’Gara, J. F., & Tucker III, C. L. (2008). An objective model for slow orientation kinetics in concentrated fiber suspensions: Theory and rheological evidence. *Journal of Rheology*, 52(5), 1179-1200.

Chapter 2

Geometrical analysis of the discontinuous mesostructures of SMC materials

Table of contents

2.1	Introduction	18
2.2	Investigation on the effect of the manufacturing parameters of SMC materials on the deformation of their mesostructures during the compression molding process.	19
2.2.1	Motivations.....	19
2.2.2	Custom-designed SMC materials.....	19
2.2.3	Compression molding using an industrial hydraulic press	21
2.2.4	Observation by tomography of mesostructures and orientation analysis	22
2.2.5	Discussion about the deformation mechanisms of SMC mesostructures.....	28
2.3	Geometric descriptors of fiber bundle stack mesostructures	31
2.3.1	Introduction.....	31
2.3.2	Definition and assumptions	31
2.3.3	Mathematical derivation of the stack	32
2.3.3.1	Introduction to integral geometry	32
2.3.3.2	Application to random stacks of in-plane fibers.....	34
2.3.3.3	Generalization to arbitrary planar orientation distributions.....	36
2.3.3.4	Application to random stacks of planar objects.....	37
2.3.3.5	Generalization to volume objects	40
2.3.4	Summary	43
2.4	Implementation of a mesostructure generator and numerical validations.....	44

2.4.1	Objectives	44
2.4.2	Implementation.....	44
2.4.3	Method	48
2.4.4	Results	48
2.4.5	Analysis and discussion	53
2.4.6	Summary about the description of random stacks.....	53
2.5	Conclusion	54
Appendices		55
2.A.	Incomplete parts molded in the industrial hydraulic press	55
2.B.	Qualitative observations of the flow patterns and the compressed SMC material...	62
2.C.	Tomography images of the SMC materials	67
2.D.	Orientation analysis of the SMC mesostructures	71
Bibliography		77

2.1 Introduction

The different approach presented in Chapter 1 to describe the rheological behavior of SMC materials during the compression molding process highlight the importance of the fibrous reinforcement and the coupling between its transformations and the behavior of the SMC material. The development of a mechanical model to handle the behavior of the fibrous mesostructure requires a kinematic description for the fiber bundle network and the identification of the physical mechanisms involved in the deformation of the SMC mesostructures.

In **Section 2.2**, an experimental campaign investigates these mechanisms on short shots molded under industrial conditions. The irregular flow patterns are described and confirm the need of a new approach for High-Performance SMC materials. A comparative analysis between the mesostructures of SMC materials for various manufacturing parameters allows us to identify the effects of the material parameters on the induced deformations of the fibrous reinforcement.

In **Section 2.3**, a mathematical model is developed from approach based on integral geometry to describe the geometry of the random and discontinuous fibrous mesostructures. A set of geometrical descriptors are obtained to characterize the different transformations observed experimentally.

In **Section 2.4**, a generator of SMC mesostructures is implemented to validate the mathematical approach and the obtained kinematic description for the fiber bundle network.

2.2 Investigation on the effect of the manufacturing parameters of SMC materials on the deformation of their mesostructures during the compression molding process.

2.2.1 Motivations

SMC materials are known to have complex behavior during the compression molding process, depending on the material parameters and the processing conditions (Le, et al., 2008). A qualitative analysis at the macro- and meso-scales is carried out on a set of five custom-designed SMC materials molded under an industrial press. The flow patterns of short shots are observed and discussed. A systematic analysis of the mesostructures has been processed by X-ray tomography to observe the different transformation mechanisms of the fibrous mesostructure, and their dependance on the material and manufacturing parameters.

2.2.2 Custom-designed SMC materials

In this study, a set of four different SMC materials are considered. All these materials are made from the same fiberglass roving and same resin formulation with different fiber lengths and volume fractions, to explore the effect of parameters encountered in SMC industrial applications.

These materials have been provided by Owens Corning company, that used its multi-end glass fiber roving referenced ME 1960¹. This roving is manufactured from continuous glass fibers brought together without twisting it into multiple tows. The glass fibers are the Advantex® glass reinforcement of Owens Corning, used in industrial applications requiring good mechanical properties, such as in SMC process for automotive applications. Fibers have a nominal diameter of 15.6µm. They are covered by a sizing system with a silane coupling agent to ensure compatibility with polyester resin and cohesion of fiber bundles.

The SMC materials are formulated with the low shrink resin (Ashland Derakane™ D760), which is an unsaturated polyester matrix containing 23.89% of mineral fillers (CaCO₃). This matrix does not contain any black pigments and have a natural light color, allowing one to distinguish the fiber bundles on the surface and by transparency for thin enough plates. Two fiber lengths have been used: 25mm (1 inch) and 50mm (2 inches) with a target fiber weight fraction of 25%_{wt.}. Two other fiber weight fractions have been used: 35%_{wt.} and 50%_{wt.}, for the smaller fiber length of 25mm.

An additional material has been manufactured with a different fiberglass roving of Owens Corning referred as Paneluxe², to observe the effect of the sizing system on the rheological behavior of the SMC material. This roving is generally not used by Owens Corning to formulate SMC materials as the cohesion of fiber bundles is weaker. This SMC material is formulated from the same Derakane™ D760 unsaturated polyester resin and Advantex® glass fibers, but there is no available data to characterize the mechanical behavior of the sizing system during the SMC compression molding process. This material will allow only for qualitative comparisons. The fiber length is 25mm and the targeted fiber weight fraction is 25%_{wt.}, which corresponds to a fiber volume fraction of 18%_{vol.}

¹ <https://www.owenscorning.com/en-us/composites/product/pe-ve-smc-roving-me1960>

² <https://www.owenscorning.com/en-us/composites/product/oc-paneluxe-roving>

The material reference with 25%_{wt.} (18%_{vol.}) with fibers of length 25mm is denoted Regular SMC (Reg-SMC-18) as it corresponds to regular SMC formulations encountered in many papers in the literature and in many semi-structural applications. The two materials where the fiber length is 25mm and fiber weight fractions of 35%_{wt.} (24%_{vol.}) and 50%_{wt.} (37%_{vol.}) are respectively denoted High-Performance SMC, respectively HP-SMC-24 and HP-SMC-37, as they correspond to a class of material encountered in research works and applications targeted for structural applications. The material reference with the fiber length of 50mm is noted as Long-Fiber SMC (LF-SMC-18). The last reference with a soft sizing system is denoted Soft-SMC-18. The parameters of the five SMC material references are listed in Table 2.1.

SMC reference	Reg-SMC-18	HP-SMC-24	HP-SMC-37	LF-SMC-18	Soft-SMC-18
Fiber weight fraction	25% _{wt.}	35% _{wt.}	50% _{wt.}	25% _{wt.}	25% _{wt.}
Fiber volume fraction	18% _{vol.}	24% _{vol.}	37% _{vol.}	18% _{vol.}	18% _{vol.}
Fiber cutting length	25mm	25mm	25mm	50mm	25mm
Sizing (roving reference)	Strong (ME 1960)	Strong (ME 1960)	Strong (ME 1960)	Strong (ME 1960)	Soft (Paneluxe)

Table 2.1: Details of the formulation for the five SMC material references.

Two batches of each SMC materials were provided by Owens Corning in separated rolls of 5kg. Each roll was weighted at the end of the manufacturing process to measure the areal density of the material and determine the effective fiber weight fraction of the material, which depends on the amount of cut rovings delivered by the chopper with respect to the belt speed. A small variation between batches of the same reference has been observed but remains acceptable for the experimental analysis; the measured fiber weight fractions are given in Table 2.2. Values are slightly smaller than the targeted fiber weight fractions and will be considered into the analysis of the experimental results.

Ref.	Reg-SMC-18	HP-SMC-24	HP-SMC-37	LF-SMC-18	Soft-SMC-18
Target	25%_{wt.}	35%_{wt.}	50%_{wt.}	25%_{wt.}	25%_{wt.}
Roll 1	24.4% _{wt.}	32.2% _{wt.}	47.5% _{wt.}	23.7% _{wt.}	24% _{wt.}
Roll 2	27.6% _{wt.}	33.7% _{wt.}	48.1% _{wt.}	24.6% _{wt.}	25.4% _{wt.}

Table 2.2: Fiber weight fraction variability for the five SMC material references.

The SMC materials are maintained between two polyethylene carrier films, wound on a roller and stored in rolls in a freezer at -18°C to arrest the curing and limit the release of volatile styrene compounds and the moisture absorption (Org  as & Dumont, 2011). The loss of styrene impacts both the curing and the rheological properties of matrix, and causes higher variability within the material (Shirrell, 1983).

2.2.3 Compression molding using an industrial hydraulic press

A series of short shots were made with an industrial hydraulic press of 280T at the Faurecia facilities in Saint-M  loir des Ondes in France. The objectives were to observe the flow front patterns after curing and demolding, and analyze the process-induced mesostructures with respect to the material parameters.

A rectangular steel mold of dimensions 800mm x 600mm was mounted on the press and heated to a constant temperature of 145°C . The two mold halves are strictly planar and parallel. A semicircle of radius 75mm is located along the side of the mold at midway to facilitate the demolding of the part (see Figure 2.1). A release agent was also applied in the cavity. A compression chamber surrounds the flat part of the mold and forces the material to flow and fill the whole cavity.

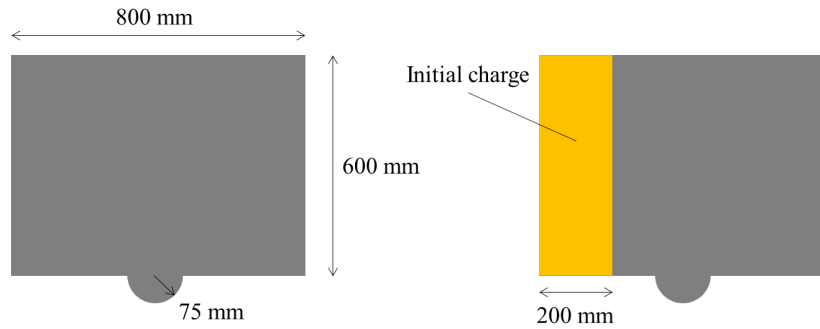


Figure 2.1: Dimensions of the compression mold and initial charge.

For each plate, an initial rectangular SMC charge was placed at the left border of the mold in order to induce a channel flow from the left to the right side of the mold, to maximize both the flow length and the material deformations. The rectangular charge is made by stacking of three plies of dimensions 600mm wide x 200mm long. The plies were cut in the width of the SMC roll of width 600mm. The initial thickness of the plies is around 2mm, but is variable depending of the SMC reference and the ply geometry which is not perfectly flat. Then, each initial charge has been weighted before being placed into the mold cavity.

The final thickness was controlled using a set of steel spacers placed around the mold cavity. Parts with three final thicknesses were formed: 5mm, 4mm and 3mm, which corresponds approximatively to part lengths of 250mm, 350mm and 450mm, depending on the initial geometry and mass of the charge.

The lower platen was fixed during the process, and the upper platen moved vertically to deform the SMC material. When the charge is placed in the mold, the upper platen moved rapidly to get closer to the charge, until the position of 15mm. Then, a constant compression velocity was enforced by the hydraulic press. Two values were used: 10T/s and 120T/s, using the conventional unit values in compression with hydraulic press. The heavy weight of the

mold and the total inertia affect the precision of the applied compression speed. The hydraulic press was not instrumented and no force can be measured on this setup. The delay between the placement of the charge and the end of the compression was less than 30s.

When the mold comes into contact with the spacers, it remains in position for 180s to cure the SMC material. Then the mold is opened to demold the part.

A total of thirty short shots have been produced with this protocol (5 SMC material references x 2 compression velocities x 3 thicknesses). Pictures of the cured panels and their respective weights are given in Appendix 2.A.

Some qualitative observations of the short shots and initial interpretations of the flow patterns are given in Appendix 2.B. To summarize, the main qualitative conclusions are:

- The flow reveals **heterogeneity** and **randomness**, not only at the flow front but also inside the filled domain where the flow may vary along the same streamline.
- The contact between the SMC material and the mold is a **mixed condition**, with **slip and no-slip boundary conditions at different locations along the mold walls**.
- **Large defects occur and affect the flow** and the evolution of the fibrous mesostructure.
- Some **solid behaviors** are observed, as the slip of layers or reinforcement breakage, that are associated with the apparition of large defects.
- Some defects are due to initial defects inherent to the manufacturing of SMC sheets.

It is clear that some observed defects disappear when the mold is completely filled to make the panel, thanks to the effect of the compression chamber which helps to close internal porosities. However, the observed defects contribute to the flow during the molding process and affect the evolution of the fibrous mesostructures. In particular, the fiber orientation depending on the shear rates is prone to be affected by the flow heterogeneities with locally high shear rates, not present in perfectly unidirectional flows. Moreover, all the defects in the initial SMC sheet contribute to the complex and stochastic evolution of the SMC material. These defects also exist also in real molding processes and cannot be completely ignored in the description of the evolution of SMC mesostructures.

To further investigate the qualitative observations and differentiate the deformations of the five material references, a series of samples from the short shots have been observed by X-ray tomography.

2.2.4 Observation by tomography of mesostructures and orientation analysis

Samples cut out from each panel molded under 120T/s have been collected to describe qualitatively their deformed mesostructures and the internal mechanisms involved in the transformation of SMC materials during the compression molding process.

The molded panels were cut in half and cylindrical samples of diameter 33mm at three locations were extracted using a die, along the same streamline in the middle of the panel (see Figure 2.2).

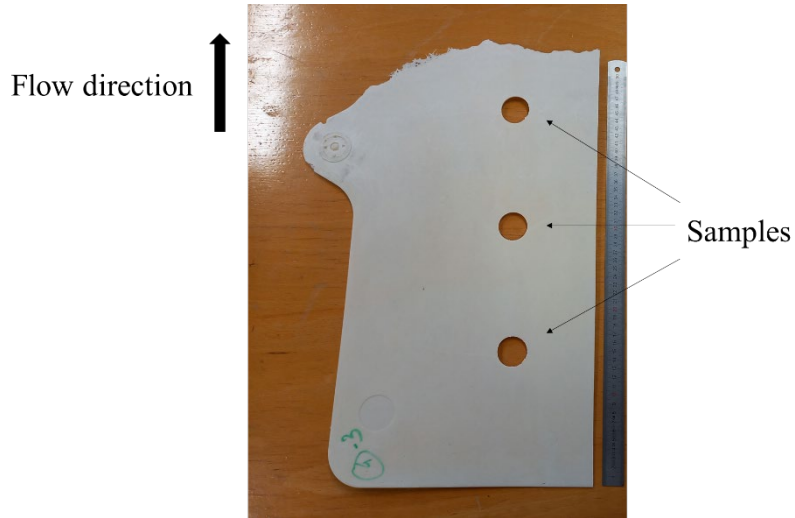


Figure 2.2: Sampling locations.

As shown in Figure 9, samples are cut from different locations in parts because they have different final thicknesses. Then, the samples in each part correspond to a same element of the charge that is deformed and transported during the compression molding process (see Figure 2.3 and Figure 2.4). Positions for the three final thicknesses are denoted by the letters A, B, C corresponding to the following locations:

- 300mm: 90mm (A), 180mm (B), 270mm (C).
- 400mm: 110mm (A), 220mm (B), 330mm (C).
- 500mm: 150mm (A), 300mm (B), 450mm (C).

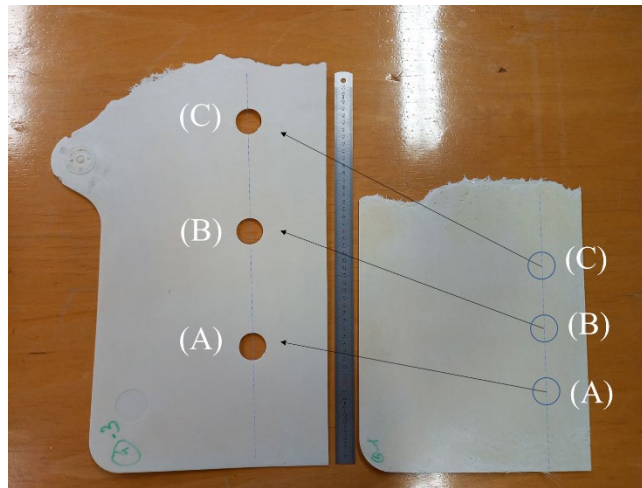


Figure 2.3: Sampling locations on two short shots. Left: 3mm thick part. Right: 5mm thick part.

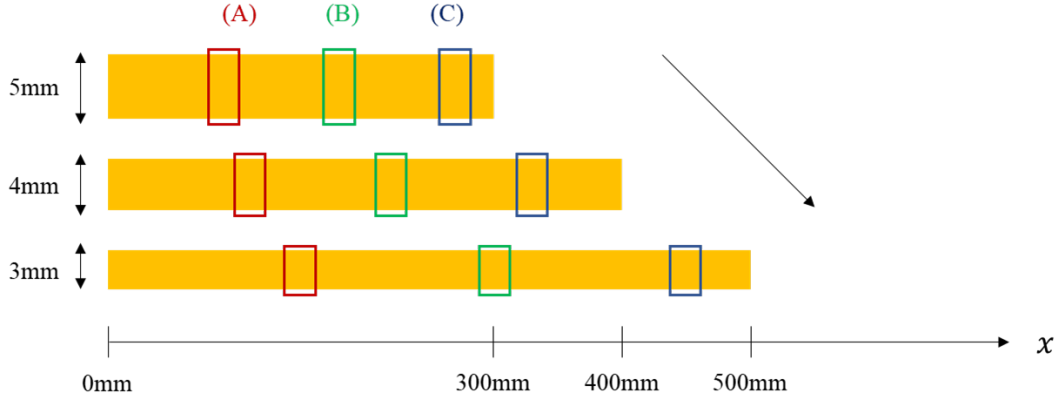


Figure 2.4: Principle of scaling the sampling locations to follow the deformation of the material.

A set of 42 cylindrical samples are collected from the panels molded at 120T/s: two panels for the Reg-SMC-18, respectively at 5mm and 4mm, and three panels of the other SMC references for the thicknesses 5mm, 4mm and 3mm (see Appendix 2.A).

The 42 SMC samples have been scanned by X-ray tomography to extract the 3D-images of their fibrous mesostructure. The X-ray source is an X-ray light bulb of 150kV. For each 3D-scan, 1440 2D-images are taken through the slice of the sample for different angles at 360°, with a time exposure of 8s per image. Each sample requires a total acquisition time of 4h. The image resolution is 17μm per pixel, so there is a minimum number of pixels of 15 pixels in the nominal width 0.5mm of a fiber bundle.

The 3D-images are reconstructed from the 2D images of material slices with an image analysis software (Figure 2.5). Here, the software ImageJ is used to analyze the mesostructures. After reconstruction, 3D-images are obtained with a resolution of 68μm per voxel.

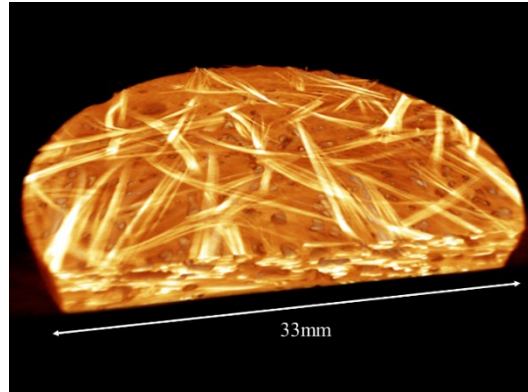


Figure 2.5: Reconstructed 3D-image of a SMC mesostructure scanned by X-ray tomography (sample C of the 5mm thick plate for the material referenced Reg-SMC-18).

As the boundary conditions at the material/mold interface remain uncertain, we decided to compare the fibrous mesostructures in the mid-plane of each sample. 2D-images obtained after the 3D reconstruction are given in Appendix 2.C.

The inherent variability of the SMC materials during the molding process produces random and heterogenous deformation of the fibrous reinforcement as observed in Appendix 2.C and

makes difficult any quantitative study. Hence only qualitative description of the different transformation mechanisms observed in the different SMC materials are discussed.

The contrast between the glass fibers and the polyester matrix allows one to distinguish both phases and the remaining voids in short shots. This is the role of the compression chamber, which under high pressure at the end of the compression molding, may be able to close the remaining voids. This last step is absent in short shots.

Mesostructures shown in Appendix 2.C reveal different types of SMC mesostructures. Considering that the 5mm thick samples are quasi-undeformed reference configurations, the accumulation of the reinforcement's deformations is visible at all sampling locations. They tend to be more pronounced for samples (B) and (C) where the flow extent was longer.

In the reference configuration of thickness 5mm, all the SMC materials present fibers arranged in bundles of parallel and mostly straight fibers in the plane, as shown in Figure 2.6. The fiber bundles are not identical tows as some of them are with larger width with some separations. No particular orientation is seen and the initial materials are mostly transversely isotropic as it will be verified by quantitative measurements in the following.

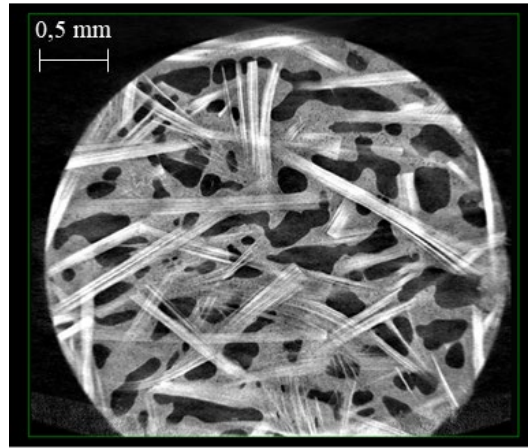


Figure 2.6: X-ray tomography scan of the middle plane of the Reg-SMC-18 (sample (A), thickness 5mm).

Different transformation mechanisms are observed on the tomography scans depending on the material reference. Generally, the characteristic described in SMC materials is the orientation state of the fiber bundles. To analyze these orientations, the package OrientationJ (Rezakhaniha, et al., 2012) of the image analysis software ImageJ is used.

The disks corresponding to the SMC material are extracted from the middle plane of the 3D-scans. The orientation analysis uses the Cubic Spline method to compute the gradient of the image as it found to be the more stable method. A local window of 5 pixels is used in the convolution of the gradient calculation. The gray images are colored with respect to the local orientation calculated by this method for some samples in Figure 2.7. The second invariant of the second order orientation tensor is calculated from the computed orientation distribution to characterize the alignment state of the fiber bundles. It is given by:

$$I_2 = 2 - 2(\mathbb{A}_{11}^2 + \mathbb{A}_{22}^2 + 2\mathbb{A}_{12}^2) = 4\mathbb{A}_I(1 - \mathbb{A}_I) \quad (2.1)$$

where \mathbb{A}_{11} , \mathbb{A}_{22} , \mathbb{A}_{12} are the components of the second order orientation tensor, and \mathbb{A}_I and $\mathbb{A}_{II} = 1 - \mathbb{A}_I$ are its eigenvalues. The second invariant describes the reduction of the relative angles between the fiber bundles. Its value for isotropic distribution in the plane is 1, and it decreases toward 0 when the fiber bundles tend to align in one direction. Figure 2.6 shows that the compression flow does not align systematically the fiber bundles in one direction. The alignment seems to be more significant for the reference Reg-SMC-18, with a low fiber content and short fibers, than for the rest of the SMC materials.

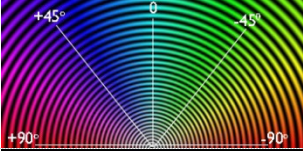
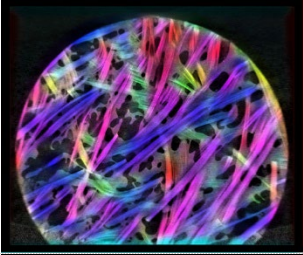
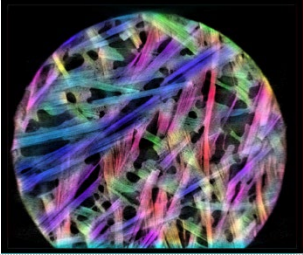
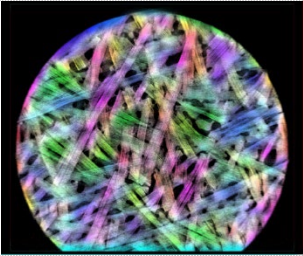
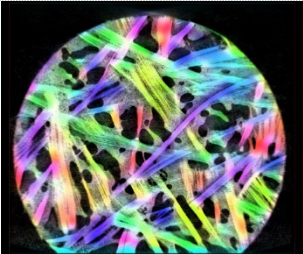
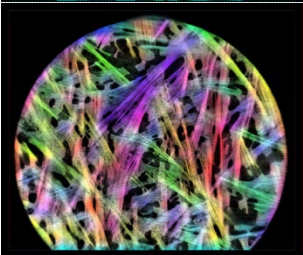
	Orientation color scale of OrientationJ.
	<p>Reg-SMC-18, 5mm, (C)</p> <p>The fiber bundles are mostly aligned along the direction 45°.</p> <p>$I_2 = 0.78$, $\mathbb{A}_I = 0.73$, $\mathbb{A}_{II} = 0.27$</p>
	<p>HP-SMC-24, 5mm, (C)</p> <p>The fiber bundles are slightly aligned along the direction 45°.</p> <p>$I_2 = 0.92$, $\mathbb{A}_I = 0.64$, $\mathbb{A}_{II} = 0.36$</p>
	<p>HP-SMC-37, 5mm, (C)</p> <p>The fiber orientations are uniformly distributed and no preferential direction is detected.</p> <p>$I_2 = 0.98$, $\mathbb{A}_I = 0.57$, $\mathbb{A}_{II} = 0.43$</p>
	<p>LF-SMC-18, 5mm, (C)</p> <p>The fiber orientations are uniformly distributed.</p> <p>$I_2 = 0.99$, $\mathbb{A}_I = 0.55$, $\mathbb{A}_{II} = 0.45$</p>
	<p>Soft-SMC-18, 5mm, (C)</p> <p>The orientations are quasi-uniformly distributed.</p> <p>$I_2 = 0.92$, $\mathbb{A}_I = 0.64$, $\mathbb{A}_{II} = 0.36$</p>

Figure 2.7: Comparison of the fiber bundle orientations for different SMC materials.

This repeated characterization at different sampling points and for different final thicknesses indicates that fiber bundles are more aligned for the Reg-SMC-18 which has low fiber content and shorter fiber bundles than the other references (see Figure 2.8), with a maximum of isotropy in average for the reference HP-SMC-37. These observations are consistent with similar analysis in (Dumont, et al., 2007), (Oter-Carbonell, 2018) and underline the complexity of industrial compression molding processes.

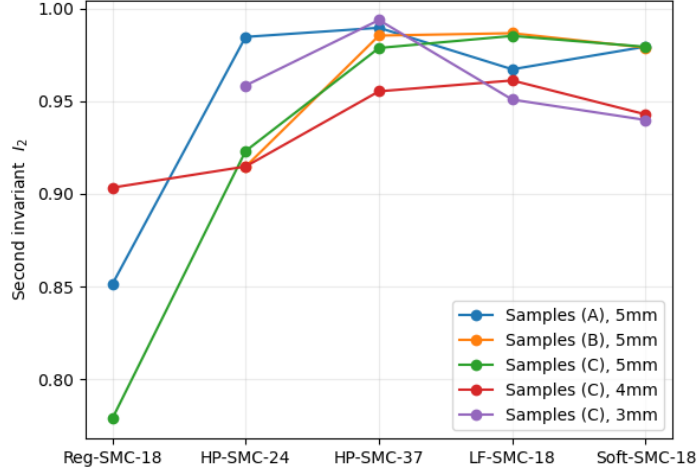


Figure 2.8: Comparison of the second invariant I_2 of the orientation tensor for the different SMC materials.

The rest of the post-treated images can be found in Appendix 2.D. It gives an overview of the variability of the deformed mesostructures, even for the same material cut out from the same location. However, the systematic analysis of fibrous mesostructures reveal different mechanisms of deformation for the fibrous reinforcement of SMC materials which is not necessarily related to the rotation and the alignment of fiber bundles, as discussed in the next section.

2.2.5 Discussion about the deformation mechanisms of SMC mesostructures

The viscous polymer matrix of the SMC material drags the fiber bundles rotating them within the flow. This mechanism produces significant modification of the fibrous reinforcement, with consequences on its mechanical properties, and have been the object of numerous studies (Advani & Tucker III, 1987), (Dumont, et al., 2003).

The qualitative observation of the scanned mesostructures indicates that the alignment of fiber bundles tends not to occur for high fiber contents and long fibers. The mesostructure may then experience other deformation modes, as observed in (Dumont, et al., 2007). For the mesostructures given in Appendices 2.C and 2.D, three other mechanisms are observed.

Fiber bundles can undergo in-plane bending, especially for the material LF-SMC-18 with 50mm-long fibers, as shown in Figure 2.9 where no fiber bundle is straight along its entire length. This bending is interpreted as a heterogenous deformation of the composite material over relatively small distances. This mechanism is also observed for the HP-SMC-24 and HP-SMC-37 with a final thickness of 3mm. The calculation of the second invariant of the local orientation tensor gives high values of I_2 for all mesostructures with curved fiber bundles ($I_2 = 0.94$ in average, with a standard deviation of 0.5), so it seems that there is no preferential direction of alignment of curved fiber bundles.

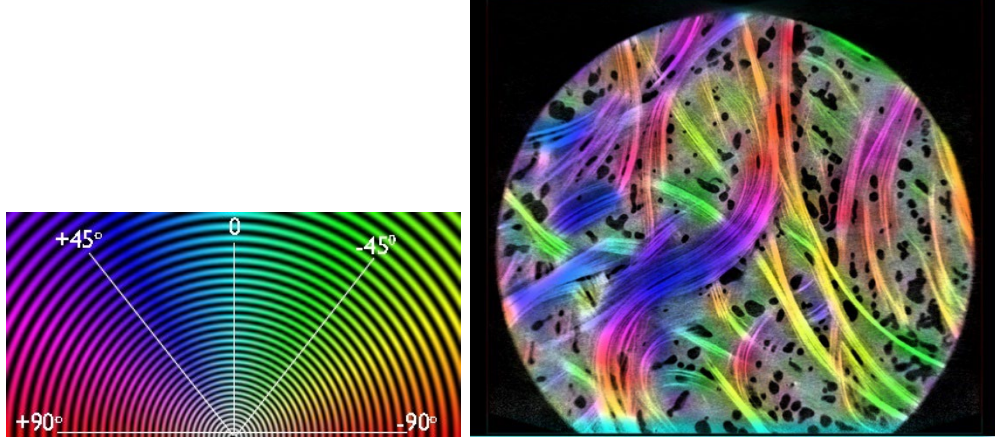


Figure 2.9: Curved fiber bundles (LF-SMC-18, 5mm, (B)).

It has been noted that for the HP-SMC-24 and especially for the HP-SMC-37, fiber bundle width becomes larger. Their width has been measured for the nine samples of HP-SMC-37 and the average values are represented in Figure 2.10. In each sample, a set of 30 fiber bundles are measured. The initial width is about 1mm in the undeformed SMC material, and increases progressively in all the observed HP-SMC-37 samples, up to the maximum value of 1.4mm at the sampling location (C) representing an in-plane deformation of the fiber bundle's cross-section of 40%. A trend seems to emerge indicating that the fiber bundles spread out with the material deformation (the width is larger for thinner plates) and with the flow extent (the width increases with the distance covered by the material). This mechanism seems to be more prevalent for SMC material with high fiber contents, where the fiber bundle network is denser and compacted. A more detailed analysis of fiber bundle width can be founded in (Oter-Carbonell, 2018).

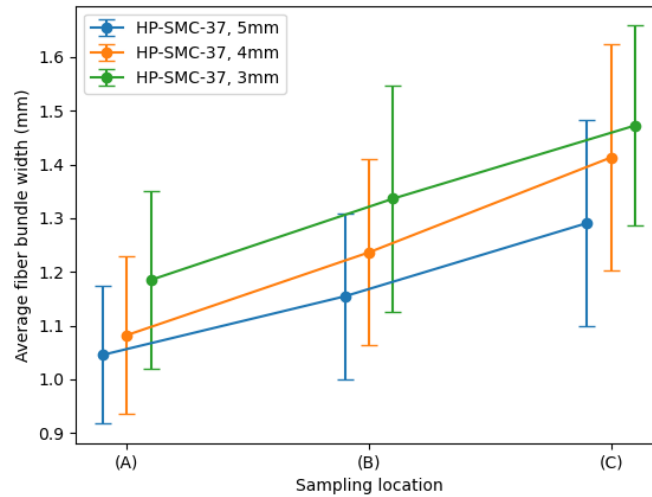


Figure 2.10: Evolution of the fiber bundle width with respect to the flow length in the HP-SMC-37. The error bars represent the standard deviation of measured fiber bundle widths for each sample.

The last deformation modes correspond to a mix between the two previous mechanisms, where the fiber bundles are bent and open up. At a certain level of deformation, the individual

filaments inside the fiber bundles split up, partially or totally. We refer to this mechanism filamentization (Oter-Carbonell, 2018). Sometimes, the fiber bundles appear to be split into smaller fiber strands, as is the case for the Reg-SMC-18 in Figure 2.6, and are probably already separated in the initial material. Filamentization occurs mainly for higher deformations, when the fiber bundles become undistinguishable due to the spreading of fibers from the bundles. The most obvious case is that of Soft-SMC-18 represented in Figure 2.11, which exhibits both the in-plane bending and the fiber spreading. For this case, the second invariant is also close to 1 ($I_2 = 0.95$) and indicates an isotropic distribution of local orientations. The filamentization is also clearly observable for the LF-SMC-18 material, and partially for the HP-SMC-24, where glass fibers in the form of short needles are intermingled with fiber bundles in an entangled and disordered mesostructure.

The filamentization is likely the most important degradation mechanism observed in the tomographic scans, as it must affect both the rheology of the SMC material and its mechanical performance, as the fibrous reinforcement is highly deformed, curved, with many misalignments between the fibers.

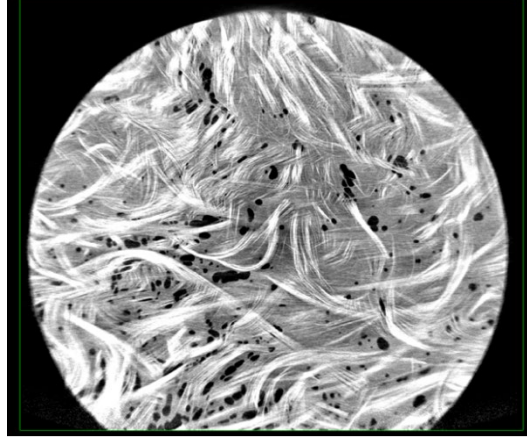


Figure 2.11: Filamentized fiber bundles (Soft-SMC-18, 3mm, (C)).

To summarize the different observations by X-ray tomography of the five SMC materials:

- **Different deformation modes** of the fibrous reinforcement are observed.
- The **reorientation** of fiber bundles is marked for the lower fiber content and relatively short fibers.
- **For high fiber contents**, fiber bundles do not align, have deformed cross-sections, and open up.
- **For long fibers**, filaments **undergo in-plane bending**, with no preferential orientations.
- **For high deformations**, the fiber bundles can **filamentize**, by spreading out from the bundle and bending, and tend to **separate into individual disordered filaments**.

These deformation mechanisms influence and evolve into different types of SMC mesostructures, depending on the material design parameters and the processing conditions. Moreover, the description of the fiber bundle population cannot be reduced to only the

description of orientations for industrial SMC materials, as this would neglect other deformation modes and the physical mechanisms involved in these transformations.

The stochastic behavior of such discontinuous materials is postulated at the mesoscale by the inherent variability of deformations of the mesostructure, and at the macroscale by irregular flow patterns and the occurrence of large defects indicative of the solid behavior of the fibrous reinforcement.

It confirms that the contacts between the fiber bundles and the solid behavior of the fibrous reinforcement play a significant role in the deformation of SMC materials during the compression molding process.

2.3 Geometric descriptors of fiber bundle stack mesostructures

2.3.1 Introduction

X-ray tomography of SMC materials reveals complex mesostructures, with intricate fiber bundles exhibiting different deformation modes depending on the manufacturing parameters. Such deformation mechanisms cannot be explained only as a result of the polymer viscous forces applied to the fibrous reinforcement. Internal forces related to the mechanical loading of the fiber bundles through the thickness of the material also need to be considered.

In order to develop a suitable mechanical model for these discontinuous and random fibrous mesostructures, it is necessary to model the material mathematically, introducing geometrical descriptors which contain structural information of the fiber bundle arrangement. Usually, complex materials are described using geometrical descriptors such as n-point correlation functions, or other mathematical objects based on this family of functions, very well documented in (Torquato, Random heterogeneous materials: microstructure and macroscopic properties, 1991). However, it is always difficult to find the most appropriate descriptors and relate them to the mechanical behavior of these complex materials.

Here, an approach based on integral geometry is developed to obtain geometrical descriptors of the SMC fibrous mesostructures from a theory adapted to address the randomness of these materials, and creation of contacts between the fiber bundles.

2.3.2 Definition and assumptions

A *stack* is a set of solid objects of arbitrary shapes, deposited on a surface and in contact with each other. The structure of the stack depends strongly on the geometry of the objects and their distributions. If the deposition or the geometry of the objects is random, we speak of *random stacks*.

First, we will consider a special case of random stacks for which the objects are oriented in the plane. This class of stacks will be called *planar random stacks*.

A large number of objects are randomly deposited on a planar surface. The direction normal to the plane defines the vertical direction in which the objects are stacked. Initially, the objects are assumed to be identical, thin, slender fibers, but generalizations will be discussed, especially for fiber bundles which have a thicker geometry.

The fibers have length l , width w and thickness e (see Figure 2.12). Then, the thinness and slenderness assumption is written:

$$e \leq w \ll l \quad (2.2)$$

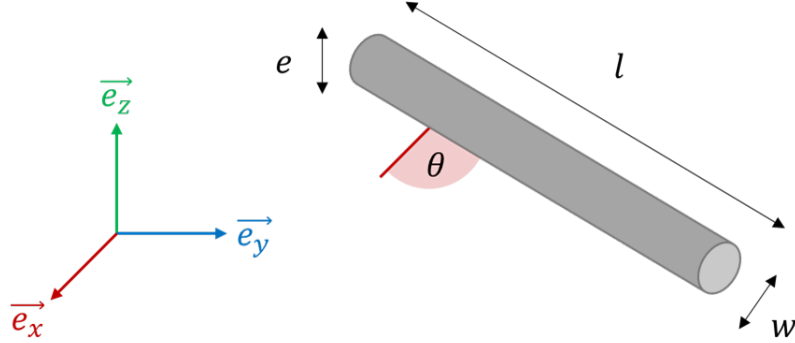


Figure 2.12: Geometrical dimensions of a fiber.

For the time being, geometrical dimensions are defined according to the intuitive notions of length, width and thickness. Objective definitions are as follows.

The fibers are deposited with a uniform distribution on the planar surface, and a uniform angular distribution in the horizontal plane.

In the absence of mechanical force, the structure resulting from the stacking of the fiber bundles will contain many empty air spaces also referred to as voids. We will call this particular state *bulky stack*. The fibers simply lie on top of each other when they are in contact. The objective of this section is to describe this state mathematically and to calculate macroscopic descriptors from the fiber geometry.

If forces are applied vertically to reduce the void space within the stack, the state will be called as a *compacted stack*.

An intermediate state of the stack will be one where it collapses under the effect of a body force, such as gravity, without inducing contact forces (or the resulting contact force will be neglected). We will denote this state as *packed stack*, which will be studied later.

2.3.3 Mathematical derivation of the stack

2.3.3.1 Introduction to integral geometry

The description of such random stacks belongs to the field of integral geometry (Deltheil, 1919), (Stoka, 1968), (Santaló, 1976), (Seneta, et al., 2001). It corresponds to the field which studies problems with connections between random events and geometrical quantities, and more precisely, its objective is to define invariant measures on geometric spaces from their symmetry properties.

The most famous case of integral geometry is the Buffon's needle problem (Buffon, 1733). It was the first example which combined geometry and probabilities and it can be adapted to address the problem of random stacks.

In the Buffon's needle problem, a small needle is dropped on a set of lines, which are classically the lines separating the planks of a floor, and the question is to calculate the probability that the needle crosses one of these lines (see Figure 2.13). The needle's length is noted l , the width of a plank is $a \geq l$. The angle between the direction of the lines and the needle is θ .

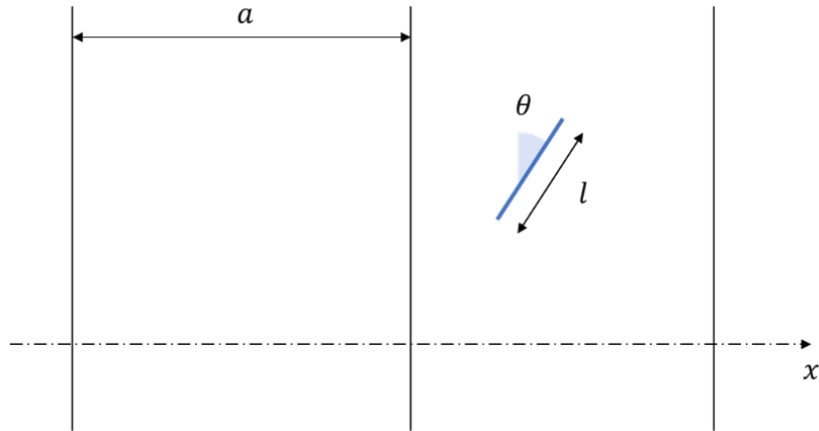


Figure 2.13: Buffon's needle problem.

The resolution of this problem involves the description of all the possible crossing configurations between the needle and a line. Using the symmetry of the repeated lines, the set of all the different configurations of the needle corresponds to $[0, \pi] \times [0, a]$. To intersect a line, the needle must fall within the vertical band $[-\frac{l}{2}|\sin \theta|, +\frac{l}{2}|\sin \theta|]$ around the line. Then, the probability that the needle crosses a line is:

$$p = \frac{\int_0^\pi l |\sin \theta| d\theta}{\int_0^\pi \int_{-a/2}^{a/2} dx d\theta} = \frac{2l}{\pi a} \quad (2.3)$$

A simple variant of this problem has been formulated for curved fibers. It is the Buffon's noodle problem (Barbier, 1860), easily solved by Barbier considering curved fibers of length l as concatenated small needles of length dl . Thanks to the linearity of the expectation operator, the problem for curved fibers simply reduced to Buffon's needle problem by integration along the fiber:

$$p = \frac{\int_0^\pi \int_0^l |\sin \theta| dl d\theta}{\int_0^\pi \int_{-a/2}^{a/2} dx d\theta} = \frac{2l}{\pi a} \quad (2.4)$$

The quantity $|\sin \theta| dl d\theta$ is called the *kinematic measure* and is the basis of the formalism of integral geometry. The kinematic measure is defined as a measure on a set of configurations which is invariant under rigid motions. It quantifies the number of different configurations that exist in a probabilistic set defined on a geometric space.

The first application of the kinematic measure for curves is the Crofton formula (Crofton, 1868), which directly generalizes the Buffon's noodle problem. Consider two intersecting curves of finite length, respectively denoted by l and l' , and calculate the number of intersections that

exist for all possible configurations of the two curves. This quantity of intersections is given by:

$$\int n(l \cap l') d\Gamma = \int_0^{2\pi} \int_0^l \int_0^{l'} |\sin \theta| dl' dl d\theta \quad (2.5)$$

where $n(l \cap l')$ is the number of intersections between the two curves for a given configuration, Γ is the continuous space of all the configurations and θ is the local relative angle between the two small segments dl and dl' . This result establishes that the average number of intersections between two curves with random orientations does not depend on their respective curvatures and is a strong result of integral geometry which leads to many non-trivial geometrical results (the reader is invited to refer to (Santaló, 1976) for more details).

In the general case of finite curves, the kinematic measure is given by:

$$d\vec{l} \wedge d\vec{l}' \wedge d\Omega = |\sin(\theta)| dl dl' d\theta = \|d\vec{l} \times d\vec{l}'\| d\theta \quad (2.6)$$

where \wedge denotes the exterior product in differential algebra, and $d\Omega$ represents the angular element of the space ($d\Omega = |\sin(\theta)|d\theta$ in 2D, and $d\Omega = |\sin(\theta)|d\theta d\varphi$ in 3D using the spherical coordinate angles θ and φ).

2.3.3.2 Application to random stacks of in-plane fibers

Integral geometry allows one to count the different stacking configurations and characterize the random stack from the geometry of fibers.

The formation of the fiber stack results from two mechanisms. To place a fiber in the stack, it must cross another fiber already placed. The fiber is then stacked on top of the other one. From then on, it will not be possible to place a new fiber under it. Stacking is a balance between the effects of length, which favors the placement of new fibers, and the effects of covered area when a new fiber is added to the stack.

To define this statistical equilibrium which occurs during the fiber stacking, we define the *Lagrangian of the stack*. Consider two populations of fibers, denoted (i) and (j) . Each population is made of identical fibers. We will denote respectively $d\vec{l}^{(i)}$ and $d\vec{l}^{(j)}$ the local vectors describing small length elements of the fibers of each population, and ϕ_i, ϕ_j the fiber volume fractions of each population. The fibers of both populations have the same width $w \ll l^{(i)}, l^{(j)}$.

It is assumed that a small quantity $d\phi_j$ of fibers from population (j) are laid on a quantity ϕ_i of population (i) . The kinematic measure of the resulting intersections is $\phi_i (d\vec{l}^{(i)} \wedge d\vec{l}^{(j)} \wedge d\Omega) d\phi_j$. This is for the length effects. For the area effects, one must consider the kinematic measure of the intersection between a long fiber (the added fiber) and a convex planar body (the in-placed fiber). The kinematic measure related to the area covering is $s_j d\phi_j$, where $s_j = l^{(j)}w$ is the projected area of the fiber. It represents the different positions of contacts on the fiber which are evaluated several times in the measure of the intersections. The variation of the Lagrangian is defined as the variation of the number of stacking configurations and is written as:

$$d\mathcal{L} = \phi_i (d\vec{l}^{(i)} \wedge d\vec{l}^{(j)} \wedge d\Omega) d\phi_j - s_j d\phi_j \quad (2.7)$$

After the integration, the Lagrangian of the stack is of the form:

$$\mathcal{L} = \frac{1}{2} \vec{\phi} \cdot \mathbb{S} \cdot \vec{\phi} - \vec{s} \cdot \vec{\phi} \quad (2.8)$$

where $\vec{\phi}$ is the vector of the volume fractions for each population, \vec{s} is the vector of the fiber areas of each population. The matrix \mathbb{S} is the *measuring operator*, whose elements are the kinematic measures $\mathbb{S}_{ij} = \int d\vec{l}^{(i)} \wedge d\vec{l}^{(j)} \wedge d\Omega$ of the intersections between the two fiber populations (i, j) .

The bulky stack, and especially its volume fractions $\vec{\phi}^*$, are defined with respect to the statistical equilibrium described by the Lagrangian of the stack:

$$\vec{\phi}^* = \arg \min_{\vec{\phi}} \mathcal{L} \iff \overline{\mathbb{S}} \cdot \vec{\phi}^* = \vec{s} \quad (2.9)$$

The *bulky volume fraction* ϕ^* is defined as the volume fraction of the bulky stack, i.e., $\phi^* = \sum_k \phi_k$.

The Lagrangian formalism of Eqs. (2.8) and (2.9) implies that the fiber volume fraction of a random stack is determined by a linear system of equations, which gives a simple description of the stack for various cases, as illustrated below.

Monodisperse population of fibers:

For a population of identical fibers with random planar orientations, the bulky volume fraction is:

$$\phi^* = \frac{1}{r} \quad (2.10)$$

with $r = l/w \gg 1$, the aspect ratio of the fibers.

Bidisperse population of fibers:

For a population of fibers of length $l^{(i)}$ and $l^{(j)}$, and of width w , the vector of the bulky volume fractions is:

$$\vec{\phi}^* = \begin{pmatrix} p_i / r^{(i)} \\ p_j / r^{(j)} \end{pmatrix} \quad (2.11)$$

with $r^{(i)}$ and $r^{(j)}$ the aspect ratios of the two groups of fibers, p_i and p_j are the fractions related to the number of fibers of each group, such as $p_i + p_j = 1$.

Phase and population equilibria:

The Lagrangian formalism allows one to impose constraints on the distribution of each group of fibers. In the case of a bidisperse population with $\phi_i^* = \phi_j^*$, the phase equilibrium constraint is added to the Lagrangian using a Lagrangian multiplier λ :

$$\mathcal{L} = \frac{1}{2} \vec{\phi} \cdot \mathbb{S} \cdot \vec{\phi} - \vec{s} \cdot \phi - \lambda(\phi_i - \phi_j) \quad (2.12)$$

The minimization of Eq. (2.12) gives:

$$\phi_i^* = \phi_j^* = \frac{1}{r^{(i)} + r^{(j)}} \quad (2.13)$$

It corresponds to a parallel assembly of two groups of fibers.

At the other extreme one can use the condition of population equilibrium $p_i = p_j$. The minimization of the Lagrangian in that case gives:

$$\phi_i^* = \frac{1}{2r^{(i)}}, \quad \phi_j^* = \frac{1}{2r^{(j)}} \quad (2.14)$$

which is a serial assembly of two groups of fibers.

2.3.3.3 Generalization to arbitrary planar orientation distributions

As seen in the previous examples, the Lagrangian formulation allows one to calculate the fiber volume fraction of random stacks for various cases. The linearity of the system of Eqs. (2.9) allows one to consider a population of fibers with identical or variable characteristics, as well as to split this population into groups with different properties. Thus, we can complete the Lagrangian formulation of Eq. (2.8) by weighting the populations by their respective statistical distributions.

In the general case, the planar orientation distribution $\psi(\theta)$ is defined as the probability to observe a fiber oriented at an angle θ . Following the developed integral geometry framework, this orientation distribution represents the global orientation for straight fibers and the local orientations for curved fibers.

In the case of identical straight fibers, the measuring operator of Eq. (2.8) becomes:

$$\mathbb{S} = \int \int \|\vec{l}(\theta) \times \vec{l}'(\theta')\| \psi(\theta, \theta') d\theta d\theta' = \alpha l^2 \quad (2.15)$$

where $\psi(\theta, \theta') = \psi(\theta)\psi(\theta')$ for independent orientations.

Solving Eq. (2.15) leads to an *angular factor* α , which measures the ratio of the current and the random distribution of orientations:

$$\alpha = \frac{\pi}{2} \int_0^{2\pi} \int_0^{2\pi} |\sin(\theta - \theta')| \psi(\theta, \theta') d\theta d\theta' \quad (2.16)$$

If the angular distribution corresponds to an isotropic distribution, the angular factor is maximum and is equal to 1. For an arbitrary distribution, $0 \leq \alpha \leq 1$, and it tends toward zero when the distribution is reduced to a single direction. It is noticed that the calculation of the angular factor corresponds to the calculation involved in the resolution of the Buffon's needle problem.

A mechanical interpretation of the angular factor would be the measure of the shear stretch to deform a configuration with initially random orientations into a configuration where fibers are partially aligned in definite directions.

In a more general case fibers are not straight, but curved in the plane. Then, they can intersect each other at multiple points, which leads to a multiplicity of the counted configurations in the definition of the Lagrangian of the stack. To avoid this redundancy in the calculation of the measuring operator, we introduce the *shape parameter* c as the average number of contacts between two intersecting fibers. This is a function of the geometry of the fibers and its direct calculation uses mathematical tools of integral geometry. Some examples of calculations are detailed in the following.

The measuring operator becomes in the general case:

$$\mathbb{S} = \frac{\alpha l^2}{c} \quad (2.17)$$

We deduce from this result the general expression of the bulky volume fraction as a function of the three descriptors of the stack:

$$\phi^* = \frac{c}{\alpha r} \quad (2.18)$$

which allows one to calculate the volume fractions of stacks for arbitrary planar objects, as detailed in the sequel.

2.3.3.4 Application to random stacks of planar objects

Here, the calculation of the bulky volume fraction is detailed for some basic cases that will be validated numerically in Section 2.4. The considered objects are all convex. Then, the calculation of the three descriptors can be simply carried out considering the perimeter of the objects as curved fibers.

Stack of disks

The simplest case involving planar objects is the case of stacked disks or thin cylinders. The shape parameter is simply $c = 2$, as there are always two crossings between two disks. As all the local orientations along the circles are equally distributed, the angular factor is $\alpha = 1$. Finally, the aspect ratio is reformulated into:

$$r = \frac{l}{w} = \frac{l^2}{s} \quad (2.19)$$

defining the “width” w of the disk from its area s and its perimeter l according to $s = lw$. Then, the aspect ratio is $r = 4\pi$, and the bulky volume fraction of stacked disks is:

$$\phi^* = \frac{1}{2\pi} \simeq 16\% \quad (2.20)$$

It is noticed that, using the isoperimetric inequality (Steiner, 1838), this value corresponds to the maximum volume fraction for a planar bulky stack.

Stack of tapes

The second case addresses the stack of rectangular tapes of length l_f and width w_b (see Figure 2.14). The calculation of the kinematic measure implies to move the tape around the other one. Then, the total surface which allows the contact between the two tapes defines different areas easily expressed in terms of the geometrical dimensions of the tape. Here, we introduce two angular factors related to the orientation θ of the tapes:

$$\alpha_b = \frac{\pi}{2} \langle |\sin(\theta - \theta')| \rangle \quad \beta_b = \frac{\pi}{2} \langle |\cos(\theta - \theta')| \rangle \quad (2.21)$$

which describes the angular alignment or misalignment with respect to the tapes and not to the fibers.

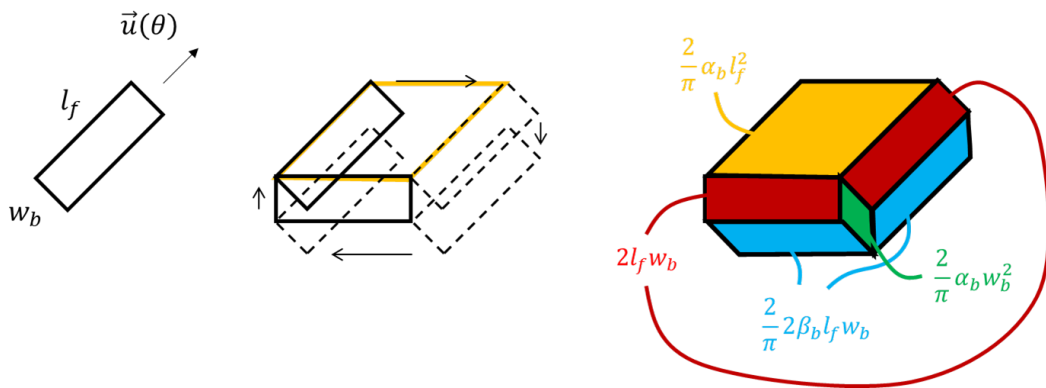


Figure 2.14: Calculation of the kinematic measure of tapes.

It comes from the method of the moving tape that the different descriptors are:

$$c = \frac{\alpha_b r_b + 2\beta_b + \alpha_b r_b^{-1}}{\alpha_b r_b + 2\beta_b + \pi + \alpha_b r_b^{-1}} \quad \alpha = \frac{\alpha_b r_b + 2\beta_b + \alpha_b r_b^{-1}}{r_b + 2 + r_b^{-1}} \quad r = r_b + 2 + r_b^{-1} \quad (2.22)$$

with $r_b = l_f/w_b$. Finally, the bulky volume fraction for planar tapes is:

$$\phi^* = \frac{c}{\alpha r} = \frac{1}{\alpha_b r_b + 2\beta_b + \pi + \alpha_b r_b^{-1}} \quad (2.23)$$

Here, we retrieve that the maximum value of ϕ^* is obtained for aligned tapes. Then, $\alpha' = 0$ and $\beta' = \frac{\pi}{2}$. The maximum bulky volume fraction is also equal to $\phi^* = \frac{1}{2\pi}$.

It can be noticed that for planar convex objects, the bulky volume fraction is directly given by the application of Santaló formula (Santaló, 1952), which is a generalization to planar convex objects of the Crofton formula. This result gives the number of intersections between two convex objects of perimeter l_1, l_2 and area s_1, s_2 as:

$$c = \frac{4\alpha l_1 l_2}{2\pi(s_1 + s_2) + \alpha l_1 l_2} \quad (2.24)$$

In the case of identical objects, the combination of Eq. (2.19) and (2.24) leads to the expression of the bulky volume fraction for planar convex objects as:

$$\phi^* = \frac{c}{\alpha r} = \frac{1}{\alpha r + \pi} \quad (2.25)$$

We deduce that the minimum value of αr is π .

Remarks on the planar stacks

Here, results have been derived for different geometries of stacked objects, linking problems for convex objects to fiber considerations. Using general results from integral geometry, bulky volume fractions can be calculated directly as a function of object shape (c), orientation (α), and dimensions (r), each of which being described by a descriptor of the stack. The reasoning applied to tapes introduces two scales of the descriptors: a set of global descriptors (c_b, α_b, r_b) at the scale of the global object, viewed as group of fibers or a fiber bundle, and a set of local descriptors (c, α, r) related to fibers. Global descriptors extend local definitions but require more complex integral geometry tools to perform the analytical calculations. Conversely, local descriptors are simpler to calculate, but their meaning is attached to the local curvilinear geometry of the objects. Regardless of the description chosen, the method has proven to be robust by directly extending the 1D fiber formulas to 2D objects, thanks to the integral definitions of the descriptors that allow to link these two classes of problems. Moreover, in the same way as the case of the straight fibers has been extended to curved fibers accounting for the multiplicity of contacts by the shape parameter c , the case of the convex planar objects can be generalized to any planar objects defining a higher order shape parameter, but this case corresponding to objects with holes will not be considered here.

Now, considering fibers as slender tapes, we have seen that the bulky volume fraction of a stack of fibers is bounded, with a maximum value if $\frac{1}{2\pi}$ (under the assumptions of planar bulky stacks). Eq. (2.18) of the bulky volume fraction is valid for fibers in the limit of $\alpha r \gg 1$. If fibers are not slender or highly aligned, the 1D representation will not be physically valid and the width of the fiber must be considered. Therefore, in what follows, we will distinguish *fibers* viewed as the 1D mathematical representation of the material line of an object, and *fiber bundles* as a 3D thin object in volume, which physically corresponds to a group of fibers.

The proposed geometrical description of planar random stacks and the numerical validations have been published in (Mahé, et al., 2021).

The current description is based on the assumption of planar fiber orientation to define a stack made of horizontal layers. We will generalize this framework to 3D objects and justify why the assumption of planar stack is directly a consequence of the thinness and slenderness property of the fibers.

2.3.3.5 Generalization to volume objects

From the beginning, the bulky stacks are characterized from the definition of the Lagrangian of the stack and the measuring operator. Returning to the initial reasoning that established the form of the Lagrangian, the bulky volume fraction results directly from an enumeration of the spatial configurations between two objects in contact, the measuring operator measures the set of all the crossing configurations between the planar objects, while the second term of the Lagrangian in Eq. (2.8) describes all the possible locations of the contact on the object. Then, denoting Ω the *measure of the contact configurations*, the bulky volume fraction is simply:

$$\phi^* = \frac{1}{\omega} \quad (2.26)$$

More precisely, ω designates the partition function of the set of all contact configurations. The notion of partition function will be developed in detailed in Chapter 3.

For example, the measure of intersections between two identical fibers, regardless of their orientation, corresponds to the ratio of the length by the width, or equivalently to the ratio of the length square l^2 divided by the fiber projected area $s = lw$. For disks, the measure of the configurations corresponds to the angle 2π , as by symmetry, the first contact point can be fixed, and the second intersection point will be in the interval $[0, 2\pi]$, each position representing a different configuration.

The proposed framework of integral geometry can be finally generalized to any type of stacked objects, as the tools of integral geometry also have appropriate algebraic properties in 3D.

Consider a convex 3D object in space. At any point on its surface, it is possible to define a collection of tangential fibers in all the directions of the tangential plane. It is the generalization of the concatenation of small length elements in the planar case. This collection is called the tangent bundle of the surface of the object. Then, taking each of these fibers independently, all the framework can be reformulated and extended for 3D convex objects.

In particular, it is possible to associate to each element on the surface of the object an average fiber element integrating the kinematic measure over the fibers of the tangent bundle. It results in:

$$d\vec{l} = \left(\frac{\kappa_I + \kappa_{II}}{2} \right) d\vec{s} \quad (2.27)$$

where κ_I and κ_{II} are the local principal curvatures of the surface. It is noticed that the direction of the length element corresponds to the normal vector of the surface.

Then, the aspect ratio in 3D can be written equivalently from the three descriptions:

$$r = \underbrace{l/w}_{1D} = \underbrace{l^2/s}_{2D} = \underbrace{\kappa^2 s}_{3D}, \quad \text{with } w = \frac{1}{\kappa} \quad (2.28)$$

where κ is the arithmetic average $\frac{\kappa_I + \kappa_{II}}{2}$ over the surface s of the object.

From there; the geometrical dimensions of the object can be generalized into objective definitions: the thickness e is the ratio of the volume over the outer area of the object, the width w is the inverse of the average curvature, and the length l (also called perimeter in integral geometry) is the ratio of the surface over the width:

$$e = \frac{v}{s} \quad w = \frac{1}{\kappa} \quad l = \frac{s}{w} = \kappa s \quad (2.29)$$

In the case of thin and slender fibers, these definitions tend toward the intuitive geometrical notions. For thin and slender fiber bundles, with a specific cross-sectional shape, a prefactor in the definition of the length will take into account the area of the cross-section. For example, in the case of an elliptical cross-section, $l = \frac{\pi}{4} l_f$, where l_f is the fiber length.

The angular factor is now defined from the surface normal vectors:

$$\alpha = \frac{\pi}{2} \langle \|\vec{n} \times \vec{n}'\| \rangle \quad (2.30)$$

The shape parameter in 3D is still the number of contacts on average between two objects. Here, for 3D convex objects, it is simply:

$$c = 1 \quad (2.31)$$

Finally, the bulky volume fraction in 3D can still be formulated according to Eq. (2.18).

In general, the calculations of the descriptors are too difficult in 3D to be carried out analytically, but it can be verified that the given definitions reduced to the 2D cases correspond well with the previous results. Then, the planar objects correspond from the 3D representation of two planar objects separated by a thin thickness. However, the 3D problem can still be formulated as a configuration measurement problem in the form of Eq. (2.26) which is more useful and has more important consequences.

The simpler example in 3D is the stack of identically spheres. Consider two spheres in contact, the measure of all the contact configurations is 4π (the solid angle). It is really similar to the

result for the disks in the plane (Eq. (2.20)). Then, the bulky volume fraction of stacked spheres is:

$$\phi^* = \frac{1}{4\pi} \simeq 8\% \quad (2.32)$$

Here, we consider all the orientations of the spaces to make the contact between the two spheres, which is not necessarily the case.

For arbitrary stacks, the volume fraction is the inverse of the measure of the contact configurations between two objects. Now, if we consider a simple transformation of the stack, as under the application of gravity, the number of possible contact configurations between two objects will be divided by 2, as the new added object cannot make contact from below. It will represent the main difference between 3D and 2D stacks of planar objects.

Removing one planar symmetry divides the number of configurations by 2, so the volume fraction is multiplied by 2. In the following, we will distinguish the bulky volume fraction, which is the unloaded volume fraction in the more general case according to the chosen space representation, and the *packed volume fraction*, which corresponds to the unloaded stack after removing the symmetry conditions. We will keep the same notation ϕ^* to designate the packed volume fraction, as for the description of SMC mesostructures, these two definitions will be equivalent.

The main example of removing the symmetries is still for the stacked spheres. The application of the gravity removes one symmetry. However, due to the double curvature of the sphere, the application of the gravity must force it to rotate in a certain direction. As a consequence, two other orthogonal symmetry planes are removed. At the end, 8 symmetries are canceled, so the sphere volume fraction is multiplied by 8. The packed volume fraction of sphere is:

$$\phi^* = \frac{2}{\pi} \simeq 64\% \quad (2.33)$$

To the best of our knowledge, this value is a very well-known experimental result in the field of granular media, but its analytical determination is still an open problem (Torquato, et al., 2000), (Donev, et al., 2004), (Song, et al., 2008), approximated by several methods (Berryman, 1983), (Ciamarra, et al., 2006) and confirmed experimentally (Scott & Kilgour, 1969), (Mehta, 1994).

In a similar way, consider stacked parallel cylinders (as it is the case with the fibers inside a fiber bundle), the bulky volume fraction is $\frac{1}{2\pi}$, and removing the vertical symmetry, plus the symmetry from the cylinder curvature, the packed volume fraction is $\phi^* = \frac{2}{\pi} \simeq 64\%$. It is the same value than for the spheres.

For planar objects with random orientations, as for fiber bundles, the packed volume fraction is simply twice the value of the bulky volume fraction. From the 3D representation, the angular factor is 1 for a 3D isotropic distribution and $\frac{1}{2}$ for a transverse isotropic distribution. Considering a square cross-section, the aspect ratio is $2 \frac{l_f}{w_b}$ as the two faces (upper and lower) are considered in the calculation of the aspect ratio.

From the macroscale, at the scale of the stack, the effects of the symmetries are also observable. The bulky stack of spheres considers a contact angle belonging to the solid angle 4π . We saw that the packing divides by 8 the number of configurations, and so far, the contact angles. Then, the angular factor for the packed stack is $\alpha = \frac{1}{8}$. It means that the contact angles between two spheres are reduced in average to a cone of solid angle $\frac{\pi}{2}$, that corresponds to a slope of 22.5° , which is also another well-known experimental value (Barabási, et al., 1999).

In (Mahé, et al., 2021), we also discussed the numerical results of (Sommer, et al.), where the authors numerically studied stacks of square platelets. The application of the gravity reduced the volume fraction by a factor 2, according to prediction for planar objects.

The relationship between the volume fraction (bulky or packed) and the symmetries of the stack is an important result which help to extend the geometrical description to arbitrary stacks in 2D or 3D. It proves also that for thin and slender objects, as fiber bundles in SMC mesostructures, the geometrical packing of the 3D isotropic stack induces a planar stack, which justifies the use of results obtained in 2D in the case of stacks of long fiber bundles.

2.3.4 Summary

In this Section, we proposed a generic geometrical framework, based on integral geometry, to describe random stacks. In a general case, the **volume fraction of a stack is equal to the inverse of the measure of the contact configurations** between two objects. This notion will be developed in Chapter 3 where we developed a statistical mechanics framework to model the constitutive behavior of a mechanically loaded stack. In simple cases, as for stacks of fiber bundles, **three geometrical descriptors have been obtained to determine the fiber bundle volume fraction** of the stack:

- The **aspect ratio** $r = l/w$ (where the length l and the width w are viewed as the generalized length and width for 3D objects, but reduces to the intuitive geometrical notion for thin and slender fiber bundles.
- The **angular factor** $\alpha = \frac{\pi}{2} \langle \|\vec{n} \times \vec{n}'\| \rangle$ (where \vec{n} and \vec{n}' are the normal or direction vector of the objects) measures the effects of the alignment and the orientation distribution.
- The **shape parameter** c is the average number of contacts between two objects. It is a function of the non-convexity of the object, but here it will be considered as 1 for straight fiber bundles.

The calculation of these descriptors and the volume fraction have been performed for different class of stacks, demonstrating the generality of this framework, and leading to a strong relationship with the symmetries of the stack.

In Section 2.4, a numerical generator of planar stacks is implemented to validate the different calculations in 2D and especially for stacks of fiber bundles.

2.4 Implementation of a mesostructure generator and numerical validations

2.4.1 Objectives

An implementation of the stacking algorithm is proposed to validate the geometrical descriptors proposed in Section 2.3 for various configurations of planar stacks and fiber bundle geometries, using a periodic deposition domain. The code is implemented in Python3 using available packages. The resulting mesostructures are reconstructed in 3D to be exported and visualized in Paraview.

2.4.2 Implementation

In this work, the fiber bundles are assumed to be 1D thin and slender objects. Other geometries with 2D shapes will be addressed as tapes or disks in a second step.

The fiber bundles are generated from four scalars: the $(x, y) \in [0, L]^2$ coordinates above a planar deposition area of side length L , an angle in the plane $\theta \in [0, 2\pi]$, and the fiber length l_f . These scalars can result from any given random or fixed functions.

```
# ~~~ Initialize the bundles ~~~
coord = np.random.rand(nbundles, 2)*SIZE
angle = np.random.rand(nbundles)*np.pi
length = np.ones(nbundles)*LENGTH
```

The fiber bundles are deposited according to their position on a square planar and periodic domain of size L . The domain has a torus periodicity, so a fiber bundle exiting from the right side will reappear on the left side, and the same applies to the two other sides. The periodicity limits the boundary effects and simulate an infinite domain for large enough side length.

The objective of the algorithm is to find all the intersections between the fiber bundles to build the stack. The complete code is given in Appendix I with the mechanical solver derived in Chapter 3.

The periodicity is handled by copying the generated fiber bundles into three domains represented in Figure 2.15. To limit the increasing size of the memory, only the fiber bundles within a square of size $L + l$ (where l denotes for the maximum fiber length) centered on the original domain are copied.

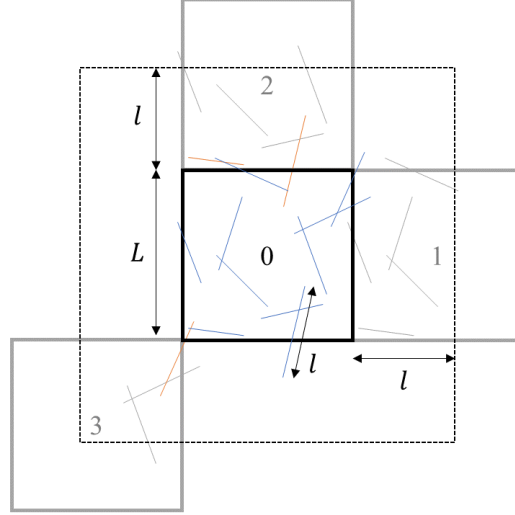


Figure 2.15: Periodic domain repetition. The dotted frame delimits the domain where the fiber bundles are copied. The orange fiber bundles indicate the additional intersections due to the torus periodicity.

A first search for close fiber bundles is carried out, considering the intersections of circular domains around each fiber bundle, with a circle diameter equal to the fiber length. The repeated pairing of fiber bundles due to the periodicity is eliminated.

```
# ~~~ Find close bundles ~~~
pairwise_dist2 = pdist(coord, 'sqeuclidean')
pairwise_ids = np.vstack(np.triu_indices(len(coord), k=1)).T
diameter2 = np.sum(length[pairwise_ids], axis=1)**2/4
close_ids = pairwise_ids[np.where(pairwise_dist2<diameter2)[0]]
```

From the list of the close fiber bundles, the intersection coordinates between the fiber bundles are calculated. Firstly, the intersections are calculated as if the fiber bundles were of infinite length.

```
# ~~~ Calculate line intersections ~~~
x, y = coord.T
a = np.tan(angle-SMALL)
b = y-a*x
a, b = a[close_ids], b[close_ids]
xint = np.diff(b)/(SMALL-np.diff(a))
yint = np.mean(a*xint+b, axis=1).reshape(-1, 1)
```

Secondly, the intersections of finite length fiber bundles are determined keeping the intersection points lying closer than half the length of the fiber bundles to their centers.

```
# ~~~ Determine segment intersections ~~~
intersect_dist2 = (x[close_ids]-xint)**2 + (y[close_ids]-yint)**2
intersect_mask = np.multiply(*(intersect_dist2<=length[close_ids]**2/4).T)
intersect_ids = close_ids[intersect_mask]
intersect_coord = np.hstack([xint[intersect_mask], yint[intersect_mask]])
```

A last step allows one to remove the last repetitions of crossings due to the periodicity. At this moment, all the intersections between the fiber bundles are known, accounting for the periodicity of the domain. To stack the fiber bundles, a loop is implemented to increment successively the altitude of the fiber bundles when they are added above the previous one. The

order of deposition is given by the index of each fiber bundle during the generation of the coordinates and the orientations. To significantly speed up the loop, the package `numba` is used.

```
def stack(layer, intersect_ids):
    for i, j in intersect_ids:
        layer[j] = max(layer[j], layer[i]+1)
    return layer

layer = stack(np.zeros(NBUNDLES, dtype=int), intersect_ids)
```

The output of the code contains all the spatial position of the fiber bundles, the coordinates of all overlaps between the fiber bundles and the curvilinear coordinates of the overlaps along the relevant fiber bundles.

The fiber bundles can be also reconstructed in 3D to generate a volume mesh of the stacked fiber bundles. The packages `pyvista` and `vtk` are used. Each fiber bundle is generated initially as a cylinder, which is then rescaled to obtain the dimensions of the fiber bundle and an elliptical cross-section (see Figure 2.16). The meshes of all fiber bundles are combined to create the volume mesh of the stack which can be exported and viewed into the visualization software Paraview as shown in Figure 2.17.

To stack bodies with other geometries, the code has been modified to concatenate the straight fibers and make polygonal geometries as large tapes (see Figure 2.18). It is also used to model folded fiber bundles with a specific angle (see Figure 2.19). Finally, disks may be stacked using the program by stopping the code to the search of close bodies (see Figure 2.20).

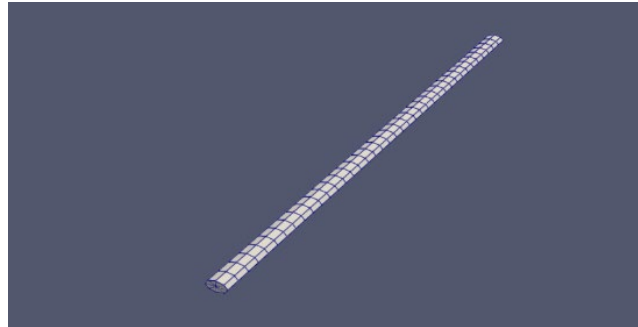
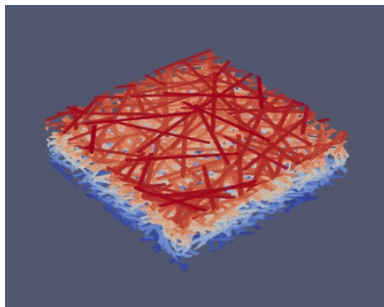
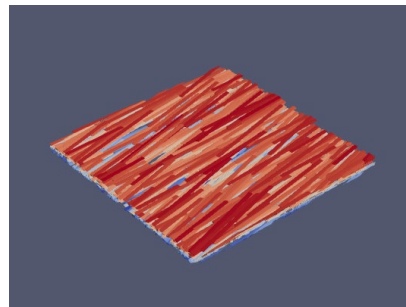


Figure 2.16: 3D view of a fiber bundle in the stack ($l = 25\text{mm}$, $w = 1\text{mm}$, $e = 0.5\text{mm}$).

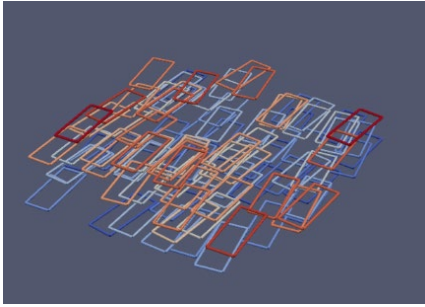


(a)

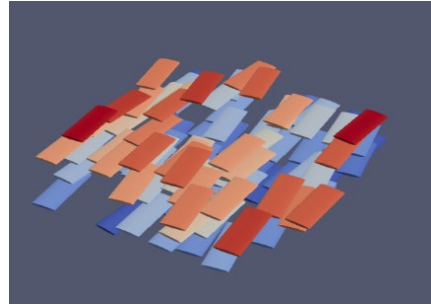


(b)

Figure 2.17: Stack of 600 fiber bundles of length 25mm on a square periodic domain of side length 50mm. The colors represent the vertices of the mesh to distinguish the fiber bundles.
(a): Transverse isotropic distribution; (b): Aligned fiber bundles.



(a)



(b)

Figure 2.18: Stack of 100 large tapes (length 25mm, width 1mm, thickness 0.1mm) on a square domain with length of 50mm. The colors represent the vertices of the mesh to distinguish the tapes.
(a): Construction with the tape contours as concatenated lines; (b): Stack with reconstructed 3D tapes.

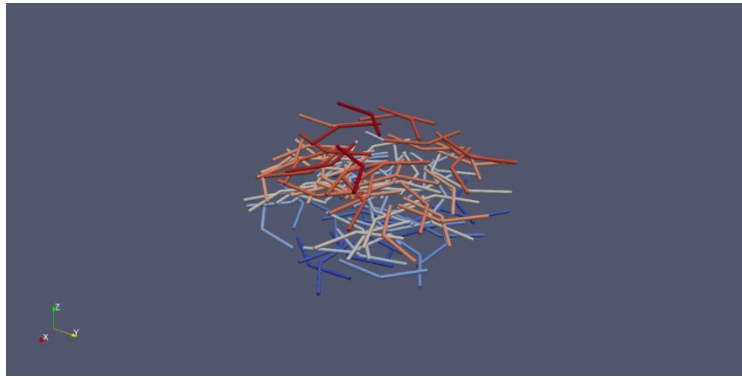


Figure 2.19: Stack of 100 curved fiber bundles of length 25mm on a square domain with length of 50mm. The curvature angle is fixed at 45° . The colors represent the vertices of the mesh to distinguish the fiber bundles.

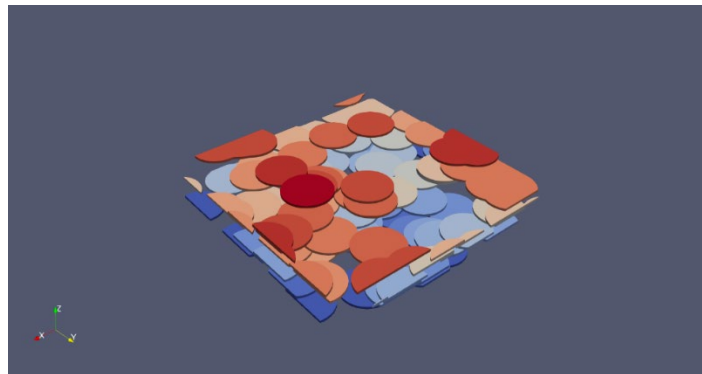


Figure 2.20: Stack of 100 disks of diameter 10mm on a square periodic domain of side length 50mm. The colors represent the vertical coordinate of the disks.

2.4.3 Method

From the proposed stacking algorithm, different cases have been studied to validate the analytical model of planar stacks presented in Section 2.3.

For the fiber bundles, the fiber length is $l_f = 25\text{mm}$, and the domain of size is $L = 125\text{mm}$. The fiber bundle has elliptical cross-section, of width $w_b = 1\text{mm}$ and thickness $e_b = 0.1\text{mm}$, to reproduce the usual dimensions encountered in SMC materials. Simulations with a random distribution have been realized using increasing number of fiber bundles: $N = 250, 1000, 4000$ and 8000 . For each case, 20 stochastic realizations are considered to calculate average properties.

From the bulky volume fraction, the bulky thickness is determined as:

$$h^* = \frac{Nv}{L^2\phi^*} \quad (2.34)$$

where v is the volume occupied by one fiber bundle. We deduce the number of fiber bundles per layer $N(z) = \frac{Ne_b}{h^*}$, with e_b the fiber bundle thickness, which will be compared to the numerical results to assess the convergence of the results.

The effects of the orientation distribution are studied in the same way, considering a uniform distribution in the interval $[-\gamma, \gamma]$ for a decreasing value of $\gamma \in [0, \frac{\pi}{2}]$. According to the definition of the angular factor, it is given in that case by:

$$\alpha = \sin \gamma \quad (2.35)$$

The effects of the shape parameter are verified with the curved fibers of Figure 2.19 for an increasing angle of curvature γ .

The effects of the aspect ratio are verified for the more general case of the rectangular tapes, for an increasing value of the tape aspect ratio. The volume fractions will be compared to the analytical values and the approximation for a fiber with $\frac{1}{r}$.

The convergence of the bulky volume fraction is tested for various geometries of planar objects and the convergence with the size of the deposition domain is verified. Simulations for random tapes, aligned tapes, square platelets and disks published in (Mahé, et al., 2021) can complete the analysis.

2.4.4 Results

Figures 2.27 to 2.30 show the evolution of the number of fiber bundles through the thickness of the stack for an increasing number of deposited fiber bundles. The results for the 20 realizations per configuration are represented in gray lines on the left figures, while the average values over the 20 realizations and the standard deviations are represented on the right figures. The numerical results are compared with the analytical predictions for a perfect stack, represented by a black rectangle of length the bulky thickness h^* and height the expected number of fiber bundles $N(z)$.

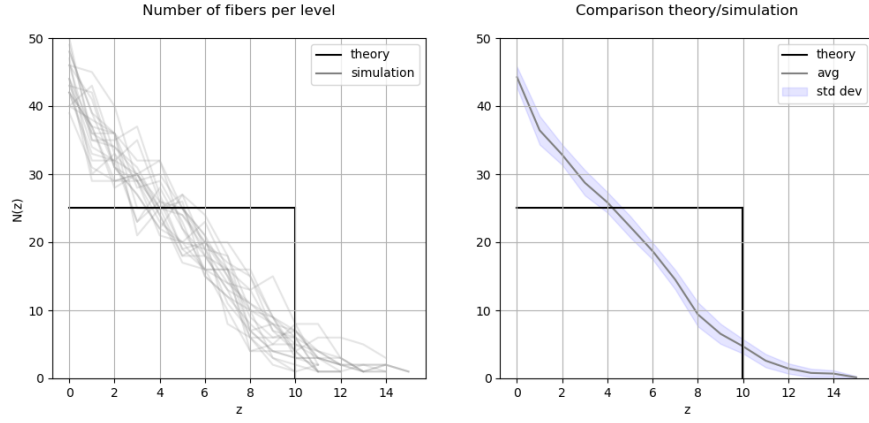


Figure 2.21: Through-thickness evolution of the number of fiber bundles for $N = 250$.

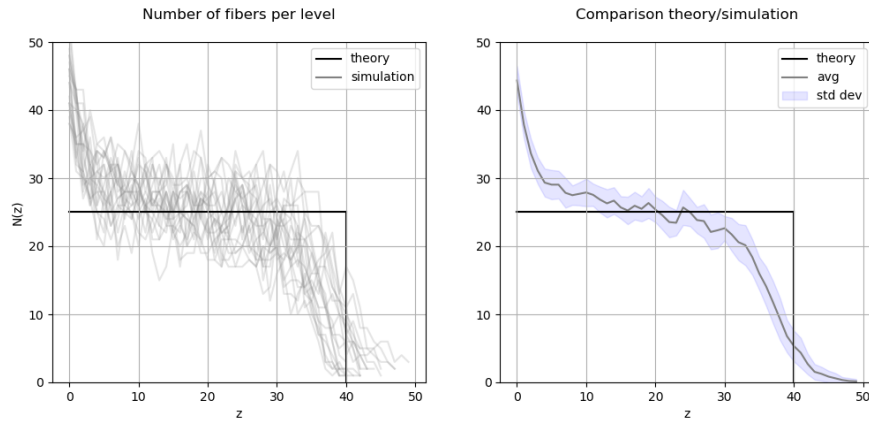


Figure 2.22: Through-thickness evolution of the number of fiber bundles for $N = 1000$.

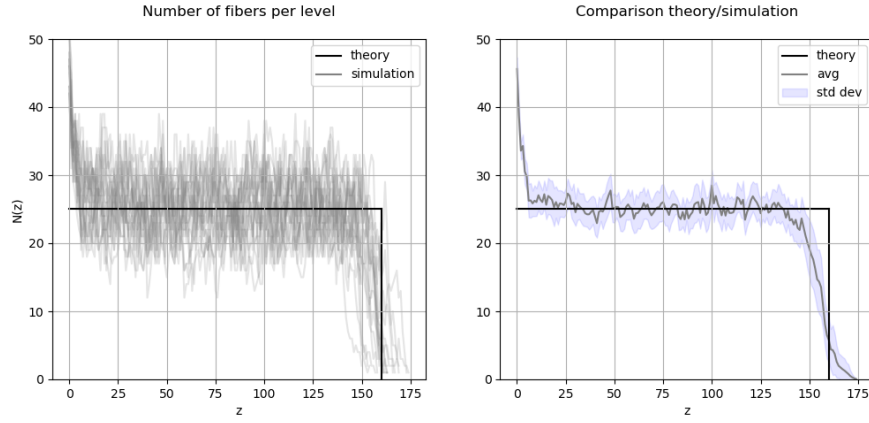


Figure 2.23: Through-thickness evolution of the number of fiber bundles for $N = 4000$.

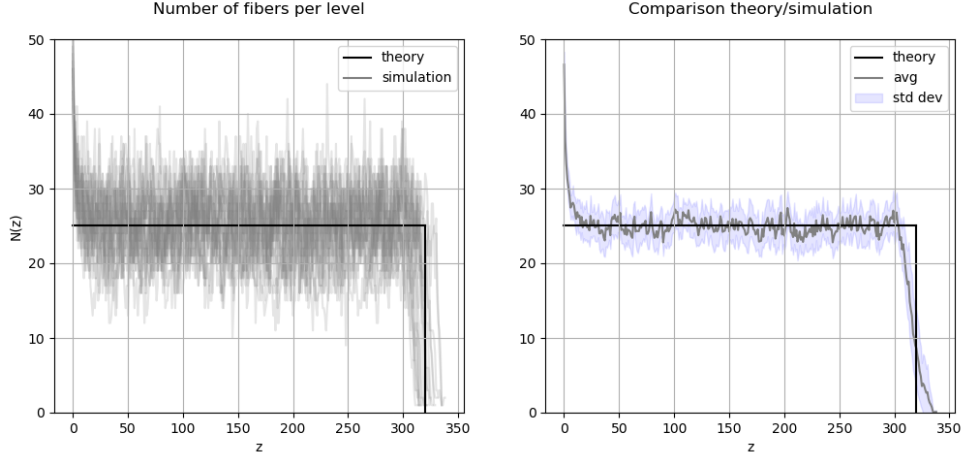


Figure 2.24: Through-thickness evolution of the number of fiber bundles for $N = 8000$.

Figure 2.25 shows the evolution of the angular factor between a random orientation distribution ($\alpha = 1$) and a unidirectional distribution ($\alpha = 0$) and compare the value of the angular factor with the ratio of the bulky volume fraction by the one for the random distribution, for 50 random realizations generated with different values of γ (the orientations are distributed in the angular interval $[-\gamma, \gamma]$). In a same way, Figure 2.26 compares the dependence of the volume fraction within the curvature of the fibers, with 50 realizations generated for an angle between 0 (straight fibers) and π (folded fiber). The calculated average number of contacts per fiber is compared with the ratio of the volume fraction by the value for straight fibers. In Figure 2.27, the bulky volume fraction calculated from 50 realizations generated with tapes of different aspect ratios is compared with the analytical solution for stacked tapes, and the approximation for slender fibers. Figures 2.34 to 2.36 show the volume fraction as a function of the number of stacked objects for various geometries. Figure 2.31 shows the evolution of the volume fraction of 20 realizations of fiber stacks for an increasing domain size.

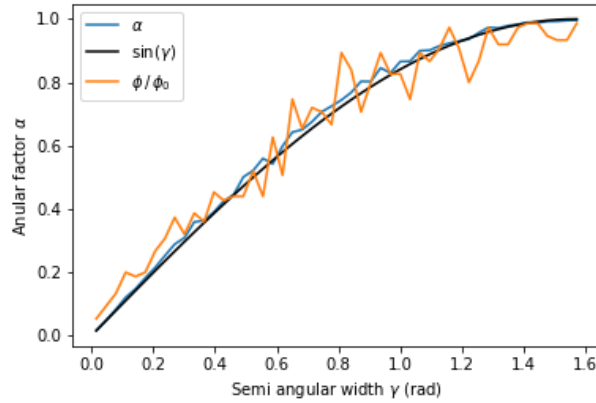


Figure 2.25: Comparison of the angular factor (in blue) with the theoretical value (black) and the value determined from the bulky volume fraction (orange) for 50 random realizations with orientation distributions parametrized by the angle $\gamma \in [0, \frac{\pi}{2}]$.

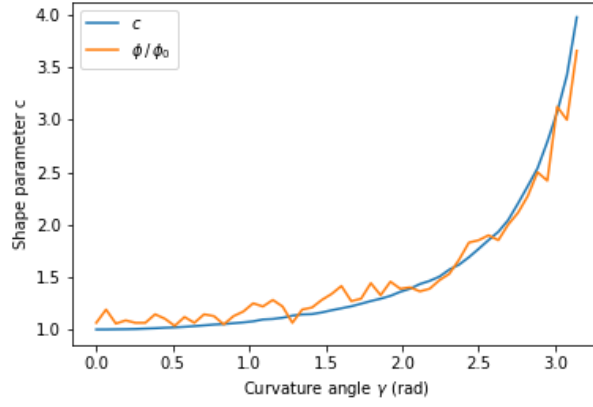


Figure 2.26: Comparison of the shape parameter (in blue) with the approximated value (black) and the value determined from the bulky volume fraction (orange) for 50 random realizations with different curvature angles $\gamma \in [0, \frac{\pi}{2}]$.

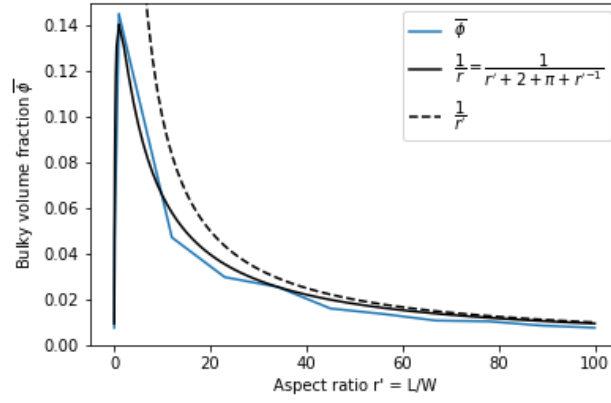


Figure 2.27: Comparison of the bulky volume fraction (in blue) with the analytical value (orange) and the approximation for slender fibers (black) for 50 random realizations with an aspect ratio $\frac{L}{w} \in [0, 100]$.

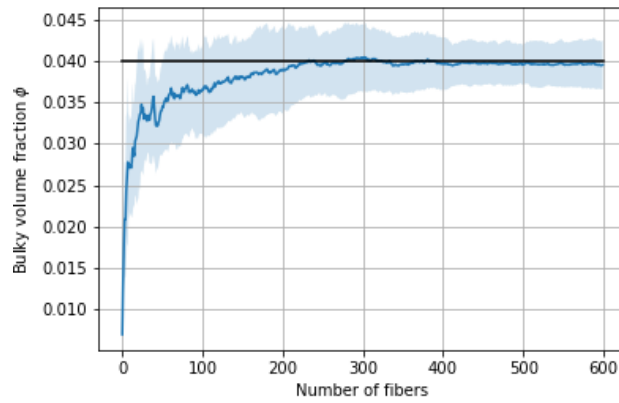


Figure 2.28: Convergence of the bulky volume fraction with the number of fibers (25mm x 1mm) for 20 random realizations on a domain of 60mm. The average value over the realizations (continuous blue line) is compared with the theoretical value given by the stack description (black line). The blue envelope gives the interval \pm the standard deviation around the average value.

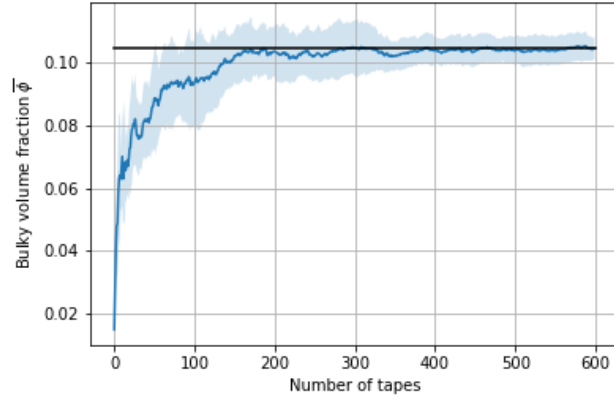


Figure 2.29: Convergence of the bulky volume fraction with the number of tapes (25mm x 6mm) for 20 random realizations on a domain of 100mm. The average value over the realizations (continuous blue line) is compared with the theoretical value given by the stack description (black line). The blue envelope gives the interval \pm the standard deviation around the average value.

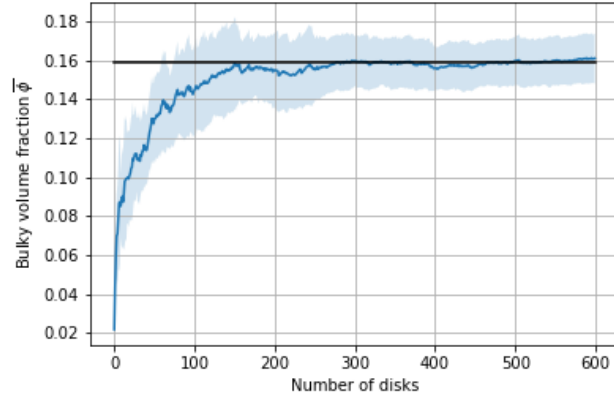


Figure 2.30: Convergence of the bulky volume fraction with the number of disks (diameter of 10mm) for 20 random realizations on a domain of 100mm. The average value over the realizations (continuous blue line) is compared with the theoretical value given by the stack description (black line). The blue envelope gives the interval \pm the standard deviation around the average value.

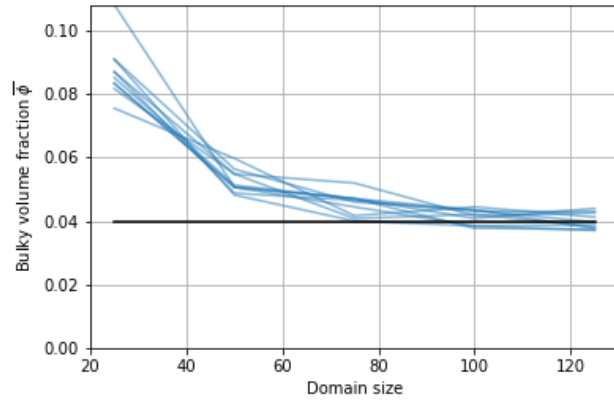


Figure 2.31: Convergence of the bulky volume fraction with the size of the deposition domain with 100 fibers (25mm x 1mm) for 20 random realizations (gray). The average value over the realizations (continuous blue line) is compared with the theoretical value given by the stack description (black line). The blue envelope gives the interval +/- the standard deviation around the average value.

2.4.5 Analysis and discussion

Figures 2.27 to 2.30 clearly show that the distribution of fiber bundles per layer converges toward the ones of the analytical model. The through-thickness distributions present a similar boundary effect for all the configurations, with a higher value along the deposition plane, and a smaller value for the top layers. This is explained by the fact that the layers are not at the statistical equilibrium in these cases. In the interior of the stack, the distribution converges rapidly toward the predicted value when the number of fiber bundles increase, with approximatively 10 layers of fiber bundles to reach the average density per layer, which represent a very small thickness for the bulky stack.

Figures 2.31 to 2.37 shows good agreements with respect to the analytical and approximated solutions. The numerical results follow the theoretical evolution of the geometrical descriptors, which validate the derivation of the bulky volume fractions as a function of the descriptors. The applications to the planar objects converge also rapidly toward the analytical value of the bulky volume fraction, with approximatively 10 layers to reach the average density of objects.

It is noticed that the obtained volume fraction, especially in the case of fiber bundles, is very low compared with industrial values encountered in industrial SMC applications. It indicates that the bulky stack model is not sufficient to describe real SMC mesostructures, which are in reality compacted by the calendaring step at the end of the manufacturing process. For a regular SMC with fiber bundles of dimensions 25mm x 1mm x 0.1mm, the bulky volume fraction is:

$$\phi^* = \frac{\pi}{100} \simeq 3.14\% \quad (2.36)$$

and considering the fiber volume fraction within a bundle of $\frac{\pi}{2} \simeq 64\%$, it is even less. Whereas an industrial SMC material has usually a fiber volume fraction between 15% up to 40%. It means that the initial stack is compacted several times, inducing an important deformation of the stack which will be the subject of Chapter 3.

2.4.6 Summary about the description of random stacks

The implemented stacking algorithm have been used to verify the proposed mathematical description of random stacks. Various geometries of planar objects have been studied, and parametric studies on the three geometrical descriptors validate the approach. The numerical results showed a fast convergence toward the analytical predictions in the core of the stack, which requires around 10 layers to reach the average densities of objects. In the same way, the top layers are incomplete due to the random deposition process and but can also be neglected for sufficiently thick stacks.

2.5 Conclusion

In this Chapter, industrial SMC materials with custom manufacturing parameters have been molded under an industrial press to observe the macroscopic patterns of flow and the internal mesostructures by X-ray tomography. The main observations are:

- The **complex and irregular flow patterns at the macroscale**, suggesting a mix of fluid and solid deformations.
- **Different transformation mechanisms of the fibrous mesostructure**, depending on the parameters of the fibrous reinforcement.
- Possible **reorientations of the fiber bundles are limited for high fiber contents**, the fiber bundles appear to be compacted.

A first approach to describe the fibrous SMC mesostructures and its different kinematics of transformation has been developed with a general framework of integral geometry. It allows to predict the volume fraction of an unloaded random stack with **three geometrical parameters of the stack** representing respectively the shape effect of the fiber bundles (c), the orientation effect (α) and the dimensional effect (r). A generalization of this framework allows one to obtain original results for planar and volume objects to help to validate the proposed approach.

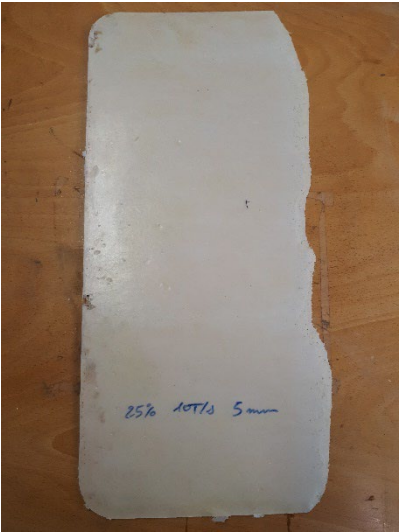
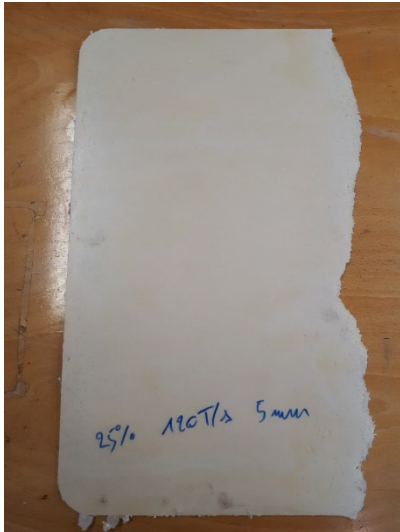
Finally, a **numerical stacking algorithm has been developed to simulate realistic SMC mesostructures** and validate the geometrical framework and the model of planar for SMC materials.

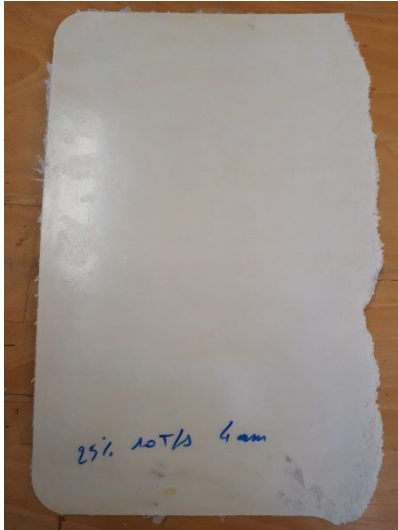
The proposed geometrical description of SMC mesostructures as bulky planar stacks returns very low values of fiber volume fractions, inconsistent with real SMC materials. This significant difference indicates the necessity to compact the fibrous mesostructures to reach high volume fractions, which corresponds to the calendaring step at the end of the SMC manufacturing process (Org  as & Dumont, 2011). The compaction of the fibrous network is likely to induce contact forces between the fiber bundles, modifying the global behavior of the fibrous reinforcement with some degree of cohesion by friction, which does not exist in classical suspension media.

Appendices

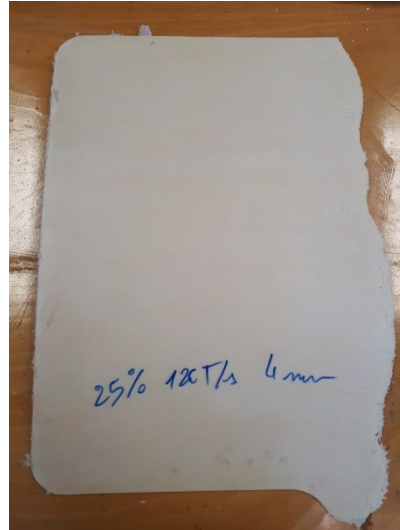
2.A. Incomplete parts molded in the industrial hydraulic press

The pictures of the final incomplete parts are given. The variability of the flow front is clearly observable. The weight of all the plates is given to determine the origin of the shape difference. All the parts have the same width of 600mm on their left side. Each column represents the same material at the same final thickness using two different compression velocities.

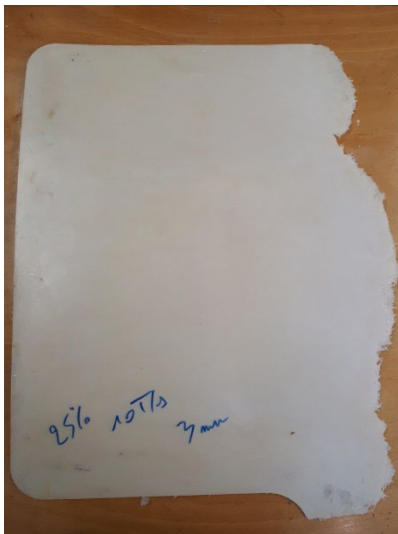
10 T/s	120 T/s
	
Reg-SMC-18, 10T/s, 5mm 751g	Reg-SMC-18, 120T/s, 5mm 989g



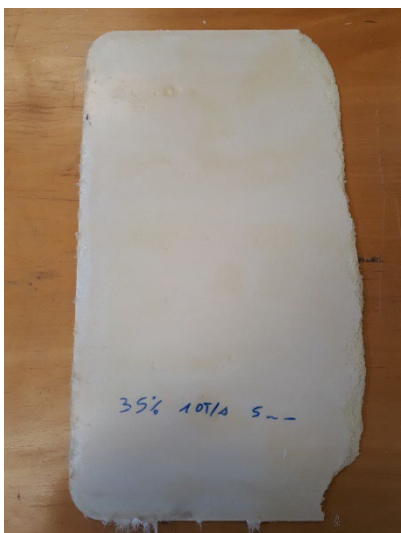
Reg-SMC-18, 10T/s, 4mm
911g



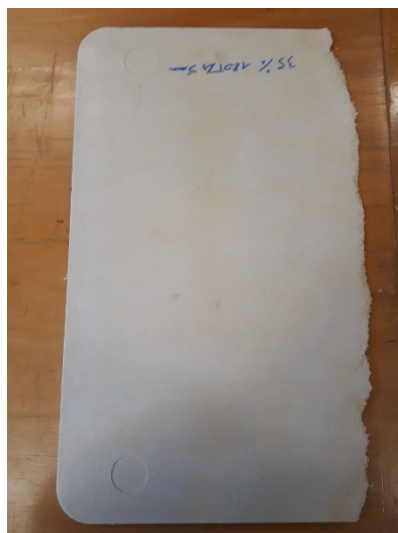
Reg-SMC-18, 120T/s, 4mm
990g



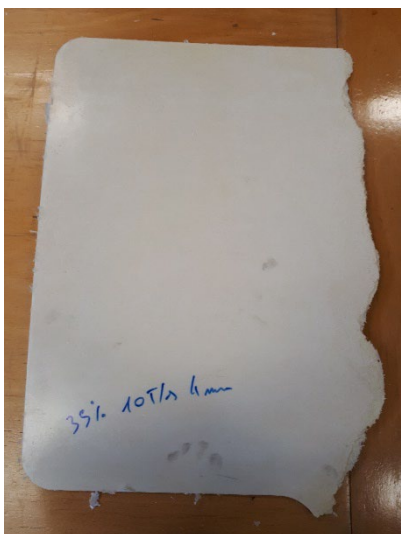
Reg-SMC-18, 10T/s, 3mm
907g



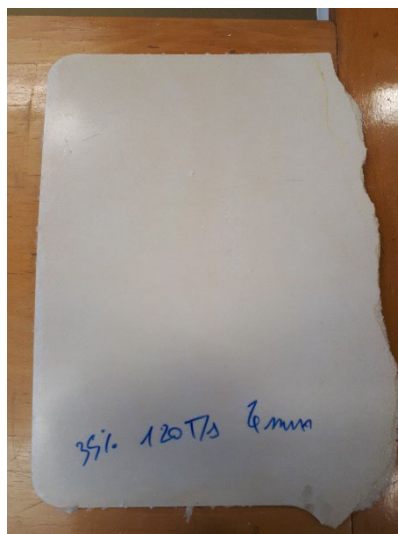
HP-SMC-24, 10T/s, 5mm
1000g



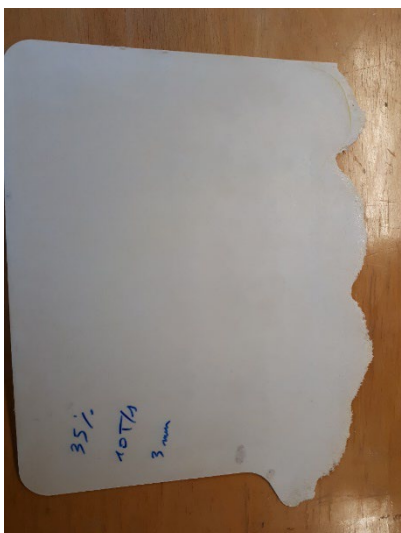
HP-SMC-24, 120T/s, 5mm
1063g



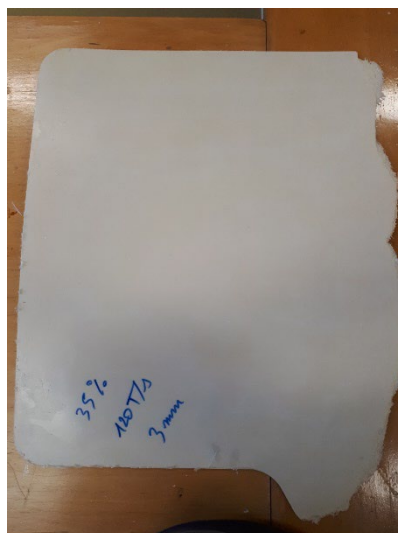
HP-SMC-24, 10T/s, 4mm
1066g



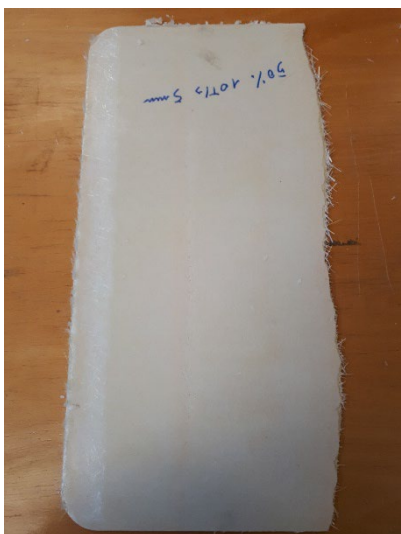
HP-SMC-24, 120T/s, 4mm
1055g



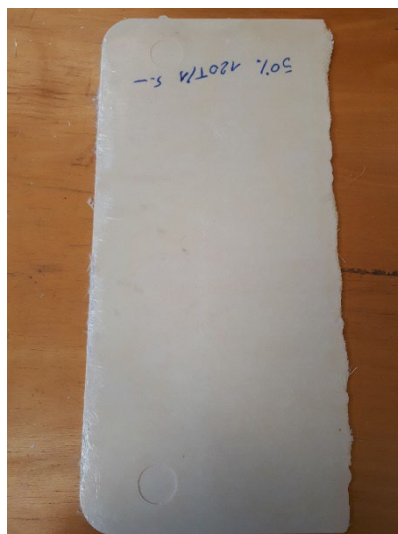
HP-SMC-24, 10T/s, 3mm
1022g



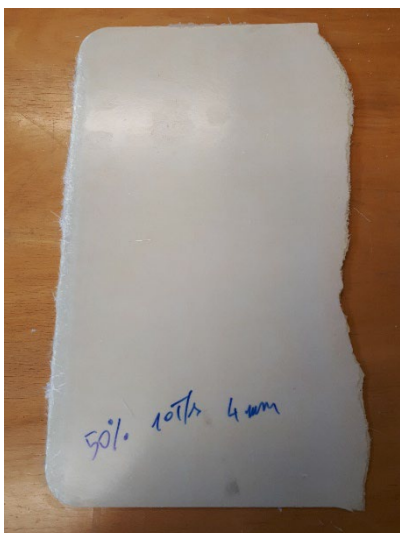
HP-SMC-24, 120T/s, 3mm
1009g



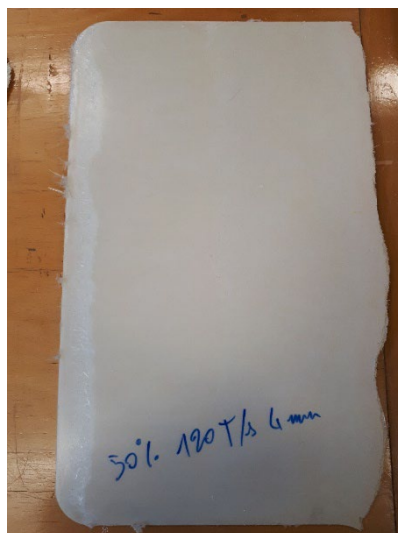
HP-SMC-37, 10T/s, 5mm
1100g



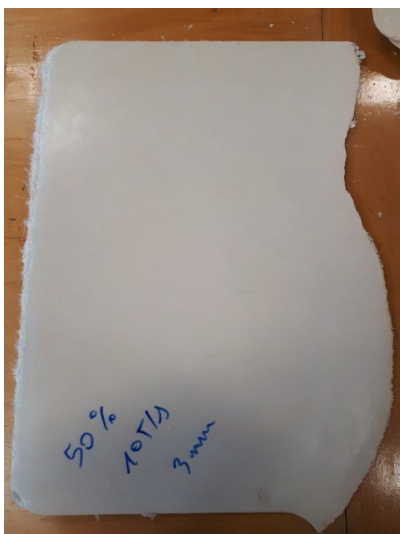
HP-SMC-37, 120T/s, 5mm
1051g



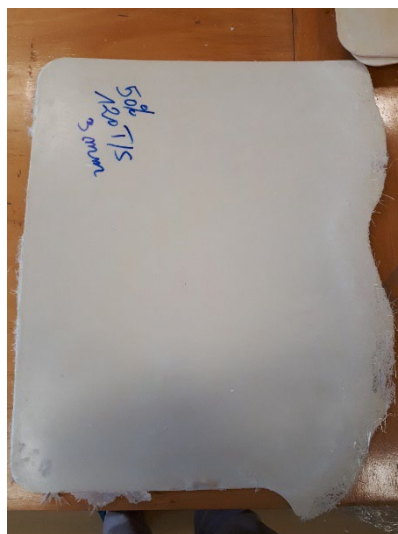
HP-SMC-37, 10T/s, 4mm
1088g



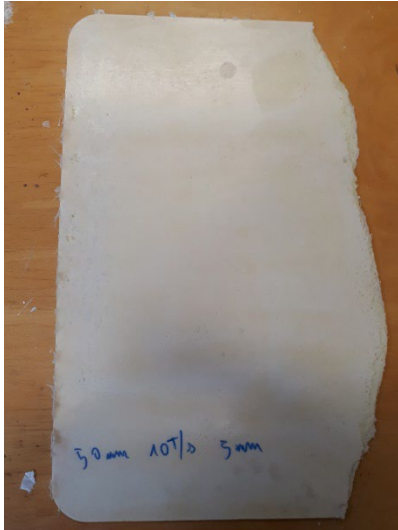
HP-SMC-37, 120T/s, 4mm
1092g



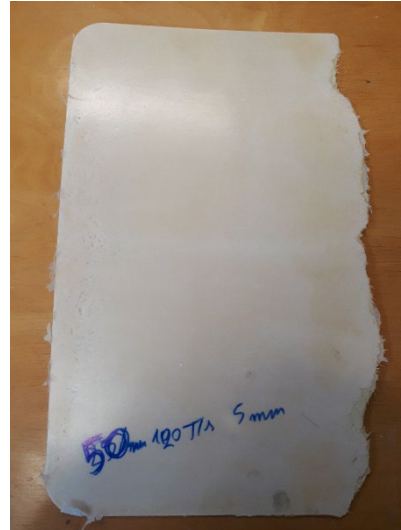
HP-SMC-37, 10T/s, 3mm
1055g



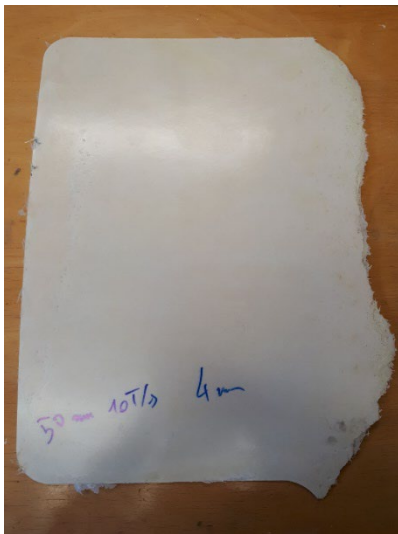
HP-SMC-37, 120T/s, 3mm
1060g



LF-SMC-18, 10T/s, 5mm
979g



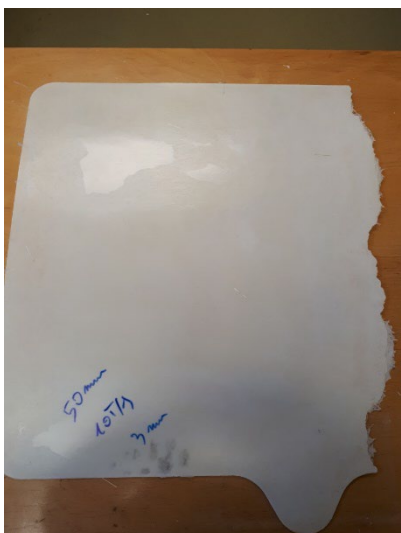
LF-SMC-18, 120T/s, 5mm
1028g



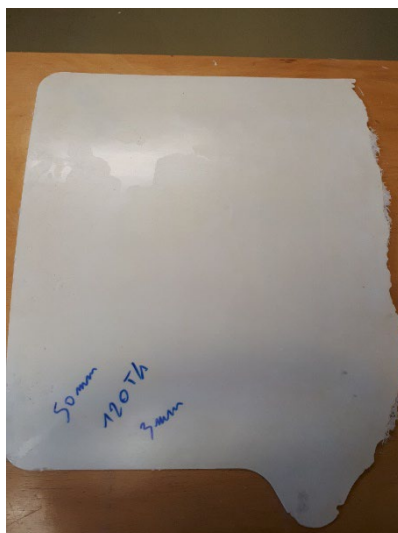
LF-SMC-18, 10T/s, 4mm
998g



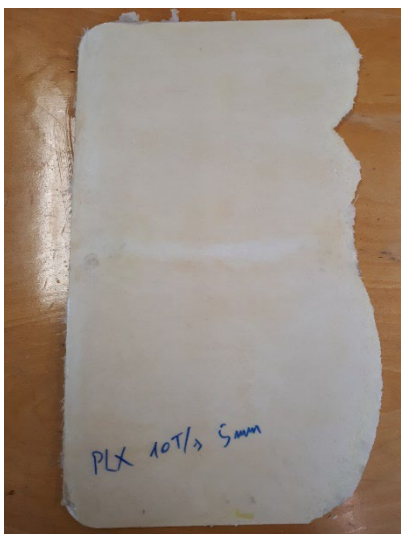
LF-SMC-18, 120T/s, 4mm
992g



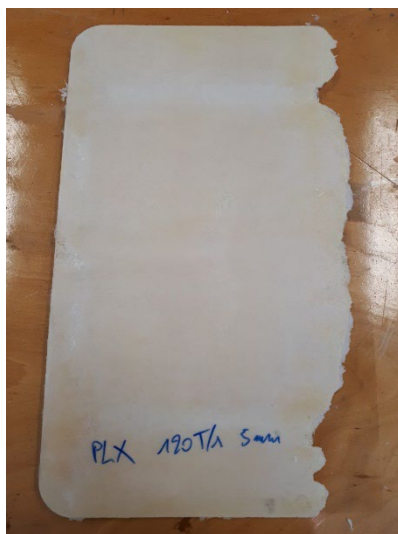
LF-SMC-18, 10T/s, 3mm
1032g



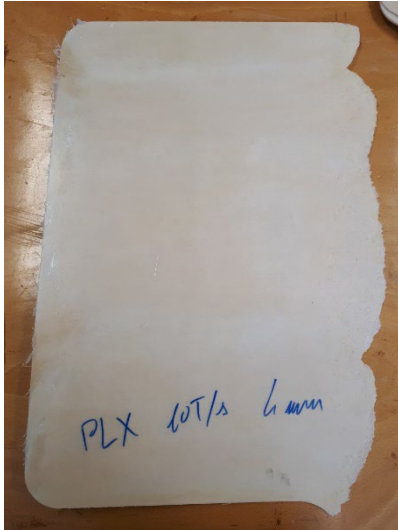
LF-SMC-18, 120T/s, 3mm
1006g



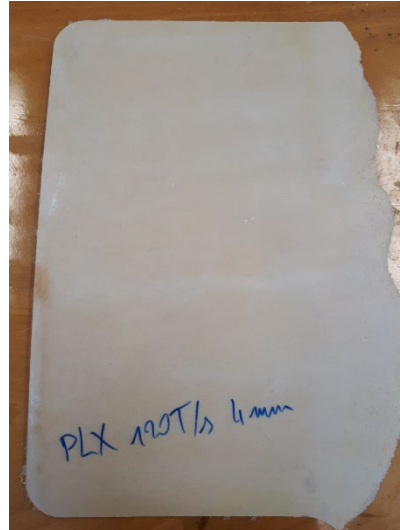
Soft-SMC-18, 10T/s, 5mm
985g



Soft-SMC-18, 120T/s, 5mm
1001g



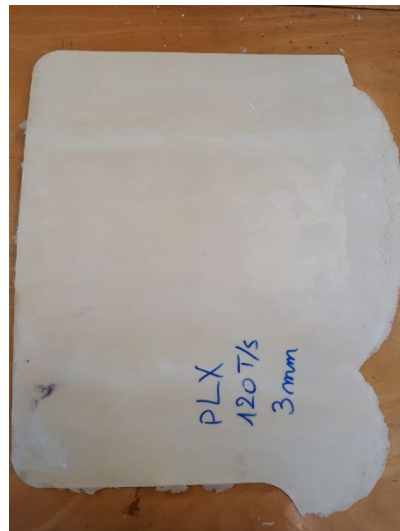
Soft-SMC-18, 10T/s, 4mm
977g



Soft-SMC-18, 120T/s, 4mm
948g



Soft-SMC-18, 10T/s, 3mm
1043g



Soft-SMC-18, 120T/s, 3mm
912g

2.B. Qualitative observations of the flow patterns and the compressed SMC material

The observation of the short shots, made with different material and molding conditions, shows a similar global pattern of filling with mostly unidirectional flow of the SMC material. A certain

variability of the flow length is observed for the same final thickness, which can be explained by the variability of the quantity of material in each ply. This variability comes partially from errors due to cutting of the fibers, but mainly from the variable distribution of material in SMC rolls due to the manufacturing process.

At the flow front, parabolic lobes are present at different locations of various sizes, highlighting a random character of the flow of SMC materials, independent of the mold. The flow is not purely unidirectional, with possible local shearing in the transverse direction.

A careful observation of the part surface indicates that the lobes are partially aligned with white continuous straps appearing in most of the plates at similar locations (see Figure 2.32). These lines should indicate a local defect induced by the manufacturing process of the material and/or due to the rolling of the SMC material. These white lines might arise due to a lack of resin or styrene because of a fold in the SMC sheet created during the production step.

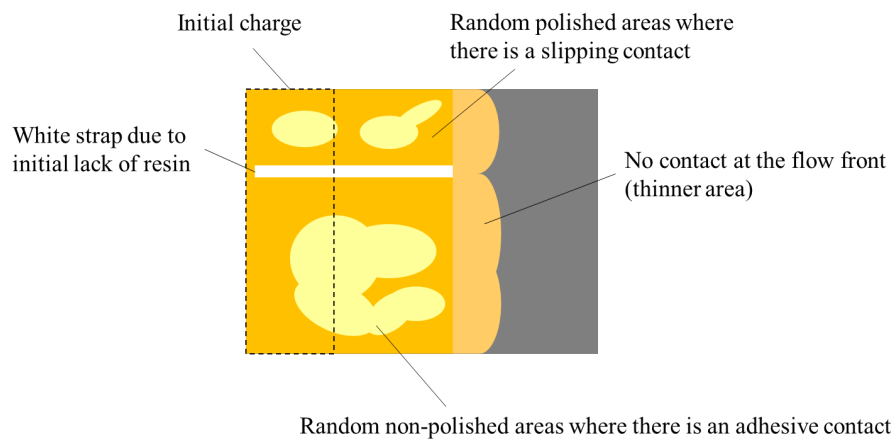


Figure 2.32: Schematic representation of the surface aspect observed on the incomplete parts.

Surfaces in contact with the mold also present two types of aspect, depending on the location (see Figure 2.32). At some locations, the surface is glossy, possibly indicating a slip contact condition within the mold. At other locations, the surface is more matt and rougher, with probably adhesive contacts with the mold. This local variability should induce a certain variability in the flow which is not necessarily unidirectional for a small element of matter that may experience more complex loading conditions and deformations. Close to the flow front, the part is thinner indicating that the material came off the mold platens.

This complexity can be detected for these SMC materials thanks to their transparency. A simple setup with a light table was used to observe directly the distribution of material inside the parts. With this method, some defects are easily revealed as shown in Figure 2.33.

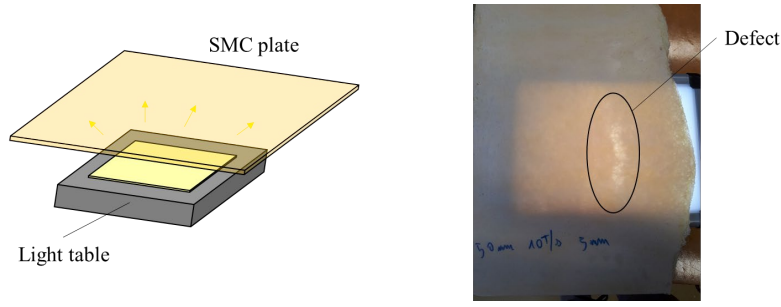


Figure 2.33: Setup with the light table to observe qualitatively the interior of the SMC parts.

Comparing the different plates, it appears that different distributions of defects are present in the part at different locations (see Figure 2.34). At the left-hand side, which corresponds to the location of the initial charge, fiber bundles seem to be oriented randomly and voids are clearly observable. Away from this zone, the fiber bundles seem to be more aligned along the channel flow direction, which is characteristic of an extensional flow of the SMC material. Behind the flow front, some large defect zones can be observed and are regularly aligned with lobes observed at the flow front. They generally present small porosities distributed on a large area or long lineal zones where the material seems to be torn. This discontinuity in the distribution of the fibrous reinforcement could arise from the breakage of the fibrous reinforcement induced by the solid deformation of the material.

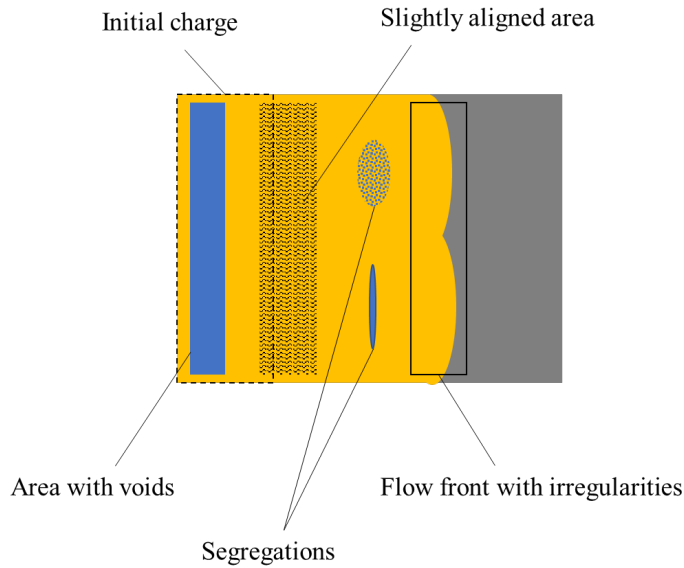


Figure 2.34: Schematic representation of internal characteristics observed in the short shots.

Some of these defects are sometimes associated with long dark lines transverse of the flow direction lying on a large portion of the width of the charge. Generally, these dark lines are observed upstream of the lineal defect and seems correspond to a large slip of one ply, that leaves an empty zone where it cannot bend, just in front of the other ply. Then, the dark line corresponds to the edge where the two plies in contact are compacted together. This mechanism explains why lobes can appear downstream of the transversal lineal defect. Additionally, the observation of a linear marker between two plies, initially straight and orthogonal to the flow direction, reveals after compression that the deformations are heterogenous along the same

streamline, as seen in Figure 2.35, where the curvature of the marker and the flow front do not match. All these defects confirm that the flow of the SMC material leads to complex internal structure with heterogeneities and porosities that impact locally the evolution of the mesostructures.

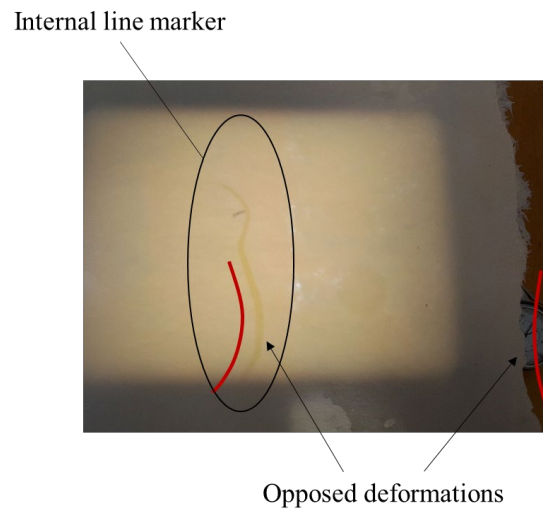


Figure 2.35: Different deformations along the same streamline.

At the flow front, the detachment of the SMC material from the mold platen results in a pressure drop, which in turn produces more porosities and leaves some dry zones at the surface where the resin cannot flow to compensate for the elongation of some material layers (see Figure 2.36). At the flow front, some fiber bundles are not aligned with the flow front and come outside of the SMC domain, while some fiber bundles are aligned some centimeters behind the flow front (see Figure 2.37).



Figure 2.36: Dry area at the flow front.

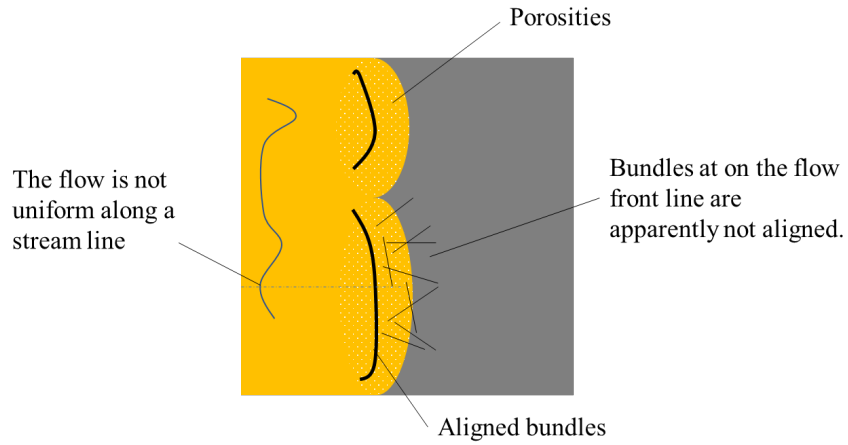
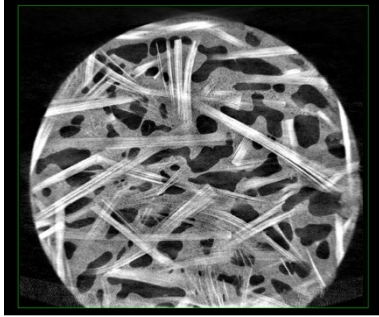


Figure 2.37: Schematic representation of different features at the flow front.

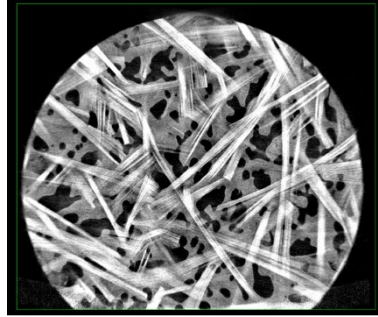
From global observations, there is no significant differences in terms of flow patterns and flow front between the different SMC material references, but the flow length increases the irregularities at the flow front and likely the heterogeneities in the rest of the SMC material. The occurrence of defects and voids seem to be more frequent for the references HP-SMC-37 and LF-SMC-18.

2.C. Tomography images of the SMC materials

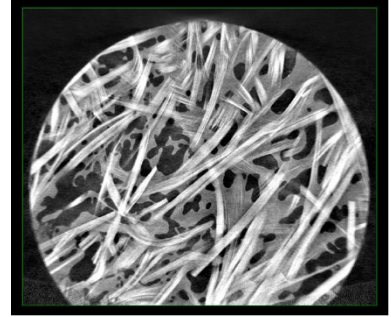
The middle plane through the thickness of each cylindrical die-cutting samples is given. The rows give the scans obtained by X-ray tomography of the samples for the different final thicknesses 5mm, 4mm, 3mm. The columns represent the three sampling locations (A), (B), (C) along a same streamline (see Figure 2.3). The diameter of all the samples is 33mm.



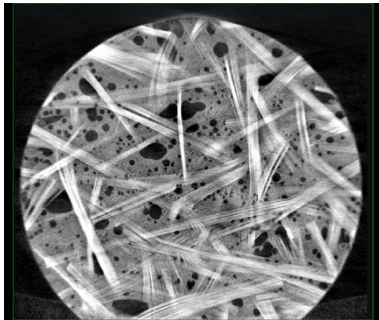
Reg-SMC-18, 5mm, (A)



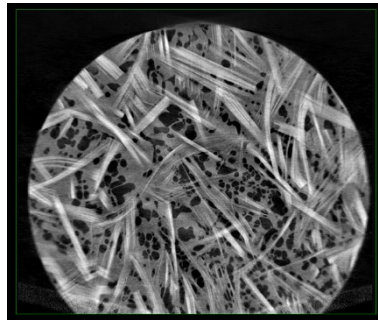
Reg-SMC-18, 5mm, (B)



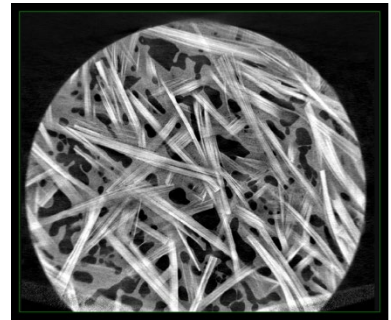
Reg-SMC-18, 5mm, (C)



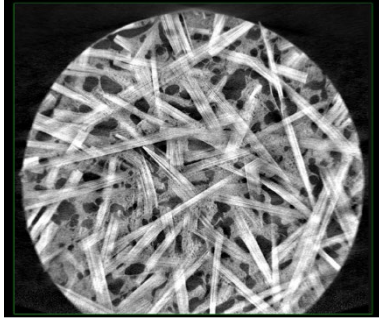
Reg-SMC-18, 4mm, (A)



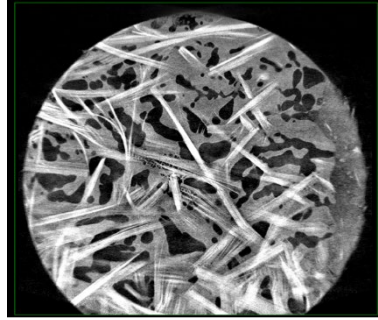
Reg-SMC-18, 4mm, (B)



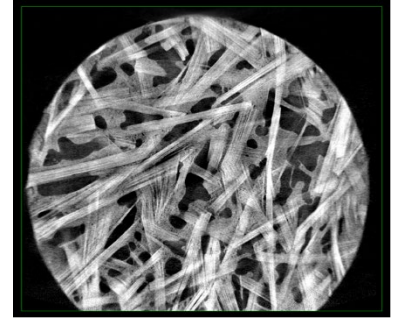
Reg-SMC-18, 4mm, (C)



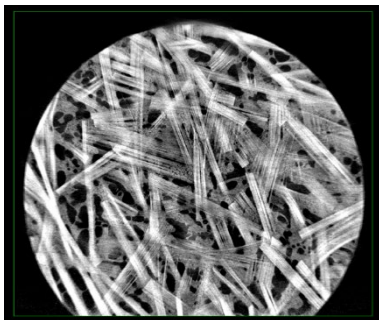
HP-SMC-24, 5mm, (A)



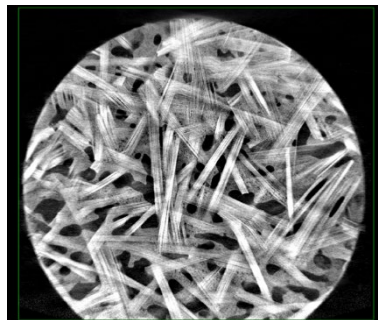
HP-SMC-24, 5mm, (B)



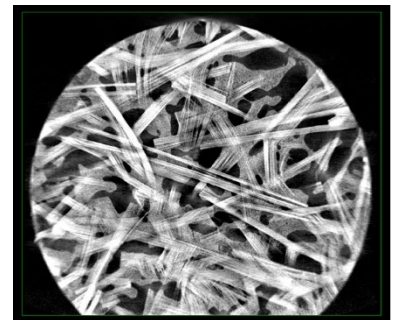
HP-SMC-24, 5mm, (C)



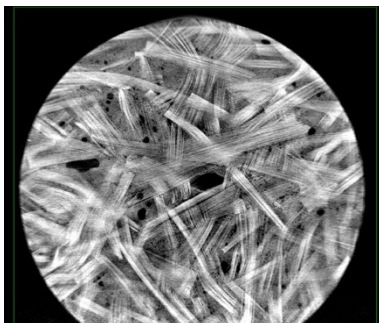
HP-SMC-24, 4mm, (A)



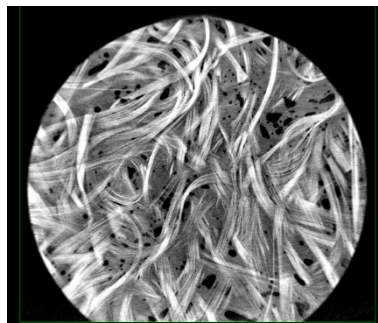
HP-SMC-24, 4mm, (B)



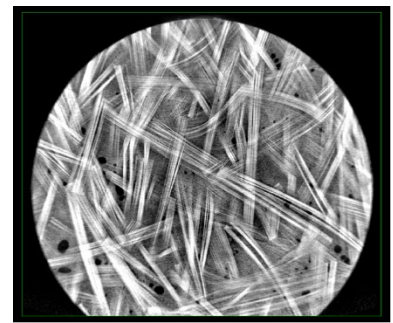
HP-SMC-24, 4mm, (C)



HP-SMC-24, 3mm, (A)



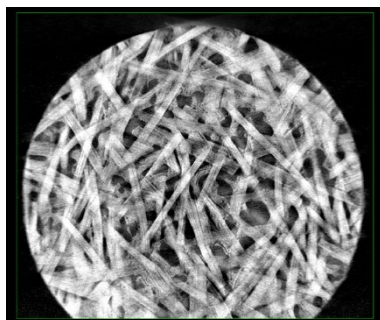
HP-SMC-24, 3mm, (B)



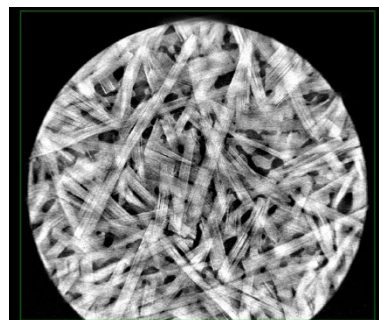
HP-SMC-24, 3mm, (C)



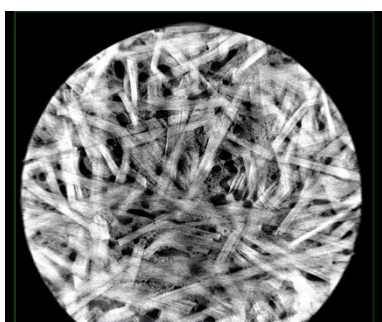
HP-SMC-37, 5mm, (A)



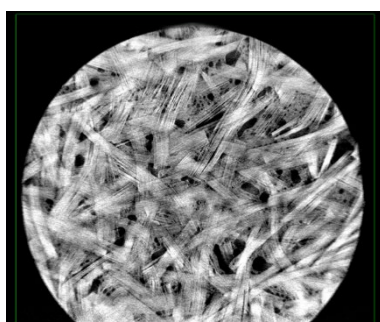
HP-SMC-37, 5mm, (B)



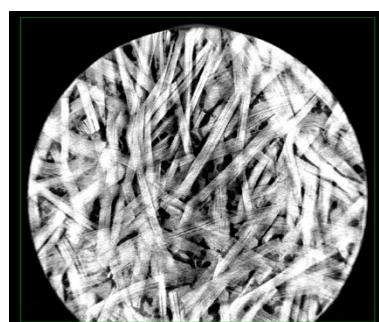
HP-SMC-37, 5mm, (C)



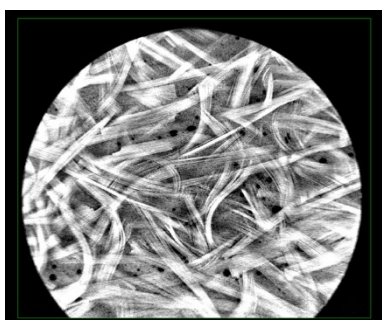
HP-SMC-37, 4mm, (A)



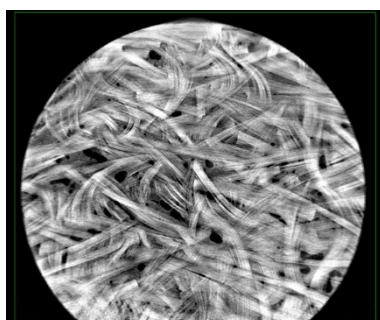
HP-SMC-37, 4mm, (B)



HP-SMC-37, 4mm, (C)



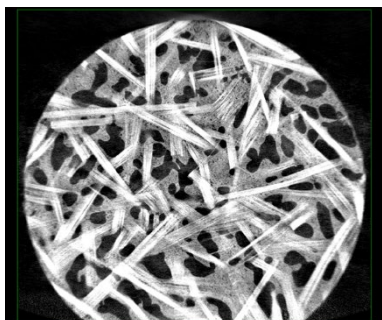
HP-SMC-37, 3mm, (A)



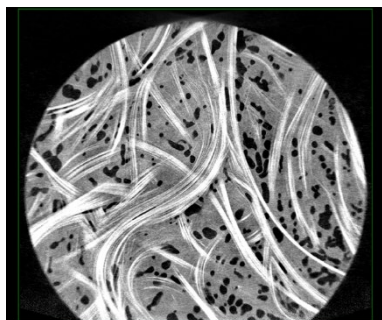
HP-SMC-37, 3mm, (B)



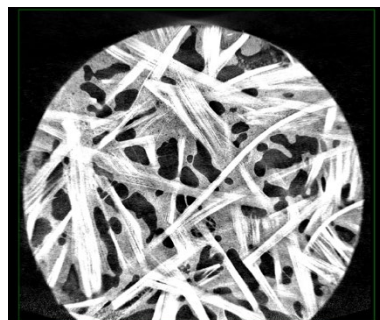
HP-SMC-37, 3mm, (C)



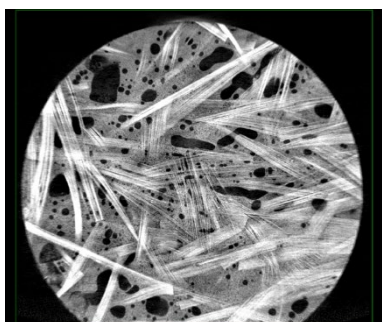
LF-SMC-18, 5mm, (A)



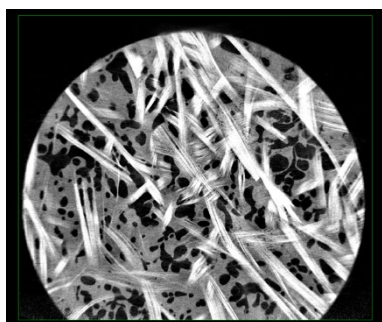
LF-SMC-18, 5mm, (B)



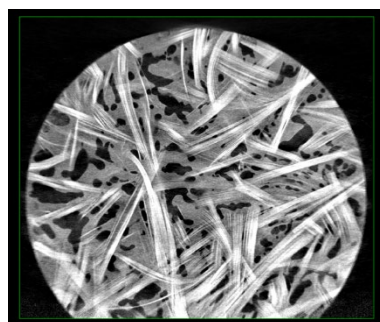
LF-SMC-18, 5mm, (C)



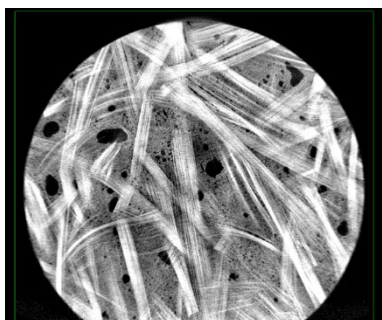
LF-SMC-18, 4mm, (A)



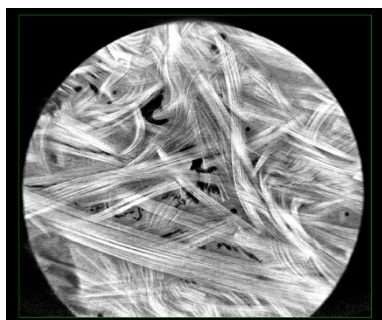
LF-SMC-18, 4mm, (B)



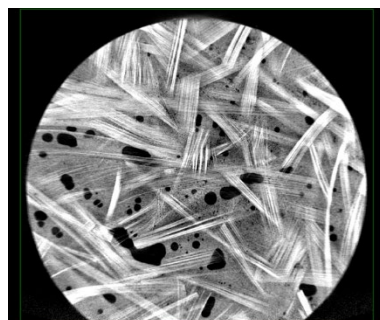
LF-SMC-18, 4mm, (C)



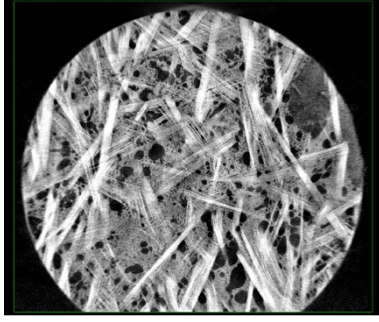
LF-SMC-18, 3mm, (A)



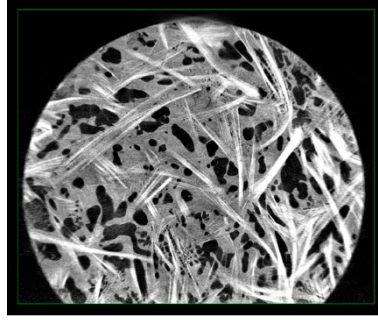
LF-SMC-18, 3mm, (B)



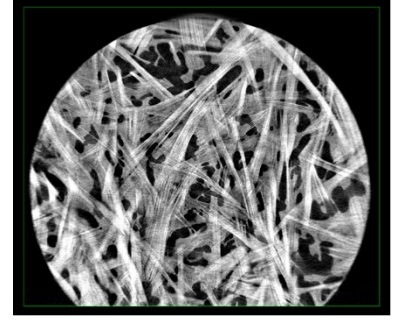
LF-SMC-18, 3mm, (C)



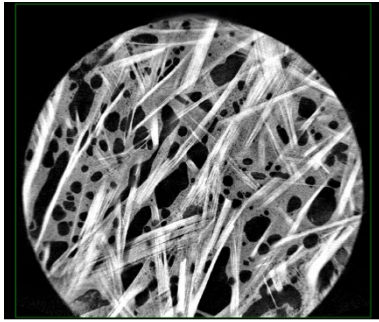
Soft-SMC-18, 5mm, (A)



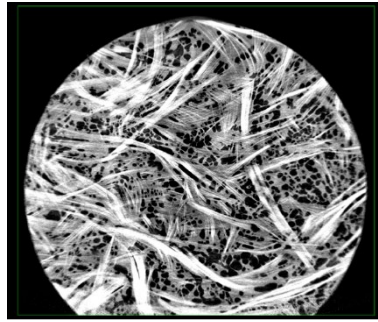
Soft-SMC-18, 5mm, (B)



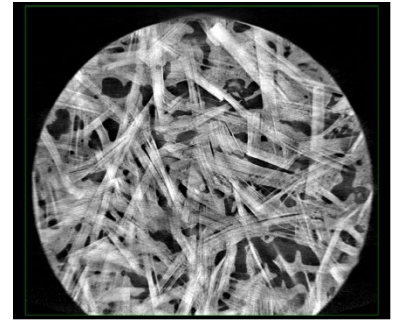
Soft-SMC-18, 5mm, (C)



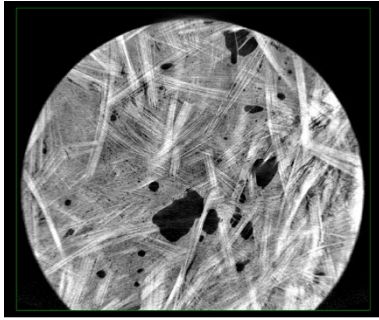
Soft-SMC-18, 4mm, (A)



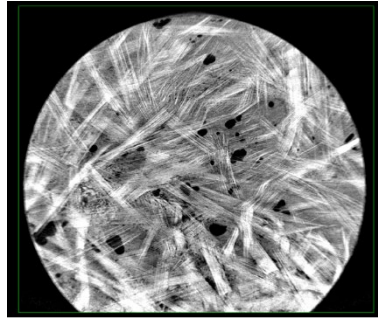
Soft-SMC-18, 4mm, (B)



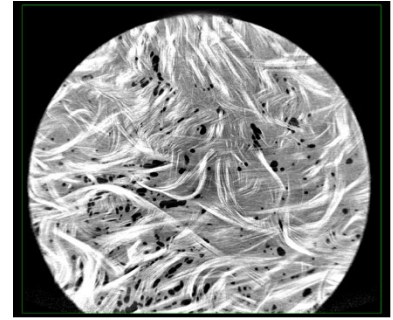
Soft-SMC-18, 4mm, (C)



Soft-SMC-18, 3mm, (A)



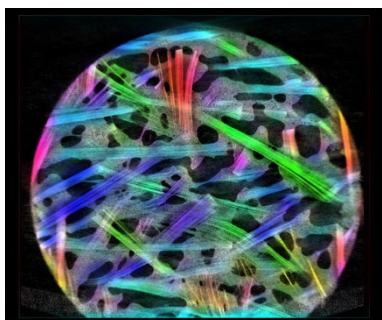
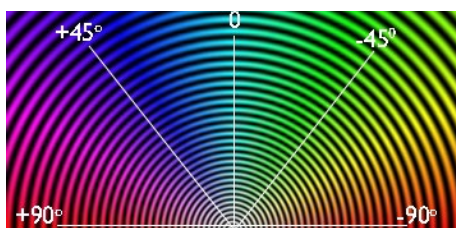
Soft-SMC-18, 3mm, (B)



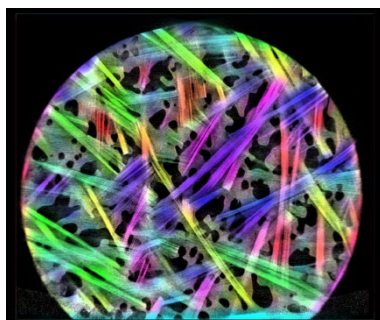
Soft-SMC-18, 3mm, (C)

2.D. Orientation analysis of the SMC mesostructures

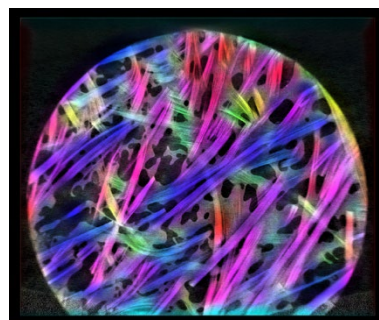
The images of Appendix 2.C are given post-treated to represent the orientation distribution for each sample at their middle plane, and give an overview of the variety of orientation states and align the other deformation mechanisms with mostly isotropic distributions.



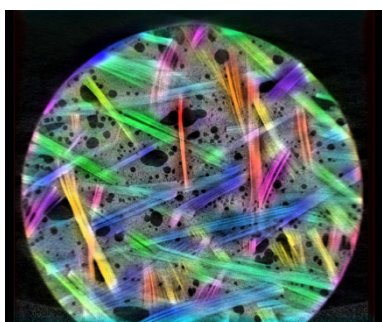
Reg-SMC-18, 5mm, (A)



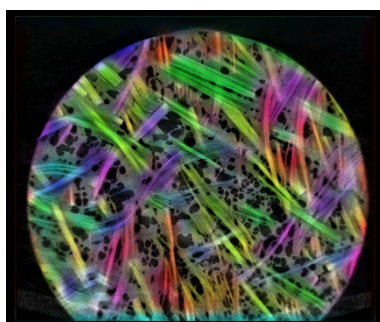
Reg-SMC-18, 5mm, (B)



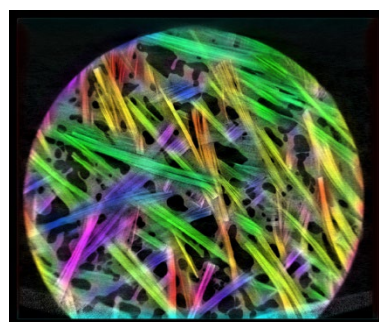
Reg-SMC-18, 5mm, (C)



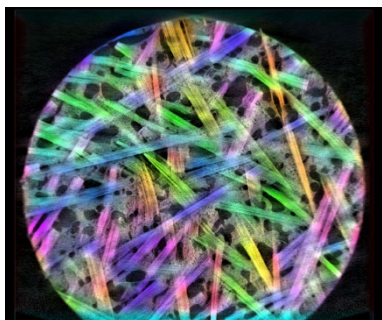
Reg-SMC-18, 4mm, (A)



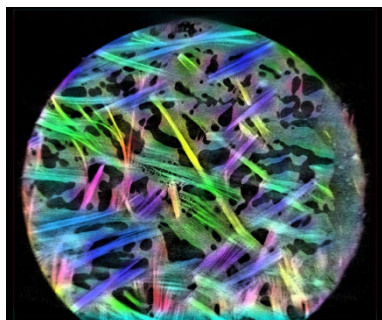
Reg-SMC-18, 4mm, (B)



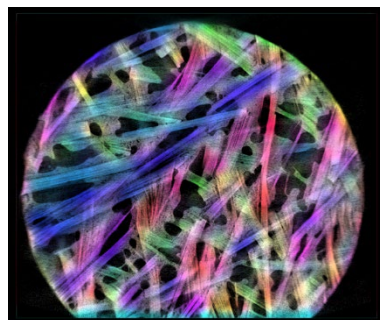
Reg-SMC-18, 4mm, (C)



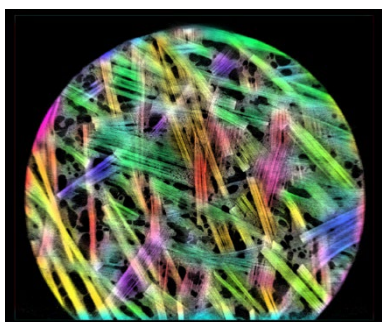
HP-SMC-24, 5mm, (A)



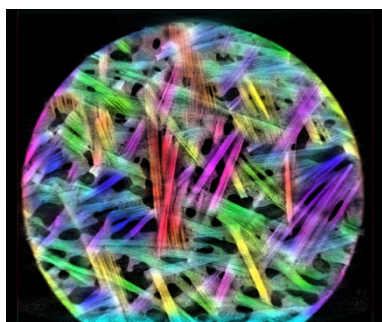
HP-SMC-24, 5mm, (B)



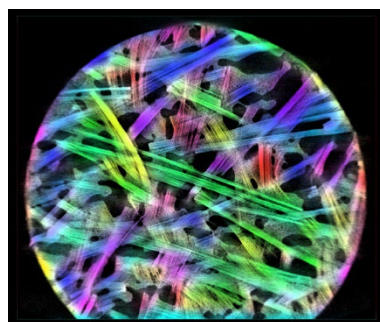
HP-SMC-24, 5mm, (C)



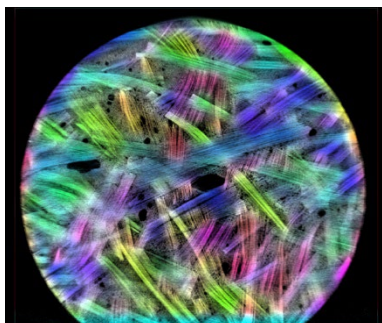
HP-SMC-24, 4mm, (A)



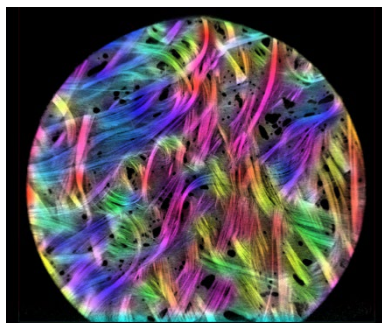
HP-SMC-24, 4mm, (B)



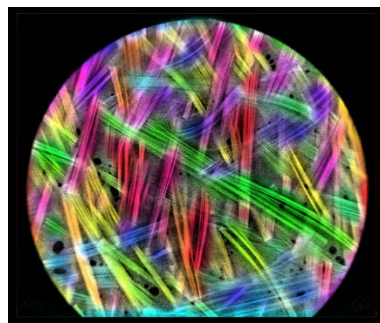
HP-SMC-24, 4mm, (C)



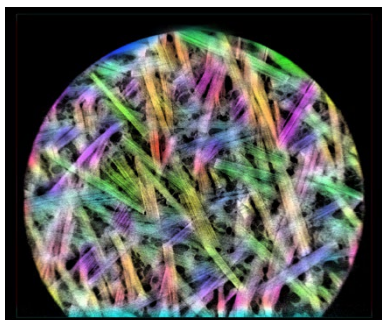
HP-SMC-24, 3mm, (A)



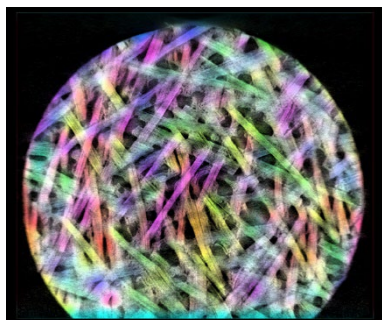
HP-SMC-24, 3mm, (B)



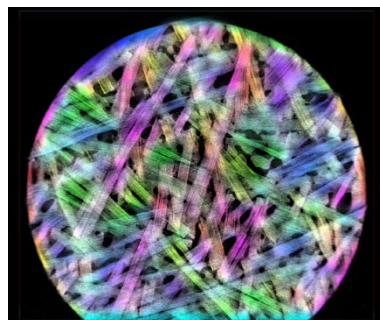
HP-SMC-24, 3mm, (C)



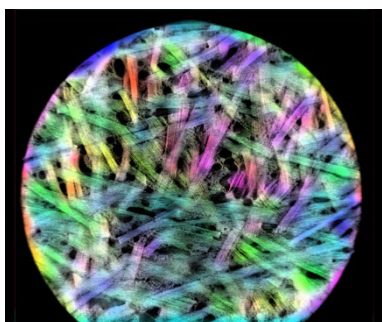
HP-SMC-37, 5mm, (A)



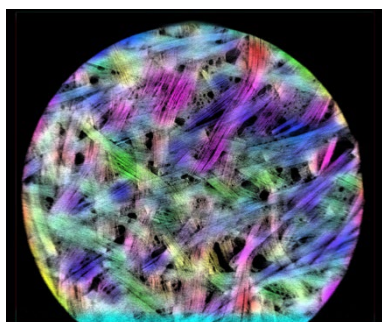
HP-SMC-37, 5mm, (B)



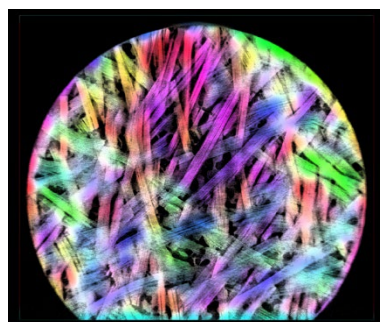
HP-SMC-37, 5mm, (C)



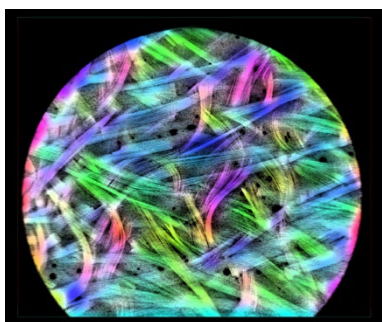
HP-SMC-37, 4mm, (A)



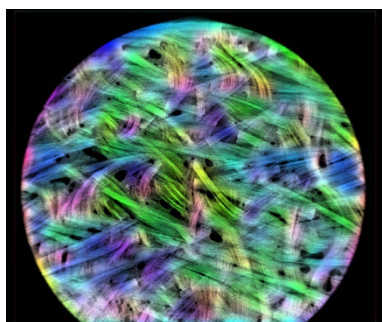
HP-SMC-37, 4mm, (B)



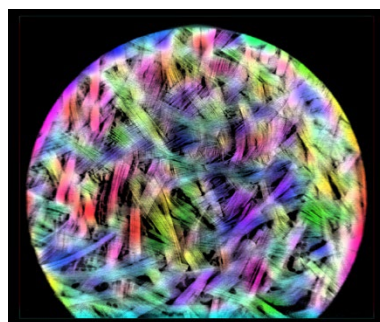
HP-SMC-37, 4mm, (C)



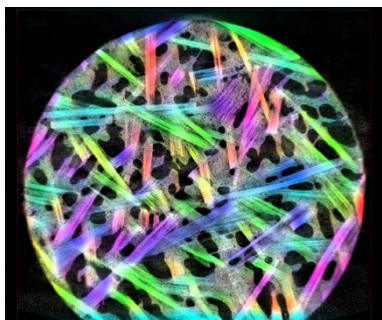
HP-SMC-37, 3mm, (A)



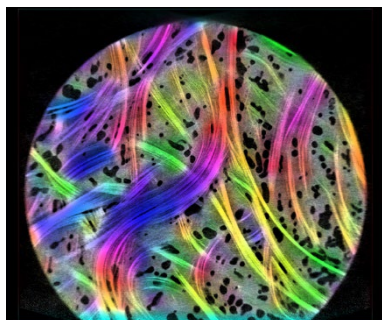
HP-SMC-37, 3mm, (B)



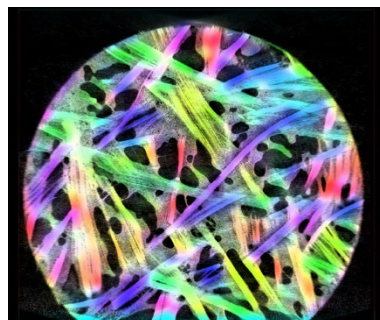
HP-SMC-37, 3mm, (C)



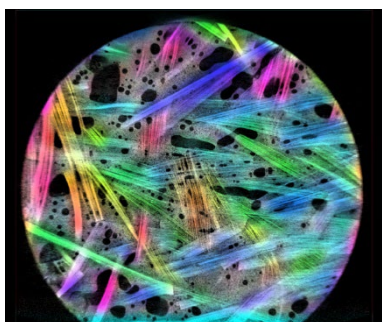
LF-SMC-18, 5mm, (A)



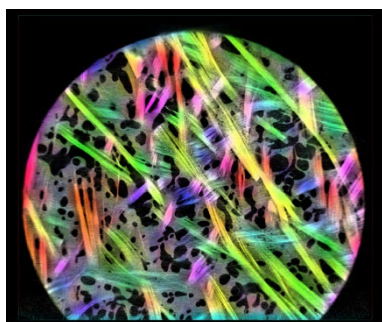
LF-SMC-18, 5mm, (B)



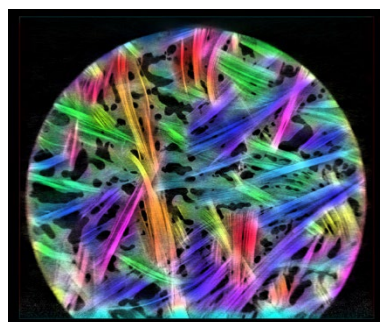
LF-SMC-18, 5mm, (C)



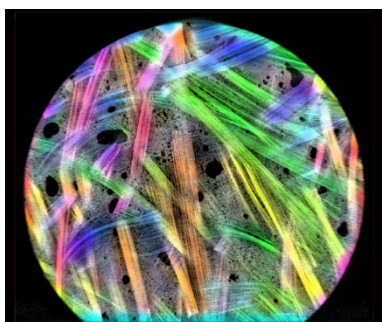
LF-SMC-18, 4mm, (A)



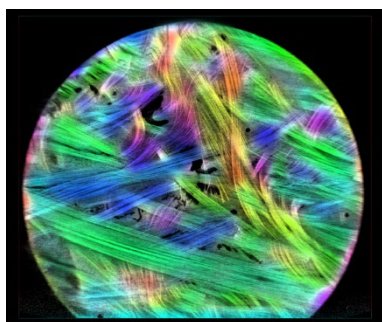
LF-SMC-18, 4mm, (B)



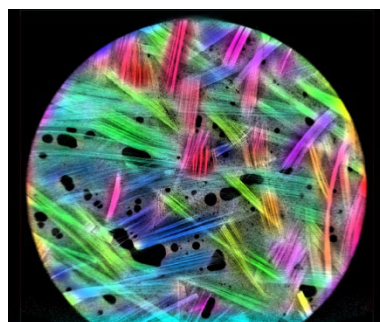
LF-SMC-18, 4mm, (C)



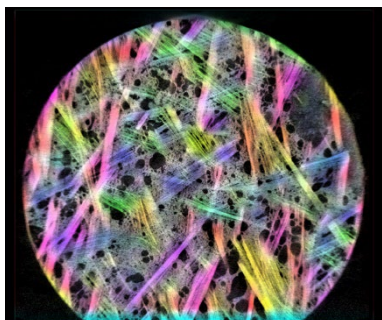
LF-SMC-18, 3mm, (A)



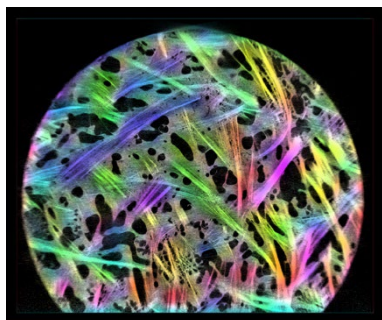
LF-SMC-18, 3mm, (B)



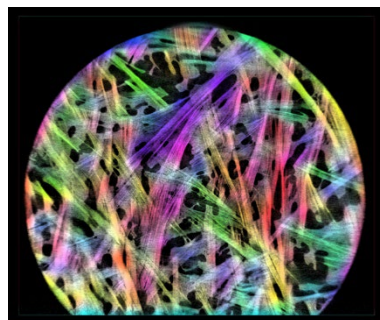
LF-SMC-18, 3mm, (C)



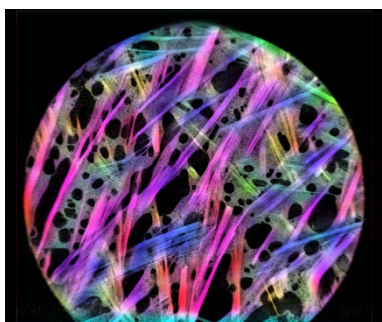
Soft-SMC-18, 5mm, (A)



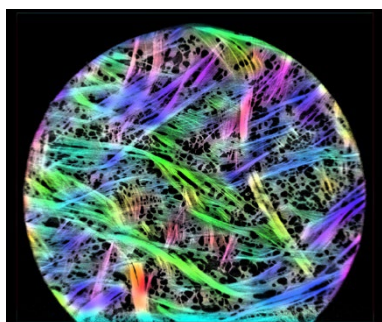
Soft-SMC-18, 5mm, (B)



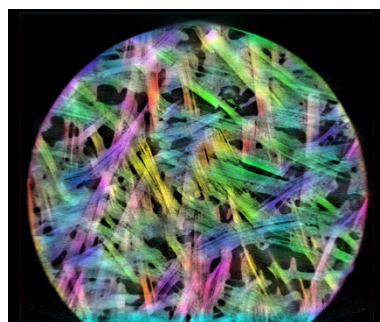
Soft-SMC-18, 5mm, (C)



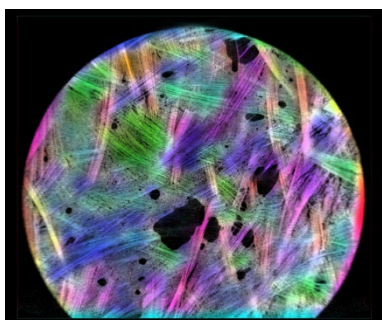
Soft-SMC-18, 4mm, (A)



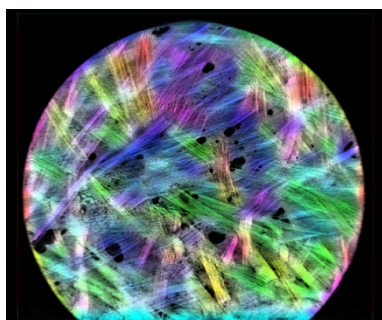
Soft-SMC-18, 4mm, (B)



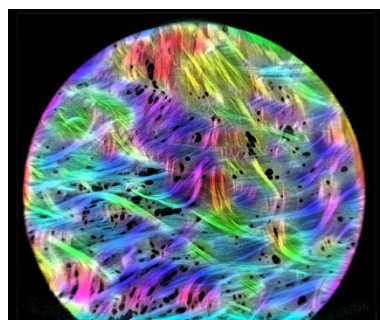
Soft-SMC-18, 4mm, (C)



Soft-SMC-18, 3mm, (A)



Soft-SMC-18, 3mm, (B)



Soft-SMC-18, 3mm, (C)

Bibliography

- [1] Advani, S. G., & Tucker III, C. L. (1987). The use of tensors to describe and predict fiber orientation in short fiber composites. *Journal of rheology*, 31(8), 751-784.
- [2] Barabási, A. L., Albert, R., & Schiffer, P. (1999). The physics of sand castles: maximum angle of stability in wet and dry granular media. *Physica A: Statistical Mechanics and its Applications*, 266(1-4), 366-371.
- [3] Barbier, E. (1860). Note sur le problème de l'aiguille et le jeu du joint couvert. *Journal de mathématiques pures et appliquées, 2ème série*, 5, 273-286.
- [4] Berryman, J. G. (1983). Random close packing of hard spheres and disks. *Physical Review A*, 27(2), 1053.
- [5] Buffon, G. L. (1733). Solutions de problèmes sur le jeu de franc-carreau. *Histoire de l'Académie royale des sciences*, 43-45.
- [6] Ciamarra, M. P., Coniglio, A., & Nicodemi, M. (2006). Thermodynamics and statistical mechanics of dense granular media. *Physical review letters*, 97(15), 158001.
- [7] Crofton, M. W. (1868). VII. on the theory of local probability, applied to straight lines drawn at random in a plane; the methods used being also extended to the proof of certain new theorems in the integral calculus. *Philosophical Transactions of the Royal Society of London*, 158, 181-199.
- [8] Deltheil, R. (1919). Sur la théorie des probabilités géométriques. *Annales de la faculté des sciences de Toulouse, 3ème série*, 11, 1-65.
- [9] Donev, A., Cisse, I., Sachs, D., Vario, E. A., Stillinger, F. H., Connelly, R., . . . Chaikin, P. M. (2004). Improving the density of jammed disordered packings using ellipsoids. *Science*, 303(5660), 990-993.
- [10] Dumont, P., Orgéas, L., Le Corre, S., & Favier, D. (2003). Anisotropic viscous behavior of sheet molding compounds (SMC) during compression molding. *International Journal of Plasticity*, 19(5), 625-646.
- [11] Dumont, P., Vassal, J. P., Orgéas, L., Michaud, V., Favier, D., & Manson, J. A. (2007). Processing, characterisation and rheology of transparent concentrated fibre-bundle suspensions. *Rheologica acta*, 46(5), 639-651.
- [12] Le, T. H., Dumont, P. J., Orgéas, L., Favier, D., Salvo, L., & Boller, E. (2008). X-ray phase contrast microtomography for the analysis of the fibrous microstructure of SMC composites. *Composites Part A: Applied Science and Manufacturing*, 39(1), 91-103.
- [13] Mahé, F., Binetruy, C., Advani, S., Férec, J., & Eck, B. (2021). A multi-scale statistical description of stacks of non-cohesive thin particles. *Powder Technology*, 399, 116988.
- [14] Mehta, A. (1994). *Granular matter: an interdisciplinary approach*. Springer Science & Business Media.
- [15] Orgéas, L., & Dumont, P. J. (2011). Sheet molding compounds. *Wiley encyclopedia of composites*, 1-36.

- [16] Oter-Carbonell, L. (2018). *Process-induced microstructure in industrial SMC compression: quantitative descriptive analysis and predictability of a state-of-the-art numerical model*. École centrale de Nantes.
- [17] Rezakhaniha, R., Agianniotis, A., Schrauwen, J. T., Griffa, A., Sage, D., Bouten, C. V., . . . Stergiopoulos, N. (2012). Experimental investigation of collagen waviness and orientation in the arterial adventitia using confocal laser scanning microscopy. *Biomechanics and Modeling in Mechanobiology*, 11, 461-473.
- [18] Santaló, L. A. (1952). Measure of sets of geodesics in a Riemannian space and applications to integral formulas in elliptic and hyperbolic spaces. *Summa Brasil. Math*, 3(1).
- [19] Santaló, L. A. (1976). *Integral geometry and geometric probability*. Cambridge university press.
- [20] Scott, G. D., & Kilgour, D. M. (1969). The density of random close packing of spheres. *Journal of Physics D: Applied Physics*, 2(6), 863.
- [21] Seneta, E., Parshall, K. H., & Jongmans, F. (2001). Nineteenth-century developments in geometric probability: JJ Sylvester, MW Crofton, J.-E. Barbier, and J. Bertrand. *Archive for history of exact sciences*, 55(6), 501-524.
- [22] Shirrell, C. D. (1983). Variability in static strengths of sheet molding compounds (SMC). *Polymer composites*, 4(3), 172-179.
- [23] Sommer, D. E., Kravchenko, S. G., & Pipes, R. B. (n.d.). A numerical study of the meso-structure variability in the compaction process of prepreg platelet molded composites. *Composites Part A: Applied Science and Manufacturing*, 138, 106010.
- [24] Song, C., Wang, P., & Makse, H. A. (2008). A phase diagram for jammed matter. *Nature*, 453(7195), 629-632.
- [25] Steiner, J. (1838). Einfacher Beweis der isoperimetrischen Hauptsätze. *J. reine angew Math.* 18, 281-296.
- [26] Stoka, M. I. (1968). Géométrie intégrale. *Mémorial des sciences mathématiques*, 165.
- [27] Torquato, S. (1991). *Random heterogeneous materials: microstructure and macroscopic properties*. Springer.
- [28] Torquato, S., Truskett, T. M., & Debenedetti, P. G. (2000). Is random close packing of spheres well defined? *Physical review letters*, 84(10), 2064.

Chapter 3

A statistical framework to characterize discontinuous fibrous media

Table of contents

3.1	Introduction.....	80
3.2	Microscopic scale	80
3.3	Mesoscopic scale	85
3.3.1	Introduction.....	85
3.3.2	Finite element formulation of a fibrous stack.....	85
3.3.3	Algorithm to solve for the deformation and contact forces	89
3.4	Compaction of fibrous mesostructures.....	93
3.4.1	Introduction.....	93
3.4.2	Theory and method	93
3.4.2.1	Statistical description and constitutive model of contact forces	93
3.4.2.2	Finite element formulation.....	98
3.4.2.3	Simulations	99
3.4.3	Results.....	101
3.4.4	Discussions.....	106
3.4.4.1	Comparison of the numerical results with the analytical model	106
3.4.4.2	Application to SMC mesostructures	107
3.5	Conclusions.....	108
	Appendices	110
3.A.	Derivation of beam equations and finite element formulations.....	110
3.B.	Statistical framework	122
	Bibliography	138

3.1 Introduction

The numerical generations of SMC mesostructures in Chapter 2 resulted in very low fiber volume fractions compared to what is encountered with industrial materials. This difference was interpreted as an initial compaction of the SMC material, carried out at the end of the manufacturing process, to increase the fiber content. This initial compaction induces an internal loading of the mesostructure, with non-negligible consequences for the compression molding process.

The behavior of a fibrous network in compaction is modeled by van Wyk's model (Van Wyk, 1946) at the macroscale, but the contact force between the fiber bundles is taken into account.

Through a multi-scale description of the SMC fibrous reinforcement, a mechanical model is formulated.

In **Section 3.2**, the fiber bundle behavior is described by a beam model. Several kinematics are presented, to lay the ground work for the more general Timoshenko beam model formulation.

In **Section 3.3**, the individual mechanical behaviors of the fiber bundles are assembled through a finite element formulation. The compaction of the fibrous mesostructure is then solved by an iterative method which allow one to simulate realistic SMC mesostructures.

In **Section 3.4**, the stacking algorithm of Chapter 2 is completed to generate realistic SMC mesostructures and is used to validate the analytical macroscopic model and the statistical description by comparing it with numerical results.

3.2 Microscopic scale

At small scale, the fibrous medium is made of fibers aligned with each other to form thin and slender bundles. We denote the length l , width w , and thickness e of the fiber bundle (consistent with the objective geometrical dimensions defined in Chapter 2 for thin and slender fiber bundles) (see Figure 3.1). The *thinness and slenderness assumption* is written as:

$$e \leq w \ll l \quad (3.1)$$

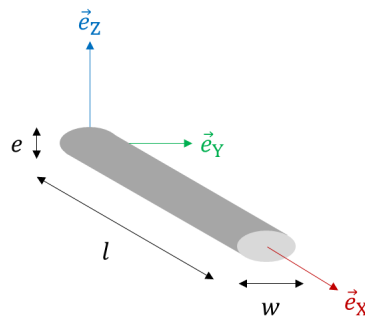


Figure 3.1: Geometrical dimensions and curvilinear coordinate systems along the fiber bundle axis.

When the fiber bundle deforms, its mechanical behavior is influenced by the internal motions of its fibers. A deformation kinematics must be formulated analytically to describe these internal mechanisms along with a constitutive law of the inner cohesive forces that maintain the integrity of the bundle. Here, the local deformations within the fiber bundle are assumed to be small, allowing the use of linear elasticity to describe its mechanical behavior.

Three kinematic models considered to represent the fiber bundles as beams (see Appendix 3.A for the complete derivations of the different models).

The simplest model is the *transverse shear model*. it assumes that the fiber bundle deforms by a vertical displacement of its transverse cross-section which remains straight and planar in the deformed configuration. The principle of minimum potential energy for this kinematics leads to the constitutive equation of the beam:

$$T_{,X} = 0 \quad \text{for } 0 < X < l \quad (3.2)$$

where $T(X)$ is the shear force as a function of the longitudinal coordinate X along the fiber bundle. Assuming a linear elastic behavior for the fiber bundle gives the model for the shear force:

$$T(X) = GS V_{,X} \quad (3.3)$$

where G is the shear modulus of the fiber bundle and S is the area of the transverse cross-section. The kinematics of the beam is only parametrized by the vertical displacement of the cross-section $V(X)$.

Resolving Eq. (3.2) with Eq. (3.3) and applying unitary boundary conditions leads to the finite element formulation of the shear model:

$$\mathbb{K} \cdot \vec{U} = \vec{F}, \quad \text{with } \mathbb{K} = \frac{GS}{l} \begin{bmatrix} 1 & -1 \\ -1 & 1 \end{bmatrix}, \quad \vec{U} = \begin{pmatrix} V_1 \\ V_2 \end{pmatrix} \quad \text{and} \quad \vec{F} = \begin{pmatrix} T_1 \\ T_2 \end{pmatrix} \quad (3.4)$$

where $V_1 = V(X=0)$ and $V_2 = V(X=l)$ are the vertical displacements at both ends which parametrize the interpolation of the deformation. \mathbb{K} is the stiffness matrix of the beam element of length l , \vec{U} is the vector of node displacements and \vec{F} is the force vector applied on the ends of the fiber bundle.

This kinematic model represents the relative sliding of fibers inside the roving, which allows to keep the cross-section straight and planar (see Figure 3.2).

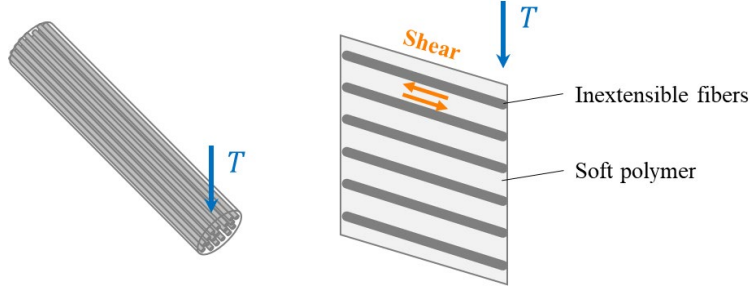


Figure 3.2: Simple slip and shear model between fibers.

The second beam model adds a second kinematic degree of freedom for the rotation of the transverse cross-section. Then, the constitutive equation of the beam becomes:

$$\begin{cases} M_{,X} = T(X) \\ T_{,X} = 0 \end{cases} \quad \text{for } 0 < X < l \quad (3.5)$$

where $M(X)$ is the bending moment and $T(X)$ the shear force applied on the transverse cross-section. The linear elastic assumption for the fiber bundle gives the beam models:

$$T(X) = GS(V_{,X} - \theta(X)) \quad M(X) = EI\theta_{,X} \quad (3.6)$$

where G and E are respectively the shear and Young's moduli, S and I are the area and inertia of the cross-section respectively. The kinematics of the beam is parametrized by the vertical displacement $V(X)$ and the rotation angle $\theta(X)$ of the cross-section.

To solve Eq. (3.5), one can add another assumption to obtain the *bending model* of the beam, considering the equality between the rotation angle and the derivative of the vertical displacement of the beam:

$$V_{,X} = \theta(X) \quad (3.7)$$

It leads to the beam model of Euler-Bernoulli. The corresponding finite element formulation is:

$$\mathbb{K} \cdot \vec{U} = \vec{F} \quad \text{with} \quad \mathbb{K} = \frac{EI}{l^3} \begin{bmatrix} 12 & 6 & -12 & 6 \\ 6l & 4l^2 & -6l & 2l^2 \\ -12 & -6 & 12 & -6 \\ 6l & 2l^2 & -6l & 4l^2 \end{bmatrix}, \quad \vec{U} = \begin{pmatrix} V_1 \\ \theta_1 \\ V_2 \\ \theta_2 \end{pmatrix} \quad \text{and} \quad \vec{F} = \begin{pmatrix} T_1 \\ M_1 \\ T_2 \\ M_2 \end{pmatrix} \quad (3.8)$$

The third model is a generalization of the bending model, called the *Timoshenko model*. It is given by the direct resolution of Eq. (3.5), which uses Eqs. (3.6). It results in two mechanical contributions corresponding to the shear and bending models, represented by the stiffness matrices:

$$\mathbb{K}^{(\text{bending})} = \int \varphi_{\theta,X}^{(i)} \cdot EI \cdot \varphi_{\theta,X}^{(j)} dX = \frac{EI}{(1 + \Psi^2)l^3} \begin{bmatrix} 12 & 6 & -12 & 6 \\ 6 & 4 & -6 & 2 \\ -12 & -6 & 12 & -6 \\ 6 & 2 & -6 & 4 \end{bmatrix} \quad (3.9)$$

$$\mathbb{K}^{(\text{shear})} = \int (\varphi_{V,X}^{(i)} - \varphi_{\theta}^{(i)}) \cdot GS \cdot (\varphi_{V,X}^{(j)} - \varphi_{\theta}^{(j)}) dX = \frac{EI}{(1 + \Psi^2)l^3} \begin{bmatrix} 0 & 0 & 0 & 0 \\ 0 & \Psi^2 & 0 & -\Psi^2 \\ 0 & 0 & 0 & 0 \\ 0 & -\Psi^2 & 0 & \Psi^2 \end{bmatrix} \quad (3.10)$$

The finite element formulation of Timoshenko kinematics is the sum the two stiffnesses:

$$\mathbb{K} \cdot \vec{U} = \vec{F} \quad \text{with} \quad \mathbb{K} = \mathbb{K}^{(\text{bending})} + \mathbb{K}^{(\text{shear})}, \quad \vec{U} = \begin{pmatrix} V_1 \\ \theta_1 l \\ V_2 \\ \theta_2 l \end{pmatrix} \quad \text{and} \quad \vec{F} = \begin{pmatrix} T_1 \\ M_1/l \\ T_2 \\ M_2/l \end{pmatrix} \quad (3.11)$$

The Timoshenko model is parametrized by the dimensionless number Ψ , defined as:

$$\Psi = \sqrt{\frac{12EI}{GSl^2}} \quad (3.12)$$

It characterizes the mechanical behavior of the beam. For low values of Ψ , the bending compliance is predominant and the fiber bundle will bend. At the other extreme, for high values of Ψ , the beam is more flexible in shear than in bending and the Timoshenko model tend towards the shear model.

A given kinematics corresponds to a mechanical model of the fiber bundle behavior, that can be solved explicitly by the general method developed in Appendix 3.A and presented in Figure 3.3. The solution of the constitutive equations of the beam provides particular solutions for the applied boundary conditions. Each of these solutions is a shape function that describes a different deformation mode of the fiber bundle according to the chosen kinematics. The deformation is formulated by an interpolation built with the shape functions, consistent with the constitutive equation to describe the beam kinematics in an exact way. The shape functions for different beam kinematics were obtained assuming that no body forces are applied to the fiber bundle. The only forces are point forces, as found in planar fibrous media loaded in through-thickness compression, where the mechanics is governed primarily by contact forces.

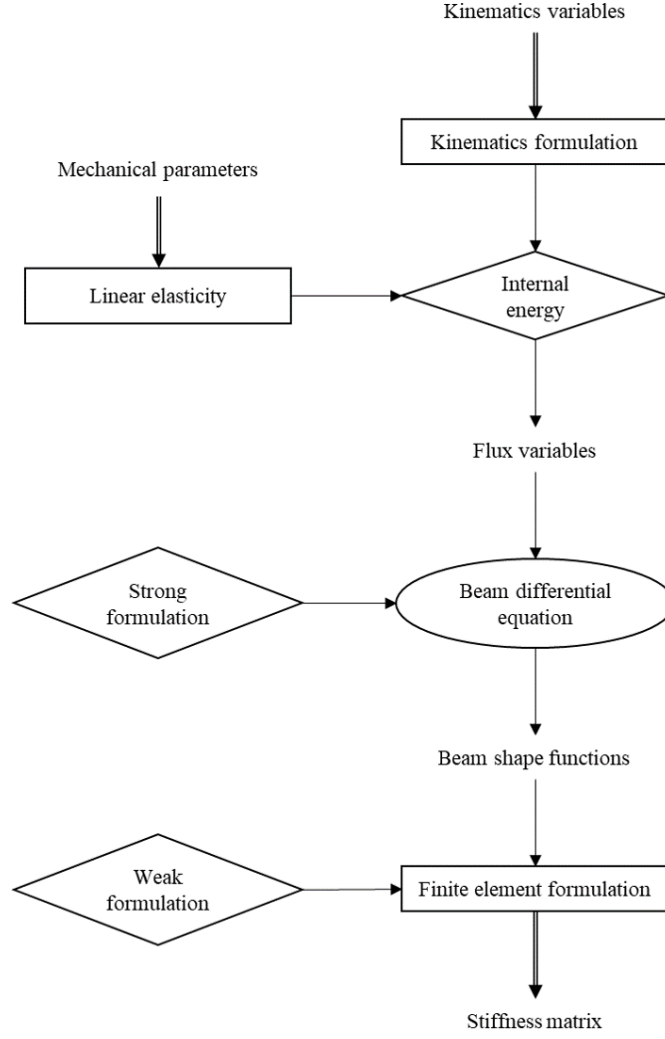


Figure 3.3: Mechanical modeling of fiber bundle using a beam theory.

A general microscopic description of the fiber bundle is obtained with the Timoshenko beam theory, that includes internal shear and bending mechanisms. In this model, the kinematics are based on the sliding and curvature of fibers inside the roving (see Figure 3.4). The coupling between these two mechanisms is expressed by a dimensionless parameter Ψ , which involves the geometry and material properties of the array of aligned fibers. A finite element formulation is written to relate the deformation to the applied forces and moments.

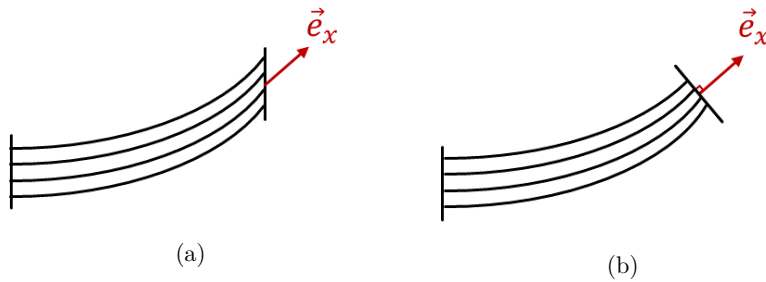


Figure 3.4: Illustration of the Timoshenko model (a) versus the Euler-Bernoulli model (b).

At the scale of a network of fiber bundles, i.e., the mesoscopic scale as illustrated in Figure 3.5, the mechanics of the fibrous medium is governed by the spatial arrangement of the fiber bundles and the network of contacts formed between them. The mechanical behavior of packed fiber bundles is difficult to model analytically and numerical approach such as finite element formulation is required to assemble the individual behaviors and describe the mechanics of the fibrous mesostructure.

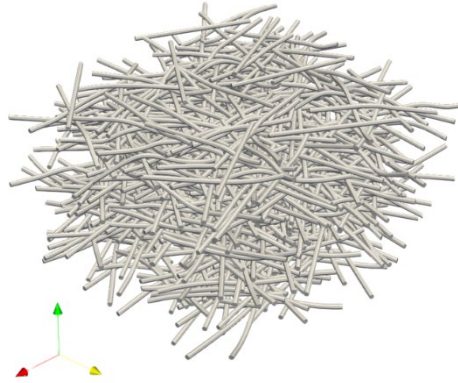


Figure 3.5: Fibrous medium at the mesoscale.

3.3 Mesoscopic scale

3.3.1 Introduction

From the microscopic problem, we obtain a general method to obtain beam constitutive models which are suitable to describe the individual kinematics of thin and slender fiber bundles. At the mesoscale, the structure and the arrangement of the fiber bundles affect the mechanical behavior of the fibrous material which complicates the mechanical formulation.

In this section, a general method based on the finite element technique is developed to take advantage of 1D beam models to drastically reduce the size of the system and facilitate the treatment of contacts. All the mechanics of the fibrous medium is condensed into a Lagrangian formulation which can be directly used for relatively large systems.

3.3.2 Finite element formulation of a fibrous stack

In a planar network of fiber bundles subjected to transverse compression, the chain of compaction forces within the structure is established through the contacts that develop during compression. This process imposes displacements and loadings on the solid constituents. Each contact applies a different loading, forcing the roving to adopt a wavy shape. The kinematics of a fiber bundle can no longer be reduced to its ends, as in the microscopic formulation, but must incorporate all of these additional Degrees of Freedom (DoFs) through an assembly of successive beam elements (see Figure 3.6-a), treated by the finite element method.

For thin and slender fiber bundles, the large majority of contacts are point-like and can be described by a finite number of Kinematic Degrees of Freedom, denoted as KDoFs. Linear contacts appear only for contacts between parallel fiber bundles, which is unlikely in a fibrous stack obtained from a random distribution of thin and slender fiber bundles. Moreover, in the limit of infinitesimal local strains, in-plane deformations, especially those related to fiber

inextensibility, are negligible compared to those in the thickness direction. The overlap points on each fiber bundles get closer to each other by moving vertically, at the same location (projected on the horizontal plane) as the contact point (see Figure 3.6-b).

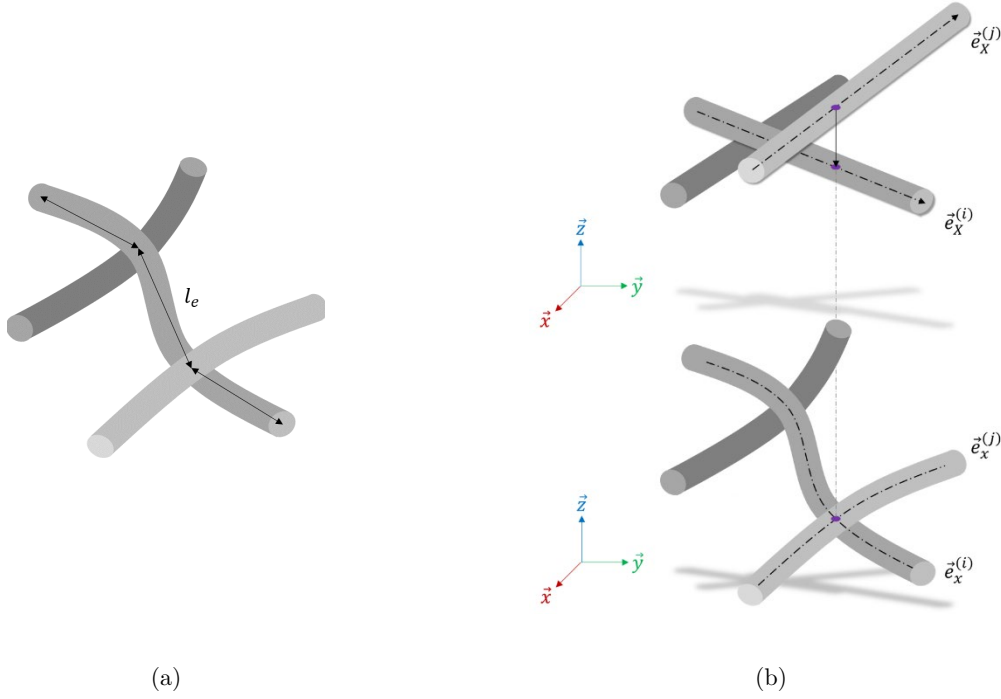


Figure 3.6: Partition of a fiber bundle into beam elements. (a): Fiber bundle elements between two contact points. (b): Side view showing contact and overlaps between the fiber bundles.

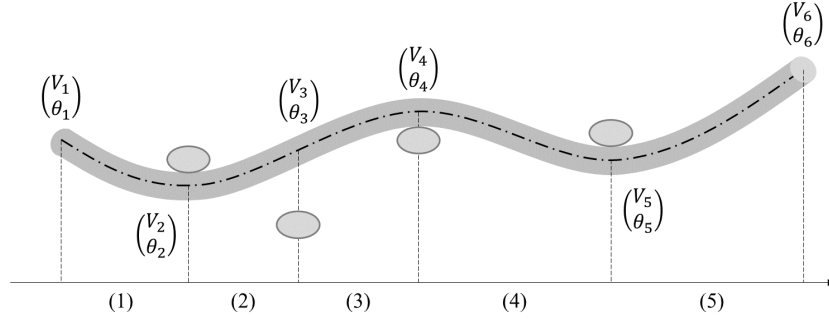


Figure 3.7: Partitioning of fiber bundle into beam elements between contact points or overlap.

Thus, the kinematic description of the fiber bundles is completed by the KDoFs attached to these overlap nodes on each bundle. The deformation field in the rest of the fibrous structure is then reconstructed from the shape functions and the beam interpolation obtained with the microscopic formulation.

The overlap points and the fiber bundle ends form a set of nodes which discretizes the fibrous medium into 1D elements, suitable for contact modeling. For this partition, all contacts will be located on the nodes and the fiber bundle elements will have a constant length during the transformation (see Figure 3.7)

The elementary stiffness of fiber bundle element is given by the Timoshenko model with:

$$\mathbb{K}_e = \frac{EI}{(1 + \Psi^2)l_e^3} \begin{bmatrix} 12 & 6l_e & -12 & 6l_e \\ 6l_e & (4 + \Psi^2)l_e^2 & -6l_e & (2 - \Psi^2)l_e^2 \\ -12 & -6l_e & 12 & -6l_e \\ 6l_e & (2 - \Psi^2)l_e^2 & -6l_e & (4 + \Psi^2)l_e^2 \end{bmatrix} \quad (3.13)$$

$$\text{with } \Psi^2 = \frac{12EI}{GS l_e^2}$$

where E and G are the Young's and shear moduli of the roving, respectively, S and I are the area and inertia of its transverse cross-section respectively and l_e is the length of the beam element. The corresponding KDoFs are $\vec{U}_e = (V_i, \theta_i, V_j, \theta_j)$, with the vertical deflection $V(X)$ and the rotation angle of the cross-section $\theta(X)$ of the two nodes (i) and (j) belonging to the element.

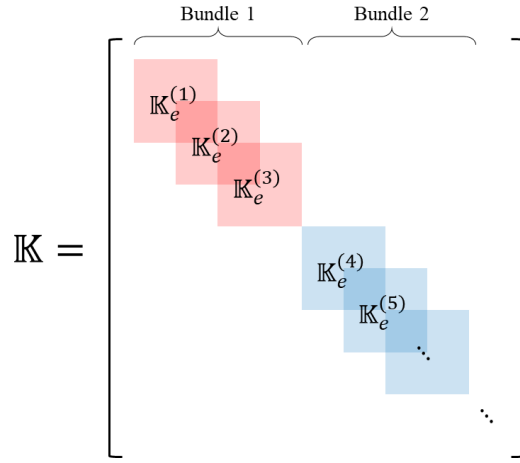


Figure 3.8: Procedure for assembling the fiber stack stiffness matrix.

Considering the displacement vector $\vec{U} = (V_1, \theta_1, V_2, \theta_2, \dots)$ as the concatenation of the nodal KDoFs of each bundle element, the stiffness matrix which describes the fibrous structure is built from an assembly of all the elementary matrices \mathbb{K}_e (see Figure 3.8).

The force vector \vec{F} of the system is built with the same assembly procedure of the local forces applied on the beam elements.

The Lagrangian of the mechanical problem is then:

$$W(\vec{U}) = \frac{1}{2} \vec{U} \cdot \mathbb{K} \cdot \vec{U} - \vec{F} \cdot \vec{U} \quad (3.14)$$

In this complex mechanical system, all the KDoFs contained in \vec{U} are not independent due to the conditions of non-interpenetration of fiber bundles.

The contact conditions require minimizing the Lagrangian under some constraints. For each overlap between two fiber bundles (i) and (j) , such that (j) is above (i) , the non-interpenetration condition is written as:

$$V^{(j)} - V^{(i)} \leq H^{(j)} - H^{(i)} + e \quad (3.15)$$

where $V^{(i)}$ and $V^{(j)}$ are the vertical deflections of the neutral fibers at the overlap point, $H^{(i)}$ and $H^{(j)}$ are their altitudes in the initial configuration and e is the thickness of the roving. The two fiber bundles are in contact as long as Eq. (3.15) is an equality. This criterion also fits the contacts conditions with the lower and upper planes that bound the stack. Thus, for each overlap point, we define the contact matrix \mathbb{C}_e and altitude vector \vec{h}_e as:

$$\mathbb{C}_e = \begin{bmatrix} 1 & 0 & 0 & 0 \\ -1 & 0 & 1 & 0 \\ 0 & 0 & -1 & 0 \end{bmatrix} \quad \vec{h}_e = \begin{pmatrix} H^{(i)} + U_{bottom} \\ H^{(j)} - H^{(i)} + e \\ H + H^{(j)} + U_{top} \end{pmatrix} \quad (3.16)$$

where H is the initial thickness of the fiber stack and U_{bottom} and U_{top} are the vertical displacements of the lower and upper planes respectively. The non-interpenetration condition for each overlap is then written in the vectorial form:

$$\mathbb{C}_e \cdot \begin{pmatrix} V^{(i)} \\ \theta^{(i)} \\ V^{(j)} \\ \theta^{(j)} \end{pmatrix} \leq \vec{h}_e \quad (3.17)$$

After assembling the contact matrix, the constrained minimization problem describing the mechanics of the stack is:

$$\min_{\vec{U}} \left(\frac{1}{2} \vec{U} \cdot \mathbb{K} \cdot \vec{U} - \vec{F} \cdot \vec{U} \right) \quad s.t. \quad \mathbb{C} \cdot \vec{U} \leq \vec{h} \quad (3.18)$$

Note: s.t. is the abbreviation for “such that”.

The resolution of this problem is done by the method of Lagrange multipliers. A new vector of unknowns \vec{f} is introduced such that each of its components f_i is associated with i -th non-interpenetration condition. The minimization problem becomes:

$$\min_{\vec{U}, \vec{f}} (\mathcal{W}) \quad s.t. \quad \vec{f} \leq 0 \quad (3.19)$$

with $\mathcal{W}(\vec{U}) = \frac{1}{2} \vec{U} \cdot \mathbb{K} \cdot \vec{U} - \vec{f} \cdot (\mathbb{C} \cdot \vec{U} - \vec{h}) - \vec{F} \cdot \vec{U}$

The vector \vec{f} vector represents the contact forces related to the non-interpenetration conditions. A contact force is zero as long as the contact condition is not verified and becomes negative to ensure that the elements do not cross if they are in contact with each other. Since the contact

conditions with the lower or upper planes are included in Eq. (3.19), the boundary conditions of the mechanical problem are taken into account in the minimization problem.

The energy functional $\mathcal{W}(\vec{U})$ is the Lagrangian of the constrained system and completely defines the mechanics of the fibrous stack. It corresponds to the potential energy of the system formed by the internal deformation energy, the work of internal and external contact forces, and the work of the external applied forces. The solution of the minimization problem given by the displacement and force vectors (\vec{U}^*, \vec{f}^*) describes the deformed fibrous medium based on the beam model and the contact conditions.

The assumption of infinitesimal strains to formulate the linear elastic behavior and the vertical displacement of the overlap nodes is consistent with the large transformations of the fibrous structure, thanks to its discrete nature and the incremental deformations which involves different contacts and degrees of freedom.

In what follows, we will focus on the resolution of a displacement formulation of this problem, with a planar stack of fiber bundles being compacted between two parallel, flat, stiff moving platens (see Figure 3.9) with no external force applied to the system.



Figure 3.9: Through-thickness compaction of a stack of fiber bundles between two moving platens.

3.3.3 Algorithm to solve for the deformation and contact forces

The parallel planes that vertically delimit the network of fiber bundles impose a certain deformation on the fibrous medium, acting as two mold halves compacting the stack. The lower and upper planes move over a distance $U_{bottom} = U/2$ and $U_{top} = -U/2$ respectively, with $U > 0$ (see Figure 3.9).

The minimization problem to be solved is nonlinear because of the inequality constraints describing the contacts. The restriction of the problem to the active conditions gives a linear system of equations as long as no contacts are created or removed:

$$\begin{aligned} & \min_{\vec{U}} \left(\frac{1}{2} \vec{U} \cdot \mathbb{K} \cdot \vec{U} \right) \quad s.t. \quad \mathbb{C}' \cdot \vec{U} = \vec{h}' \\ \Leftrightarrow & \min_{\vec{U}, \vec{f}'} \left(\frac{1}{2} \vec{U} \cdot \mathbb{K} \cdot \vec{U} - \vec{f}' \cdot (\mathbb{C}' \cdot \vec{U} - \vec{h}') \right) \quad s.t. \quad \vec{f}' \leq 0 \end{aligned} \tag{3.20}$$

where the rows of \mathbb{C}' , \vec{h}' and \vec{f}' correspond to the lines of \mathbb{C} , \vec{h} and \vec{f} for which the contact conditions are active. The vector of unknowns of the problem becomes the vector $\vec{x} = (\vec{U}, \vec{f})$. Minimizing the energy functional means canceling its derivatives with respect to $\vec{x}' = (\vec{U}, \vec{f}')$ which gives the linear system to solve:

$$\underbrace{\begin{bmatrix} \mathbb{K} & -\mathbb{C}'^T \\ -\mathbb{C}' & 0 \end{bmatrix}}_{\mathbb{P}} \cdot \underbrace{\begin{pmatrix} \vec{U} \\ \vec{f}' \end{pmatrix}}_{\vec{x}'} = \underbrace{\begin{pmatrix} 0 \\ -\vec{h}' \end{pmatrix}}_{\vec{q}} \quad (3.21)$$

The matrix \mathbb{P} of the system in Eq. (3.21) is constant as long as there is no change in the contacts. Then, the stiffness of the stack is piecewise linear, and differentiating Eq. (3.21) gives:

$$\mathbb{P} \cdot \frac{d\vec{x}'}{dU} = \frac{d\vec{q}}{dU} \quad (3.22)$$

The vector \vec{h} depends linearly on U as a result of its construction (Eq. (3.16)). The derivative of \vec{q} with respect to U is a vector where the only non-zero elements are $-1/2$ for active contacts with the upper plane and $+1/2$ for the ones with the lower plane.

The resolution of the Eqs. (3.22) gives the increment of the nodal displacements and the contact forces between the fiber bundles for a small displacement δU . We define the vector of relative distance and the vector of pseudo-velocity:

$$\vec{d} = \vec{h} - \mathbb{C} \cdot \vec{U} \quad (\geq 0) \quad (3.23)$$

$$\vec{v} = \frac{d\vec{h}}{dU} - \mathbb{C} \cdot \frac{d\vec{U}}{dU} \quad (\geq 0) \quad (3.24)$$

The increment of displacement δU necessary to create a new contact in the system is given by:

$$\delta U = -\min(\{d_i/v_i \mid v_i > 0\}) \quad (> 0) \quad (3.25)$$

The nodal displacements \vec{U} are incremented by $\frac{d\vec{U}}{dU} \delta U$ and the contact forces by $\frac{d\vec{f}}{dU} \delta U$. The procedure can then be iterated by updating the system matrix \mathbb{P} and the vector \vec{q} before solving the update mechanical problem.

An iterative solution method, shown in Figure 3.10, is thus proposed for the calculation of the deformations and contact forces during the compaction of the fibrous stack:

1. The stiffness and contact matrices \mathbb{K} and contact matrices \mathbb{C} are calculated from the beam law (e.g., Timoshenko beam law) and the definition of the elements between the overlapping points in the fiber bundle network.
2. The nodal displacements, the contact forces and the displacement U are initially zero.
3. The active contacts are determined from the set of conditions: $\mathbb{C} \cdot \vec{U} = \vec{h}$.
4. The matrix \mathbb{P} and the vector \vec{q} are constructed from \mathbb{K} and the active rows of \mathbb{C} and \vec{h} .

5. We solve the system of Eq. (3.22) to obtain $\frac{d\vec{x}}{dU}$.
6. The displacement increment δU is calculated to create the next contact.
7. The solution vector \vec{x} is incremented by $\frac{d\vec{x}}{dU} \delta U$.
8. If the stop condition is not reached, the procedure returns to Step 3.

The stop condition that will be used for the compaction of fibrous stacks is a target value of the fiber bundle volume fraction: $\phi \geq \phi_{target}$. If ϕ^* is the volume fraction of the initial stack, the volume fraction after the displacement $U > 0$ of the planes is:

$$\phi = \frac{\phi^*}{1 + U/H} \quad (3.26)$$

The application of this algorithm allows one to directly calculate the deformation of the fibrous medium and to obtain the contact forces by linking the microscopic behavior of a single roving to the behavior of the fiber bundle structure at the mesoscopic scale.

This algorithm has been implemented to complete the stacking algorithm presented in Chapter 2. It will be used in Section 3.4 and compared to analytical solutions for the different beam kinematics of Section 3.2. The complete code is given in Appendix I. The interest of the algorithm lies in the reduction of the model thanks to the integrated beam model and the exact resolution between the contact points, which makes this resolution sufficiently efficient to be applied to large systems. However, applications are limited to the mesoscopic scale with an explicit description of fibrous structures of reasonable size¹. In order to extend the modeling approach to larger scales, a homogenization framework must be proposed to represent the fibrous medium from a macroscopic point of view, without solving a direct mechanical problem, while capturing the influence of underlying heterogeneities.

¹ The total number of overlaps in the network is about $N^2/2$. Therefore, the matrices \mathbb{K} and \mathbb{C} are both $\sim N^2/2$ in size (in number of rows), and $\mathbb{P} \sim N^2$, which becomes bigger with the compaction. The quadratic complexity in this system of equations makes it a large problem, which is difficult to solve in a reasonable computational time for $N \gg 1$.

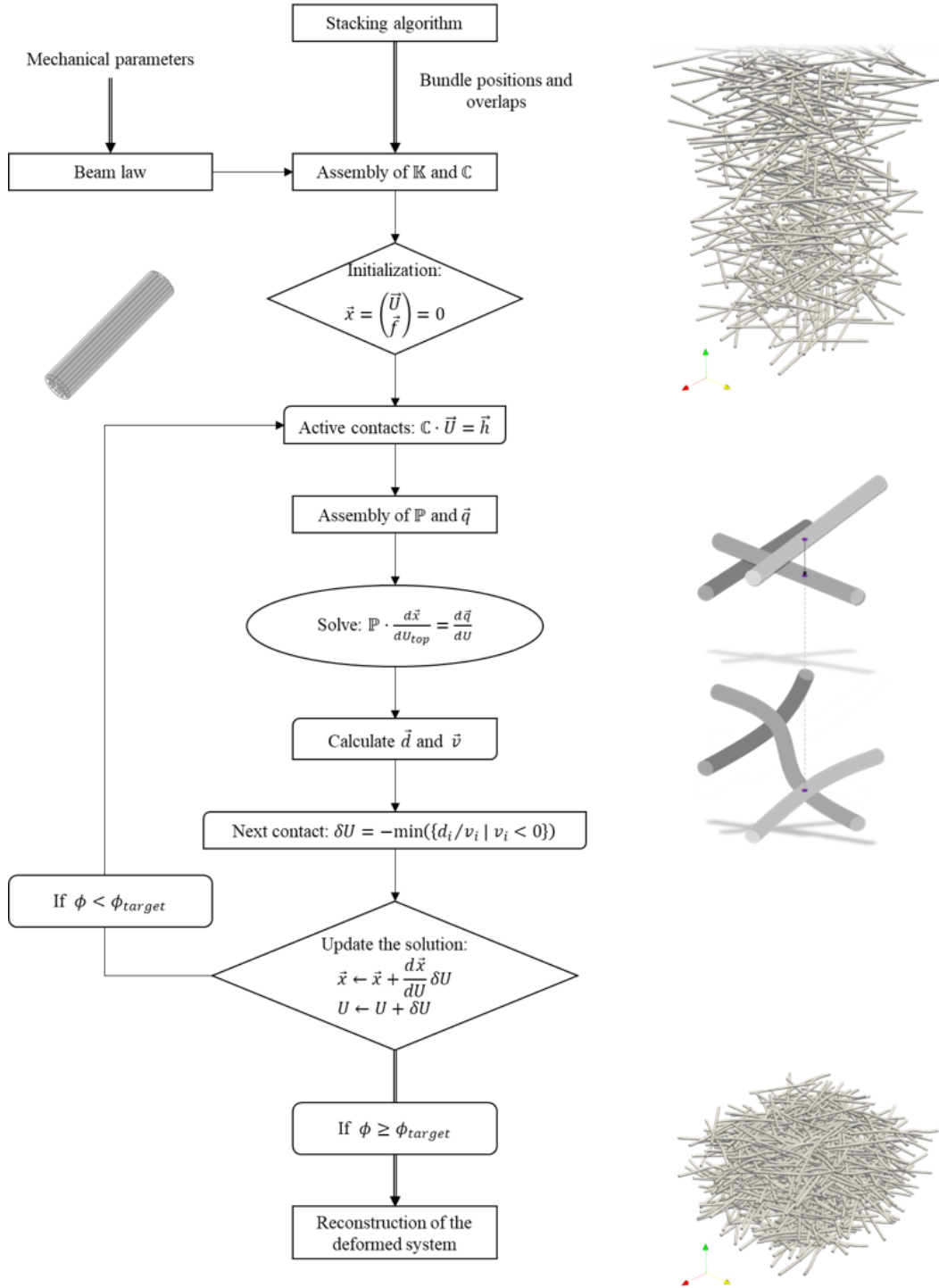


Figure 3.10: Resolution scheme for the compaction of a planar stack of fiber bundles.

3.4 Compaction of fibrous mesostructures

3.4.1 Introduction

Generating numerically fibrous mesostructures, and more generally, creating digital complex materials is a common strategy to study their properties as a function of their geometrical characteristics. In the case of SMC materials, there have been efforts to study the creation of fibrous networks or simulate the flow and the transport of fiber bundles. However, due to the very high numerical cost of such resolutions, these simulations are generally simplified, considering a sub-population of fiber bundles immersed in an effective medium, or neglecting part of the physical mechanisms involved in the definitions.

In the last few years, the generation of fibrous mesostructures has been addressed by several numerical strategies. Most of these techniques can be classified into two groups. The first family of method relies on the random generation of fibrous mesostructures by algorithms based on the Random Sequential Algorithm (RSA) (Görthofer, et al., 2020). Its principle is to add successively solid objects in the domain, without colliding, to fill the empty spaces of the formed network. This purely geometrical method is easy to implement and helps to generate efficiently sets of straight fiber bundles for low fiber volume fractions. The scalability of this method is known to be poor. To increase the fiber volume fraction, a subsequent step of numerical compaction is required. The second family of method relies on the direct 3D resolution of a finite element formulation in which the internal contacts are accounted for at each iteration (Fliegner, et al., 2014). Then, the mechanical behavior is naturally incorporated into the model but results in a very large system of equations to solve. Authors in (Fliegner, et al., 2014) also indicate limitations of the method to a small bundle volume fraction, due to the increasing size of the system of equations and the number of contacts in the structure.

The stacking algorithm presented in Chapter 2 is extended to simulate the compaction of random stacks of fiber bundles, using the iterative finite element algorithm of Section 3.3. The resulting algorithm is proposed to efficiently simulate realistic random fibrous mesostructures with predominantly planar orientations of fiber bundles, as for SMC mesostructures, and considering the mechanical behavior of the fibrous network. Contacts between the fiber bundles and contact forces are studied with respect to the generation parameters and the compaction of the fibrous medium. Numerical simulations are compared with the analytical results of the statistical framework and discussed specifically for SMC materials.

3.4.2 Theory and method

3.4.2.1 Statistical description and constitutive model of contact forces

The statistical framework developed in Appendix 3.B allows one to homogenize and solve macroscopically the mechanical compaction of the fibrous mesostructure describing the probabilistic distribution of the contact forces.

In the general case, fiber bundles of finite length are considered as straight, thin and slender objects of length l , width w and thickness e , and modeled mechanically as 1D beams. Here, we use the objective geometrical dimensions introduced in Chapter 2, which is the same as considering a square transverse cross-section of the fiber bundle of area $S = we$ and bending inertia $I = \frac{1}{12}we^3$. The volume of the fiber bundle is $v = lwe$.

Imposing a value of the fiber bundle volume fraction ϕ is equivalent to imposing a displacement field u on the fibrous network. The mean value of the discrete contact forces within the fibrous network is denoted by $f^\#$. Then, the principle of maximum entropy for a stack of fiber bundles of average contact energy $\langle \epsilon \rangle = \frac{1}{2} f^\# u$, which depends on a single degree of freedom, u , gives a distribution of contact force f in the form of an exponential distribution (see Appendix 3.B):

$$p(f)df = e^{-f/f^\#} \frac{df}{f^\#} \quad (3.27)$$

The reduction to a single degree of freedom leads to the elementary solutions for the shear and bending beams:

$$df_{shear}^\# = \frac{GS}{l_e} ed\varepsilon \quad df_{bending}^\# = \frac{EI}{l_e^3} ed\varepsilon \quad (3.28)$$

where $d\varepsilon$ is the variation of the fiber bundle strain. G and E are the fiber bundle shear and Young's moduli.

$$\Psi(l) = \sqrt{\frac{12EI}{GS l^2}} = \frac{e}{l} \sqrt{\frac{E}{G}} \quad (3.29)$$

In the general case of Timoshenko beam, the two behaviors are considered in the energetical formulation $\epsilon = \frac{1}{2} f^\# (u_{shear} + u_{bending})$, leading to the equivalent of a serial assembly of the two behaviors:

$$df^\# = - \left(\frac{l\lambda}{GS} + \frac{l^3 \lambda^3}{EI} \right)^{-1} \frac{ed\lambda}{\lambda} \quad (3.30)$$

By integration, the average contact force within the fibrous network is:

$$f^\# = \frac{GSe}{l} \left((\lambda^{-1} - 1) + \frac{1}{\Psi} \left(\arctan \left(\frac{\lambda}{\Psi} \right) - \arctan \left(\frac{1}{\Psi} \right) \right) \right), \text{ for } \lambda \leq 1 \quad (3.31)$$

Here λ is the vertical *stretch ratio*, defined as:

$$\lambda = \frac{\phi^*}{\phi} = \frac{h}{h^*} \quad (3.32)$$

where ϕ is the fiber bundle volume fraction, ϕ^* is the fiber bundle volume fraction of the unloaded bulky (or loose) fibrous medium, and similarly, h is the thickness of the fibrous stack, h^* is the thickness of the bulky stack. The stretch ratio measures the transformation of the fibrous medium, relative to a reference stat, the *bulky configuration* (see Chapter 2), for which there is no force between the fiber bundles.

It can be noted that the first term $\varepsilon^{(-1)} = (\lambda^{-1} - 1)$ corresponds to the mesoscopic strain associated with the shear deformation and is dominant for $\Psi \rightarrow +\infty$, compared with the second term which is related to the bending. At the other extreme, a series expansion of Eq. (3.31) allows one to retrieve the bending behavior, for $\Psi \rightarrow 0$, with a strain $\varepsilon^{(-3)} = \frac{1}{3}(\lambda^{-3} - 1)$ at the first order:

$$f^\# = \frac{12EIe}{l^3} \left(\frac{(\lambda^{-3} - 1)}{3} + \Psi^2 \frac{(\lambda^{-5} - 1)}{5} + \Psi^4 \frac{(\lambda^{-7} - 1)}{7} + \dots + \Psi^{n-3} \varepsilon^{(-n)} + \dots \right) \quad (3.33)$$

The analytical model of the average contact force within the fibrous network leads to the definition of a *mesoscopic strain* $\varepsilon^\#$ as a function of the *compaction ratio* λ^{-1} , which is equal by definition to the ratio between the fiber bundle volume fraction ϕ over the bulky volume fraction ϕ^* . By convention, $\varepsilon^\#$ is positive for compacted mesostructures and negative for a suspension of fiber bundles. The mesoscopic strain becomes null when ϕ is equal to the bulky volume fraction ϕ^* , which is a geometrical characteristic of the mesostructure depending on the shape, orientation and dimensions of the fiber bundles (see Chapter 2). Hence:

$$\phi^* = \frac{1}{\alpha r} \quad (3.34)$$

with α the angular factor for the bundle orientation and r is the aspect ratio of the bundle (in the generalized form of Chapter 2). Note that the angular factor can change with fiber bundle in-plane reorientations, as it is the case for SMC-like materials, with fiber bundles immersed in a continuous matrix phase.

The definition of the mesoscopic strain depends on the mechanical model for the fiber bundles and the material parameters. It can always be written as a linear combination or a series of Seth-Hill strain measurements, defined by:

$$d\varepsilon^{(n)} = -\lambda^n \frac{d\lambda}{\lambda} \quad \text{with} \quad \varepsilon^{(n)} \xrightarrow{\lambda \rightarrow 1} 0 \quad (3.35)$$

where the negative sign is for the positive notation in compression. The limit at $\lambda = 1$ defines the infinitesimal strain $d\varepsilon \underset{\lambda \rightarrow 1}{=} -d\lambda \underset{\lambda \rightarrow 1}{=} d(\lambda^{-1})$, towards which all strain measurements tend at $\lambda = 1$, including the mesoscopic strain. For a dry compaction (with only vertical motions of the fiber bundles), the infinitesimal strain corresponds to the incremental of *macroscopic strain* of the fibrous medium of thickness h :

$$d\varepsilon = -\frac{dh}{h} \quad \text{and} \quad d\varepsilon^\# \underset{\lambda \rightarrow 1}{\sim} d\varepsilon \quad (3.36)$$

It allows one to define, in the general case, the mechanical stiffness k of the fibrous mesostructure as a constant material parameter with:

$$ke = \frac{df^\#}{d\varepsilon^\#} = \left. \frac{df^\#}{d\varepsilon} \right|_{\lambda=1}, \quad \text{for } \lambda \leq 1 \iff \varepsilon \geq 0 \quad (3.37)$$

where e is the fiber bundle thickness.

The form of the mesoscopic strain characterizes the evolution of the contact forces with respect to the fibrous mesostructure properties, in particular with the fiber bundle volume fraction. Replacing the compaction ratio by its definition to make ϕ appear in Eq. (3.31) and (3.33) gives, respectively for the shear and bending modes, a linear and cubic evolution of the average contact force with respect to the fiber bundle volume fraction. This evolution is represented in Figure 3.11 for different values of Ψ , illustrating the transition that the Timoshenko model allows between the shear and bending beam models.

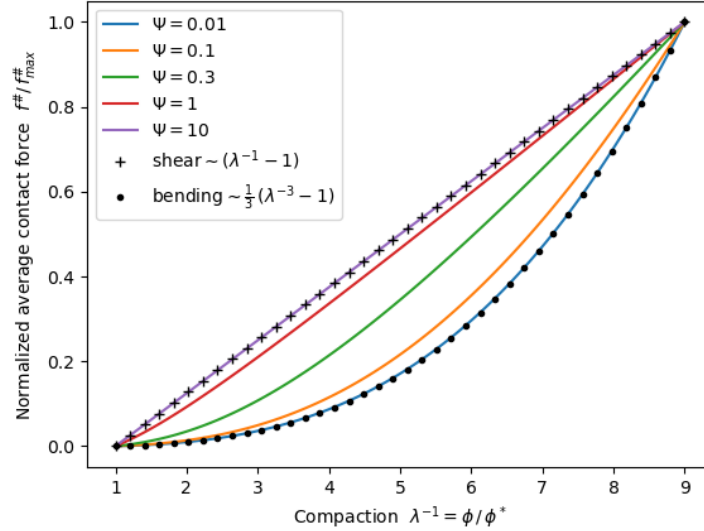


Figure 3.11: Average mesoscale contact force $f^{\#}$ as a function of the compaction $\lambda^{-1} = \phi/\phi^*$ and parametrized by Ψ , from the bending model, with a cubic mesoscopic strain $\varepsilon^{\#} \sim (\phi^3 - \phi^{*3})$, to the shear model, with a linear mesoscopic strain $\varepsilon^{\#} \sim (\phi - \phi^*)$. The force is normalized by the maximum force value at $\lambda^{-1} = 9$.

At the macroscale, the packing force is the sum of all the contact forces between the fiber bundles and the force of the compression platens. The stacking model of Chapter 2 predicts that the average area per fiber bundle element, and thus, per contact point, is in average $\alpha(l\lambda)^2$, where α is the angular factor (see Chapter 2) and $l\lambda$ is the fiber bundle length, rescaled by λ which corresponds to the typical length of a beam element. Hence the packing stress, defined as the resultant of the contact forces on a platen divided by the area covered by the fiber bundle stack, is given incrementally by:

$$d\Sigma = \frac{df^{\#}}{\alpha(l\lambda)^2} = \frac{ke}{\alpha l^2} \cdot \lambda^{-2} d\varepsilon^{\#} \quad (3.38)$$

After integration, the packing stress is given by:

$$\Sigma = \frac{GSe}{\alpha l^3} \left(\frac{(\lambda^{-3} - 1)}{3} - \frac{1}{\Psi^2} (\lambda^{-1} - 1) - \frac{1}{\Psi^3} \left(\arctan \left(\frac{\lambda}{\Psi} \right) - \arctan \left(\frac{1}{\Psi} \right) \right) \right), \text{ for } \lambda \leq 1 \quad (3.39)$$

Here again, the first term $\varepsilon^{(-3)} = \frac{1}{3}(\lambda^{-3} - 1)$ corresponds to the shear behavior and is valid for $\Psi \rightarrow +\infty$. At the other extreme, the bending behavior with a strain $\varepsilon^{(-5)} = \frac{1}{5}(\lambda^{-5} - 1)$ appears at the first order of the series expansion of Eq. (3.39) for $\Psi \rightarrow 0$:

$$\Sigma = \frac{12EIe}{\alpha l^5} \left(\frac{(\lambda^{-5} - 1)}{5} + \Psi^2 \frac{(\lambda^{-7} - 1)}{7} + \Psi^4 \frac{(\lambda^{-9} - 1)}{9} + \dots + \Psi^{n-5} \varepsilon^{(-n)} + \dots \right) \quad (3.40)$$

In the same way as for the contact force, the packing pressure, respectively for the shear and bending models, has a cubic and quintic dependance within the fiber bundle volume fraction, as illustrating in Figure 3.12, with the transition between these two models for different values of Ψ . As it can be seen compared with the results at the mesoscale, the increasing number of contacts between the fibrous network and the platens tends to increase by 2 the order of the strain related to the packing stress, with respect to the mesoscale strain.

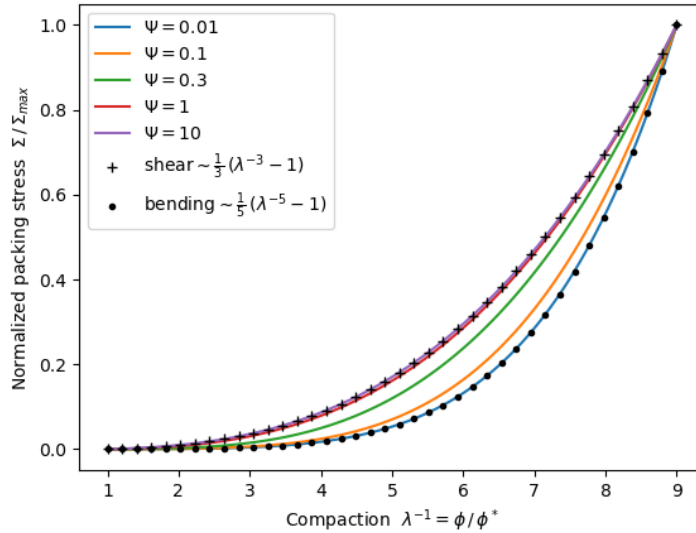


Figure 3.12: Macroscale packing stress Σ as a function of the compaction $\lambda^{-1} = \phi/\phi^*$ and parametrized by Ψ , from the bending model, with a quintic mesoscopic strain $\varepsilon^\# \sim (\phi^3 - \phi^{*3})$, to the shear model, with a linear mesoscopic strain $\varepsilon^\# \sim (\phi - \phi^*)$. The force is normalized by the maximum stress value at $\lambda^{-1} = 9$.

It can be noted that the two models, for the local contact force and the global packing stress, depends on the same mechanical stiffness but have a different order of strain measurement. Thanks to this relationship, the macroscopic compaction of a dry fibrous medium can help to identify the material parameters, which can then be used to calculate the distribution of the contact forces at the mesoscale.

Here, we retrieve the experimental results of (Schofield, 1938) and (Van Wyk, 1946) for the compaction of fibrous media, with a cubic or quintic behavior of the packing stress, depending on the mechanical behavior of the fiber bundles. The analytical macroscopic results are consistent with the literature results (Durville, 2005), (Rodney, et al., 2005), (Picu, 2011), in particular with the approach of (Toll, 1998) who obtained the form in power law, without the expression of the mechanical stiffness and the bulky volume fraction as functions of the material parameters. With our proposed model, the expression of the packing stress is derived by a more physical approach, completing the model of Toll and extending it to more complex behaviors than with coupled deformation kinematics. But more importantly, it gives a complete statistical description of local contact forces within the fibrous mesostructure.

To corroborate our proposed approach, finite element based numerical simulations are developed and their results are compared with the above analytical results.

3.4.2.2 Finite element formulation

Fiber bundles are numerically stacked on a planar and periodic domain with the stacking algorithm of Chapter 2 (see Figure 3.13). The overlaps between the fiber bundles defines the nodes and 1D elements of the mesh, assuming small deformations of the fiber bundles.

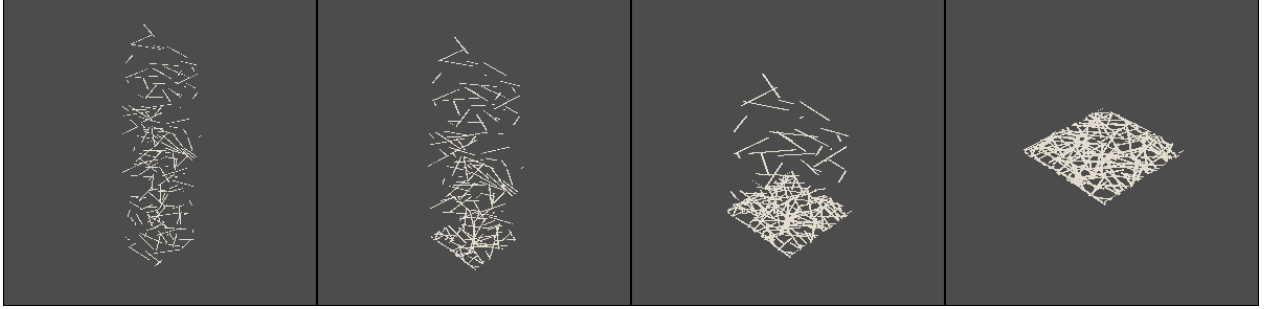


Figure 3.13: Numerical stacking of fiber bundles in the vertical direction (100 fiber bundles of length 25mm on a periodic square domain of length 50mm).

In Section 3.2, we obtained the finite element formulation of a Timoshenko beam element. The kinematic degrees of freedom (KDoFs) of a beam element are the vertical displacements ($V^{(i)}, V^{(j)}$) and the rotation angles ($\theta^{(i)}, \theta^{(j)}$) of the fiber bundle ends. The stiffness matrix and vector of KDoFs of a Timoshenko beam element of length l_e are:

$$\mathbb{K}_e = \frac{EI}{(1+\Psi(l_e)^2)l_e^3} \begin{bmatrix} 12 & 6l_e & -12 & 6l_e \\ 6l_e & (4 + \Psi(l_e)^2)l_e^2 & -6l_e & (2 - \Psi(l_e)^2)l_e^2 \\ -12 & -6l_e & 12 & -6l_e \\ 6l_e & (2 - \Psi(l_e)^2)l_e^2 & -6l_e & (4 + \Psi(l_e)^2)l_e^2 \end{bmatrix}, \quad \vec{U}_e = \begin{pmatrix} V^{(i)} \\ \theta^{(i)} \\ V^{(j)} \\ \theta^{(j)} \end{pmatrix} \quad (3.41)$$

where the stiffness matrix is parameterized by the dimensionless number $\Psi(l_e)$ defined in Eq. (3.29).

For low values of Ψ , it tends toward the formulation of a simple bending beam:

$$\mathbb{K}_e = \frac{EI}{l_e^3} \begin{bmatrix} 12 & 6l_e & -12 & 6l_e \\ 6l_e & 4l_e^2 & -6l_e & 2l_e^2 \\ -12 & -6l_e & 12 & -6l_e \\ 6l_e & 2l_e^2 & -6l_e & 4l_e^2 \end{bmatrix}, \quad \vec{U}_e = \begin{pmatrix} V^{(i)} \\ \theta^{(i)} \\ V^{(j)} \\ \theta^{(j)} \end{pmatrix} \quad (3.42)$$

For high values of Ψ , the shear compliance becomes dominant and the finite element formulation is equivalent to the reduced formulation:

$$\mathbb{K}_e = \frac{GS}{l_e} \begin{bmatrix} 1 & -1 \\ -1 & 1 \end{bmatrix}, \quad \vec{U}_e = \begin{pmatrix} V^{(i)} \\ V^{(j)} \end{pmatrix} \quad (3.43)$$

The elementary formulations of Timoshenko beams are assembled to specify the minimization problem:

$$\min_{\vec{U}, \vec{f}} \left(\frac{1}{2} \vec{U} \cdot \mathbb{K} \cdot \vec{U} - \vec{f} \cdot (\mathbb{C} \cdot \vec{U} - \vec{h}) \right) \quad \text{s. t.} \quad \mathbb{C} \cdot \vec{U} \geq \vec{h} \quad \text{and} \quad \vec{f} \geq 0 \quad (3.44)$$

which defines the vector of contact forces \vec{f} associated with the contact conditions (internal and external) at all nodes of the mesh. Here and in the following, we use the positive notation for compressive forces, strains, stresses and downward displacements. The contact matrix \mathbb{C} and the vector of vertical distances \vec{h} describe the overlaps between the fiber bundles by the inequality constraints $\mathbb{C} \cdot \vec{U} \geq \vec{h}$. These inequalities also include external contacts with parallel platens, vertically delimiting the stack of fiber bundles and imposing its vertical compaction by a vertical displacement.

The minimization problem is solved iteratively as detailed in Section 3.3, solving at each iteration the linear system of equations, written in terms of displacement and force increments, $\delta\vec{U}$ and $\delta\vec{f}$:

$$\mathbb{K} \cdot \delta\vec{U} = \mathbb{C}^T \cdot \delta\vec{f} \quad \text{with} \quad \mathbb{C} \cdot \vec{U} \geq \vec{h} \quad \text{and} \quad \vec{f} \geq 0 \quad (3.45)$$

3.4.2.3 Simulations

The previous finite element formulation and iterative solving algorithm were implemented in Python3, using the core libraries of the Anaconda distribution, and Paraview to export 3D rendered mesostructures. The shear, bending and Timoshenko models are included. The full Python script is provided in Appendix I.

The linear solver uses sparse matrices and a sparse solver to optimize the calculation. The stiffness and contact matrices are completely assembled initially. Then, during the solving iterations, the linear system corresponding to active contacts is extracted and re-numbered using the reverse Cuthill–McKee algorithm to transform the sparse system of equations into the form of a band matrix that is easier to solve.

The code is run on an 11th Gen Intel® Core™ i9-11950H @ 2.60GHz \times 16, with 64GB of RAM. The calculation on 8 cores for 600 fiber bundles of length 25mm, randomly dropped on a planar square domain of length 50mm and compacted from 3% to 30%, lasts 780s using the

Timoshenko model (it corresponds to ~ 32000 DoFs and the number of contacts increases from ~ 850 to ~ 3500) and 55s for the simplified shear model with a single degree of freedom per node.

To validate the convergence of the numerical results and compare with the analytical model of contact forces, fibrous mesostructures are generated with 600 fiber bundles of length 25mm on a periodic square domain of length 50mm (see Figure 3.14). The fiber bundle width and thickness are respectively 1mm and 0.1mm respectively. The initial fiber bundle bulky volume fraction predicted by Eq. (3.34) is, for a random orientation distribution, $\phi^* = 4\%$. The fibrous mesostructures are compacted to reach a fiber bundle volume fraction $\phi = 30\%$, which corresponds to a compaction ratio $\lambda^{-1} = 7.5$ for the random orientation distribution. The statistical distributions and mean values of contact forces (represented in Figure 3.15) are compared with the analytical model for different mechanical and generation parameters.

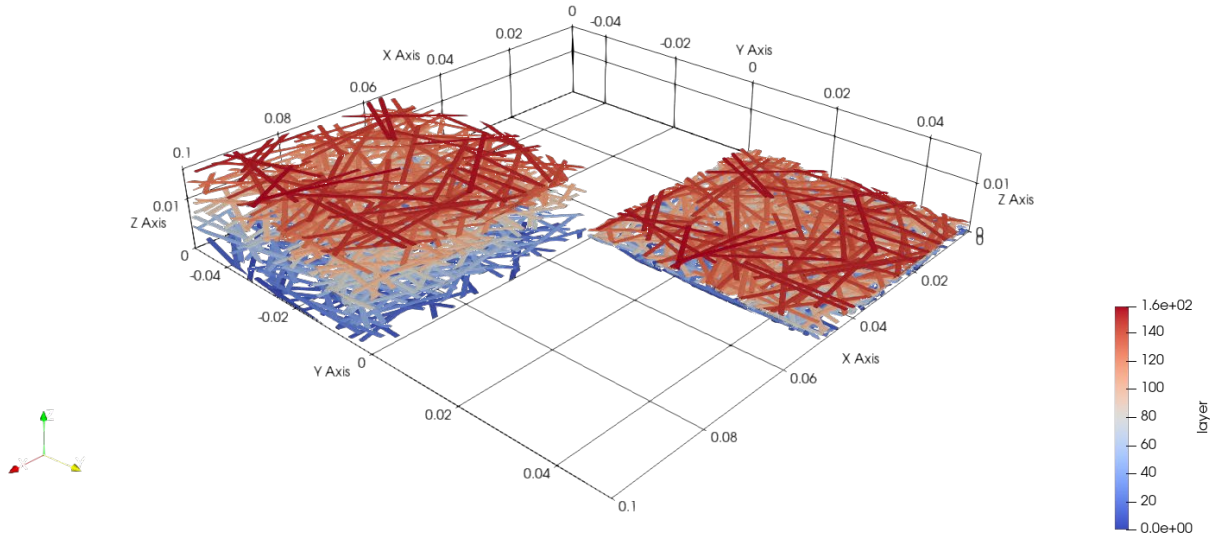


Figure 3.14: Bulky (4%) and compacted (30%) fibrous mesostructure made of 600 fiber bundles of length 25mm, randomly dropped on a periodic square domain of length 50mm.

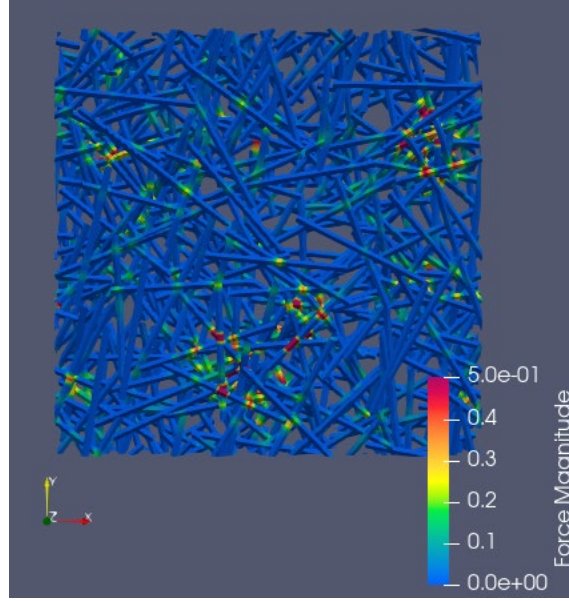


Figure 3.15: Statistical variation of contact forces within the fibrous network (100 fiber bundles of length 25mm on a square domain of length 50mm, using the shear model).

3.4.3 Results

In Figure 3.16 to Figure 3.19, numerical random fibrous mesostructures are compacted using the simplified shear model of Eq. (3.43) (Figure 3.16) and the Timoshenko model (Figure 3.17 to Figure 3.19). A total of 20 random realizations of fibrous mesostructures are generated per series, using the same mesostructure parameters. The histograms of the numerical contact forces at $\phi = 30\%$ are superimposed on the left figures. The numerical exponential distribution of each simulated mesostructure is calculated from the mean contact force and plotted in red. The analytical model of the average contact force is shown in dotted line and compared with the numerical distributions. The evolution of the mean contact force of each simulation is shown in the right figures (gray) and compared with the analytical model (black). The bulky volume fractions involved in the calculation of λ^{-1} are calculated from the numerical initial volume fractions to avoid convergence issues.

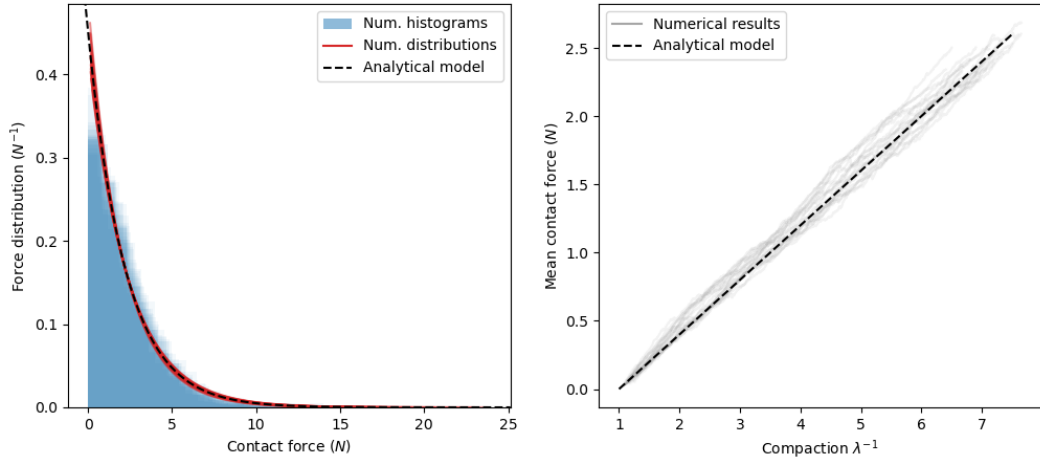


Figure 3.16: Simplified shear model (a single DoF per node, $G = 1\text{GPa}$). Distribution of contact forces (left) and evolution of the mean contact force with the compaction (right) for 20 random realizations of fibrous mesostructures.

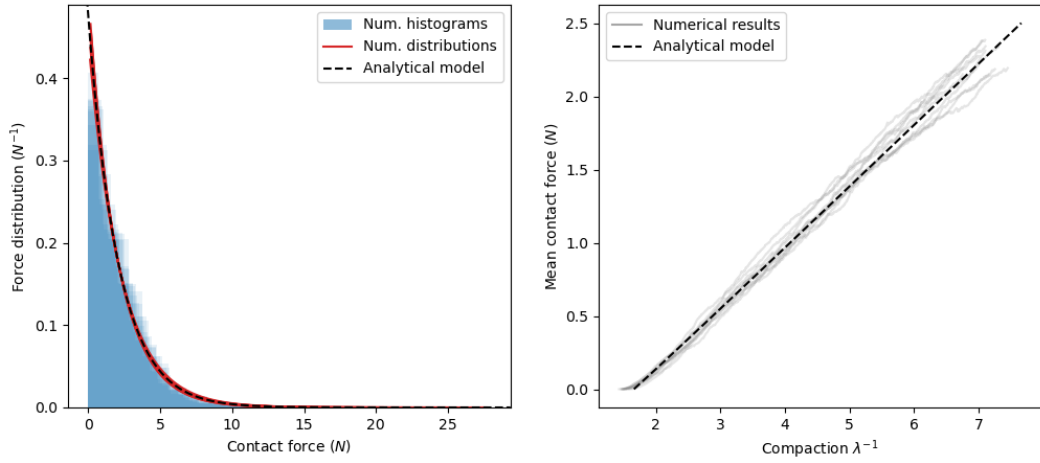


Figure 3.17: Timoshenko model for $\Psi \gg 1$ (shear, $G = 1\text{GPa}$). Distribution of contact forces (left) and evolution of the mean contact force with the compaction (right) for 20 random realizations of fibrous mesostructures.

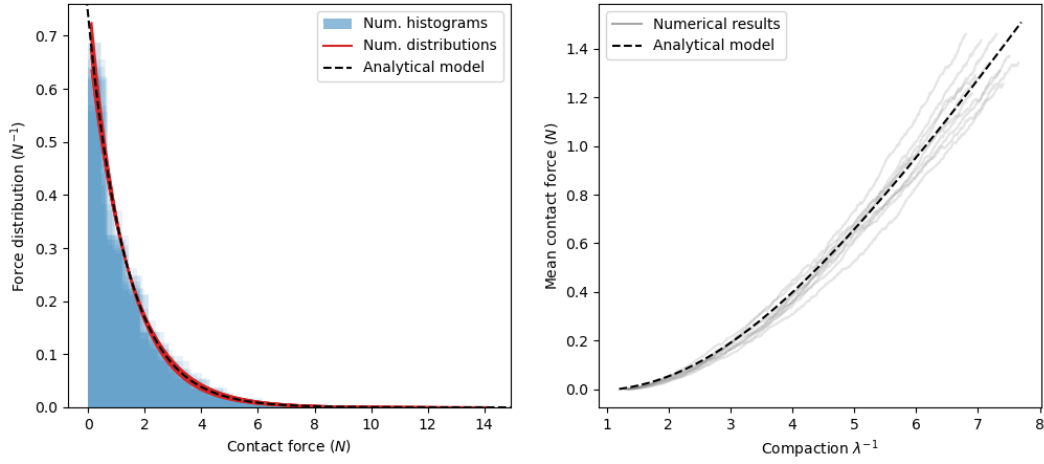


Figure 3.18: Timoshenko model for $\Psi = 0.3$ ($G = 1\text{GPa}$, $E = 6000\text{GPa}$). Distribution of contact forces (left) and evolution of the mean contact force with the compaction (right) for 20 random realizations of fibrous mesostructures.

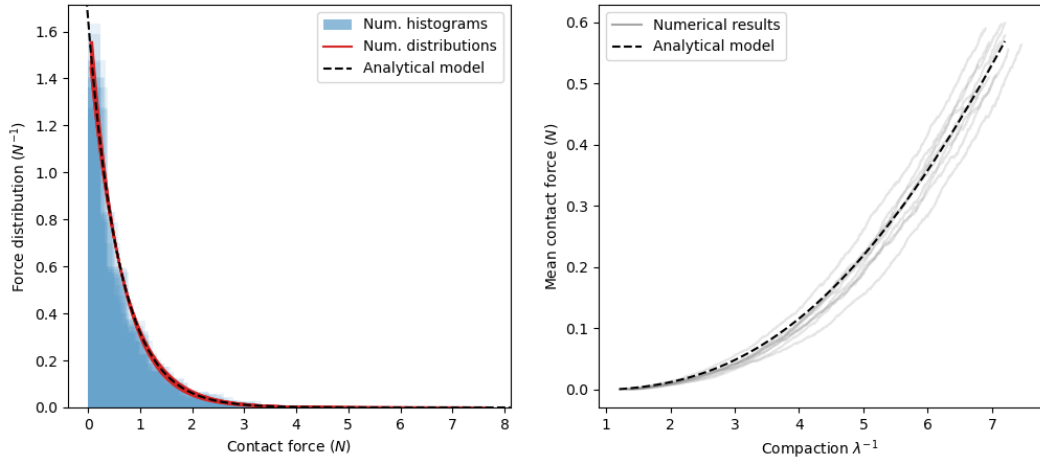


Figure 3.19: Timoshenko model for $\Psi \ll 1$ (bending, $E = 1000\text{GPa}$). Distribution of contact forces (left) and evolution of the mean contact force with the compaction (right) for 20 random realizations of fibrous mesostructures.

Figure 3.20 shows the distributions and mean values of contact forces at $\phi = 30\%$ for different sizes of the square domain, with a length from 1 to 4 times the fiber bundle length. The convergence of the mean contact forces is compared with the convergence of the bulky volume fraction towards their respective analytical values. A total of 5 random realizations of fibrous mesostructures are generated per domain size.

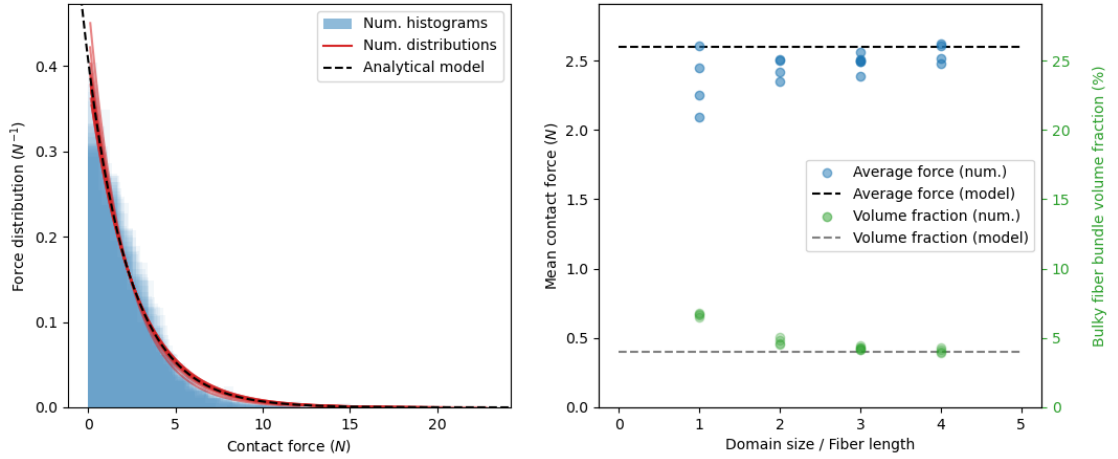


Figure 3.20: Effect of the domain length and convergence of the results (shear model, $G = 1\text{GPa}$). Distribution of contact forces (left) and mean contact force at $\phi = 30\%$ vs. the domain length divided by the fiber bundle length (right), compared with the evolution of the initial bulky fiber bundle volume fraction.

Figure 3.21 shows the distributions and mean values of contact forces at $\phi = 30\%$ for different numbers of fiber bundles N , from 50 to 800 in steps of 50 fiber bundles. The convergence of the mean contact forces is compared with the convergence of the bulky volume fraction towards their respective analytical values. 10 random realizations of fibrous mesostructures are generated per value of N (15 random realizations for $N = 50$).

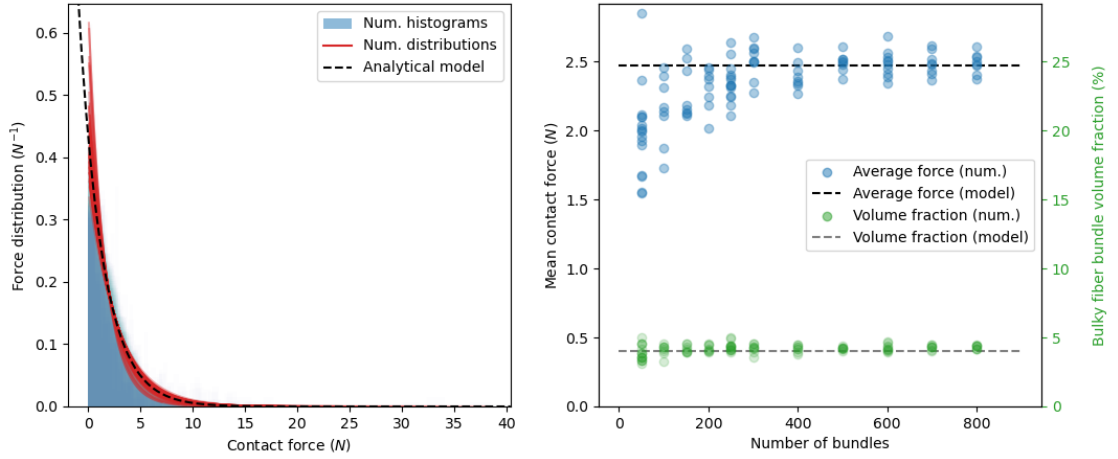


Figure 3.21: Effect of the number of fiber bundles and convergence of the results (shear model, $G = 1\text{GPa}$). Distribution of contact forces (left) and mean contact force at $\phi = 30\%$ vs. the number of fiber bundles (right), compared with the evolution of the initial bulky fiber bundle volume fraction.

In Figure 3.22, the mean contact forces at $\phi = 30\%$ using the shear model are compared with the analytical model. 100 random realizations of fibrous mesostructures are generated with different angular factors from 1 (random orientation) to 0.2 (mostly aligned orientations).

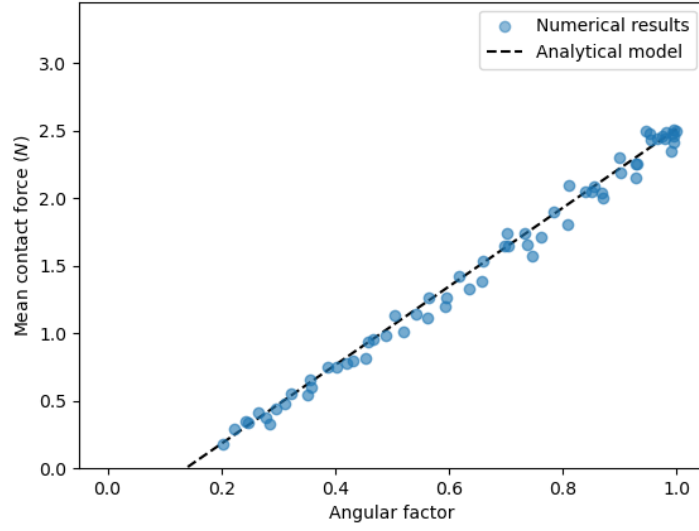


Figure 3.22: Mean contact force for the shear model ($G = 1\text{GPa}$) at $\phi = 30\%$ vs. the angular factor α for 100 random realizations of fibrous mesostructures with $\alpha \in [0.2, 1]$.

In Figure 3.23, the mean contact forces at $\phi = 30\%$ using the bending model are compared with the analytical model. 25 random realizations of fibrous mesostructures are generated with different angular factors from 1 (random orientation) to 0.2 (mostly aligned orientations).

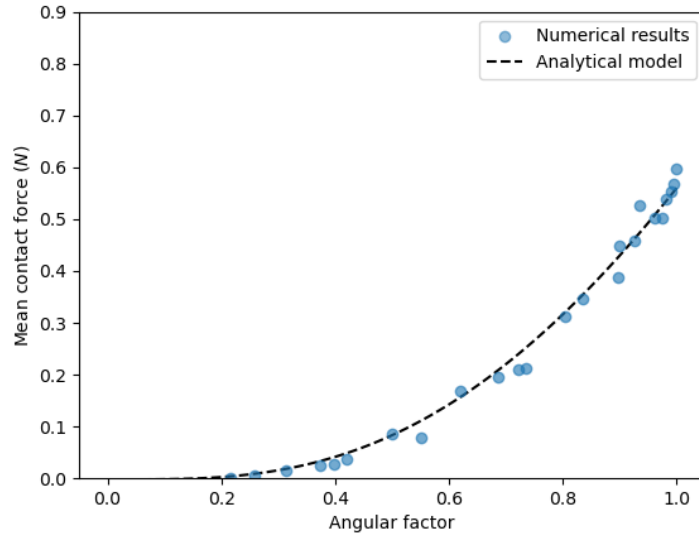


Figure 3.23: Mean contact force for the bending model ($E = 1000\text{GPa}$) at $\phi = 30\%$ vs. the angular factor α for 25 random realizations of fibrous mesostructures with $\alpha \in [0.2, 1]$.

In Figure 3.24, the mean contact forces at $\phi = 30\%$ using different values of the parameter of the Timoshenko model Ψ . The numerical results for 40 random realizations of fibrous mesostructures are compared with the analytical model, highlighting the non-linear transition between the shear and bending models.

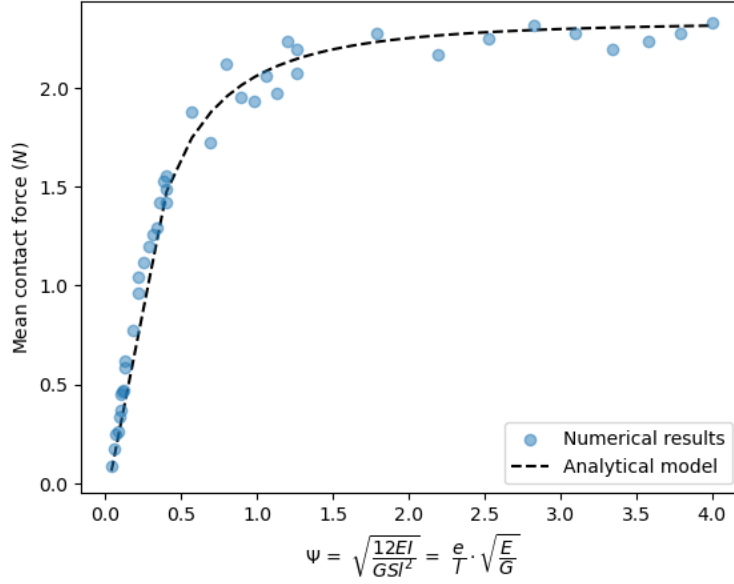


Figure 3.24: Evolution of the mean contact force at $\phi = 30\%$ for different values of Ψ , compared with the analytical model. 40 random realizations of fibrous mesostructures were generated with a shear modulus $G = 1\text{GPa}$ and different values of dimensionless number $\Psi \in [0,4]$.

3.4.4 Discussions

3.4.4.1 Comparison of the numerical results with the analytical model

The proposed algorithm to generate random fibrous mesostructures appears to be efficient, with a relatively short simulation time compared with alternative approaches. A similar method using finite element, without the discretization strategy between the overlapping points, was presented by (Fliegner, et al., 3D microstructure modeling of long fiber reinforced thermoplastics, 2014). The authors explained that the algorithm is limited to relatively low volume fractions (up to 8%, then a relaxation method must be used to reach 25%). In our case, the iterative solver based on beam models can generate rapidly very compacted mesostructures of relatively large sizes (165s for a final compaction ratio of 12, using the shear model for 600 fiber bundles of length 25mm and a domain of size 50mm). Then, the proposed solver can be used to carry out statistical analysis on large sets of mesostructures.

The numerical results with different simulation conditions given in Figure 3.16 to Figure 3.21 shows the reliability of the statistical model derived using the principle of maximum entropy. The contact forces are described by an exponential distribution, of which only the parameter (the average contact force) is likely to change depending on the simulation parameters. In particular, Figure 3.20 and Figure 3.21 shows a significant variation of the mean contact force, which simply rescales the exponential distribution of the contact force. The fluctuations of the mean contact forces are explained by the fluctuations of the initial fiber bundle volume fraction, which varies for small fiber bundle populations (low values of N) and small sizes of the stack (low values of L). These variations are explained by a defect of convergence for small populations, the fiber bundle volume fraction is higher in the lower layers of the stack, and boundary effects for small sizes of the stack, with interferences between the fiber bundles close to the periodic borders. These two effects have been observed in Chapter 2. However, the fiber

bundle volume fraction converges rapidly towards the analytical bulky volume fraction ϕ^* and the mean contact force tends toward the analytical value $f^\#$ of the model.

The model of the average contact force is validated by the numerical simulations for the three models (shear, bending and Timoshenko) and captures correctly the dependance of the contact force in the orientation distribution for the shear and bending models, respectively with linear and cubic evolutions with respect to the angular factor, involved in the definition of the mesoscale strain. The non-linear evolution of the average contact force with respect to the values of the material parameters is validated by the agreement of the numerical results with the analytical model in Figure 3.24.

3.4.4.2 Application to SMC mesostructures

The proposed model for the mesoscopic mechanical behavior of random fiber bundles is represented in Figure 3.25 as a function of the fiber bundle aspect ratio r and for different values of the parameter $r\Psi = (e/w)\sqrt{E/G}$, which does not depend on the fiber bundle length. It shows that for relatively long fiber bundles, the contact force tends rapidly to a constant value f^∞ , corresponding to the average contact force within a continuous mat made of infinite length fiber bundles. At the other extreme, the force vanishes for low aspect ratios, and then remains equal to zero as there is no contact and mechanical efforts between the fiber bundles. It corresponds to a dilute suspension of fiber bundles. The mechanical model is consistent with the well-known types of fibrous media, from the dilute regimes to mat structures. However, this representation can be discussed in the case of significant contact forces. In that case, the important mechanical loads can activate other deformation mechanisms of the fiber bundles, such as the compression of fiber bundles and the filamentization observed in Chapter 2, which will require one to adapt the mechanical beam model for the fiber bundles.

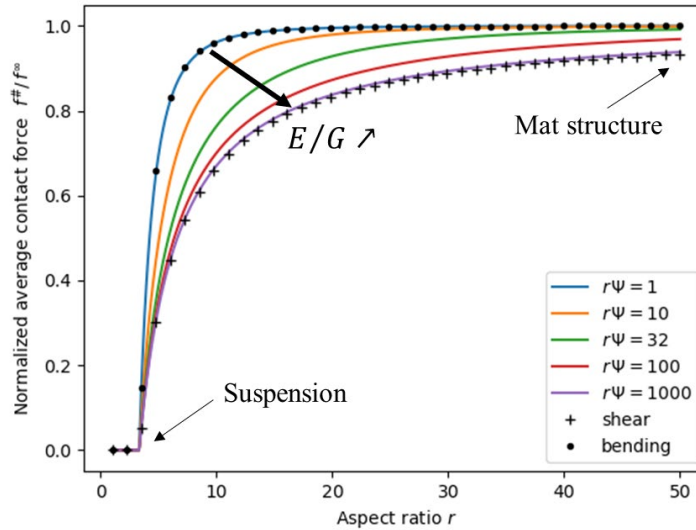


Figure 3.25: Mean contact force $f^\#$ at $\phi = 30\%$ as a function of the fiber bundle aspect ratio r and the dimensionless parameter Ψ of the Timoshenko model. The force is normalized by the contact force for fiber bundles of infinite length f^∞ .

In case of the SMC material, it appears that the fiber bundle aspect ratio, which is commonly between 10 and 50, is likely to belong to the interval after the important transition, as shown

in Figure 3.25 for $\phi = 30\%$. We can conclude that SMC materials, especially with high fiber contents, have significant contact forces between the fiber bundles which should not be neglected in a modeling approach.

During the compression molding process, the flow of the material and its deformation modify the fibrous mesostructure. This evolution is taken into account when defining the bulky volume fraction ϕ^* which is the reference unloaded state of the mesostructure, likely to change during the transformation. Thanks to the universal distribution of contact forces as an exponential distribution obtained in Appendix 3.B, the proposed framework to describe statistically the mechanics of discontinuous fibrous media can be applied to the SMC mesostructures during the molding process.

3.5 Conclusions

The statistical formalism presented in this section allows one to describe the mechanical behavior of any fibrous medium, consisting of chopped fiber bundles assembled by stacking and compaction into a discontinuous and porous structure.

The multi-scale nature of these structures requires the description at three different scales of:

- the movements of fibers inside the fiber bundle (microscopic scale)
- the deformation of the structure formed by the network of fiber bundles (mesoscopic scale)
- the distribution of material states at large scale (macroscopic scale)

At the microscopic scale, the mechanical behavior of the fiber bundle is obtained using a beam theory. Three different models for their deformation are presented to deal with shear, bending and their coupled modes respectively. By solving the constitutive equations of the beam model, an exact solution of the fiber bundle deformation is obtained for a given choice of the transformation kinematics. A finite element formulation is obtained from the shape functions of the roving.

At the mesoscopic scale, the fibrous structure is a planar stack of fiber bundles in which contacts play an important role in the transfer of forces and the behavior of the medium. The finite element model developed for the fiber bundle is reused to describe the deformation of the fiber bundle elements between the contact points. The mechanics of contacts result in a constrained optimization problem. Since the system is linear as long as the set of contacts remains unchanged, the optimization problem is solved iteratively. **The proposed procedure allows one to efficiently solve large structures but remains limited to mesoscopic problems.** This algorithm can be implemented to simulate realizations of compacted mesostructures.

At the macroscopic scale, the huge number of fiber bundles and degrees of freedom of the system makes it impossible to use an exact description of the medium. Therefore, **we use a probabilistic description of the fibrous system using a reformulation of the tools of statistical physics.** The set of admissible states of the fibrous system are described by the partition function of the system which encodes all its possible realizations. This set is split into two parts: the set of possible manifold configurations and the set of admissible mechanical

states. We deduce the probability laws that govern its state variables, as described in the Appendix 3.B.

In the case of a fibrous medium under compaction, the distribution allows one to trace the local behavior at the contacts between fiber bundles. With the mesoscopic model, we have demonstrated that small local deformations lead to large transformations of the macroscopic system. We can thus reduce the global behavior to elementary contributions and express it from the microscopic behavior model of the fiber bundles.

The multiscale model of the stack not only describes the average forces inside the fibrous network, but also provides the entire statistical distribution of these forces. The statistical formalism completely describes the fibrous medium by naturally linking the three scales to finally depend only on the material parameters of the fiber bundles and the boundary conditions imposed on the system.

Appendices

3.A. Derivation of beam equations and finite element formulations

The local curvilinear coordinate system (X, Y, Z) is defined with respect to fibers in the bundle in the undeformed configuration. The associated unitary vectors are denoted $(\vec{e}_X, \vec{e}_Y, \vec{e}_Z)$, where X is the longitudinal direction, Y and Z are the horizontal and vertical transverse directions (see Figure 3.26-a). Similarly, we refer to the curvilinear coordinate system in the deformed configuration and its unitary vectors $(\vec{e}_x, \vec{e}_y, \vec{e}_z)$ as (x, y, z) (see Figure 3.26-b).

The transformation kinematics is given by the expression of the vector displacement field at each point of the fiber bundle with respect to the undeformed configuration:

$$\vec{u} = u_X(X, Y, Z)\vec{e}_X + u_Y(X, Y, Z)\vec{e}_Y + u_Z(X, Y, Z)\vec{e}_Z \quad (3.46)$$

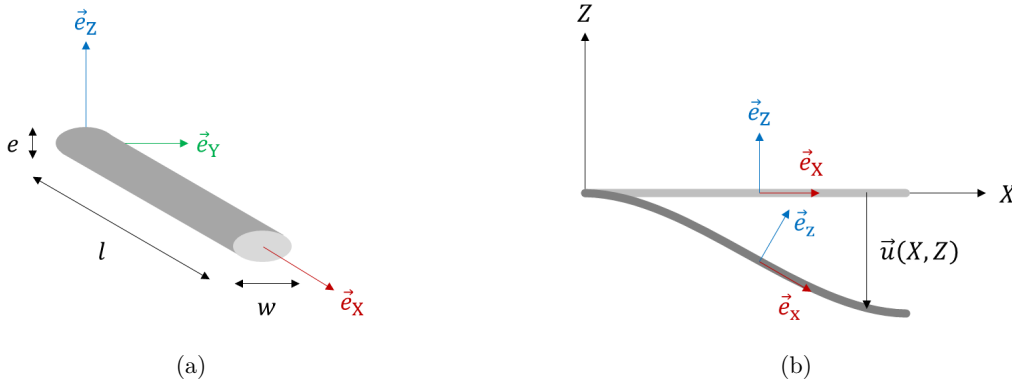


Figure 3.26: Geometrical dimensions and curvilinear coordinate systems along the (a) undeformed fiber bundle and (b) the deformed fiber bundle.

The choice of an analytical expression for the displacement field conditions the mechanical model. According to the slender geometry of fiber bundles, several beam models will be discussed, each based on a different choice of kinematics.

The neutral fiber of the fibrous roving is defined as its geometrical centerline. In the case of a thin and slender fiber bundle, the deformation is essentially reduced to the deformation of the neutral fiber, as shown by a dimensional analysis:

$$\frac{\Delta \vec{u}}{l} \sim \frac{\partial \vec{u}}{\partial X} \ll \frac{\partial \vec{u}}{\partial Y} \ll \frac{\partial \vec{u}}{\partial Z} \sim \frac{\Delta \vec{u}}{e} \quad (3.47)$$

The displacement components of \vec{u} depend primarily on the transverse coordinates Y and Z and can be expressed in polynomial form (or an infinite series) in Y and Z . The polynomial coefficients are then slowly evolving functions with respect to the longitudinal coordinate X .

The choice of these polynomial coefficients defines the kinematics considered. In compaction problems, where the macroscopic load is aligned with the vertical direction, the displacement

depends mainly on the Z coordinate and lies locally in the (X, Z) plane of the fiber bundle. The beam kinematics is expressed by a planar displacement of the fibers, polynomial in Z :

$$\begin{aligned}\vec{u} = & (A^{(0)}(X) + A^{(1)}(X)Z + A^{(2)}(X)Z^2 + \dots)\vec{e}_X \\ & + (B^{(0)}(X) + B^{(1)}(X)Z + B^{(2)}(X)Z^2 + \dots)\vec{e}_Z\end{aligned}\quad (3.48)$$

where $A^{(i)}$ and $B^{(i)}$ are the polynomial coefficients, or functions of the longitudinal coordinate with a relative slow evolution.

The symmetric part of the displacement gradient $\nabla\vec{u}$ gives the infinitesimal strain at each point of the bundle:

$$\bar{\bar{\varepsilon}} = \text{symm}(\nabla\vec{u}) = \begin{bmatrix} u_{X,X} & 0 & \frac{u_{X,Z} + u_{Z,X}}{2} \\ & 0 & 0 \\ \text{symm.} & & u_{Z,Z} \end{bmatrix} \quad (3.49)$$

For a linear elastic behavior of the fiber bundle, the Cauchy stress tensor $\bar{\bar{\sigma}}$ is proportional to the infinitesimal strain tensor according to the law:

$$\bar{\bar{\sigma}} = \mathbb{H} : \bar{\bar{\varepsilon}} \quad (3.50)$$

The components of the fourth order tensor \mathbb{H} characterize the material properties of the fibrous roving for different mechanical loadings. The Lagrangian of the mechanical problem is:

$$\mathcal{W}(\vec{u}) = \underbrace{\frac{1}{2} \int \bar{\bar{\sigma}} : \bar{\bar{\varepsilon}} dV}_{\mathcal{W}_{int}} - \underbrace{\left(\oint \vec{u} \cdot \vec{T} dS + \int \vec{u} \cdot \vec{g} dV \right)}_{\mathcal{W}_{ext}} \quad (3.51)$$

where the term \vec{T} refers to a surface force and \vec{g} is a body force, both imposed by external sources.

The first integral defined inside the fiber bundle is the internal strain energy \mathcal{W}_{int} . The second integral defined on the fiber bundle ends is the work of the external forces \mathcal{W}_{ext} . The solution of the mechanical problem \vec{u}^* is given by the minimum of the energy functional $\mathcal{W}(\vec{u})$, i.e., \vec{u}^* is a solution of the system of partial differential equations:

$$\frac{\partial \mathcal{W}}{\partial \vec{u}^*} \delta \vec{u} = 0 \quad (3.52)$$

where $\partial \mathcal{W} / \partial \vec{u}^*$ denotes the derivative of the Lagrangian in $\vec{u} = \vec{u}^*$. This is the weak formulation of the mechanical problem for a virtual increment of displacement $\delta \vec{u}$ around the equilibrium position:

$$\forall \delta \vec{u}, \delta \mathcal{W}(\vec{u}) = \int \nabla \delta \vec{u} : \bar{\bar{\sigma}} dV - \oint \delta \vec{u} \cdot \vec{T} dS - \int \delta \vec{u} \cdot \vec{g} dV \quad (3.53)$$

Integration by parts of the weak formulation leads to the strong formulation of the mechanical problem, defined for any material domain inside the fiber bundle:

$$\forall \delta \vec{u}, \delta \mathcal{W}(\vec{u}) = \int \delta \vec{u} \cdot \nabla \cdot \bar{\bar{\sigma}} dV - \oint \delta \vec{u} \cdot \bar{\bar{\sigma}} \cdot \vec{n} dS - \oint \delta \vec{u} \cdot \vec{T} dS - \int \delta \vec{u} \cdot \vec{g} dV \quad (3.54)$$

The fundamental equations of continuum mechanics are then the solutions of the strong formulation given by:

$$\vec{T} dS = \bar{\bar{\sigma}} \cdot \vec{n} dS \quad (\nabla \cdot \bar{\bar{\sigma}} + \vec{g}) dV = 0 \quad (3.55)$$

The first equation in Eqs. (3.55) defines the internal stress from the boundary conditions. The second describes the balance of internal forces. These two equations allow one to solve a mechanical problem formulated in force to obtain the stress field. For a problem formulated in displacement, the material law must be introduced into the internal balance relationship to obtain a differential equation on the displacement field.

Repeating these calculations for a specific choice of beam kinematics, Eqs. (3.55) gives the partial differential equations describing the deformation of the fiber bundle, while the weak formulation will allow one to assemble the individual behaviors by a finite element formulation in order to model sets of fiber bundles.

Transverse shear

In a planar fibrous medium under compaction, deformations of the fiber bundles are mainly vertical along the thickness direction of the fiber bundles. The simplest deformation model consists in postulating a displacement field along the Z direction, homogenous over the entire transverse cross-section of the fiber bundle, which corresponds the deflection of its neutral fiber $V(X)$:

$$\vec{u} = V(X) \vec{e}_Z \quad (3.56)$$

The cross-section remains straight and planar in the deformed configuration. The infinitesimal strain tensor gives a simple shear deformation state in the plane (X, Z) :

$$\bar{\bar{\varepsilon}} = \begin{bmatrix} 0 & V_{,X}/2 \\ V_{,X}/2 & 0 \end{bmatrix} \quad (3.57)$$

and the internal strain energy involves only the transverse shear stress σ_{XZ} :

$$\mathcal{W}_{int} = \frac{1}{2} \int V_{,X} \sigma_{XZ} dV \quad (3.58)$$

The integration over the cross-section defines the shear force $T(X)$ applied to the fiber bundle through its thickness (see Figure 3.27):

$$\mathcal{W}_{int} = \frac{1}{2} \int V_{,X} T(X) dX \quad \text{with} \quad T(X) = \int \sigma_{XZ} dY dZ \quad (3.59)$$

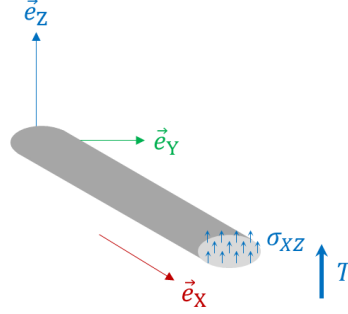


Figure 3.27: Shear stress and shear force.

The linear elastic law of a simple shear is written:

$$\sigma_{XZ} = G V_{,X} \quad (3.60)$$

where G is the shear modulus of the fibrous roving.

The uniaxial tensile and transverse shear problems are very similar in terms of equations and lead to the same type of constitutive model. In the presence of a vertical body force $\vec{g} = g(X)\vec{e}_Z$ and surface forces T_1 and T_2 applied to the fiber bundle ends, the constitutive equation of the shear kinematics is:

$$T_{,X} + g(X) = 0 \quad \text{for} \quad 0 < X < l, \quad \text{with} \quad \begin{cases} T(X=0) = T_1 \\ T(X=l) = T_2 \end{cases} \quad (3.61)$$

where the shear force $T(X)$ is expressed by:

$$T(X) = G S V_{,X} \quad \text{with} \quad S = \int dY dZ \quad (3.62)$$

In the absence of body force, the deflection of the neutral fiber verifies the constitutive equation:

$$V_{,XX} = 0 \quad (3.63)$$

This constitutive equation of the sheared fiber bundle provides a linear displacement field along its length. Two integration constants particularize this kinematics and correspond to the displacements at both ends, noted $V_1 = V(X=0)$ and $V_2 = V(X=l)$. Two particular solutions are obtained for these boundary conditions $\vec{V} = (V_1, V_2) = (1, 0)$ and $(0, 1)$:

$$\varphi^{(1)}(X) = 1 - \frac{X}{l} \qquad \varphi^{(2)}(X) = \frac{X}{l} \qquad (3.64)$$

These solutions are the shape functions of the fiber bundle and constitute a basis for the deformations of the fiber bundle. The displacement field of the beam is a linear combination of the shape functions:

$$\vec{u} = (\varphi^{(1)}(X)V_1 + \varphi^{(2)}(X)V_2)\vec{e}_Z \qquad (3.65)$$

which is also a solution of the constitutive equation of the beam. The internal energy is reformulated in terms of the displacements of the beam ends by introducing this interpolation into the weak formulation. It leads to the finite element formulation:

$$\mathbb{K} \cdot \vec{U} = \vec{F}, \text{ with } \mathbb{K} = \frac{GS}{l} \begin{bmatrix} 1 & -1 \\ -1 & 1 \end{bmatrix}, \quad \vec{U} = \begin{pmatrix} V_1 \\ V_2 \end{pmatrix} \text{ and } \vec{F} = \begin{pmatrix} T_1 \\ T_2 \end{pmatrix} \qquad (3.66)$$

where $V_1 = V(X=0)$ and $V_2 = V(X=l)$ are the vertical displacements at both ends which parametrize the interpolation of the deformation. This kinematic model represents the relative sliding of fibers inside the roving, which allows to keep the cross-section straight and planar (see Figure 3.28).

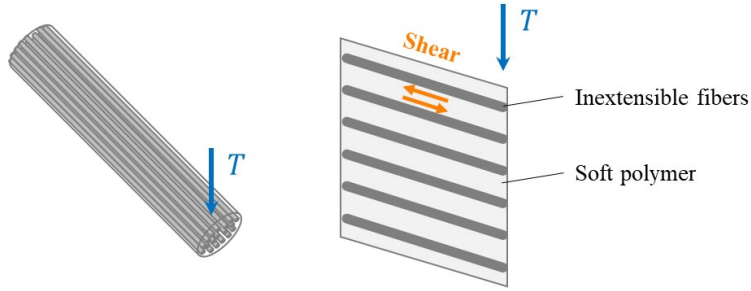


Figure 3.28: Simple slip and shear model between fibers.

Bending

The previous shear kinematics is completed to add a degree of freedom in bending of the fibers, which is more suitable for long fiber bundles. The rotation of the cross-section around the transverse horizontal axis \vec{e}_Y , noted $\theta(X) \geq 0$ for a rotation in the counterclockwise direction, is defined from the initial longitudinal direction \vec{e}_X in the plane (X, Z) (see Figure 3.29). The displacement field becomes:

$$\vec{u} = -\sin \theta(X) Z \vec{e}_X + (V(X) - (\cos \theta(X) - 1)Z) \vec{e}_Z \qquad (3.67)$$

This kinematics would lead to a complex system of differential equations to solve and must be simplified. In the limit of small rotations ($\theta \ll 1$), it becomes:

$$\vec{u} = -\theta(X)Z \vec{e}_X + V(X) \vec{e}_Z \qquad (3.68)$$

The deformation state is locally a combination of the longitudinal tension/compression expressed with respect to the curvature $\theta_{,X}$ and the transverse simple shear expressed by the difference between the slope of the fiber bundle and the angle of rotation of its cross-section:

$$\bar{\varepsilon} = \begin{bmatrix} -\theta_{,X}Z & (V_{,X} - \theta(X))/2 \\ (V_{,X} - \theta(X))/2 & 0 \end{bmatrix} \quad (3.69)$$

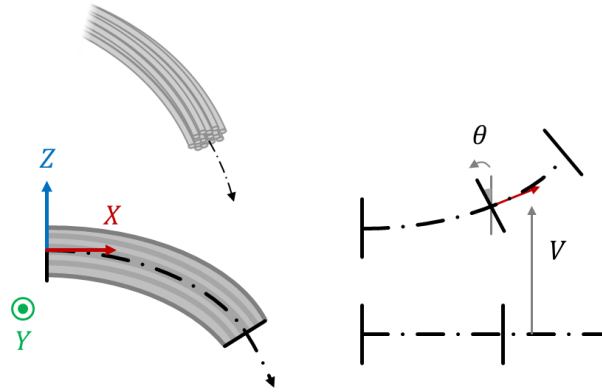


Figure 3.29: Rotational kinematics of the fiber bundle in bending.

The internal energy involves the longitudinal and transverse stress:

$$\mathcal{W}_{int} = \frac{1}{2} \int (V_{,X} - \theta(X)) \sigma_{XZ} dV - \frac{1}{2} \int \theta_{,X} Z \sigma_{XX} dV \quad (3.70)$$

The integration over the cross-section defines the shear force $T(X)$ and the bending moment $M(X)$ (see Figure 3.30):

$$\begin{aligned} \mathcal{W}_{int} &= \frac{1}{2} \int (V_{,X} - \theta(X)) T dX - \frac{1}{2} \int \theta_{,X} M(X) dX \\ \text{with } T(X) &= \int 2\sigma_{XZ} dY dZ \\ \text{and } M(X) &= \int Z \sigma_{XX} dY dZ \end{aligned} \quad (3.71)$$

The linear elastic laws for the longitudinal and transverse shear stress are:

$$\begin{aligned} \sigma_{XX} &= E\varepsilon_{XX} = -E\theta_{,X}Z \\ \sigma_{XZ} &= 2G\varepsilon_{XZ} = G(V_{,X} - \theta(X)) \end{aligned} \quad (3.72)$$

where E is the Young's modulus and G is the transverse shear modulus of the roving. Introducing these laws into the internal energy expression leads to the weak formulation:

$$\mathcal{W}_{int} = \frac{1}{2} \int GS \left(V_{,X} - \theta(X) \right)^2 dX + \frac{1}{2} \int EI \theta_{,X}^2 dX \quad (3.73)$$

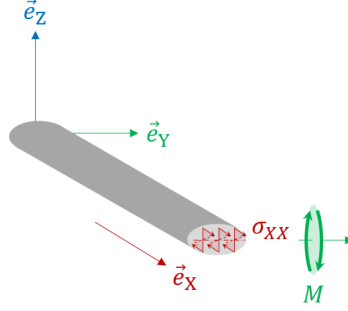


Figure 3.30: Tensile stress (linear part) and bending moment.

It gives the expressions of the shear force and the bending moment:

$$T(X) = GS \left(V_{,X} - \theta(X) \right) \quad M(X) = EI \theta_{,X} \quad (3.74)$$

where the area S and the quadratic moment of inertia² I of the cross-section are defined by:

$$S = \int dYdZ \quad I = \int Z^2 dYdZ \quad (3.75)$$

Integration by part of the internal energy leads to the strong formulation of the mechanical problem:

$$\begin{aligned} \mathcal{W}_{int} = & \oint T(X)V(X) + \oint M(X)\theta(X) - \frac{1}{2} \int T_{,X}V(X)dX - \frac{1}{2} \int T(X)\theta(X)dX \\ & + \frac{1}{2} \int M_{,X}\theta(X)dX \end{aligned} \quad (3.76)$$

In absence of body force and moment, the balance between the internal strain energy and the work of external forces provides the constitutive equations for the bending of the fiber bundle:

$$\begin{cases} M_{,X} = T(X) \\ T_{,X} = 0 \end{cases} \quad \text{for } 0 < X < l, \quad \text{with} \quad \begin{cases} T(X=0) = T_1 \\ T(X=l) = T_2 \\ M(X=0) = M_1 \\ M(X=l) = M_2 \end{cases} \quad (3.77)$$

If the cross-section is constant along the entire length of the fiber bundle, constitutive Eqs. (3.77) become:

² For a rectangular cross-section of width w and thickness e , the quadratic moment of inertia around the axis \vec{e}_Y is: $I = \frac{we^3}{12}$. For an elliptical cross-section of axes w and e , the moment of inertia is: $I = \frac{\pi we^3}{4 \cdot 16}$.

$$\begin{cases} EI\theta_{,XX} = GS(V_{,X} - \theta) \\ (V_{,X} - \theta)_{,X} = 0 \end{cases} \iff \begin{cases} \theta_{,XXX} = 0 \\ V_{,XX} = \theta_{,X} \end{cases} \quad (3.78)$$

Combining both differential equations, we obtain (in absence of body force and moments):

$$\implies V_{,XXXX} = 0 \quad \text{and} \quad \theta_{,XXX} = 0 \quad (3.79)$$

The solutions of these equations give the vertical deflection in cubic form and the rotation of the cross-section in quadratic form. Two approaches exist to solve these equations and obtain the shape functions for the interpolation of the bending bundle deformation.

Note: The initial assumption of small rotations leads to neglecting the buckling of the transverse cross-section³, which occurs for thick fiber bundles and large deformations. It is due to an asymmetric slip of the fibers with respect to the neutral fiber (see Figure 3.31).

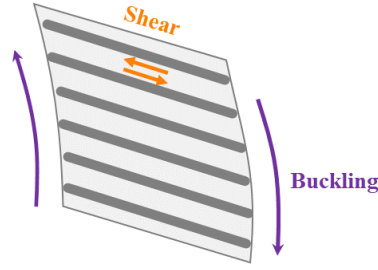


Figure 3.31: Buckling of the cross-section of the fiber bundle.

Euler-Bernoulli beam theory

The simplest model is the Euler-Bernoulli model which assumes the equality between the rotation of the cross-section $\theta(X)$ and the derivative of the vertical deflection of the fiber bundle $V_{,X}$:

$$V_{,X} = \theta(X) \quad (3.80)$$

³ The same calculations give, starting directly from Eq. (23), the non-linear constitutive equations for large deformations of thick fiber bundles:

$$(M_{,X} - T(X)) \sin \theta(X) + (B_{,X} - P(X)) \cos \theta(X) = 0 \quad ; \quad T_{,X} = 0 \quad ; \quad P_{,X} = 0$$

with:

- the shear force $T(X) = \int 2\sigma_{XZ} dY dZ = GS(V_{,X} - \sin \theta(X))$
- the vertical tensile force $P(X) = \int \sigma_{ZZ} dY dZ = KS(1 - \cos \theta(X))$
– with K the transverse tensile/compression modulus of the fiber bundle
- the bending moment $M(X) = \int Z\sigma_{ZZ} dY dZ = EI \cos \theta(X) \theta_{,X}$
- the buckling moment $B(X) = \int 2Z\sigma_{XZ} dY dZ = GI \sin \theta(X) \theta_{,X}$

As a result, the shear force is null inside the bundle. This assumption is valid in the limit of small deformations of thin fiber bundles. Solutions of the constitutive Eq. (3.79) for the unitary boundary conditions $\vec{U} = (V_1, \theta_1, V_2, \theta_2) = (1, 0, 0, 0), (0, 1, 0, 0), (0, 0, 1, 0)$ and $(0, 0, 0, 1)$ allow to express the basis of the shape functions (see Figure 3.32):

$$\begin{aligned}\varphi^{(1)}(X) &= 1 - 3\left(\frac{X}{l}\right)^2 + 2\left(\frac{X}{l}\right)^3 & \varphi^{(3)}(X) &= 3\left(\frac{X}{l}\right)^2 - 2\left(\frac{X}{l}\right)^3 \\ \varphi^{(2)}(X) &= X - 2\frac{X^2}{l} + \frac{X^3}{l^2} & \varphi^{(4)}(X) &= -\frac{X^2}{l} + \frac{X^3}{l^2}\end{aligned}\tag{3.81}$$

Each shape function corresponds to a different deformation mode of the fiber bundle. The bending kinematics is a linear combination of these orthogonal modes.

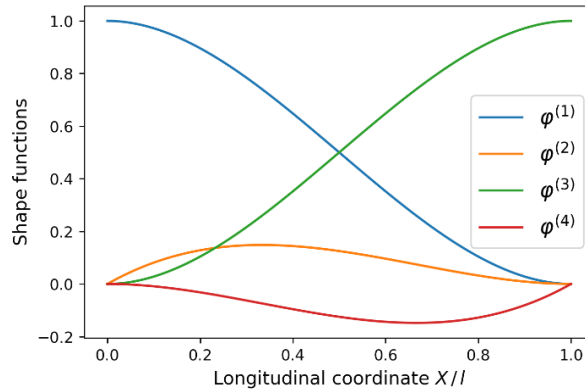


Figure 3.32: Shape functions of the fiber bundle in bending for the Euler-Bernoulli model.

The deflection of the neutral fiber and the rotation angle of the transverse cross-section are given by the interpolation:

$$\begin{aligned}V(X) &= \varphi^{(1)}(X)V_1 + \varphi^{(2)}(X)\theta_1 + \varphi^{(3)}(X)V_2 + \varphi^{(4)}(X)\theta_2 \\ \theta(X) &= \varphi_{,X}^{(1)}(X)V_1 + \varphi_{,X}^{(2)}(X)\theta_1 + \varphi_{,X}^{(3)}(X)V_2 + \varphi_{,X}^{(4)}(X)\theta_2\end{aligned}\tag{3.82}$$

The internal energy is reduced to the bending term only:

$$\mathcal{W}_{int} = \frac{1}{2} \int EI \theta_{,X}^2 dX\tag{3.83}$$

The finite element formulation of the bending is written from the second derivative of the shape functions. It results after integration the linear system of equations in:

$$\mathbb{K} \cdot \vec{U} = \vec{F} \quad \text{with} \quad \mathbb{K} = \frac{EI}{l^3} \begin{bmatrix} 12 & 6 & -12 & 6 \\ 6l & 4l^2 & -6l & 2l^2 \\ -12 & -6 & 12 & -6 \\ 6l & 2l^2 & -6l & 4l^2 \end{bmatrix}, \quad (3.84)$$

$$\vec{U} = \begin{pmatrix} V_1 \\ \theta_1 \\ V_2 \\ \theta_2 \end{pmatrix} \quad \text{and} \quad \vec{F} = \begin{pmatrix} T_1 \\ M_1 \\ T_2 \\ M_2 \end{pmatrix}$$

Solving Eqs. (3.84) provides the deflections and the rotations at the fiber bundle ends. The fields $V(X)$ and $\theta(X)$ are linear combinations of the shape functions, parametrized by the solution of the finite element system. They constitute a particular solution of the constitutive equation.

This model is valid as long as the assumption in Eq. (3.80) remains correct. To satisfy it, the fibers inside the roving must bend to maintain a straight cross-section, which is true near the neutral fiber. For thicker fiber bundles, the assumption is not necessarily satisfied, leading to the Timoshenko beam model.

Timoshenko beam theory

For thicker fiber bundles, the kinematic assumption of Euler-Bernoulli is no longer valid and one cannot assume Eq. (3.80). It is then necessary to solve directly Eqs. (3.78) to obtain the shape functions of the fiber bundle deflection $V(X)$ and the rotation angle of its cross-section $\theta(X)$. The difference between $V_{,X}$ and $\theta(X)$ depends on the longitudinal variation of the fiber curvature and is constant over the bundle length:

$$V_{,X} - \theta = \frac{EI}{GS} \theta_{,XX} = \text{cste} \quad (3.85)$$

This gap measures the relative slip of fibers within the roving. If it is zero, we recover the Euler-Bernoulli model with only fiber curvature inside the fiber bundle. At the other extreme, the model corresponds to the transverse shear model with only fiber slippage. There is thus a competition between these two mechanisms, that is characterized by the dimensionless number Ψ^2 defined as the ratio of the bending to the shear stiffnesses:

$$\Psi^2 = \frac{12EI}{GS l^2} \quad (3.86)$$

The direct resolution of Eqs. (3.78) gives different shape functions for the interpolation of the deflection and the rotation angle of the cross-section, both parametrized by Ψ (see Figure 3.33):

- For the deflection $V(X)$:

$$\varphi_V^{(1)}(X) = 1 + \frac{1}{(1+\Psi^2)} \left(2\left(\frac{X}{l}\right)^3 - 3\left(\frac{X}{l}\right)^2 - \Psi^2 \left(\frac{X}{l}\right) \right) \quad (3.87)$$

$$\varphi_V^{(2)}(X) = \frac{l}{(1+\Psi^2)} \left(\left(\frac{X}{l}\right)^3 - \left(2 + \frac{\Psi^2}{2}\right) \left(\frac{X}{l}\right)^2 + \left(1 + \frac{\Psi^2}{2}\right) \left(\frac{X}{l}\right) \right)$$

$$\varphi_V^{(3)}(X) = \frac{-1}{(1+\Psi^2)} \left(2 \left(\frac{X}{l}\right)^3 - 3 \left(\frac{X}{l}\right)^2 - \Psi^2 \left(\frac{X}{l}\right) \right)$$

$$\varphi_V^{(4)}(X) = \frac{l}{(1+\Psi^2)} \left(\left(\frac{X}{l}\right)^3 - \left(1 - \frac{\Psi^2}{2}\right) \left(\frac{X}{l}\right)^2 - \frac{\Psi^2}{2} \left(\frac{X}{l}\right) \right)$$

with $V(X) = \varphi_V^{(1)}(X)V_1 + \varphi_V^{(2)}(X)\theta_1 + \varphi_V^{(3)}(X)V_2 + \varphi_V^{(4)}(X)\theta_2$.

- For the rotation angle of the cross-section $\theta(X)$:

$$\varphi_\theta^{(1)}(X) = \frac{6}{(1+\Psi^2)l} \left(\left(\frac{X}{l}\right)^2 - \left(\frac{X}{l}\right) \right)$$

$$\varphi_\theta^{(2)}(X) = 1 + \frac{1}{(1+\Psi^2)} \left(3 \left(\frac{X}{l}\right)^2 - (4 + \Psi^2) \left(\frac{X}{l}\right) \right)$$

$$\varphi_\theta^{(3)}(X) = \frac{-6}{(1+\Psi^2)l} \left(\left(\frac{X}{l}\right)^2 - \left(\frac{X}{l}\right) \right)$$

$$\varphi_\theta^{(4)}(X) = \frac{1}{(1+\Psi^2)} \left(3 \left(\frac{X}{l}\right)^2 - (2 - \Psi^2) \left(\frac{X}{l}\right) \right)$$

(3.88)

with $\theta(X) = \varphi_\theta^{(1)}(X)V_1 + \varphi_\theta^{(2)}(X)\theta_1 + \varphi_\theta^{(3)}(X)V_2 + \varphi_\theta^{(4)}(X)\theta_2$.

The coupling between the two sets of shape functions depends on the material parameter Ψ^2 and induces complex deformation modes. At low values of Ψ , the shape functions of the deflection are the one of Euler-Bernoulli model, and their derivatives correspond to those of the rotation angle. For high values of Ψ , we recover the two shape functions of the shear model deflection with constant zero rotation angles, plus two new modes with linear evolution of $\theta(X)$. Timoshenko kinematics describes the transition between the shear model and the Euler-Bernoulli bending model. It can be noticed that the most compliant behavior tends to be predominant in the total deformation of the fiber bundle.

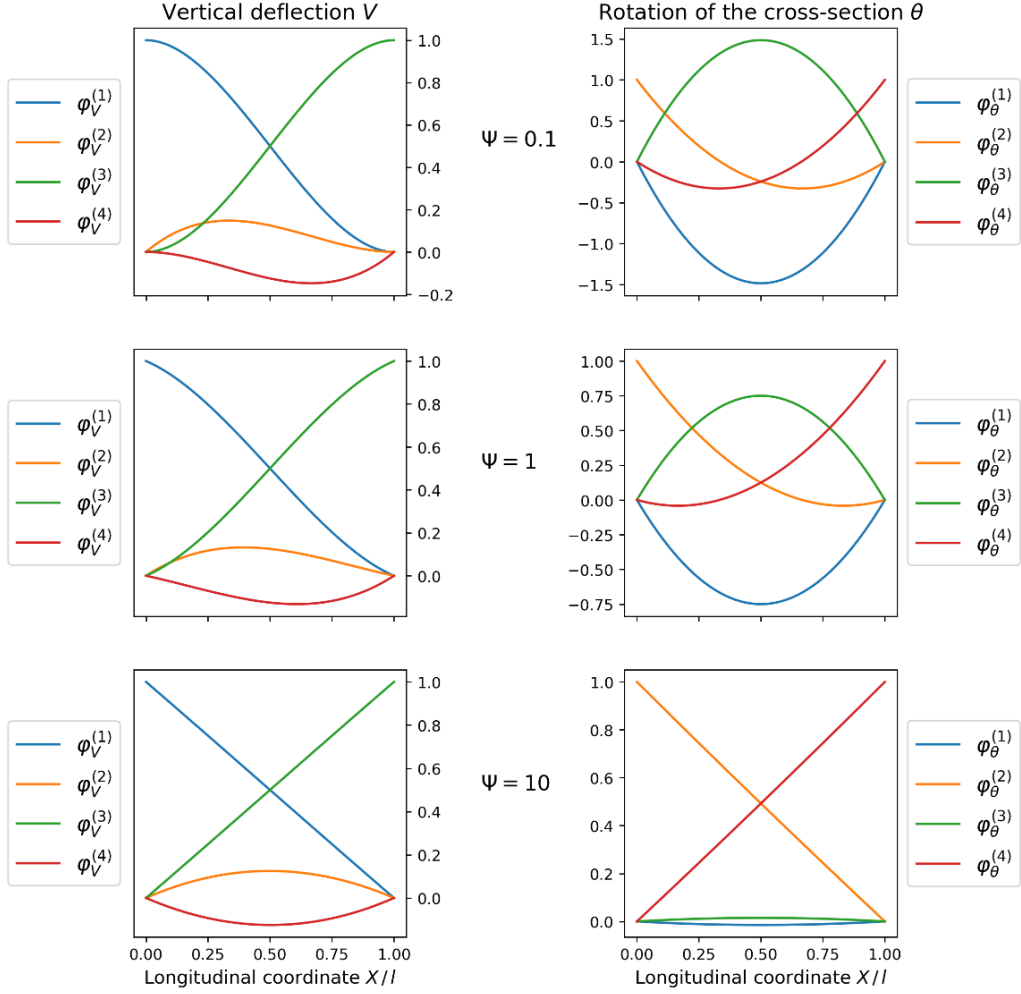


Figure 3.33: Shape functions of the vertical deflection $V(X)$ (left column) and the cross-section rotation (right column) for different values of the material parameter: $\Psi = 0.1, 1$ and 10 .

The quadratic formulation of the internal energy now involves two terms corresponding to the transverse shear and bending respectively. The calculation of each term using the shape functions results in a stiffness matrix for each mechanism:

$$\mathbb{K}^{(\text{bending})} = \int \varphi_{\theta,X}^{(i)} \cdot EI \cdot \varphi_{\theta,X}^{(j)} dX = \frac{EI}{(1 + \Psi^2)l^3} \begin{bmatrix} 12 & 6 & -12 & 6 \\ 6 & 4 & -6 & 2 \\ -12 & -6 & 12 & -6 \\ 6 & 2 & -6 & 4 \end{bmatrix} \quad (3.89)$$

$$\begin{aligned} \mathbb{K}^{(\text{shear})} &= \int (\varphi_{V,X}^{(i)} - \varphi_{\theta}^{(i)}) \cdot GS \cdot (\varphi_{V,X}^{(j)} - \varphi_{\theta}^{(j)}) dX \\ &= \frac{EI}{(1 + \Psi^2)l^3} \begin{bmatrix} 0 & 0 & 0 & 0 \\ 0 & \Psi^2 & 0 & -\Psi^2 \\ 0 & 0 & 0 & 0 \\ 0 & -\Psi^2 & 0 & \Psi^2 \end{bmatrix} \end{aligned} \quad (3.90)$$

The finite element formulation of Timoshenko kinematics is the sum the two stiffnesses:

$$\mathbb{K} \cdot \vec{U} = \vec{F} \quad \text{with} \quad \mathbb{K} = \mathbb{K}^{(\text{bending})} + \mathbb{K}^{(\text{shear})}, \quad \vec{U} = \begin{pmatrix} V_1 \\ \theta_1 l \\ V_2 \\ \theta_2 l \end{pmatrix} \quad \text{and} \quad \vec{F} = \begin{pmatrix} T_1 \\ M_1/l \\ T_2 \\ M_2/l \end{pmatrix} \quad (3.91)$$

3.B. Statistical framework

Preliminaries

The fibrous reinforcement of SMC materials consists of a network of fiber bundles in contact. The deformation of this material during the compression molding process involves different scales and associated problems:

- At the microscopic scale, the fiber bundle and its fibers deform like a beam (microscopic problem).
- At the mesoscopic scale, the bundles come into contact and form a structure (mesoscopic problem).
- At the macroscopic scale, the fibrous structure represents a system too large to be represented directly and need a constitutive law.

Microscopic problem:

A bundle composed of parallel fibers is modeled from a beam theory owing to its thin and slender geometry (see Section 3.2). For a given choice of kinematics, the strong formulation of the microscopic problem, integrated over the transverse cross-section, gives the constitutive laws of the beam as differential equations. Solving these equations for applied boundary conditions of unit deflection gives the shape functions that represent the orthogonal deformation modes of the fiber bundle. Any deformation of the roving can then be decomposed exactly as a linear combination of the shape functions. The parameters of this interpolation are the Kinematic Degrees of Freedom (KDoFs) of the fiber bundle ends (displacements, rotations, etc. depending on the choice of kinematics). Using this interpolation in the weak formulation of the mechanical problem, we obtain, after integration on the fiber bundle, the finite element formulation of the microscopic problem in the form:

$$\mathbb{K} \cdot \vec{U} = \vec{F} \quad (3.92)$$

with \mathbb{K} denotes the stiffness matrix of the fiber bundle, \vec{U} the displacement vector containing the KDoFs and \vec{F} the force vector applied on the fiber bundle.

Mesoscopic problem:

At the mesoscopic scale, the network of fiber bundles in contact forms a structure whose mechanical behavior depends on the spatial arrangement of the fiber bundles and the internal/external contacts (see Section 3.3). The fiber bundle is no longer modeled as a single beam, but as a succession of beam elements and nodes where the DoFs are defined. The treatment of contacts by the finite element method requires that they correspond to the nodes of the fiber bundles. The fibrous structure is discretized into a set of 1D elements whose nodes correspond to the fiber bundle ends and all the overlapping points between the fiber bundles (which is possible in the limit of infinitesimal strains for the fiber bundles but large transformations at the scale of the structure). The assembly of the finite element formulations allows one to get a large linear system describing the mechanical behavior of the fibrous structure. The contacts are formulated as a problem of minimization under inequality constraints. The method of Lagrange multipliers is used to introduce the internal and external contact forces into the Lagrangian of the mechanical problem:

$$\mathcal{W}(\vec{U}) = \frac{1}{2} \vec{U} \cdot \mathbb{K} \cdot \vec{U} - \vec{f} \cdot (\mathbb{C} \cdot \vec{U} - \vec{h}) - \vec{F} \cdot \vec{U} \quad (3.93)$$

with:

- \mathbb{K} , the stiffness matrix of the network of fiber bundles.
- \mathbb{C} and \vec{h} , respectively the contact matrix and the vector of altitudes, giving the non-interpenetration conditions (internal and external) as: $\mathbb{C} \cdot \vec{U} \leq \vec{h}$, with equality for the contacts.
- \vec{f} , the vector of contact forces, with $\vec{f} \leq 0$.
- \vec{F} , the vector of external forces.
- \vec{U} , the displacement vector.

The unknowns of the associated minimization problem are the KDoFs of the system, contained in the displacement vector \vec{U} , and the contact forces \vec{f} . The mesoscopic problem is non-linear (it is actually piecewise linear), but linear as long as the set of contacts is not modified. At any mechanical state, the Lagrangian formulation is simplified by considering only the active contact conditions (given by $\mathbb{C}' \cdot \vec{U} = \vec{h}'$ and $\vec{f}' \leq 0$, with \mathbb{C}' , \vec{h}' and \vec{f}' formed by the lines of \mathbb{C} , \vec{h} and \vec{f} of the active conditions).

The minimization of the Lagrangian provides the linear system of equations:

$$\underbrace{\begin{bmatrix} \mathbb{K} & -\mathbb{C}'^T \\ -\mathbb{C}' & 0 \end{bmatrix}}_{\mathbb{P}} \cdot \underbrace{\begin{pmatrix} \vec{U} \\ \vec{f}' \end{pmatrix}}_{\vec{x}'} = \underbrace{\begin{pmatrix} \vec{F} \\ -\vec{h}' \end{pmatrix}}_{\vec{q}} \quad (3.94)$$

By differentiation, the mesoscopic problem is reformulated into an incremental problem by solving the system:

$$\mathbb{P} \cdot \delta \vec{x}' = \delta \vec{q}' \quad (3.95)$$

for small variation of the mechanical state of the fibrous system. The solution $\delta\vec{x}^*$ gives the evolution of the internal forces and displacements with respect to a variation of the external conditions $\delta\vec{q}$. Including the internal and external contact forces, as well as the external forces \vec{F} in the generalized force vector \vec{F}' , the energy evolution of a mechanical state initially at equilibrium $\mathcal{W}^*(\vec{U}) = E$ for a small increment of energy δE is written:

$$\begin{aligned} E + \delta E = & \underbrace{\left(\frac{1}{2}\vec{U} \cdot \mathbb{K} \cdot \vec{U} - \vec{F}' \cdot \vec{U}\right)}_E + \underbrace{(\vec{U} \cdot \mathbb{K} - \vec{F}') \cdot \delta\vec{U}}_0 \\ & - \underbrace{\vec{U} \cdot \delta\vec{F}'}_0 + \underbrace{\left(\frac{1}{2}\delta\vec{U} \cdot \mathbb{K} \cdot \delta\vec{U} - \vec{F}' \cdot \delta\vec{U}\right)}_{\delta E} \end{aligned} \quad (3.96)$$

The first term on the right-hand side gives the initial energy at equilibrium. The second and third terms are zero and correspond respectively to the equilibrium of the internal and external forces⁴. The last term gives the energy increment as $\delta E = \mathcal{W}^*(\delta\vec{U})$ as the energy associated to $\delta\vec{U}$. The stack of fiber bundles evolves through a succession of mechanical states at equilibrium, which justifies the equivalence between the mesoscopic problem and its incremental formulation. The mesoscopic problem can be reduced to the study of these energy increments associated with quasi-static transformations.

Macroscopic problem:

At the macroscopic scale, the mechanics of the fibrous stack is still described by the Lagrangian formulation of Eq. (3.93), but the large size of the system of equations in Eq. (3.94) limits its direct resolution. Moreover, the exact initial configuration of the fibrous network remains generally unknown and is only described by global descriptors. The mesoscopic problem is non deterministic, it can no longer be solved explicitly. Here we propose to study it through a probabilistic approach that governs its mechanical states. The macroscopic problem is therefore stochastic. An appropriate mathematical framework is needed to predict the macroscopic behavior from the behavior of ensembles of fiber bundles, without postulating any law. It is described in the sequel, and is known as statistical mechanics, a branch of statistical physics.

The deformation of the fibrous structure is described kinematically by a set of degrees of freedom (DoFs) \vec{U} . These DoFs correspond to the nodal motions of the fiber bundle elements and are defined by the formulation of the microscopic problem. These are the kinematic DoFs (KDoFs) of the fiber bundle stack. Note that the KDoFs are not necessarily independent: when there is contact between two fiber bundles, the DoFs in vertical displacements of the two fiber

⁴ The same decomposition can be written from the system of Eq. (64) and shows explicitly the balance of internal and external forces:

$$\begin{aligned} W_{int} + \delta W_{int} = & \underbrace{\left(\frac{1}{2}\vec{x} \cdot \mathbb{P} \cdot \vec{x}\right)}_{W_{int}} + (\delta\vec{x} \cdot \mathbb{P} \cdot \vec{x}) + \underbrace{\left(\frac{1}{2}\delta\vec{x} \cdot \mathbb{P} \cdot \delta\vec{x}\right)}_{\delta W_{int}} \\ W_{ext} + \delta W_{ext} = & \underbrace{(\vec{x} \cdot \vec{q})}_{W_{ext}} + \left(\delta\vec{x} \cdot \vec{q} + \underbrace{\vec{x} \cdot \delta\vec{q}}_{=0}\right) + \underbrace{(\delta\vec{x} \cdot \delta\vec{q})}_{\delta W_{ext}} \end{aligned}$$

with $\mathbb{P} \cdot \vec{x} = \vec{q}$ (internal balance)
and $\vec{x} \cdot \delta\vec{q} = \vec{F} \cdot \delta\vec{U} - \vec{f} \cdot \delta\vec{h} = 0$ (compensation of external forces).

bundles are equal to avoid interpenetration. Of the two KDoFs initially independent before contact, only one independent KDoF remains after contact.

In the Lagrangian formulation, the KDoFs do not necessarily correspond to DoFs of the internal energy. The internal deformation energy is written locally as: $\mathcal{W}_{int} \propto \frac{1}{2}(u_i - u_j)^2$ with a quadratic function of the relative displacements, not the absolute displacements of the fiber bundles which correspond to rigid body motions. We define the Quadratic DoFs (QDoFs) as the DoFs of the internal energy. Taking the energy formulation in Eq. (3.93), the energy of the mesoscopic problem is decomposed into:

$$\mathcal{W}(\vec{U}) = \underbrace{\frac{1}{2}\vec{U} \cdot \mathbb{K} \cdot \vec{U}}_{\text{internal deformation energy}} - \underbrace{\vec{f} \cdot (\mathbb{C} \cdot \vec{U} - \vec{h})}_{\text{work of the internal and external contact forces}} - \underbrace{\vec{F} \cdot \vec{U}}_{\text{work of the external forces}} \quad (3.97)$$

and results in a linear system of equations for the incremental formulation:

$$\mathbb{K} \cdot \delta\vec{U} = \delta\vec{F} + \delta\vec{f} \cdot (\mathbb{C} \cdot \delta\vec{U} - \delta\vec{h}) = \delta\vec{F}' \quad (3.98)$$

where \vec{F}' is the generalized force vector that includes internal and external contact forces, as well as external forces. The KDoFs of \vec{U} can be reorganized into two sets: the independent KDoFs (arbitrarily taking only every other displacement for the nodes in contact) in a vector $\vec{U}^{(i)}$ and the remaining KDoFs in a vector $\vec{U}^{(d)}$ which depends on the KDoFs of $\vec{U}^{(i)}$. The generalized force vector is also decomposed into imposed forces $\vec{F}'^{(d)}$ and unknown forces $\vec{F}'^{(i)}$.

The system of Eqs. (3.98) is decomposed into blocks describing the mechanics of the stack at a given mechanical state:

$$\begin{bmatrix} \mathbb{K}^{(ii)} & \mathbb{K}^{(id)} \\ \mathbb{K}^{(di)} & \mathbb{K}^{(dd)} \end{bmatrix} \cdot \begin{pmatrix} \delta\vec{U}^{(i)} \\ \delta\vec{U}^{(d)} \end{pmatrix} = \begin{pmatrix} \delta\vec{F}'^{(d)} \\ \delta\vec{F}'^{(i)} \end{pmatrix} \quad (3.99)$$

which leads from the point of view of the internal deformation energy to the reduced system of equations of unknowns $\delta\vec{U}^{(i)}$:

$$\mathbb{K}^{(ii)} \cdot \delta\vec{U}^{(i)} = \vec{F}'^{(d)} - \mathbb{K}^{(id)} \cdot \delta\vec{U}^{(d)} \quad (3.100)$$

The reduced system given by $\mathbb{K}^{(ii)}$ corresponds to the independent QDoFs of the stack. Unlike the stiffness matrix \mathbb{K} which is not invertible as such, the reduced stiffness matrix $\mathbb{K}^{(ii)}$ is invertible and diagonalizable. The size of this reduced matrix, called M , gives the number of independent QDoFs⁵ of the stack in the corresponding mechanical state. The number of KDoFs is then $2M$.

⁵ In the general framework of statistical physics, M is an integer or half-integer: $M \in \frac{1}{2}\mathbb{N}$. If the KDoFs are quadratic, M is half-integer (for example, the velocities of particles in thermodynamics are quadratic degrees of freedom for the kinetic energy: $E_c = \sum \frac{1}{2}mv_i^2$). Otherwise, M is integer (in static mechanics, displacements are the kinematic degrees of freedom of the system and the relative displacements are the quadratic degrees of freedom of the potential energy: $E_p = \sum \frac{1}{2}ku_{(ij)}^2$ with $u_{(ij)} = x_i - x_j$).

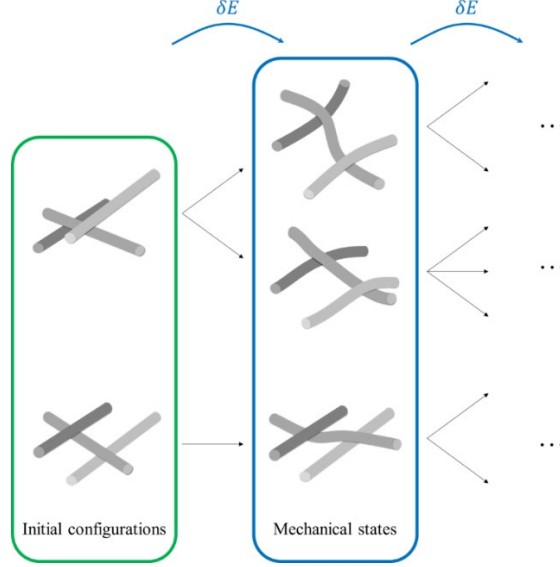


Figure 3.34: Evolution of different initial configurations for different mechanical states.

Distribution of states

For a given set of fiber bundles, the internal deformation energy at equilibrium is, with the previous notations:

$$\mathcal{W}_{int}^* = \frac{1}{2} \vec{U}^{(i)*} \cdot \mathbb{K}^{(ii)} \cdot \vec{U}^{(i)*} \quad (3.101)$$

where $\mathbb{K}^{(ii)}$ is diagonalizable and $\vec{U}^{(i)*}$ is the vector of independent QDoFs of size M . Renormalization of the basis of the QDoFs by $\sqrt{\frac{1}{2}\mathbb{K}_i^{(ii)}}$ where the $\{\mathbb{K}_i^{(ii)}\}$ denotes the eigenvalues of the reduced stiffness matrix, then the matrix $\mathbb{K}^{(ii)}$ can be expressed as a spherical matrix in its eigenbase (all diagonal elements of $\mathbb{K}^{(ii)}$ are equal).

The same value of internal deformation energy E corresponds to a set of admissible mechanical states of the fibrous network. In the absence of explicit boundary conditions imposed on this set, it is not possible to specify in which mechanical state the system is and as a result all of them must be considered. All these states are solutions of the same potential energy minimization problem and none of them is to be preferred in terms of occurrence. Otherwise, some "force" should steer the set of fiber bundles towards the most likely state and would modify the formulation of \mathcal{W}_{int}^* . This is the fundamental postulate of statistical physics:

All admissible states of the same energy are equiprobable.

We define $\rho(E, M)$ the density of admissible mechanical states of the set of fiber bundles with M QDoFs and internal energy lower than or equal to E . This function quantifies the number of mechanical states accessible by the set of fiber bundles.

Each state is equiprobable and all QDoFs are indistinguishable from each other in the energy sense, i.e., they all contribute equally to \mathcal{W}_{int}^* . In the basis of the normalized QDoFs denoted

$\{u_k = (x_{i_k} - x_{j_k})\}$ where the x_{i_k} and x_{j_k} denote the KDoFs, the energy surface E is described by the equation on the elements of $\vec{U}^{(i)}_{j_k}$:

$$E = u_1^2 + u_2^2 + \dots + u_M^2 \quad (3.102)$$

The surface of the mechanical states in the KDoFs basis is obtained by expanding the QDoFs with respect to the KDoFs:

$$E = x_{i_1}^2 + x_{j_1}^2 + \dots + x_{i_M}^2 + x_{j_M}^2 - 2x_{i_1}x_{j_1} - \dots - 2x_{i_M}x_{j_M} \quad (3.103)$$

The cross terms can be eliminated for each QDoFs by some rotation of the reference frame.

According to Eq. (3.103), the set of mechanical states of internal energy in the interval $[E, E + \delta E]$ draws a sphere with $M - 1$ dimensional sphere in the space of QDoFs with M dimensions (see Figure 3.35). The surface of this sphere (i.e., the derivative of its volume) gives the density of mechanical states $\partial\rho(E, M)$ in the form:

$$\partial\rho(E, M) \propto \frac{E^{M-1}}{\Gamma(M)} \delta E \quad (3.104)$$

where Γ denotes the Gamma function⁶ and the term $\Gamma(M)$ accounts for the indistinguishability of the QDoFs. For the density to be dimensionless, we introduce an energy constant ϵ_0 that we will specify in the following with the help of the behavior law. This constant corresponds to the energy of an elementary configuration with a single QDoF. By integration, the density of mechanical states of the fibrous stack is:

$$\rho(E, M) = \frac{1}{\Gamma(M+1)} \left(\frac{E}{\epsilon_0} \right)^M \quad (3.105)$$

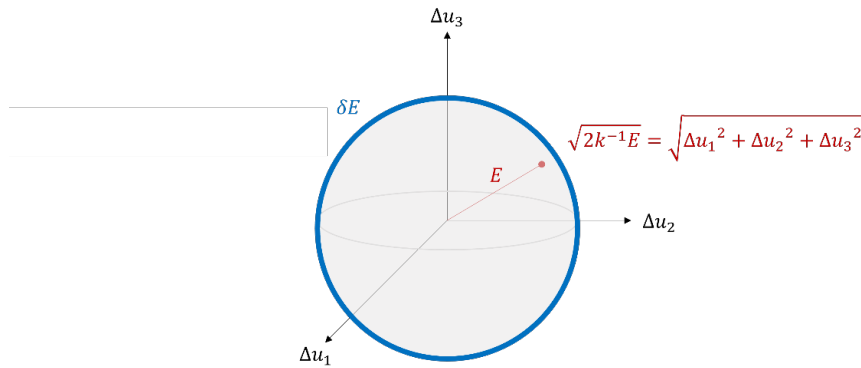


Figure 3.35: Spherical shell of energy E and thickness δE in the basis of the QDoFs.

⁶ The function Γ is defined by the integral: $\Gamma(z) = \int_0^{+\infty} t^{z-1} e^{-t} dt$, on the private complex plane of negative integers. If M is a positive integer, $\Gamma(M+1) = M!$

The same reasoning applies to the spatial configurations of the stack and the initial arrangements of its fiber bundles. The volume of the stack is the sum of the volumes occupied by N fiber bundles including the gaps between them. For identical fiber bundles, the density of spatial configurations of bulky stacks is given by:

$$\rho(N, V) = \frac{1}{N!} \left(\frac{V}{v} \right)^N \quad (3.106)$$

where the factor $\frac{1}{N!}$ allows to take into account the indiscernibility of the fiber bundles and v is the volume of one roving. In order for the reduction of the system to a single fiber bundle to give a unitary density of configurations, the bulky volume V is scaled by the volume v of a single fiber bundle.

For a given fibrous medium described by a set of extensive state variables (N, V, E, M) with N the number of fiber bundles, V the bulky volume, E the internal energy and M the number of QDoFs; to each initial (bulky) configuration of $\rho(N, V)$ corresponds a set of mechanical states $\rho(E, M)$. The variables N , V , E and M do not have to be independent of each other. The set of possible states of the fibrous stack is described by the product of the density of the bulky configurations and the density of the mechanical states of each configuration (see Figure 3.36):

$$\rho(N, V, E, M) = \frac{1}{N!} \left(\frac{V}{v} \right)^N \frac{1}{\Gamma(M+1)} \left(\frac{E}{\epsilon_0} \right)^M \quad (3.107)$$

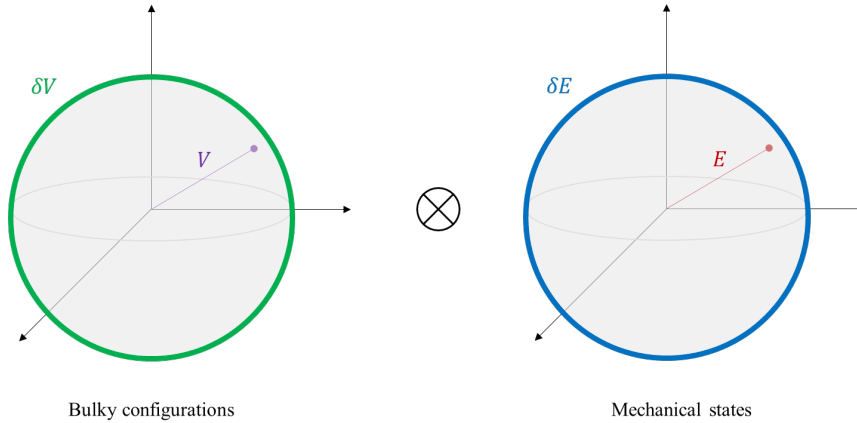


Figure 3.36: Factorization of the fibrous stack states.

For an elementary system of one fiber bundle or one QDoF, each of these set reduces to a point and we find either the density of the bulky configurations or the density of the mechanical states of the stack.

For the density of mechanical states to be unitary in the case of a system with a single internal QDoF, the constant ϵ_0 is taken as the energy of a QDoF in a bulky configuration. As the energy cannot be zero in the bulky configuration, it is defined to within a constant. This ambiguity is removed by systematically defining the energy to an additive constant.

Within the limit of large systems ($N \gg 1$ and $M \gg 1$), the density of states of the stack is:

$$\begin{aligned}\rho(N, V, E, M) &\sim \left(\frac{V}{Nv}\right)^N \left(\frac{E}{M\epsilon_0}\right)^M e^{-(N+M)} \\ &\sim \phi^{*-N} \left(\frac{\epsilon}{\epsilon_0}\right)^M e^{-(N+M)}\end{aligned}\tag{3.108}$$

where $\phi^* = \frac{Nv}{V}$ is the bulky volume fraction and $\epsilon = \frac{E}{M}$ the contribution of each QDoFs to the internal energy.

The density of states of the stack (i.e., spatial configurations \otimes mechanical states) describes the distribution of all possible states of the stack as a function of its state variables. The larger this density is, the larger the number of admissible states is. It then becomes more and more difficult to determine with certainty the current state of the stack. We propose to define a measure of this uncertainty in the statistical physics framework in order to define probabilistic distributions and describe the system at the macroscopic scale.

Partition function

The energy partition function is defined as:

$$\Omega(\beta) = \int e^{-\beta E} \partial\rho(E) \tag{3.109}$$

as a function of the parameter β which can be a real or complex number. The partition function generalizes the counting of the configurations of the fibrous stack in all its mechanical states (for $\beta = 0$) by "weighting" the states by their energy. Moments of the distribution of energy states are obtained by successive differentiation:

$$\Omega(0) = \int \partial\rho = \rho \tag{3.110}$$

and:

$$\left. \frac{\partial^n \Omega}{\partial(-\beta)^n} \right|_{\beta=0} = \int E^n \partial\rho(E) \tag{3.111}$$

For a system with M independent quadratic degrees of freedom, the partition function can be factorized:

$$\Omega(\beta) = \int e^{-\beta(\sum_{i=1}^M E_i)} \partial\rho(E) = \prod_{i=1}^M \omega_i(\beta) \tag{3.112}$$

with $\omega_i(\beta) = \int e^{-\beta E_i} \partial\rho(E_i)$ the partition function associated with the i -th degree of freedom. The factorization of the partition function allows to separate the independent deformation

modes of the fibrous stack. The density of mechanical states is recovered from the partition function by inverse Laplace transform:

$$\rho(E) = \frac{1}{2i\pi} \oint e^{\beta E} \Omega(\beta) d\beta \quad (3.113)$$

where the integral is defined on a complex contour surrounding the singularities of the integrand (see (Wilf, 2005) or (Texier & Roux, 2020) for more details).

Entropy

The entropy of the density of states is defined as the logarithm of the partition function:

$$\mathcal{S}(\beta) = \ln \Omega(\beta) \quad (3.114)$$

In the same way that the partition function holds the moments of the distribution, the entropy holds the cumulants of the distribution. The first two cumulants are the expectation and variance of the energy distribution:

$$\left. \frac{\partial \mathcal{S}}{\partial(-\beta)} \right|_{\beta=0} = \text{Esp}[E] \quad (3.115)$$

$$\left. \frac{\partial^2 \mathcal{S}}{\partial(-\beta)^2} \right|_{\beta=0} = \text{Var}[E] \quad (3.116)$$

Since the partition function of a stack with M quadratic degrees of freedom is proportional to $\omega(\beta)^M$, the entropy increases proportionally to M , which makes it an extensive function. The cumulants are also extensive quantities.

In some cases, the calculation of the inverse Laplace transform is not possible and it is preferable to use the method of steepest descent (Brillouin, 1916), (Curry, 1944) to approximate the integral of Eq. (3.113) by:

$$\frac{1}{2i\pi} \oint e^{\beta E + \mathcal{S}(\beta)} d\beta \simeq \frac{e^{\beta^* E + \mathcal{S}(\beta^*)}}{\sqrt{2\pi \mathcal{S}''(\beta^*)}} \quad (3.117)$$

where β^* minimizes the function $\beta \mapsto \beta E + \mathcal{S}(\beta)$ and is given by:

$$\left. \frac{\partial \mathcal{S}}{\partial \beta} \right|_{\beta=\beta^*} = -E \quad (3.118)$$

with $\frac{\partial^2 \mathcal{S}}{\partial \beta^2} = \text{Var}[E] \geq 0$ and where we use the notation convention: $\frac{\partial \mathcal{S}}{\partial \beta^*} = \left. \frac{\partial \mathcal{S}}{\partial \beta} \right|_{\beta=\beta^*}$

We define the entropy at statistical equilibrium:

$$\mathcal{S}^*(E) = \beta^* E + \mathcal{S}(\beta^*) \quad (3.119)$$

which verifies the following properties:

$$\frac{\partial \mathcal{S}^*}{\partial E} = \beta^* \quad \frac{\partial^2 \mathcal{S}^*}{\partial E^2} \leq 0 \quad (3.120)$$

Around the equilibrium, β^* minimizes the entropy while E maximizes it; it is a saddle point of entropy (see Figure 3.37), hence the name of the method. It is shown that in the limit of large systems, all the definitions of entropy tend rapidly to the same value at equilibrium, hence the efficiency of the col method. This method allows, among other things, to obtain the probabilistic distributions of sums of random quantities, such as the energy and the contact forces between fiber bundles.

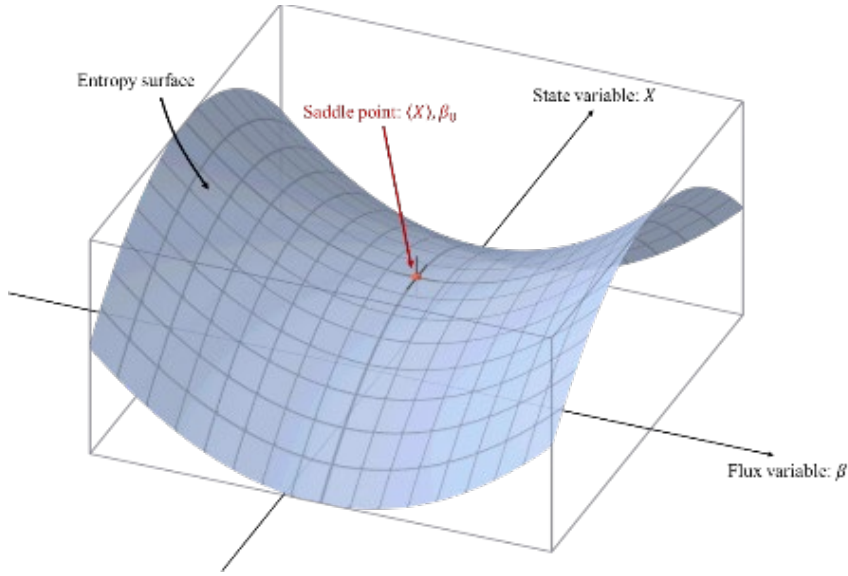


Figure 3.37: Saddle point of the entropy function.

The saddle-point approximation method and the inverse Laplace transform justify the notion of stacking entropy and the physical meaning of the maximization principle to describe the distribution of mechanical states. The entropy at equilibrium is obtained as the logarithm of the density of states:

$$\mathcal{S}^*(E) = \ln \rho(E) \quad (3.121)$$

This entropy⁷ quantifies the missing information about the state of the fibrous stack. The greater the number of possible configurations, the more uncertain the current state of the system is and justifies the probabilistic description of the medium.

⁷ Also called microcanonical entropy in statistical physics and is multiplied by the Boltzmann constant. More precisely, the microcanonical entropy corresponds to $S = \ln \rho$ since it is defined at fixed energy.

Entropy is a dimensionless function of the state variables, i.e., of the extensive parameters describing the system, and must have the following properties:

1. **Additivity and subadditivity:** $\mathcal{S}^*(\rho_1 \otimes \rho_2) \leq \mathcal{S}^*(\rho_1) + \mathcal{S}^*(\rho_2)$, for two joint systems of densities ρ_1, ρ_2 and of joint density $\rho_1 \otimes \rho_2$. There is equality if and only if the two systems are independent.
2. **Growth:** Entropy is a strictly increasing function of the density of states.
3. **Certain event:** If the current state of the system is certain, all the information is known. We pose $\mathcal{S}^*(1) = 0$.

For an arbitrary partition of the set of admissible configurations into two disjointed packets of states of density ρ_1, ρ_2 the stack can be found with probability P_1 in a configuration of packet 1, and with probability P_2 in packet 2 (with $P_1 + P_2 = 1$). The entropy associated with an admissible configuration is the entropy of its packet. The subadditivity property of entropy implies that the total entropy multiplied by the number of configurations $(\rho_1 \otimes \rho_2) \ln(\rho_1 \otimes \rho_2)$ is decomposed into three terms:

- The entropy associated with packet 1: $\rho_1 \ln(\rho_1)$.
- The entropy associated with packet 2: $\rho_2 \ln(\rho_2)$.
- Entropy related to the interdependencies between the two packets: $\mathcal{S}^*(\{\rho_1, \rho_2\})$

We then have:

$$\begin{aligned} (\rho_1 \otimes \rho_2) \ln(\rho_1 \otimes \rho_2) &= \rho_1 \ln(\rho_1) + \rho_2 \ln(\rho_2) + \mathcal{S}^*(\{\rho_1, \rho_2\}) \\ \Leftrightarrow \mathcal{S}^*(\{\rho_1, \rho_2\}) &= - \left(\frac{\rho_1}{\rho_1 \otimes \rho_2} \right) \ln \left(\frac{\rho_1}{\rho_1 \otimes \rho_2} \right) - \left(\frac{\rho_2}{\rho_1 \otimes \rho_2} \right) \ln \left(\frac{\rho_2}{\rho_1 \otimes \rho_2} \right) \end{aligned} \quad (3.122)$$

By posing $P_1 = \rho_1/(\rho_1 + \rho_2)$ and $P_2 = \rho_2/(\rho_1 + \rho_2)$, the probabilities associated to each packet, the entropy is reformulated from the distribution of the probabilities associated to each packet of states:

$$\mathcal{S}^*(\{P_m\}) = - \sum_m P_m \ln P_m \quad (3.123)$$

It is a convex function of $\{P_m\}$. This reformulation allows us to obtain the probability distribution of a random system as the solution that minimizes the entropy and maximizes the lack of information about the system; it is the least biased solution to describe the system. We impose that $\{P_m\}$ is a probability distribution using a Lagrange multiplier Λ :

$$\mathcal{S} = - \sum_m P_m \ln P_m - \Lambda \left(\sum_m P_m - 1 \right) \quad (3.124)$$

The distribution of mechanical states is therefore a uniform law in accordance with the fundamental postulate of statistical physics:

$$\frac{\partial \mathcal{S}}{\partial p_m^*} = -(1 + \ln P_m) - \Lambda = 0 \iff P_m = \text{cste} = \frac{1}{\partial \rho} \quad (3.125)$$

We can also assume that the stack has a definite average energy:

$$\mathcal{S} = - \sum_m P_m \ln P_m - \beta \left(\sum_m P_m E_m - E \right) \quad (3.126)$$

We obtain a distribution of the states according to the values of the energy $\{E_m\}$:

$$\frac{\partial \mathcal{S}}{\partial p_m^*} = -(1 + \ln P_m) - \beta E_m = 0 \iff P_m \propto e^{-\beta E_m} \quad (3.127)$$

The normalization constant of the distribution is given by the partition function of the stack:

$$\Omega(\beta) = \sum_m P_m e^{-\beta E_m} = \int e^{-\beta E} \partial \rho(E) \quad (3.128)$$

More generally, any extensive (and continuous) state variable of the system follows an energy-like distribution of the form:

$$p(E)dE = \frac{e^{-\beta E}}{\Omega(\beta)} \partial \rho(E) \quad (3.129)$$

Distributions of probability

The partition function for configurations with volume less than or equal to V is:

$$\Omega(\gamma) = \int \frac{1}{(N-1)!} \left(\frac{V}{v} \right)^{N-1} \frac{dV}{v} = \frac{1}{(\gamma v)^N} \quad (3.130)$$

The corresponding entropy is:

$$\mathcal{S}(\gamma) = -N \ln(\gamma v) \quad (3.131)$$

We deduce the value of the parameter γ at equilibrium:

$$\frac{\partial \mathcal{S}}{\partial \gamma^*} = -\frac{N}{\gamma^*} = -V \iff \gamma^* = \frac{N}{V} \quad (3.132)$$

By introducing the volume fraction of bundles $\phi^* = \frac{Nv}{V}$, we have:

$$\gamma^* v = \phi^* \quad (3.133)$$

We derive the equilibrium entropy for bulky stacks:

$$\mathcal{S}^*(V) = \gamma^* V + \mathcal{S}(\gamma^*) = N\{-\ln \phi^* + 1\} \quad (3.134)$$

and in particular that the number of fixed average volume configurations is (...):

$$\Omega(\gamma^*) = \phi^{*-N} \quad (3.135)$$

The inverse of the bulky volume fraction thus gives the contribution of each fiber bundle to the set of possible configurations.

The same reasoning can be used for the number of fiber bundles N . The partition function is then:

$$\Omega(\alpha) = \sum_{N=1}^{\infty} \frac{1}{N!} \left(\frac{V}{v}\right)^N e^{-\alpha N} = \exp\left(\frac{V}{v} e^{-\alpha}\right) \quad (3.136)$$

and entropy:

$$\mathcal{S}(\alpha) = \frac{V}{v} e^{-\alpha} \quad (3.137)$$

At statistical equilibrium, we obtain that $\alpha^* = -\ln \phi^*$ and the entropy at equilibrium is:

$$\mathcal{S}^*(N) = \alpha^* N + \mathcal{S}(\alpha^*) = N\{-\ln \phi^* + 1\} \quad (3.138)$$

The calculation of the distribution of the number of fiber bundles shows that N obeys a Poisson distribution:

$$P(N) = \frac{\langle N \rangle^N}{N!} e^{-\langle N \rangle} \quad (3.139)$$

This is the analog of the Gamma distribution for a discrete state variable. The larger the system, the more spread the distribution of configurations is (see Figure 3.38), which corresponds to a large number of admissible configurations of the system.

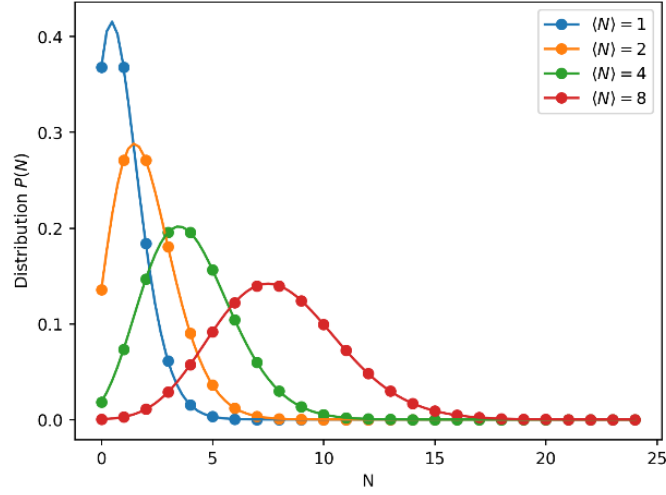


Figure 3.38: Evolution of the distribution of the number of fiber bundles in a domain of $V = \frac{\langle N \rangle v}{\phi}$ increasing.

The density of energy states E is $\partial\rho(E) = \frac{1}{\Gamma(M)} \left(\frac{E}{\epsilon_0}\right)^{M-1} dE$ according to Eq. (3.104), where M is the number of QDoFs of the system. The calculation of its partition function gives:

$$\Omega(\beta) = \int \frac{1}{\Gamma(M)} \left(\frac{E}{\epsilon_0}\right)^{M-1} e^{-\beta E} dE = \frac{1}{(\beta\epsilon_0)^M} \quad (3.140)$$

We deduce the probability distribution of the energy at M fixed:

$$p(E|M)dE = \frac{(\beta^* E)^{M-1} e^{-\beta^* E}}{\Gamma(M)} \beta dE \quad \text{with} \quad \beta^* = \frac{M}{\langle E \rangle} \quad (3.141)$$

which satisfies the normality condition $\int p(E|M)dE = 1$. The internal energy of the fibrous stack knowing the number of quadratic degrees of freedom is given by the Gamma law of parameters β^* and M (see Figure 3.39). For $M = 1$, the probability law is an exponential law which locally characterizes the energy distribution. As the number of quadratic and independent degrees of freedom increases, the distribution becomes more peaked around the mean and tends towards the normal distribution. The energy distribution depends on the size of the system studied.

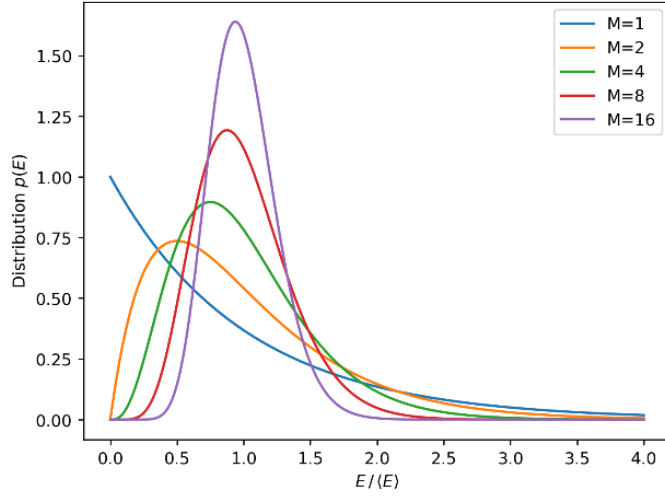


Figure 3.39: Evolution of the energy distribution for an increasing number of QDoFs.

The logarithm of the partition function gives the entropy:

$$\mathcal{S}(\beta) = -M \ln(\beta \epsilon_0) \quad (3.142)$$

The saddle point of entropy is:

$$\frac{\partial \mathcal{S}}{\partial \beta^*} = -\frac{M}{\beta^*} = -E \iff \beta^* = \frac{M}{E} = \frac{1}{\epsilon} \quad (3.143)$$

where ϵ is the average contribution to the energy per quadratic degree of freedom. We deduce the expression of the entropy at equilibrium:

$$\mathcal{S}^*(E) = M \left\{ \ln \left(\frac{\epsilon}{\epsilon_0} \right) + 1 \right\} \quad (3.144)$$

and the properties of energy distribution:

$$\frac{\partial \mathcal{S}}{\partial \beta^*} = -\frac{M}{\beta^*} = -\text{Esp}[E] \quad (3.145)$$

$$\frac{\partial^2 \mathcal{S}}{\partial \beta^{*2}} = \frac{M}{\beta^{*2}} = \frac{\langle E \rangle^2}{M} = \text{Var}[E] \quad (3.146)$$

$$\frac{\partial \mathcal{S}^*}{\partial E} = \frac{M}{E} = \beta^* \quad (3.147)$$

These results are relevant in the mechanics of fibrous media. For a flat stack compacted in the thickness direction, the work of the contact forces is:

$$E = \sum_{i \in \{\text{contacts}\}} f_i u_i \quad (3.148)$$

Since the mechanical problem is formulated in displacement (the boundary conditions are only imposed displacements), calculating the energy amounts to calculating the contact forces. These forces follow locally the same distribution as the mechanical energy in exponential law:

$$p(f)df = e^{-f/\langle f \rangle} \frac{df}{\langle f \rangle} \quad (3.149)$$

The result of F of M independent forces is distributed according to the Gamma distribution:

$$p(F|M)dF = \frac{(\beta^* F)^{M-1} e^{-\beta^* F}}{\Gamma(M)} \beta^* dF \quad \text{with } \beta^* = \frac{M}{\langle F \rangle} \quad (3.150)$$

The statistical physics formalism developed here and applied to fibrous stacks allows to describe the whole statistical distribution of internal forces of the ensemble of fiber bundles. It depends only on one parameter, the mean value of the force. A constitutive law must be formulated to express this average force with respect to the mechanical and geometrical parameters of the fibrous medium.

Bibliography

- [1] Brillouin, L. (1916). Sur une méthode de calcul approchée de certaines intégrales dite méthode du col. *Annales scientifiques de l'École Normale Supérieure*, 33, 17-69.
- [2] Curry, H. B. (1944). The method of steepest descent for non-linear minimization problems. *Quarterly of Applied Mathematics*, 2(3), 258-261.
- [3] Durville, D. (2005). Numerical simulation of entangled materials mechanical properties. *Journal of materials science*, 40(22), 5941-5948.
- [4] Fliegner, S., Luke, M., & Gumbsch, P. (2014). 3D microstructure modeling of long fiber reinforced thermoplastics. *Composites Science and Technology*, 104, 136-145.
- [5] Fliegner, S., Luke, M., & Gumbsch, P. (2014). 3D microstructure modeling of long fiber reinforced thermoplastics. *Composites Science and Technology*, 104, 136-145.
- [6] Görthofer, J., Schneider, M., Ospald, F., Hrymak, A., & Böhlke, T. (2020). Computational homogenization of sheet molding compound composites based on high fidelity representative volume elements. *Computational Materials Science*, 174, 109456.
- [7] Mahé, F., Binetruy, C., Advani, S., Férec, J., & Eck, B. (2021). A multi-scale statistical description of stacks of non-cohesive thin particles. *Powder Technology*, 399, 116988.
- [8] Orgéas, L., & Dumont, P. J. (2011). Sheet molding compounds. *Wiley encyclopedia of composites*, 1-36.
- [9] Picu, R. C. (2011). Mechanics of random fiber networks—a review. *Soft Matter*, 7(15), 6768-6785.
- [10] Rodney, D., Fivel, M., & Dendievel, R. (2005). Discrete modeling of the mechanics of entangled materials. *Physical review letters*, 95(10), 108004.
- [11] Schofield, J. (1938). 21—Researches on wool felting. *Journal of the Textile Institute Transactions*, 29(10), ., 29(10), T239-T252.
- [12] Texier, C., & Roux, G. (2020). *Physique statistique: des processus élémentaires aux phénomènes collectifs*. Dunod.
- [13] Toll, S. (1998). Packing mechanics of fiber reinforcements. *Polymer Engineering & Science*, 38(8), 1337-1350.
- [14] Van Wyk, C. M. (1946). 20—Note on the compressibility of wool. *Journal of the Textile Institute Transactions*, 37(12), T285-T292.
- [15] Wilf, H. S. (2005). *generatingfunctionology*. CRC press.

Chapter 4

Development and characterization of a new rheological model for SMC materials

Table of contents

4.1	Introduction	140
4.2	Compression tests and internal friction mechanisms	141
4.2.1	Objectives	141
4.2.2	Preparation of the samples	141
4.2.3	Experimental protocol	142
4.2.4	Results	144
4.2.5	Analysis and discussion	145
4.2.5.1	Initial friction effect	145
4.2.5.2	Comments on the rheological behavior observed during the squeeze-flow	146
4.2.6	Conclusion	147
4.3	Characterization of SMC material parameters during compression molding	147
4.3.1	Objectives	147
4.3.2	Industrial SMC materials	148
4.3.3	Description of the experimental setup	150
4.3.4	Experimental protocol	151
4.3.5	Methods	153
4.3.5.1	Geometrical dimensions of the SMC samples	153
4.3.5.2	SMC rheological model	155
4.3.6	Results	157

4.3.7	Analysis and discussions	165
4.3.7.1	Description of the experimental curves	165
4.3.7.2	Identification of the mechanical behaviors	166
4.3.7.3	Discussion about the rheological model	170
4.3.8	Conclusion	173
4.4	General conclusions.....	174
Appendices		175
4.A.	Comparison of compression curves for different parameters of SMC formulations and compression molding process.....	175
4.B.	Derivation of the compression stress formula.....	177
4.C.	Phase averages and averaging theorem	183
Bibliography		187

4.1 Introduction

In Chapter 2, observation of SMC mesostructures showed that different transport mechanisms of the chopped fiber bundles occur during the compression molding process, which are known to affect the rheology of SMC materials (Merhi, et al., 2005), the flow during the compression process and the mechanical properties of the molded parts (Boylan & Castro, 2003). The identification and characterization of the rheological properties of these materials is difficult due to this complexity and the multi-physics coupling effects during the compression of SMC materials, which leads to the development of different characterization protocols (Silva-Nieto, et al., 1981), (Barone & Caulk, 1986), (Dumont, et al., 2007), (Guiraud, 2011), (Hohberg, et al., 2017), usually based on force displacement relationship during compression of the material between two parallel platens.

Different rheological models are presented in the literature to describe the viscosity of SMC materials (Dumont, et al., 2003), its dependance on the molding temperature (Kotsikos & Gibson, 1998), (Dumont, et al., 2007), and on the properties of the chopped fiber bundles (Merhi, et al., 2004), and on the coupling with the fiber orientation (Jackson, et al., 1986) (Advani & Tucker III, 1987). However, the mechanical loading of the fibrous reinforcement modeled in Chapter 3 is generally ignored. Some works investigated the effect of the fiber length and the fiber content on the viscosity of SMC materials (Le Corre, et al., 2005) but they too do not include the mechanical loading of the evolving mesostructure.

In **Section 4.2**, an experimental campaign on different SMC materials establishes the relationship between the stress required to compress the SMC materials and the contact stress between the fiber bundles derived in Chapter 3 with a lubricated friction model.

In **Section 4.3**, a full SMC model combining the internal friction of the fibrous mesostructure and the viscous behavior of the matrix is presented. The model is validated with a

characterization experiment developed for industrial needs and applied on glass and carbon SMC materials.

4.2 Compression tests and internal friction mechanisms

4.2.1 Objectives

SMC materials containing long fibers with high volume fraction usually are in bundle form and exhibit a complex mesostructure of an entangled fibrous network. The fiber bundles are in contact with each other and the mechanical behavior of the mesostructure is assumed to play a significant role when describing the rheological behavior of these SMC materials. To identify this behavior, compression experiments are conducted with different mesostructure parameters of such SMC materials. The stress measurement will highlight the non-fluid behavior of the materials and will be compared to a friction model, which is based on the mechanical formulation developed in Chapter 3 for random fibrous mesostructures.

4.2.2 Preparation of the samples

A set of samples is made from the same SMC material references used in Chapter 2. The SMC materials are made with glass fiber rovings ME 1960¹ specifically for this set of experiments by Owens Corning with a low shrink unsaturated polyester thermosetting matrix Ashland DerakaneTM D760 charged with 23.89% of mineral fillers CaCO₃, corresponding to an industrial formulation.

Four materials with different fiber cutting lengths (25mm, 50mm) and fiber weight fractions (25%_{wt.}, 35%_{wt.}, 50%_{wt.}, i.e., in volume fractions 18%_{vol.}, 24%_{vol.}, 37%_{vol.} respectively) were supplied by Owens Corning for this study. The nomenclature and the formulation associated with each SMC material are summarized in Table 4.1. The manufacturing process and the storage conditions of these SMC materials are detailed in Chapter 2. The fiber bundle orientation distribution is assumed to be transversely isotropic, with a random orientation in the plane, according to the manufacturing parameters and the previous mesoscopic observations. The fiber bundles have a length of 25mm or 50mm, depending on the material reference, a width of 1mm and a thickness of 0.05mm for all the initial SMC references.

¹ <https://www.owenscorning.com/en-us/composites/product/pe-ve-smc-roving-me1960>

SMC reference	Reg-SMC-18	HP-SMC-24	HP-SMC-37	LF-SMC-18
Fiber weight fraction	25% _{wt.}	35% _{wt.}	50% _{wt.}	25% _{wt.}
Fiber volume fraction	18% _{vol.}	24% _{vol.}	37% _{vol.}	18% _{vol.}
Fiber cutting length	25mm	25mm	25mm	50mm

Table 4.1: Details of the formulation for the four SMC material references.

A circular ply is cut from the SMC roll provided by Owens Corning using a circular die of 100 mm in diameter. The sample is prepared by stacking three such plies on top of each other by hand without pre-compaction. A set of six samples is prepared for each SMC reference material. In total, 24 samples are realized for the four types of SMC materials provided.

4.2.3 Experimental protocol

The compression tests are performed on a universal traction/compression testing machine Instron 5584, equipped with a load cell of 100kN. The load cell is mounted on a vertical moving crosshead, controlled in displacement and velocity by an electromechanical system. Two steel circular platens of diameter 100mm are mounted on the testing machine (see Figure 4.1-a). The upper platen is mounted on a vertical column connected to the load cell. The lower platen is static, fixed on a ball joint to ensure the parallelism between the two platens. The proper parallelism was verified using a pressure sensitive paper Prescale® Fujifilm.



(a)



(b)

Figure 4.1: Lab-scale experimental compression setup: (a) View of the platens inside the heated room; (b) Outside view with the heated chamber and the Instron testing machine.

The platens are placed in a heated chamber (see Figure 4.1-b) at 140°C twenty minutes before the tests so the platens are heated and are also in equilibrium with the chamber temperature.

The ambient temperature of the room was controlled at 23°C and the SMC materials were at the ambient temperature before the tests.

During the tests, the SMC charge is not directly in contact with the steel plate of the mold. Two rigid and temperature resistant polyamide films are placed between the sample and the two platens, in order to protect the mold and have repeated close to identical boundary conditions for all the experimental tests. Each film has a thickness of 0.1mm. These plastic films induce no-slip boundary conditions, which will eliminate this parameter when analyzing the results. No deformation through the thickness of the plastic films is observed after the compression tests, so we can assume that they display elastic behavior during the experiment.

Before the compression experiments, a compliance test is conducted with the heated platens with the polyamide films to determine the mechanical response of the experimental setup in compression. A compression test with no SMC material is performed for a force up to 80kN. The displacement corresponding to the compression of the setup components is measured as a function of the force. During the compression experiments, this displacement is subtracted from the results to obtain the effective variation of the thickness of the samples.

Initially, the gap between the two platens is 30mm in the opened configuration. The circular sample is placed on the lower platen which covers the platen entirely as the platen and the sample are of the same diameter of 100 mm. Then the heating chamber is closed. A first command is given to the upper platen to get close to the sample about 7mm from the lower platen, with a vertical velocity of 10mm/s. Then, a constant velocity is imposed by the Instron until the sample reaches a final position of 2mm. Two compression velocities are tested in this experimental campaign: 1mm/s and 5mm/s. The rest of the experimental parameters remain the same. The compression test lasts 3.3s or 7.3s depending on the closing speed of 5 mm/s or 1 mm/s respectively.

As there is no compression chamber in this experiment, the SMC material is free to flow outside of the platens. This is a compression experiment with constant compression area. The effect of the gravity in the driving of the flow is neglected as it is insignificant compared to the viscous forces.

Before reopening the mold, a waiting period of 300s ensures the curing of the resin. Then the platens are reopened to demold the compressed sample. During the experiments, the time, the displacement corrected from the setup compliance, and the compression force are recorded with a frequency of 500Hz. The zero position of the displacement is taken at the contact between the two platens, so the displacement corresponds to the distance between the two platens, from 30mm initially to 2mm at the end of the compression test.

Three samples of each material type are used for compress them at two different closing speeds. The experimental campaign is then composed of two compression speeds and four material types resulting in a total 8 experimental cases with 3 samples repeated for each case.

4.2.4 Results

The experimental compression curve is divided into two parts (see Figure 4.2). First, the upper mold comes into contact with the sample and a non-linear behavior is observed, corresponding to the compaction of the sample through the thickness. No flow and in-plane deformations are observed during this step. At the beginning, the three plies initially not properly nested are compacted and brought into contact. The empty spaces and voids between the plies are removed. At the end of this step, the porosities inside the plies are compressed and partially closed. Then, a change of slope in the graph signals a change in behavior and marks the beginning of the flow of the SMC material between the platens, with an increasing force until the end of the experiment, when the displacement reaches 2mm. The location of the change of slope provides the required pressure at which the in-plane flow of the SMC material initiates. The compression curves for all the experiments are given in Appendix 4.A.

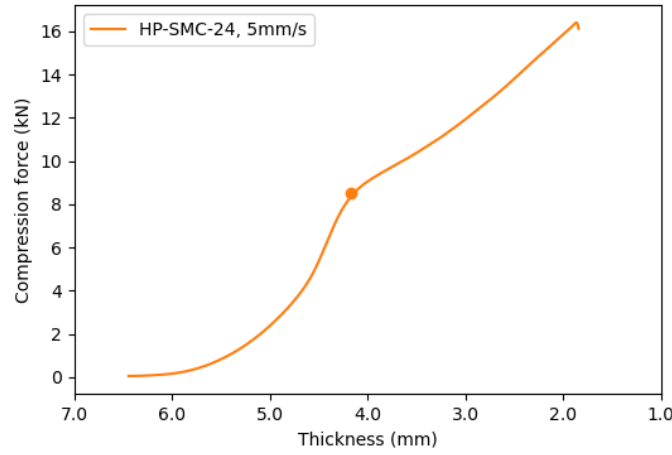


Figure 4.2: Typical compression curve for the HP-SMC-24 with the closing speed of 5mm/s.

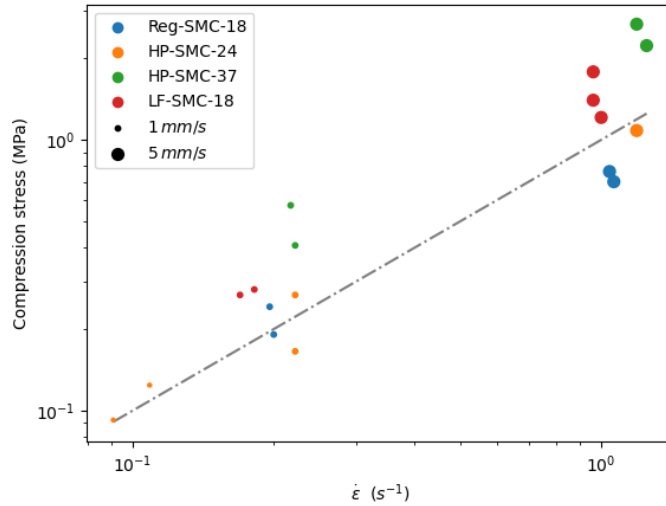


Figure 4.3: Initial compression stress as a function of the compression strain rate (for 1mm/s and 5mm/s).

In Figure 4.3, the compression stress at the beginning of the squeeze-flow is given for all the tests as a function of the compression strain rate $\dot{\epsilon} = -\dot{h}/h$. For the same SMC material type,

the compression stress seems to evolve linearly with the compression strain rate, as the pressure is multiplied by 5 between the two compression velocities 1mm/s and 5mm/s.

According to the mechanical model of fibrous mesostructures developed in Chapter 3, the internal stress associated with the contacts between the fiber bundles depends on the mesostructure compaction strain, defined as:

$$\varepsilon^\# = (\phi\alpha r - 1)^+ \quad (4.1)$$

where:

- α is the angular factor defined in Chapter 2. It is equal to 1 for random distributions, as assumed for the different SMC materials at the beginning of the test.
- r is the fiber bundle aspect ratio.
- ϕ is the fiber bundle volume fraction.

The symbol $()^+$ denotes the positive part of $\varepsilon^\#$.

The results of Figure 4.3 are plotted against the mesostructure strain compaction $\varepsilon^\#$ and the macroscopic compression strain rate in Figure 4.4. Both quantities are divided by the volume fraction of the matrix to reduce the quantities to the matrix domain, considering the fluid phase average. A linear behavior is observed in Figure 4.4. A linear relationship is obtained by a linear regression.

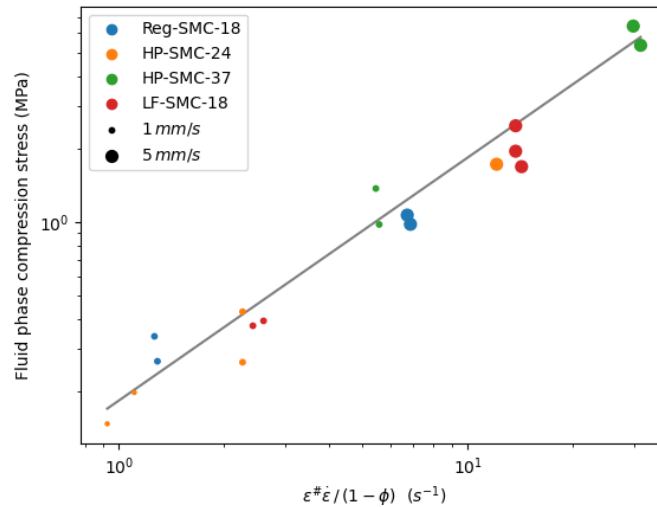


Figure 4.4: Initial compression expressed in terms of the matrix phase in a log-log diagram.
(Linear regression: $y = 0.18(MPa \cdot s) \times x$, $R^2 = 0.98$)

4.2.5 Analysis and discussion

4.2.5.1 Initial friction effect

From the compression experiments, the different SMC materials clearly show two different mechanical behaviors: a non-linear behavior before the squeeze-flow, corresponding to the

closure of the porosities inside the material (inter-ply and intra-ply); and a fluid behavior with an initial stress threshold during the squeeze-flow.

With regards to the linear dependance of the initial stress threshold on the compaction strain of the mesostructure and the high value of stress required to initiate the squeeze-flow (1MPa for a compression velocity of 1mm/s), the threshold behavior is interpreted as the consequence of the internal contact forces between the fiber bundles through a friction mechanism.

Considering the elastic mechanical model of mesostructure developed in Chapter 3, the contact stress between the fiber bundles on an average can be expressed as:

$$\sigma^\# = \frac{K}{\alpha r} \varepsilon^\# \quad (4.2)$$

where K is a mechanical parameter associated with the fibrous mesostructure. Then, for a simple linear friction model such as Coulomb law, the friction stress threshold is given by:

$$\tau^\# = \eta \sigma^\# \quad (4.3)$$

where η is the friction coefficient. From the experimental results shown in Figure 4.4, the friction coefficient is of the form:

$$\eta = \phi_m \cdot \eta_{fm} \cdot \dot{\varepsilon} \cdot \alpha r \quad (4.4)$$

where ϕ_m is the volume fraction of the matrix, η_{fm} is a constant parameter of the friction (expressed in seconds) related to the materials used for the fibers and the matrix, and $\dot{\varepsilon}$ is the compression strain rate. The dependance of the friction coefficient on the shear rate is due to the lubricated nature of the fiber bundle contacts. The dependance of the friction coefficient on αr is due to the shape aspect of the interface between the matrix and the fiber bundles (see Appendix 4.B).

The friction stress using Eq. (3) and (4), can be written as:

$$\tau^\# = \phi_m \cdot \eta_{fm} \cdot \dot{\varepsilon} \cdot K \varepsilon^\# \quad (4.5)$$

in accordance with the linear relationship expressed by the plot in Figure 4.4. The friction is then parametrized by the product $\eta_{fm} K$ of the friction and mechanical parameters of the SMC material whose value is given by the linear regression is given by the slope of the line in Figure 4.4 and is equal to 0.18MPa.s. However, the limitation of the test due to the small platen area does not allow one to identify the viscous behavior of the material and its potential contribution in the initial compression stress. We cannot conclude about the value of the friction parameter here. An improved characterization experiment presented in Section 4.3 will reveal more about this parameter and provide a full rheological model for SMC materials.

4.2.5.2 Comments on the rheological behavior observed during the squeeze-flow

From the comparison of the compression curves in Appendix 4.A, it appears that the four SMC materials have different behavior at low and high velocities. At a velocity of 1mm/s, the curves

of the compression force versus the displacement describe a plateau curve or a bell curve during the squeeze-flow and is relevant of a plastic like behavior. This behavior and this shape of compression curve have been observed in (Dumont, et al., 2003), (Dumont, et al., 2007), and is typical of the rheology described by the plug-flow model of Barone and Caulk (Barone & Caulk, 1986), (Castro & Griffith, 1989). The drop in force at the end of the test in some cases can be explained by the effect of the gravity applied to the part of the matter outside of the platens which is entrained by its own weight. At the velocity of 5mm/s, the curves describe a linear or parabolic profile, corresponding to a non-linear viscous behavior, more described by Hele-Shaw models (Silva-Nieto, et al., 1981) (Lee, et al., 1984), (Advani & Tucker III, 1990). The difference between the two cases is the compression velocity and indicates a role of the shear rate into the rheological behavior of the composite material. These two different rheologies have been documented in (Dumont, et al., 2007) and are consistent with the used compression velocities. It has been observed in the literature that the initial temperature of the SMC material influences its behavior in a similar way (Lee, et al., 1981), (Kotsikos & Gibson, 1998), with a plastic like behavior for high temperatures, and viscous behavior for low velocities. A variation of temperature through the thickness is likely to impact locally the rheology of SMC materials, especially close to the mold platens where the gradient of temperature is very important (with a temperature of the platen around 140°C and a temperature of the SMC material around 23°C). The compression velocity modifies the thickness of the sample and influences its rise in temperature, affecting the variation of its viscosity.

4.2.6 Conclusion

From a series of compression tests at constant area using SMC materials designed with different manufacturing parameters, the influence of the fibrous mesostructure on the rheological behavior of the composite material has been explored. The initial stress to induce the flow of the material is related to the load imposed on the mesostructure. The estimation of the latter combines a lubricated friction model to describe the interactions between the fiber bundles and a mechanical model of compaction of fibrous mesostructure derived in Chapter 3. This model explains the dependence of the initial compression stress on the fiber length and the fiber content of SMC materials. Due to the small size of the compression platens, the rheological behavior of SMC materials cannot be studied and limits the accuracy of the friction parameter measurements. An improved characterization experiment is developed in Section 4.3 to extend the investigations about the effect of the mechanical behavior of the fibrous mesostructure on the rheology of SMC materials.

4.3 Characterization of SMC material parameters during compression molding

4.3.1 Objectives

The use of a material behavior model in industrial applications requires a characterization method to identify the material parameters of the model. The protocol must be simple, using a laboratory-scale testing setup, adapted for the industrial needs and with a low cost for the required equipment. In Section 4.2, an experimental campaign tested the behavior of different SMC materials and validated a rheological model which accounts for the mechanical loading of the fibrous reinforcement by a friction mechanism. This experiment provided results with a

significant variability due to the small size of the mold platens and the limitation of the testing machine to reproduce the industrial molding conditions required for such materials.

Here, an improved characterization approach is developed in order to identify the material parameters of the SMC material from a squeeze-flow compression, with large size heating platens able to mold SMC plates under controlled molding conditions. The method is applied to various classes of industrially used SMC materials, with glass or carbon fibers and different formulations of unsaturated polyester resins.

4.3.2 Industrial SMC materials

Three commercial unsaturated polyester-based SMC materials with different formulations of matrix and fibrous reinforcement were used to perform the experiments.

The first material LF-SM-30 is a long fiber SMC material (see Figure 4.5). It contains 30% vol. of long glass fibers of length 50mm. The fibers are arranged in chopped fiber bundles of width 1mm and thickness 0.1mm. The matrix is an unsaturated polyester resin with low shrinkage coefficient and contains 42% w.t. of mineral fillers (CaCO_3), fire retardant fillers ($\text{Al}(\text{OH})_3$) and black pigments. The density of the material listed in its technical data sheet is 1860kg/m³. This material must be molded at a temperature between 145°C and 155°C and under a pressure between 50 and 100 bars. The curing time is estimated to be 90s for a final thickness of 3mm.

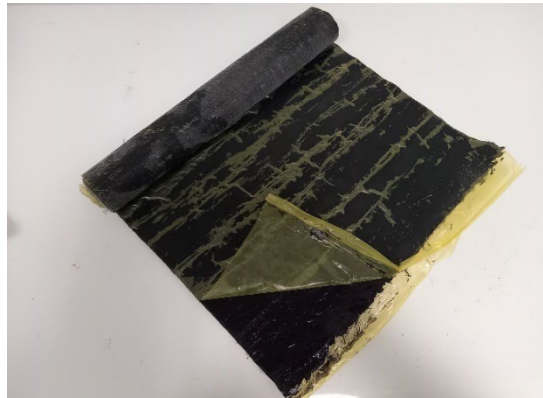


Figure 4.5: Roll of LF-SMC-30.

The second material CF-SMC-50 is a carbon fiber SMC. It contains 50% vol. of carbon fibers arranged in chopped strands of width 5mm and thickness 0.5mm (see Figure 4.6). The matrix is a low-profile unsaturated polyester resin with 1% vol. of organic charges. The composite has a density of 1350kg/m³. The CF-SMC-50 must be molded at 100 bars between 145°C and 155°C. The curing time is estimated to be 180s.



Figure 4.6: Undeformed sheet of CF-SMC-50. The carbon fiber strands are clearly visible from the surface.

The third material HP-SMC-26 contains 26%_{vol.} of glass fibers in chopped fiber bundles of width 1mm and thickness 0.1mm. The matrix is a low-profile unsaturated polyester resin containing 42%_{vol.} of mineral fillers (CaCO_3). The absence of pigments gives the paste a natural light color (see Figure 4.7). Its density is 1810kg/m³. The molding temperature is between 150°C and 155°C, with a molding pressure between 50 and 100 bars. The curing time is 120s for a thickness of 3mm.



Figure 4.7: Photo of HP-SMC-26 material.

All the materials are stored in rolls at a temperature of -18°C and maintained between polyethylene carrier films to avoid styrene release.

Circular samples are cut using a die with a diameter of 100mm (see Figure 4.8). The diameter is longer than the fiber length for all three SMC material types: four times the fiber length of CF-SMC-50 and HP-SMC-26 and twice the fiber length of LF-SMC-30. A sample is made by stacking four of these circular plies with orientations 0°/90°/0°/90° with respect to the direction of the roll to avoid potential anisotropy of the initial material induced by the manufacturing process.



Figure 4.8: SMC circular sample of LF-SMC-30 between polyamide films.

The thickness of each ply of the LF-SMC-30 and the HP-SMC-26 is between 1.5mm and 2mm. A ply of CF-SMC-50 is around 1.2mm.

The samples are weighted before the test. Then, they are placed between two rigid films of polyamide to protect the platens and induce no-slip boundary conditions at the upper and lower boundaries of the SMC sample. No deformation through the thickness of the plastic films has been observed. The cumulative thickness of the two films is 0.1mm.

A set of 58 circular samples of the three SMC references were tested under various processing conditions.

4.3.3 Description of the experimental setup

The testing machine is a Shimadzu Ag-Xplus capable of applying a load up to 100kN. It is a bi-column machine for traction/compression/bending tests (see Figure 4.9). The crosshead is controlled in position, with a speed of 0.5mm/min to 500mm/min under normal conditions, with a maximum closing speed of 1000mm/min. A load cell of 100kN is equipped on the crosshead. The mold is made of two parallel steel platens, with a square molding area of dimensions 260mm x 260mm (see Figure 4.10). The lower platen is mounted on a ball joint to ensure the parallelism, which is on a static column attached to the frame of the testing machine. The upper platen is directly connected to the load cell and moves with the crosshead.



Figure 4.9: Compression testing machine Shimadzu Ag-Xplus.

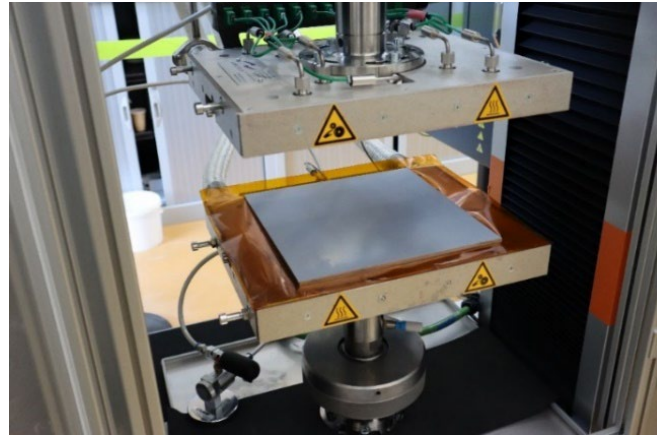


Figure 4.10: Compression platens of dimensions 260mm x 260mm.

The temperature of platens is controlled by a regulatory system transporting a heat-transfer fluid inside two heating and cooling circuits in each platen. The two platens are heated to the same temperature. A thermal probe inside the platen allows one to control the temperature in the lower platen during the compression test.

To prevent damage to the load cell due to high temperatures, a cooling system is installed between the upper platen and the load cell. An air stream is injected continuously through the column and cools the metal by the Venturi effect. The load cell remains at room temperature during the test. The same system is installed between the lower platen and the ball joint.

4.3.4 Experimental protocol

The objective of the tests is to measure the force required to induce the flow of the SMC material by compression. The results will allow one to determine the viscosity of the composite

material and the internal friction forces in the fibrous network by inverse method. The cylindrical sample of SMC is compressed with the platen moving at a constant speed. In the absence of initial anisotropy of the material, the SMC flow is assumed to be radial.

The contact position between the two platens is designated by 0mm. The measurements of displacements are provided with respect to this reference position. The open position of the platens is set to 150 mm. The compression platens are treated with a Teflon film and a release agent as a safety precaution, the SMC charges are placed between plastic films. The temperature regulatory system is set at 150°C. A difference of 5°C is detected between the regulation system and the measured temperature in the platens. The platens are at a constant temperature of 145°C during the tests. Only one temperature control can be given for both platens. A compliance test is performed with the heated platens and without SMC sample to establish the force/displacement relationship of the components of the testing machine. The deformation contribution of the setup is subtracted from the measured displacements during the test. A maximum force of 90kN is defined during the test. The test ends if the measured force reaches this limit.

For each test:

- The SMC sample is placed in the center of the square molding area.
- The upper platen moves quickly (with a given command of 15mm/s) to the position 11mm.
- The velocity of the platen progressively decreases until the 9mm position, slightly above the contact with the sample. The velocity drops from 15mm/s to 0.5mm/s.
- Then, the platen moves with a constant velocity of 0.5mm/s or 1mm/s to the 1.8mm position (the target command for the machine is 1.85mm).
- The platen remains in position during the curing of the resin.
- The plate is slowly raised at 0.02mm/s to the 2mm position to limit the opening effort.
- The upper platen returns to its initial position of 150mm at 5mm/s, then the sample is removed.

The acquisition is defined during the test at 100Hz (one point every 0.01s). A test lasts between 120s and 210s depending on the curing time of the SMC material, with a compression phase of about 15s. There are about 10s between the placement of the charge and the contact with the upper platen. The outputs of the test are the displacement of the platen and the compression force versus time, the compression velocity is recalculated from the displacement.

Due to the weight and inertia of the steel platens, position control is difficult for high compression velocities. For a velocity of 0.5mm/s, the displacement control is given with an increment of 0.05mm compared to the targeted position.

During the compression test, the velocity of the platen is slightly slower than the command and decreases at the end of the compression test, due to the control of the machine and the viscous resistance of the SMC material (see Figure 4.11). The velocity must not be considered constant and is recalculated from the displacement measurement.

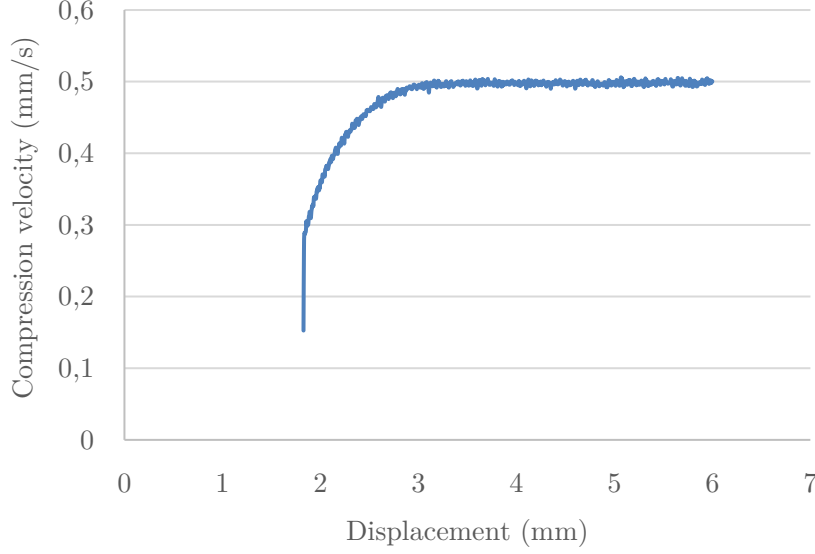


Figure 4.11: Evolution of the compression velocity during the test.

Two compression velocities are used for the CF-SMC-50 and the HP-SMC-26: 0.5mm/s and 1mm/s. For the LF-SMC-30, the maximum compression force constrains the tests to 0.5mm/s.

4.3.5 Methods

4.3.5.1 Geometrical dimensions of the SMC samples

The displacement is corrected for the setup compliance and the thickness of the polyamide films. The compression velocity is recalculated from the displacement measurement.

From the force curve, four points P_0 , P_1 , P_2 and P_3 are computed to isolate the part of the curve which corresponds to the flow of the SMC material (between P_2 and P_3) (see Figure 4.12). The point P_1 is defined by the first peak of the time derivative of the force, which is smoothed by a rolling average to reduce the numerical noise. The point P_0 is defined as the point before P_1 where the force derivative reaches 10% of the value at P_1 , and P_2 is defined as $P_1 + (P_1 - P_0)$, assuming that the first peak of the force derivative is symmetric about the inflection point of the force centered at P_1 . The last point P_3 is the maximum of the force, at the end of the compression. These points define the different parts of the test. Until P_0 , the platen is not in contact with the SMC material. Between P_0 and P_2 , the charge is compacted with a deformation through the thickness and the material does not flow in the plane. Between P_2 and P_3 , the compression imposed by the platens induces the SMC flow of the sample. The force measured during this step is the mechanical signature of the flowing SMC material (see Figure 4.13).

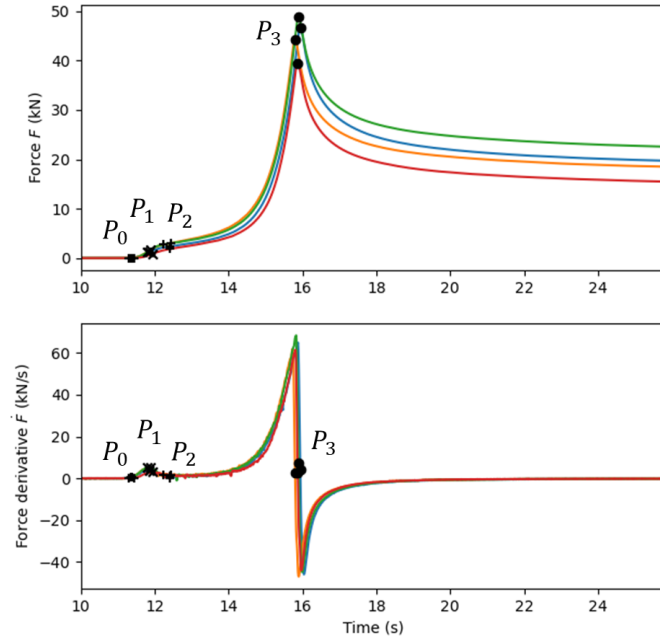


Figure 4.12: Determination of the points P_0 , P_1 , P_2 and P_3 for different compression tests (For material CF-SMC-50 compressed at 1mm/s).

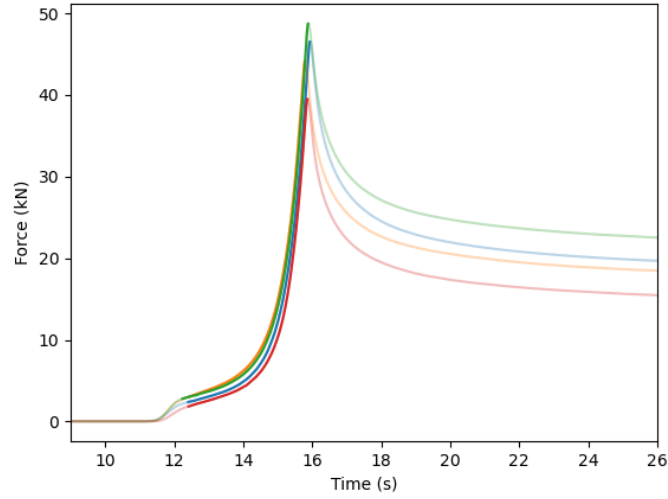


Figure 4.13: The compression phase is highlighted for the different experimental curves (For material CF-SMC-50 compressed at 1mm/s).

The displacement measured at the point P_2 gives the thickness of the sample h_0 which signifies the beginning of squeeze-flow and is considered as the initial thickness of the sample, for which the porosities are closed and the targeted fiber volume fraction is reached.

From the sample weight m and the density ρ of the SMC material, the initial radius of the charge is recalculated to remove the geometrical uncertainty relative to the sample. The initial radius is calculated as:

$$R_0 = \sqrt{\frac{m}{\pi \rho h_0}} \quad (4.6)$$

The radius is determined with respect to the thickness h by:

$$R = R_0 \sqrt{\frac{h_0}{h}} \quad (4.7)$$

The compression stress is defined as the ratio of the measured force by the sample area of radius R (positive for a compression):

$$\Sigma = \frac{F}{\pi R^2} \quad (4.8)$$

For each test, the compression stress between the points P_2 and P_3 is used to identify the rheological parameters by a non-linear least squares method.

4.3.5.2 SMC rheological model

The rheological behavior of a SMC material is assumed to be the result of the following three mechanisms:

- A linear viscous behavior of constant viscosity μ for the reactive resin containing fillers and fiber bundles.
- A plastic model to represent the compression stress threshold observed in Section 4.2, interpreted as the consequence of the friction forces within the fibrous reinforcement.
- An elastic behavior of the fibrous reinforcement modeled in Chapter 3 which influences the internal friction forces.

The material is considered incompressible during the flow of the SMC material, with no relative average velocity between fluid and fibrous phases (in the absence of segregation):

$$\langle \vec{v}^{(m)} \rangle = \langle \vec{v}^{(f)} \rangle \quad (4.9)$$

where $\langle \vec{v}^{(m)} \rangle$ and $\langle \vec{v}^{(f)} \rangle$ are respectively the average velocity of the fluid matrix and the fibrous reinforcement (see Appendix 4.C).

According to the conclusions of Section 4.2, the friction stress threshold $\tau^\#$ is proportional to the mesoscopic deformation and the compression strain rate $\dot{\epsilon}$ in the form:

$$\tau^\# = \eta \sigma^\# \quad (4.10)$$

$$\text{with } \eta = \underbrace{\phi_m \cdot \eta_{fm}}_H \cdot \dot{\varepsilon} \cdot \alpha r, \quad \sigma^\# = \frac{K}{\alpha r} \underbrace{(\phi \alpha r - 1)^+}_{\varepsilon^\#}$$

where:

- η is the friction coefficient, describing the interaction between the matrix and the fibers which results from the cohesion and the internal friction forces.
- $\sigma^\#$ is the contact stress between the fiber bundles (in MPa).
- ϕ_m is the matrix volume fraction.
- η_{fm} is a material constant of the friction (in seconds), which depends on the nature of the fiber rovings and the matrix.
- H is the friction parameter (in seconds).
- $\dot{\varepsilon} = -\dot{h}/h$ is the compression strain rate, with h the gap between the mold platens.
- α is the angular factor defined in Chapter 2, which measures the alignment state of the fiber bundles. It is equal to 1 for random distributions, as assumed for the different SMC materials at the beginning of the test.
- r is the fiber bundle aspect ratio.
- K is the mechanical parameter of the fibrous mesostructure (in MPa).
- $\varepsilon^\#$ is the mesostructure compaction strain.
- ϕ the fiber bundle volume fraction.

The symbol $()^+$ denotes the positive part of $\varepsilon^\#$.

Rearranging Eq. (4.10), the friction stress can be reformulated with respect to the strain rate introducing a friction viscosity $\mu^\#$:

$$\tau^\# = \mu^\# \dot{\varepsilon} \quad \text{where } \mu^\# = HK\varepsilon^\# \quad (4.11)$$

The resulting compression stress is given by (see Appendix 4.B for the full derivation of the model):

$$\Sigma = \frac{3}{2} \left(\frac{R}{h} \right)^2 \mu \dot{\varepsilon} + \mu^\# \dot{\varepsilon} \quad (4.12)$$

The first term results from the viscous contribution of viscosity μ , assumed constant during the test, and is determined by the analytic solution of a thin and radial squeeze-flow with no-slip boundary conditions (Engmann, et al., 2005). The second term describes the friction between the fiber bundles and is likely to evolve during the compression with the deformation of the fibrous mesostructure.

A development of the first order of the friction stress, detailed in Appendix 4.B, is used to capture this evolution with respect to the macroscopic deformation and improve the determination of the rheological parameters of the SMC materials. The compression model used to characterize the SMC materials from the experimental measurements is:

$$\Sigma = \frac{3}{2} \left(\frac{R}{h} \right)^2 \mu \dot{\varepsilon} + \mu_0^\# \dot{\varepsilon}_0 - k_0 \varepsilon \quad (4.13)$$

where $\varepsilon = -\ln\left(\frac{h}{h_0}\right)$ is the logarithmic compression strain, $\dot{\varepsilon} = -\dot{h}/h$ is the compression strain rate and $\dot{\varepsilon}_0 = -\dot{h}_0/h_0$ is the initial compression strain rate (here, we use the positive convention for a compression to note the strain, the strain rate and the stress).

The solid stress contribution is assumed to be homogenous in the sample and to evolve slowly during the compression test, with a relaxation parametrized by the stiffness $k_0 = \left. \frac{-\partial \tau^\#}{\partial \varepsilon} \right|_0$.

The resulting model of Eq. (4.13) is a combination of viscosity, plasticity and linear elasticity. It is similar to the model of (Silva-Nieto, et al., 1981) and will be discussed in the following.

The rheological parameters μ , $\mu_0^\#$ and k_0 are identified for each sample, using the particular thickness and radius determined by the method explained previously. Then, the average value of the parameters is estimated to characterize each of the three SMC reference materials. The relationship with the mechanical properties of the fiber bundles will be developed afterwards as their identification is indirectly found from the values of the rheological parameters.

4.3.6 Results

The comparisons between the experimental curves and the model with the identified rheological parameters are presented in Figures 4.14 to 4.23. The results are presented as the compression force vs. the displacement and the compression stress vs. the logarithmic compression strain. The part of the curve corresponding to the squeeze-flow is highlighted on the force curves. The rest of the test is removed from the stress curves. The labels in the legends of each figure give the sample identification number.

The parameters corresponding to each curve and their average value are given in Table 4.2 (LF-SMC-30, 0.5mm/s), Table 4.3 (CF-SMC-50, 0.5mm/s), Table 4.4 (CF-SMC-50, 1mm/s), Table 4.5 (HP-SMC-26, 0.5mm/s) and Table 4.6 (HP-SMC-26, 1mm/s). The uncertainties are given as the standard deviations associated with each value, and the relative error is calculated as the ratio between the standard deviation and the average value.

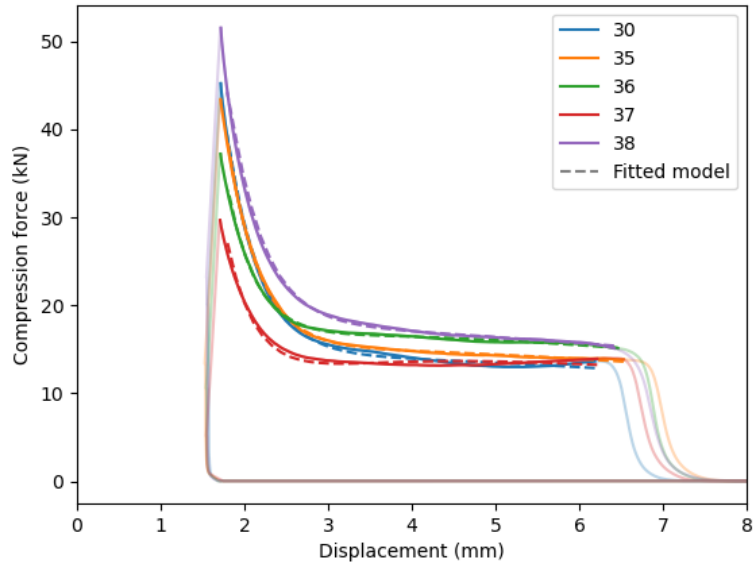


Figure 4.14: Experimental compression force vs. displacement for the 5 samples of LF-SMC-30 and comparison with the fitted model. Compression velocity: 0.5mm/s.

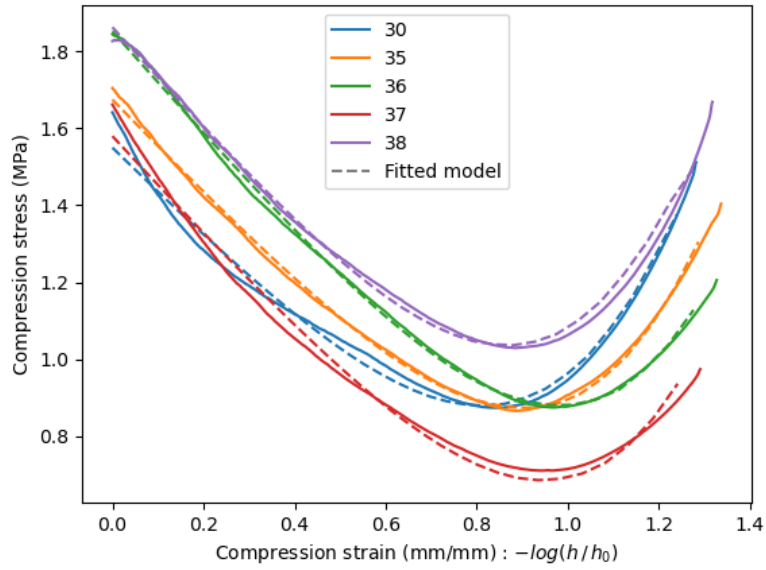


Figure 4.15: Experimental compression stress vs. logarithmic compression strain for the LF-SMC-30 and comparison with the fitted model. Compression velocity: 0.5mm/s

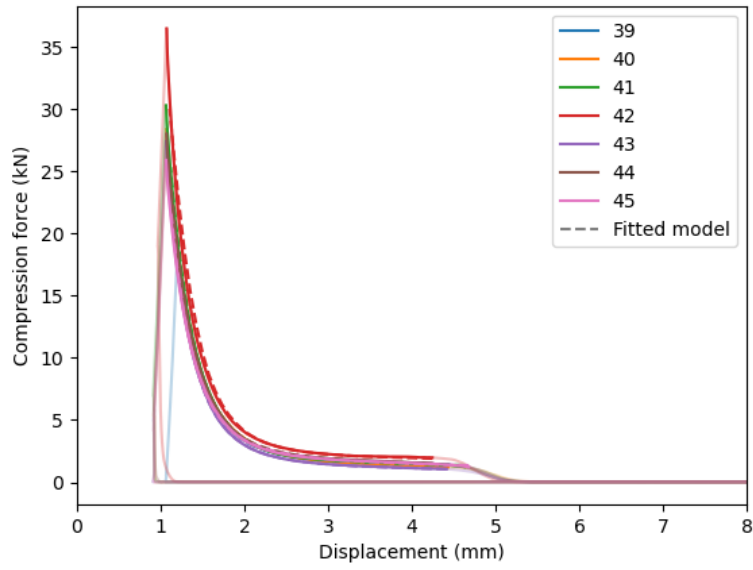


Figure 4.16: Experimental compression force vs. displacement for the CF-SMC-50 and comparison with the fitted model. Compression velocity: 0.5mm/s

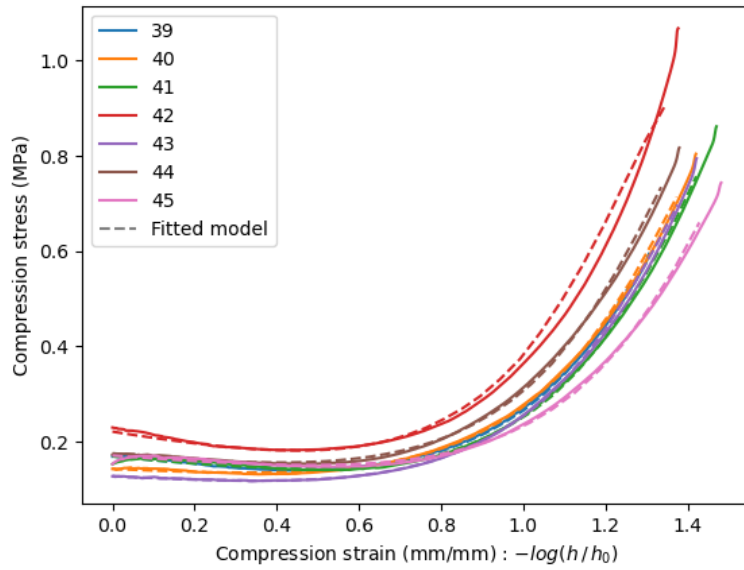


Figure 4.17: Experimental compression stress vs. logarithmic compression strain for the CF-SMC-50 and comparison with the fitted model. Compression velocity: 0.5mm/s

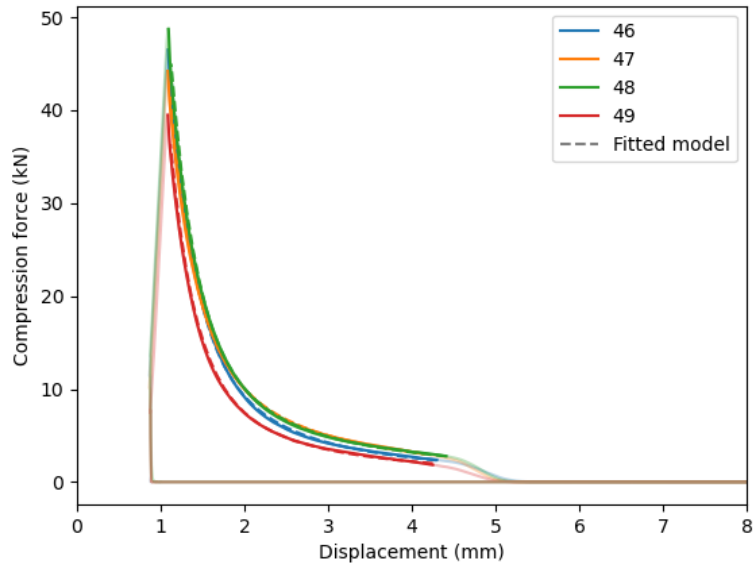


Figure 4.18: Experimental compression force vs. displacement for the CF-SMC-50 and comparison with the fitted model. Compression velocity: 1mm/s

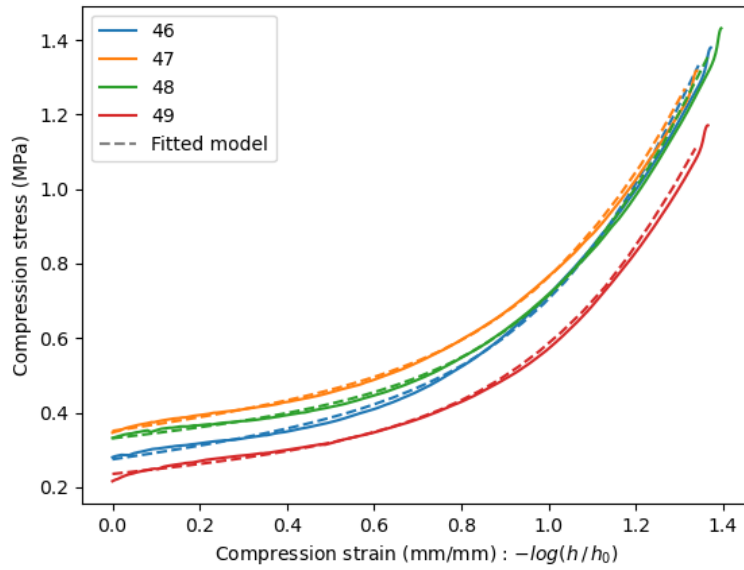


Figure 4.19: Experimental compression stress vs. logarithmic compression strain for the CF-SMC-50 and comparison with the fitted model. Compression velocity: 1mm/s

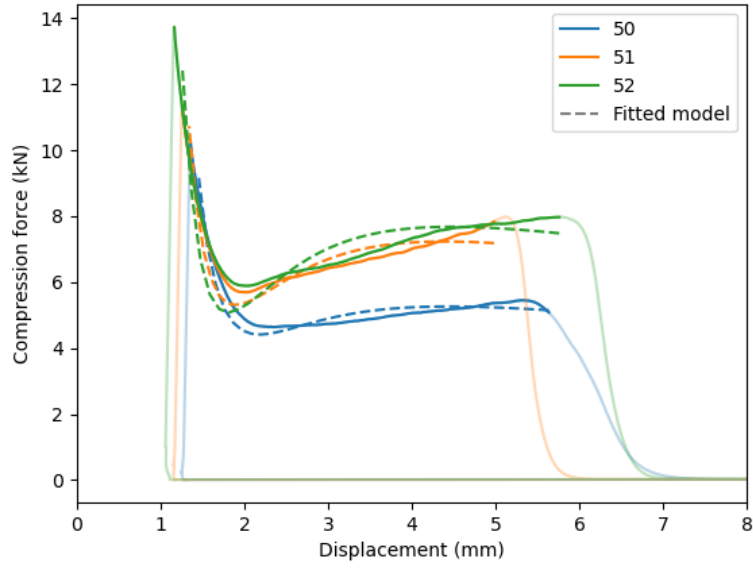


Figure 4.20: Experimental compression force vs. displacement for the HP-SMC-26 and comparison with the fitted model. Compression velocity: 0.5mm/s

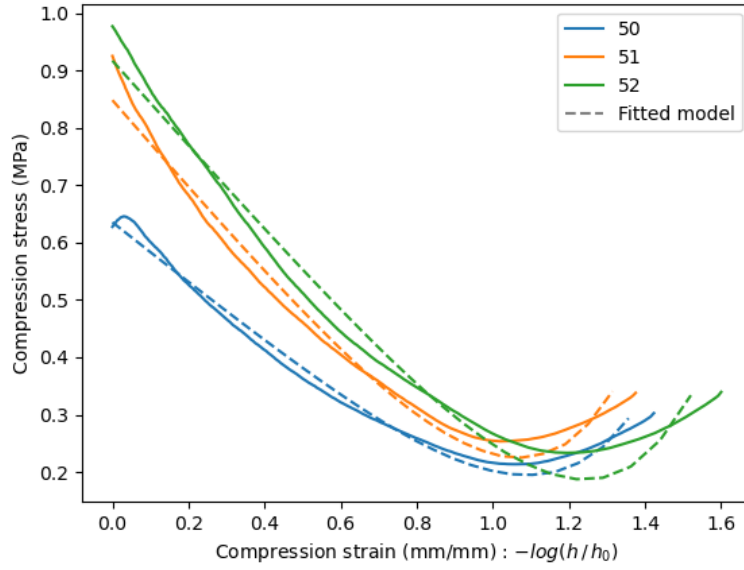


Figure 4.21: Experimental compression stress vs. logarithmic compression strain for the HP-SMC-26 and comparison with the fitted model. Compression velocity: 0.5mm/s

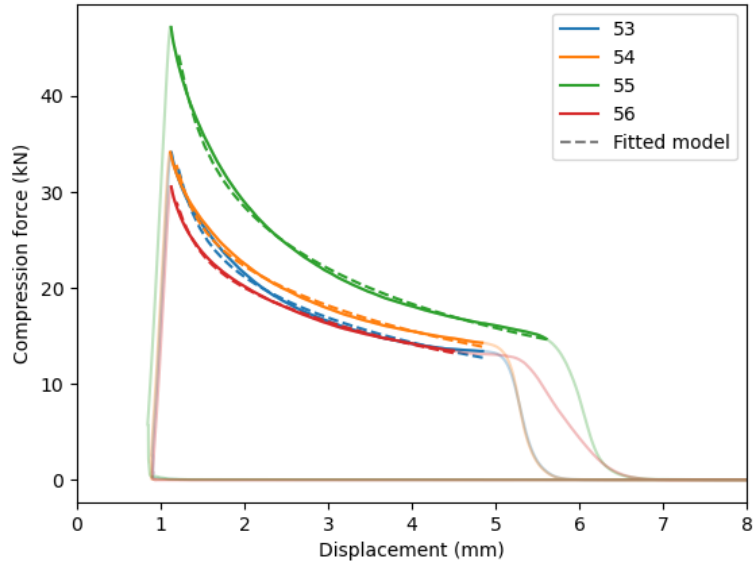


Figure 4.22: Experimental compression force vs. displacement for the HP-SMC-26 and comparison with the fitted model. Compression velocity: 0.5mm/s

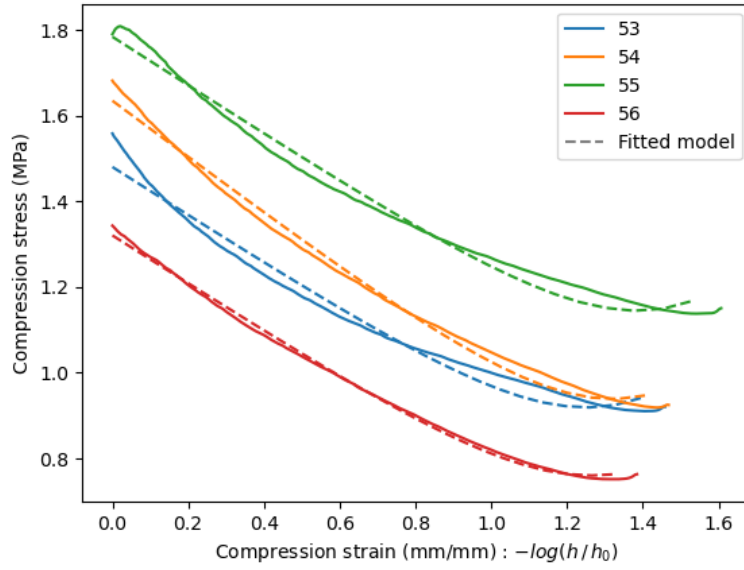


Figure 4.23: Experimental compression stress vs. logarithmic compression strain for the HP-SMC-26 and comparison with the fitted model. Compression velocity: 1mm/s

Label	μ (<i>Pa. s</i>)	$\mu_0^\#$ (<i>MPa. s</i>)	k_0 (<i>kPa</i>)	h_0 (<i>mm</i>)	R_0 (<i>mm</i>)
30	1527	18.9	1203	6.19	51.42
35	1374	21.9	1253	6.53	50.86
36	1065	24.0	1362	6.46	51.07
37	989	19.5	1305	6.21	51.66
38	1581	21.1	1359	6.42	51.33
Mean	1310 \pm 270	21.7 \pm 2.4	1300 \pm 70	6.4 \pm 0.2	51.3 \pm 0.3
Rel. error	20%	11%	5%	3%	0.5%

Table 4.2: Model parameters for the LF-SMC-30 molded at 0.5mm/s.

Label	μ (<i>Pa. s</i>)	$\mu_0^\#$ (<i>MPa. s</i>)	k_0 (<i>kPa</i>)	h_0 (<i>mm</i>)	R_0 (<i>mm</i>)
39	178	1.48	101	4,45	51,44
40	163	1.24	55	4,43	52,08
41	186	1.55	97	4,63	50,73
42	257	1.83	165	4,25	52,38
43	166	1.11	62	4,42	51,46
44	175	1.46	95	4,25	52,4
45	147	1.60	74	4,68	50,19
Mean	182 \pm 35	1.5 \pm 0.2	93 \pm 37	4.4 \pm 0.2	51.5 \pm 0.8
Rel. error	19%	13%	40%	5%	2%

Table 4.3: Model parameters for the CF-SMC-50 molded at 0.5mm/s.

Label	μ (<i>Pa.s</i>)	$\mu_0^\#$ (<i>MPa.s</i>)	k_0 (<i>kPa</i>)	h_0 (<i>mm</i>)	R_0 (<i>mm</i>)
46	120	1.16	-147	4,30	52,16
47	96	1.45	-150	4,14	52,87
48	124	1.46	-113	4,41	51,79
49	98	0.99	-102	4,25	52,34
Mean	110±14	1.3±0.2	-130±20	4.3±0.1	52.3±0.5
Rel. error	13%	15%	15%	2%	1%

Table 4.4: Model parameters for the CF-SMC-50 molded at 1mm/s.

Label	μ (<i>Pa.s</i>)	$\mu^\#$ (<i>MPa.s</i>)	k_0 (<i>kPa</i>)	h_0 (<i>mm</i>)	R_0 (<i>mm</i>)
50	169	7.29	531	5,64	50,79
51	181	8.33	772	4,98	51,93
52	140	10.57	746	5,76	50,96
Mean	163±20	8.7±1.7	680±130	5.5±0.4	51.2±0.6
Rel. error	12%	20%	20%	7%	1%

Table 4.5: Model parameters for the HP-SMC-26 molded at 0.5mm/s.

Label	μ (<i>Pa.s</i>)	$\mu_0^\#$ (<i>MPa.s</i>)	k_0 (<i>kPa</i>)	h_0 (<i>mm</i>)	R_0 (<i>mm</i>)
53	29.7	7.2	566	4,85	52,37
54	27.1	8.0	659	4,84	52,03
55	29.5	10.5	569	5,61	51,15
56	20.4	6.0	564	4,50	56,49
Mean	27±4	7.9±1.9	590±47	5.0±0.5	53.0±2.4
Rel. error	15%	24%	8%	10%	5%

Table 4.6: Model parameters for the HP-SMC-26 molded at 1mm/s.

4.3.7 Analysis and discussions

4.3.7.1 Description of the experimental curves

The typical curves of the force, the displacement and the compression velocity are represented in Figure 4.24. The compression test is separated into four steps:

- When the force is zero, the upper platen is not in contact with the SMC charge and no force is registered.
- When the platen touches the sample, the force increases rapidly. During this step, the material does not flow in the plane, the only deformation is a vertical compression. The sample is compacted and the porosities between the plies and within the plies are progressively closed.
- At the end of the compaction, the SMC material begins to flow in the plane. The force adopts a different evolution, marked by a change in slope. The force after this increases non-linearly up to the end of the compression test.
- After the compression peak, the upper platen stops its displacement. The SMC material creeps. The force decreases rapidly toward a certain plateau, directly followed by a drop in force characterizing the polymerization of the thermosetting resin. Then, the force remains constant until the opening of the mold, with a solid behavior of the SMC material. The force becomes zero once the platen is opened to release the composite.

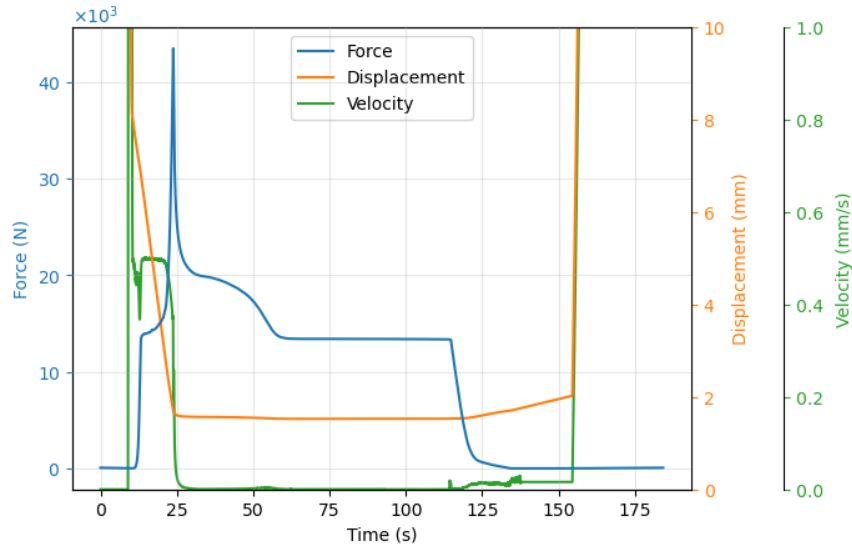


Figure 4.24: Typical SMC compression curves.
(Sample 35, material: LF-SMC-30, compression velocity: 0.5mm/s)

From the typical response of the SMC material, the rapid compression test allows one to compress the sample well before the resin starts to gel. The drop in force occurs between 50s and 60s depending on the SMC material, whereas the compression test ends at 25s. The curing reaction can be ignored in the evolution of the force and the viscosity of the SMC materials.

The Figures 4.14 to 4.23 shows the comparison between the experimental forces and stress with the analytical model presented in Eq. (4.13) after fitting the model parameters. The variation of the values of force and stress is expected due to the geometrical variations of thickness and

radius, as listed in Tables 4.2 to 4.6. The proposed rheological model is in good agreement with the experimental results and correctly follows the curves for all the tests, even if the behavior may be slightly different.

4.3.7.2 Identification of the mechanical behaviors

The comparison between the different experimental curves, especially those related to the compression stress, shows different rheological behavior as a function of the compression velocity for the different SMC materials. At high compression strain rates, the stress increases non-linearly with respect to $\dot{\epsilon}$. At low compression strain rates, the compression stress tends to decrease first, before increasing again as the strain rate increases. This complex behavior can be explained by the combination of two contributions: a viscous one which is always increasing with respect to the compression strain rate, and a slowly decreasing contribution corresponding due to the solid elasto-plastic response (see Figure 4.25 and Figure 4.26). Without these two mechanical contributions, the experimental curves cannot be fitted, as the viscous term alone would induce a very small stress at the beginning of the compression which rapidly increases near the end of the test, even for a non-linear viscosity.

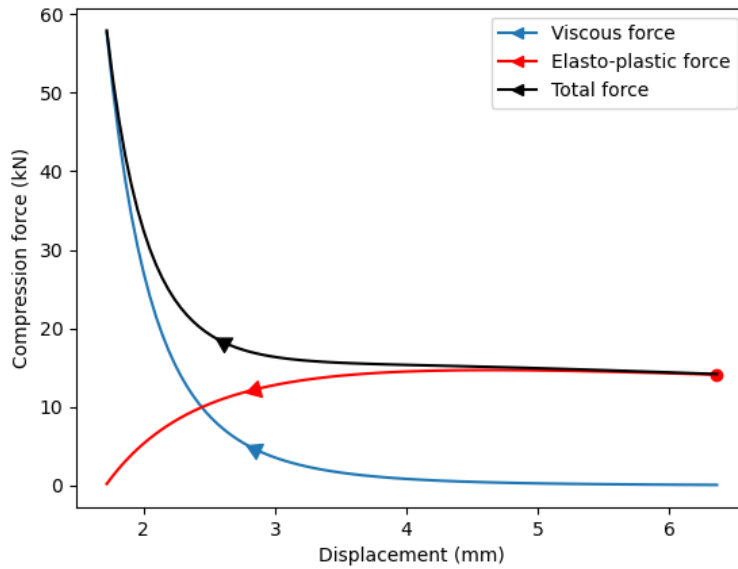


Figure 4.25: Viscous and elasto-plastic contributions to the compression force of the LF-SMC-30 at a constant compression velocity of 0.5mm/s.

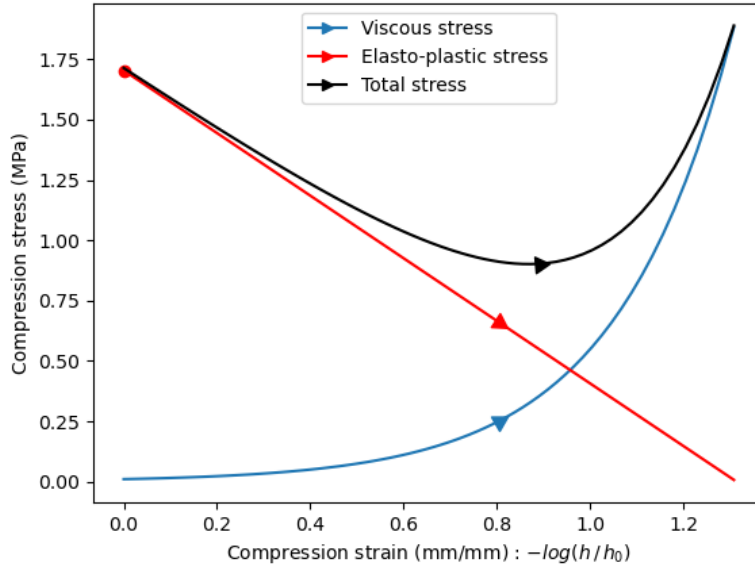


Figure 4.26: Viscous and elasto-plastic contributions to the compression stress of the LF-SMC-30 at a constant compression velocity of 0.5mm/s.

The effect of these two mechanical behaviors is clearly visible for the LF-SMC-30 and slightly for the CF-SMC-50, for which the viscous term is dominant, but the decrease in stress is observable at the compression velocity of 0.5mm/s. For the HP-SMC-26, the elasto-plastic term is dominant. The molding conditions were not suitable to load the SMC material sufficiently to reach the viscous domain.

The proposed model is consistent with results in literature of SMC rheology, as the internal friction and viscous effects have been observed (Lee, et al., 1981), (Barone & Caulk, 1985), (Dumont, et al., 2007), most of the time with only one of them depending on the material and the processing conditions.

No significant non-linearity in the viscosity μ was noticed, as the proposed model fits the experimental curves well for a compression strain rate which is multiplied five times between the beginning to the end of the compression. However, a difference in the identified viscosities is observed for a same material reference at two different compression velocities, probably explained by the temperature dependance of the viscosity and the longer heating time for slow compression velocities. This dependence does not affect the fit of the experimental curves.

The CF-SMC-50 and HP-SMC-26 materials have similar values of viscosity μ : 182Pa.s for the carbon SMC and 163Pa.s for the glass SMC at the same compression velocity of 0.5mm/s. These values correspond to the usual range of order for the viscosity of an unsaturated polyester SMC material (Yang & Suspene, 1991) (Han & Lem, 1983). For the LF-SMC-50, the viscosity is much higher (1300Pa.s), probably due to longer fibers and their effect on the effective viscosity of the composite material, as documented in (Crowson & Folkes, 1980), (Boylan, et al., 2003), (Huq & Azaiez, 2005). The very low value of the viscosity measured for the HP-SMC-26 at 1mm/s is explained by the predominance of the elasto-plastic behavior which overshadows the viscous behavior. The identification of μ is not relevant in that case.

The values of the additional viscosity $\mu_0^\#$ are of the order of MPa.s for all the tested SMC materials and represent a significant stress contribution compared with the linear viscosity μ expressed in Pa.s. According to the friction model developed in Section 4.2 (see also Appendix 4.B), the initial friction viscosity $\mu_0^\#$ depends on the fibrous mesostructure according to:

$$\mu_0^\# = HK(\phi r - 1) \quad \text{with} \quad H = \phi_m \eta_{fm} \quad \text{and} \quad K = G_f \left(\frac{e_b}{w_b} \right)^3 \quad (4.14)$$

where G_f is the transverse shear modulus of the fibers, e_b and w_b are the thickness and the width of the fiber bundle. Considering Eq. (4.14), the parameter $\mu_0^\#$ is reformulated in terms of the properties of the fibrous reinforcement.

We assume a similar value of the friction material constant for all the SMC references as $\eta_{fm} = 0.05s$ (it leads to a friction coefficient of ~ 0.1 for the compression strain rate of $0.1s^{-1}$ and the aspect ratio of fiber bundles of 25. This corresponds to usual values of friction coefficient encountered in lubricated friction problems with liquid polymers (Zeng, 2013)), the identified shear moduli of different fiber rovings are:

	LF-SMC-30	CF-SMC-50	HP-SMC-26
$G_f =$	21GPa \pm 2GPa	9GPa \pm 1GPa	19GPa \pm 2GPa

Table 4.7: Shear modulus of SMC fibers.

The shear moduli of the two glass fiber rovings are similar according to their respective uncertainties, with an average value of 20GPa. The shear modulus of the carbon roving at 9GPa is significantly lower, approximatively the half of the value of the glass fiber rovings. These values are close to the usual transverse shear modulus of the glass and carbon fibers (Tsai, 1999), and correspond at least in order of magnitude, respecting the smaller value for the transverse shear stiffness of the carbon fibers. The real value can only be determined precisely if the friction parameter H is measured by an independent experiment. However, it is not necessary as H and K appear only as a product in the proposed SMC model.

(Oter-Carbonell, 2018) and (Dumont, et al., 2007) carried out experiments with a similar protocol and provide the full compression curves for glass fiber SMC. Neglecting the viscosity and the elastic terms at the beginning of the squeeze-flow, the transverse shear modulus has been calculated from their different tests and gives similar values: $G_f = 19GPa \pm 1GPa$ for (Oter-Carbonell, 2018) and $G_f = 20GPa \pm 2GPa$ for (Dumont, et al., 2007). In the work by (Romanenko, 2022) with a carbon fiber SMC, the calculated shear modulus is $G_f = 10GPa \pm 1GPa$ and is close to the one that we obtained. The obtained values are consistent with published values obtained by other experimental characterization.

The last parameter identified by the experiment is the relaxation stiffness k_0 . This parameter is the derivative of the friction stress with respect to the vertical strain at the beginning of the flow. It describes the evolution of the fibrous reinforcement and the reduction of internal forces due to the relaxation of the mesostructure (clearly seen in Figure 4.25 and Figure 4.26). Differentiating Eq. (4.11) with respect to ε (see Appendix 4.B), the relaxation parameter k_0 can be expressed as:

$$k_0 = \left. \frac{-\partial \tau^\#}{\partial \varepsilon} \right|_0 = \eta K \phi \alpha r \left(\underbrace{\left| \frac{\partial \alpha}{\alpha \partial \varepsilon} \right|_0}_{(1)} + \underbrace{\left| \frac{\partial r}{r \partial \varepsilon} \right|_0}_{(2)} - \underbrace{\left| \frac{\partial \phi}{\phi \partial \varepsilon} \right|_0}_{(3)} \right) - \tau_0^\# \quad (4.15)$$

The relaxation includes the different mesostructure transformations: the angular alignment (1), the fiber bundle transverse spreading (2) and the compaction of the mesostructure (3). It is not possible in the present experiment to obtain the terms related to each transformation individually. The parameter k_0 is positive if the friction stress decreases during the compression (with the mechanisms (1) or (2)), and positive if the fiber bundles are compacted (3). If k_0 is close to zero, it means that the different mechanisms balance, or that the fiber bundles are translated with a simple slip between them, keeping the mesostructure in a constant mechanical state.

The relative variations of the mesostructure deformation with respect to the macroscopic deformation is measured by the evolution coefficient C , defined as:

$$C = \frac{-\partial \varepsilon^\#}{\partial \varepsilon} = \frac{\tau^\# + k}{\eta K} \quad (4.16)$$

In the case where the only transformation kinematics is the reorientation of the fiber bundles, the terms (2) and (3) vanish. Since term (1) describes the evolution of the relative angles between two fiber bundles, it can be related to the evolution coefficient (denoted κ) present in RSC and SRF models for slow kinematics of fiber bundle orientations (Wang, et al., 2008):

$$C = \phi r \left| \frac{\partial \alpha}{\partial \varepsilon} \right| \quad (4.17)$$

The measured initial values C_0 for the different SMC materials are given in Table 4.8. If C is close to 1, the in-plane deformations of the fibrous mesostructure are equal to the shear of the flow (only possible if the friction term is zero). The lower the C the slower the rotations of the fiber bundles. The values of $k_0 = \left. \frac{-\partial \tau^\#}{\partial \varepsilon} \right|_0$, scaled by $\eta_0 K$, are given in Table 4.9 and highlight the difference between the transformation modes observed for the different tests, with negative values only occurring if the fiber bundles are mechanically loaded during the test. From these results, increasing the compression velocity is likely to reduce the reorientations and activate other transformation modes, as for the CF-SMC-50 for which the sign of k_0 changes between the 0.5mm/s and 1mm/s tests. In this case, it indicates that deformation of the fiber bundles occurs for high compression velocities, consistent with fiber bundles spreading observed in carbon SMC mesostructures (Chen, et al., 2019). This compaction is directly observable in Figure 4.18, where the stress is increasing, which differs from the behavior of the other test series. Optimal compression conditions should exist to induce the flow of the SMC material, limiting the deformation and the loading of the fiber bundles. However, the experimental data is limited to conclude on the factors affecting the evolution of the fibrous mesostructure and would require further investigation.

	LF-SMC-30	CF-SMC-50	HP-SMC-26
0.5mm/s	0.80	1.0	0.7
1mm/s	No test	0.4	0.5

Table 4.8: Average evolution coefficient C_0 for the different series of experiments.

	LF-SMC-30	CF-SMC-50	HP-SMC-26
0.5mm/s	0.35	0.38	0.32
1mm/s	No test	-0.30	0.14

Table 4.9: Average evolution coefficient $\frac{k_0}{\eta_0 K}$ for the different series of experiments.

4.3.7.3 Discussion about the rheological model

The proposed model, described in Eqs. (4.10), (4.12) and (4.16), is a visco-elasto-plastic model, where the viscous behavior describes the matrix phase and the elasto-plastic behavior is relative to the effect of the friction forces inside the fibrous mesostructure. The two terms summed in Eq. (4.12) reflect the parallel assembly of both behaviors, similar to the model used by (Silva-Nieto, et al., 1981) (see Figure 4.27-a) based on a phenomenological approach. Here, the model is improved in a new formulation, physically based on the mechanical behavior of the evolving mesostructure. The rheological scheme of the model is shown in Figure 4.27-b. In this figure, the viscous behavior corresponds to the blue part and is parametrized by the viscosity μ , the friction of the fibrous reinforcement is represented by the red part, with the friction coefficient η , the mechanical parameter K and the evolution coefficient C . According to the parallel assembly, the two stress contributions are well summed. When the SMC material is compressed, it can deform in two different ways:

- if the viscous stress is high enough ($\tau = \mu\dot{\gamma} > \tau^\#$, where τ is the viscous shear stress of the fluid and $\dot{\gamma}$ is the shear rate), the fiber bundles are transported (Figure 4.27-c). Depending on the value of the coefficient C , the fibrous reinforcement can be relaxed if $C > 0$ (the fiber bundles are aligned), or loaded if $C < 0$.
- if the viscous forces are smaller than the friction threshold, the fiber bundles cannot be transported and relaxed, they are loaded by the imposed compression load and deformed (Figure 4.27-d). Then, a relative motion between the fluid phase and the fiber bundles can occur and induce a segregated flow.

This new model correctly describes the different deformation modes of the SMC materials, as described in Chapter 2, and is consistent with the experimental results of the proposed characterization test. Compared to the model by (Silva-Nieto, et al., 1981), represented in

Figure 4.27-a, the elastic loading of the fibrous network can evolve during the flow, with a deformation of the mesostructure evolving in the opposite direction to the macroscopic deformation of the flow, resulting in a relaxation of the material. This complex kinematics cannot be represented by usual rheological schemes which have been improved with the representation of Figure 4.27-b.

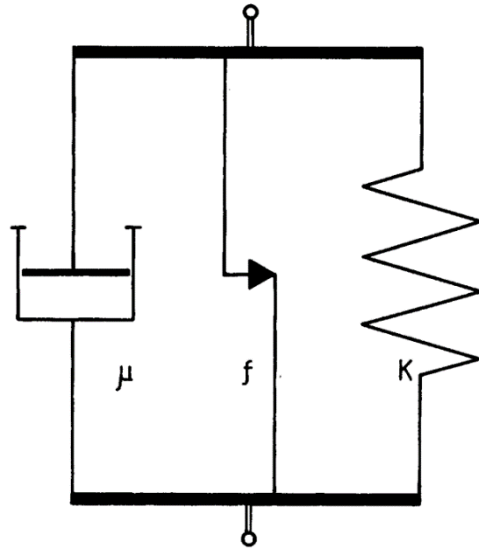
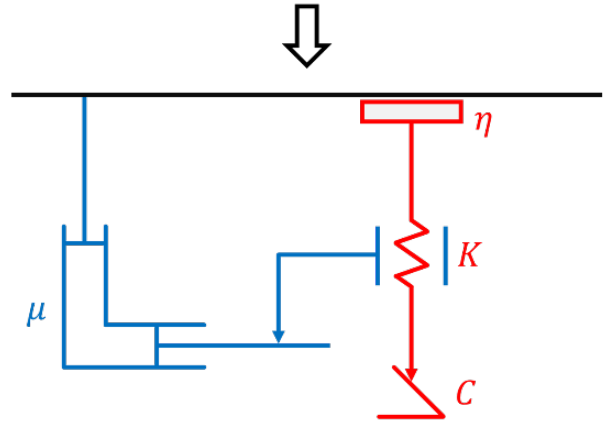
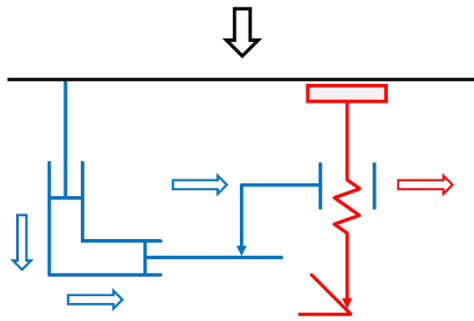


Fig. 1. Analogue model for SMC equation of state.

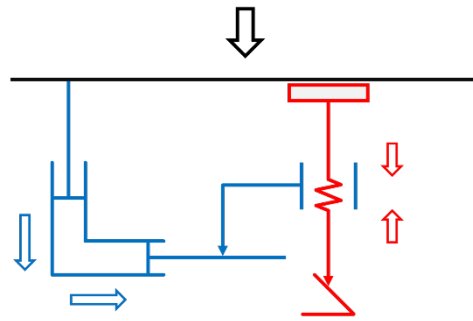
(a)



(b)



(c)



(d)

Figure 4.27: SMC rheological model:

- (a): Visco-elasto-plastic model in parallel for SMC materials found in (Silva-Nieto, et al., 1981).
- (b): SMC model described by the Eqs. (4.10), (4.12) and (4.16).
- (c): Flow and relaxation of the fibrous reinforcement. The viscous matrix flows and transport the fiber bundles. The compaction of the fibrous reinforcement decreases.
- (d): Segregation and compaction of the fibrous reinforcement. The viscous matrix flows and slips on the fibrous reinforcement. The fiber bundles are not transported and are compacted.

4.3.8 Conclusion

A simple rheological experiment is set up with the compression of a cylindrical charge between two parallel platens to reproduce industrial molding conditions applied to commercial SMC materials.

From a simple rheological model of an elasto-visco-plastic behavior, three material parameters are obtained to characterize each of these mechanical behaviors and reveal that the squeeze-flow of SMC materials is mostly governed by solid behaviors at the beginning of the compression, then by fluid behaviors for the high compression strain rates at the end of the compression. The elasto-plastic contribution related to the compaction and the internal friction between the fiber bundles is significant for high fiber contents and long fibers.

The effects of the temperature and the curing reaction on the rheology of the polyester resin have been discussed and considered negligible (during the compression test) with regard to the ability of the model to fit the compression curves for a large range of compression strain rates and for different durations of the experiment.

The use of the friction model for the fibrous mesostructure allows one to retrieve the dependence of the material parameters of the SMC model in the geometrical parameters of the fiber bundles and the shear modulus of the rovings.

This result can provide guidance to optimize the manufacturing parameters of the SMC materials with the aim to improve the molding process, maintaining the mechanical performances of the final parts. The introduction of the solid deformation term in the SMC model helps to determine remaining parameters directly from the force measurements.

Once the material is characterized, the analytical solution of the compression stress allows one to control the compression parameters to govern the deformation of the material and particularly the deformation of its mesostructure. A consequence of this work could be the extension of this analysis to an industrial problem and the piloting of the processing parameters to control the evolution of the mesostructure from the force measurement, in order to improve the final performance of the parts produced.

4.4 General conclusions

In this chapter, different characterization experiments have been carried out on different SMC materials with commercial formulations using glass or carbon fibers which provide the following conclusions:

- **Establishment of the friction model:** the molding stress required to squeeze and induce the flow of SMC materials depends on the mesostructure compaction strain metrics as defined in Chapter 3 and the compression strain rate with a linear relationship. It has been concluded that this initial stress reveals the internal friction forces between the fiber bundles which are opposed to the flow.
- **Derivation of a full SMC model based on the mechanical behavior of the fibrous mesostructure:** the mechanical model of the compaction of fibrous mesostructure presented in Chapter 3 is used to determine the expression of the friction coefficient from the experimental results.
- **A characterization protocol has been developed to identify the parameters of the model** based on the radial squeeze flow of a SMC material.
- **The relationship between the stress and the properties of the fiber roving has been formulated** from the mechanical model proposed in Chapter 3 and provides good agreement with the experimental differences between the glass and carbon SMC materials.
- The thermal and curing effects does not affect the material characterization, but the **inherent variability of the materials is significant** and requires repeated testing to correctly identify the material properties.
- **The evolution of the mesostructure is directly sensed in the force measurement** and could help to characterize its evolution with respect to the molding conditions.
- The effect of the compression velocity and the SMC formulation seems to affect the deformation of the mesostructure, through the **mechanical loading of the fiber bundles at high compression strain rates**.

Appendices

4.A. Comparison of compression curves for different parameters of SMC formulations and compression molding process

The compression curves for the different compression tests are given. The thickness is determined from the displacement of the crosshead measured by the testing machine, corrected by its compliance. The force is normalized by the compression velocity. The results are compared for two compression velocities per SMC material: 1mm/s and 5mm/s.

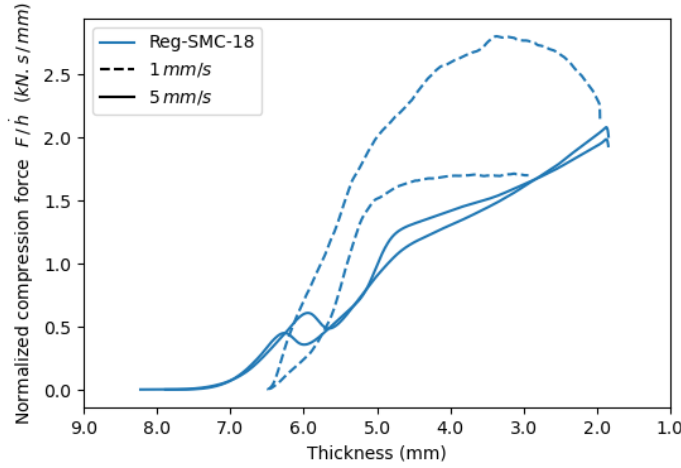


Figure 4.28: Comparison of results for the Reg-SMC-18.

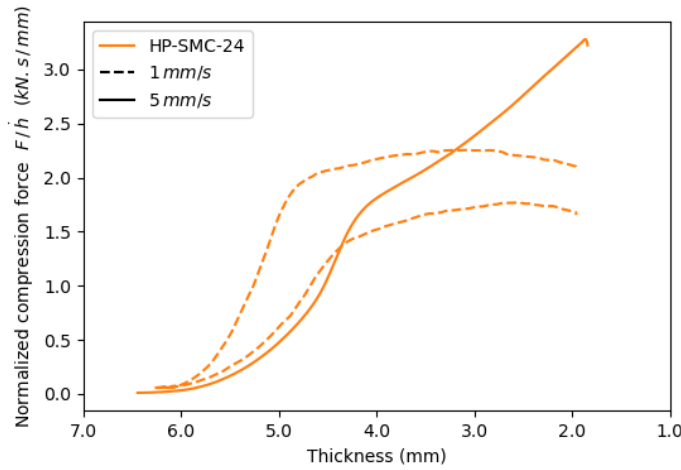


Figure 4.29: Comparison of results for the HP-SMC-24.

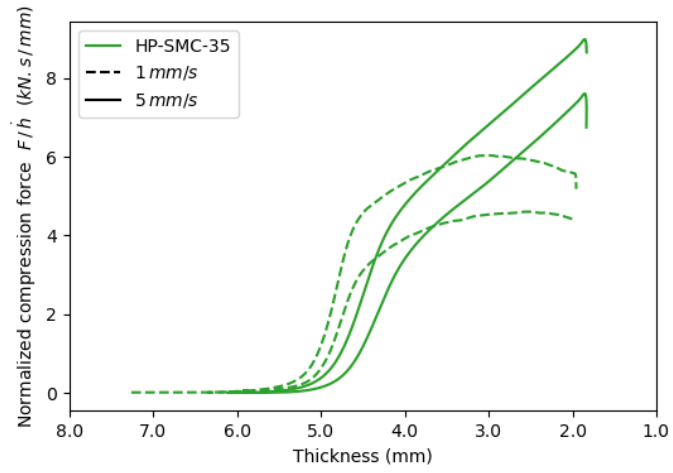


Figure 4.30: Comparison of results for the HP-SMC-37.

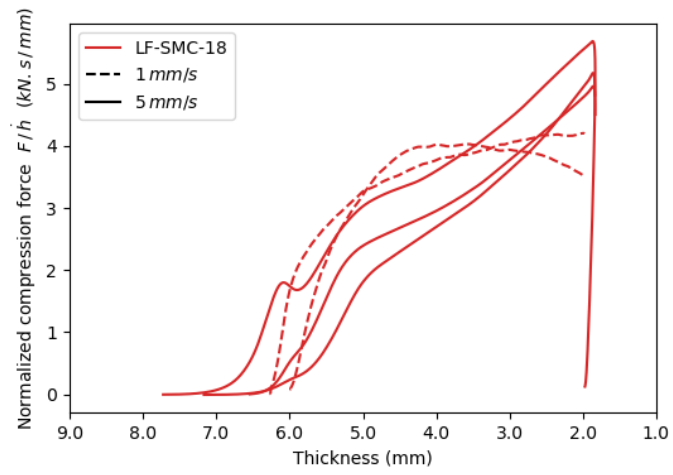


Figure 4.31: Comparison of results for the LF-SMC-18.

4.B. Derivation of the compression stress formula

Viscous term:

The flow is assumed to be quasi-stationary (with a small Reynolds number), with no gravity. The fluid is incompressible and Newtonian, with a constant viscosity μ . Its velocity is written \vec{v} and the pressure is denoted by p .

The conservation of the mass is written for an incompressible fluid:

$$\nabla \cdot \vec{v} = 0 \quad (4.18)$$

and the conservation of the linear momentum corresponds to the Stokes equation:

$$-\nabla p + \mu \nabla^2 \vec{v} = 0 \quad (4.19)$$

The initial charge is cylindrical and the material is assumed transverse isotropic in the plane, so there is no privileged direction and the compression problem respect the cylindrical symmetries. The flow in the plane is radial (see Figure 4.32). The cylindrical coordinate system (r, θ, z) is used. The gap between the two platens is noted h . The two platens are getting closer with a relative velocity \dot{h} . The origin of the coordinate system is taken at the center of the SMC charge. The radius of the charge is noted R . The fluid is assumed to not slip along the platens.

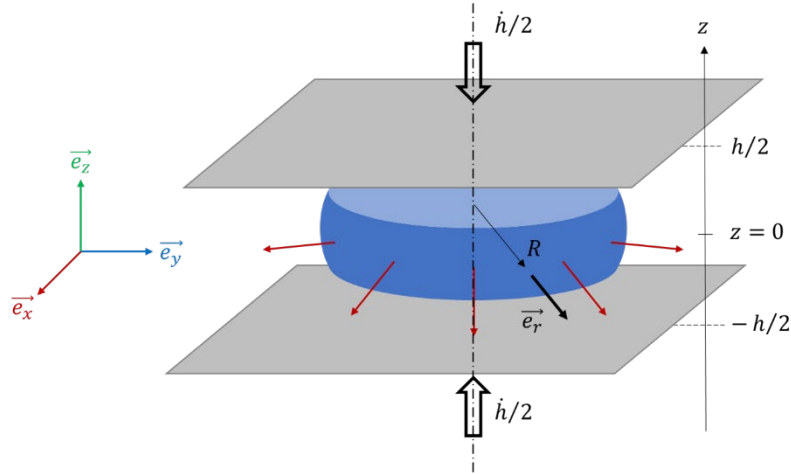


Figure 4.32: Cylindrical symmetry of the radial squeeze-flow.

In the cylindrical coordinate system, Eq. (4.18) and (4.19) become:

$$v_{r,r} + \frac{v_r}{r} + v_{z,z} = 0 \quad (4.20)$$

$$\dots \quad (4.21)$$

$$\mu \left(v_{z,rr} + \frac{v_{z,r}}{r} + v_{z,zz} \right) = p_{,z}$$

and combining these two equations simplifies Eq. (4.21) into:

$$\begin{aligned} \mu (v_{r,z} - v_{z,r})_{,z} &= p_{,r} \\ \mu \left(v_{z,rr} + \frac{v_{z,r}}{r} + v_{z,zz} \right) &= p_{,z} \end{aligned} \quad (4.22)$$

Considering the lubrication approximation: $h \ll R$, the derivatives of the velocity through the thickness are preponderant compared with the other directions: $v_{z,r} \ll v_{r,z}$. Then, the radial velocity is solution of:

$$v_{r,zz} = \frac{1}{\mu} p_{,r} \quad (4.23)$$

By integration using the no-slip boundary conditions, it comes:

$$v_r = \frac{-p_{,r}}{2\mu} \left(\frac{h^2}{4} - z^2 \right) \quad (4.24)$$

The conservation of the volume of fluid between the two platens is expressed in integral form of a cylinder of radius r :

$$2 \int_{-h/2}^{h/2} v_r(r, z) dz = r(-\dot{h}) \quad (4.25)$$

Combining Eq. (4.24) and (4.25) gives a differential equation on the pressure field:

$$\frac{-p_{,r}}{\mu} \frac{h^3}{6} = r(-\dot{h}) \quad (4.26)$$

The radial velocity results in a parabolic profile through the thickness and is linear with respect to the radial coordinate:

$$v_r = \frac{3r(-\dot{h})}{4h} \left(1 - \left(\frac{2z}{h} \right)^2 \right) \quad (4.27)$$

and the pressure is quadratic with respect to the radial coordinate:

$$p = \frac{3\mu(-\dot{h})}{h^3} (R^2 - r^2) \quad (4.28)$$

Thanks to the conservation of the volume of Eq. (4.20), the vertical velocity is:

$$v_z = \frac{-\dot{h}}{2h} z \left(3 - \left(\frac{2z}{h} \right)^2 \right) \quad (4.29)$$

The vertical shear rate is zero at the platens, so there is only the pressure, which contributes to the compression stress. The integration of the pressure over the disk of radius R and divided by the disk area gives the compression stress imposed by the platens to deform the fluid:

$$\Sigma = \frac{2}{R^2} \int_0^R p(r) r dr = \frac{3}{2} \left(\frac{R}{h} \right)^2 \mu \dot{\varepsilon} \quad (4.30)$$

with the $\dot{\varepsilon} = -\dot{h}/h$ the compression strain rate.

Solid term:

The fibers are assumed to be incompressible, and the fiber bundles are compacted vertically, through the thickness of the SMC material, and deform according to a shear kinematics. The internal friction threshold is the product of the friction coefficient and the normal contact stress $\sigma^\#$ within the fibrous network. According to the statistical mechanical model of fibrous mesostructures proposed in Chapter 3, the average of this contact stress is:

$$\sigma^\# = \frac{K}{\alpha r} \underbrace{(\phi \alpha r - 1)^+}_{\varepsilon^\#} \quad (4.31)$$

where K is the mechanical parameter of the fiber bundles and $\varepsilon^\#$ is a metric of the mesostructure deformation, as a function of the fiber bundle volume fraction ϕ , the angular factor α and the fiber bundle aspect ratio r , defined in detail from the geometrical approach and the stacking model of Chapter 2.

Inside the bundle, the fibers are stacked in the transverse cross-section of the fiber bundle. The fiber volume fraction of $\frac{1}{2\pi}$ in the bulky state, and $\frac{2}{\pi} \simeq 64\%$ after being packed, according to the generalized stacking model of Chapter 2. Then, the fiber bundle volume fraction is related to the fiber volume fraction within the SMC material by:

$$\phi = \frac{\pi}{2} \phi_f \quad (4.32)$$

The angular factor is initially equal to 1 as we assume a transverse isotropic distribution of fiber bundle orientations in the plane.

Using the generalized definition of the aspect ratio given in Chapter 2, the aspect ratio of the fiber bundles of elliptical transverse cross-section is:

$$r = \frac{\pi l_f}{4 w_b} \quad (4.33)$$

with l_f the fiber length and w_b the fiber bundle width.

The mechanical parameter K is related to the fiber bundle cross-section shear modulus according to the compaction model of Chapter 3:

$$K = G_b \left(\frac{e_b}{w_b} \right)^2 \quad (4.34)$$

where e_b and w_b are respectively the thickness and the width of the fiber bundles. Considering the assembly of fibers inside the bundle as a stack, the fiber bundle shear modulus G_b is related to the fiber shear modulus G_f according to:

$$G_b = G_f \left(\frac{e_b}{w_b} \right) \quad (4.35)$$

Homogenized friction model:

The conservation of the linear momentum is written for any subdomain of the composite material:

$$\nabla \cdot \bar{\bar{\sigma}} = 0 \quad (4.36)$$

in the absence of external body forces.

Assuming no gradient of volume fraction, the average of the divergence term of Eq. (4.36) (see Appendix 4.C) allows to separate the stress into the contributions of the two phases, plus an interaction term defined over the interface between the phases:

$$\langle \nabla \cdot \bar{\bar{\sigma}}^{(m)} \rangle = \phi_m \nabla \cdot \langle \bar{\bar{\sigma}}^{(m)} \rangle_m + \frac{1}{V} \oint \bar{\bar{\sigma}}^{(m)} \cdot d\vec{S}^{(m \rightarrow f)} \quad (4.37)$$

where $d\vec{S}^{(m \rightarrow f)}$ is the surface normal vector pointing outward, from the matrix to the fiber phase.

Here, we consider that the fiber bundles are completely immersed within the incompressible matrix phase. Then, the compression force imposed by the boundary conditions corresponds to the integrated pressure forces of the matrix phase, reducing the Eq. (4.37) to the matrix phase. Using Eq. (4.19) to develop the fluid stress tensor, the Eq. (4.37) becomes:

$$\underbrace{-\phi_m \nabla \langle p^{(m)} \rangle_m}_{(1)} + \underbrace{\mu \phi_m \nabla^2 \langle \vec{v}^{(m)} \rangle_m}_{(2)} + \underbrace{\frac{1}{V} \oint \bar{\bar{\sigma}}^{(m)} \cdot d\vec{S}^{(m \rightarrow f)}}_{(3)} = 0 \quad (4.38)$$

where μ is the viscosity of the matrix, $\langle p^{(m)} \rangle_m$ and $\langle \vec{v}^{(m)} \rangle_m$ are respectively the intrinsic matrix average of pressure and velocity. The first term corresponds to the pressure forces and is simply the gradient of pressure within the composite material. The second term describes the viscous forces characterized by the matrix viscosity μ . Finally, the interaction term (3) between the

matrix and the fiber bundles corresponds to the resulting effect of the friction forces between the fiber bundles on the matrix, thanks to the cohesion between the matrix and the fibers.

As the fiber bundles are thin and slender, the contacts between them are assumed quasi-punctual and oriented vertically (see Chapter 2). Then, they do not induce anisotropy in the plane. Considering two fiber bundles in contact, the friction threshold is the same to move any one of the two fiber bundles. It is concluded that the friction stress act as a scalar field on the flow, which allows to simplify the interaction term into:

$$\frac{1}{V} \oint \vec{\sigma}^{(m)} \cdot d\vec{S}^{(m \rightarrow f)} = \nabla \tau^\# \quad (4.39)$$

and $\tau^\# = \eta \sigma^\#$

where η is the friction coefficient which relates the friction stress field $\tau^\#$ applied to the flow to the contact stress $\sigma^\#$ within the fibrous network. The friction coefficient should depend on the natures of the matrix and the fibers, on the shape of the interface between the two phases, and according to the conclusions of Section 4.2, the friction is lubricated and the friction coefficient is proportional to the compression strain rate.

From a dimensional analysis, the friction coefficient is of the form:

$$\eta = \underbrace{\phi_m \cdot \eta_{fm}}_H \cdot \dot{\epsilon} \cdot \alpha r \quad (4.40)$$

where the factor ϕ_m comes from the matrix phase average, η_{fm} is a constant parameter which depends on the nature of the used materials, $\dot{\epsilon} = -\dot{h}/h$ is the macroscopic compression strain rate and αr represents the average ratio of the in-plane area of an elementary matrix cell around a fiber bundle (αl^2) and the fiber bundle surface (lw) (see Figure 4.33). It is the shape parameter which represents balance between the viscous drag forces associated to the elementary cell and the interaction cohesive force at the interface between the matrix and the fibers.

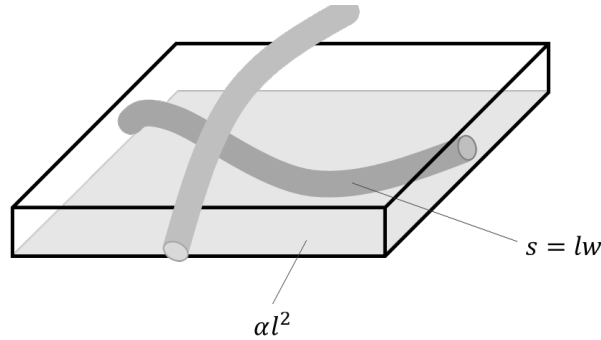


Figure 4.33: Elementary matrix cell of area αl^2 , containing a fiber bundle surface $s = lw$.

To simplify the notations, the matrix volume fraction and the material coefficient are merged into a friction parameter $H = \phi_m \eta_{fm}$.

The fibrous network is assumed to “flow” like a plastic medium, with a perfect slip with respect to the mold platens (even if it is not in contact with the platens, a fluid film is between the fiber bundles and the platens). The deformations of the fibrous mesostructure are taken into account in the mesostructure descriptors ϕ , α and r .

The plastic like deformation of the fibrous phase gives a simple expression of the stress contribution. Integrating the friction stress over the platen results in a compression stress equal to the average value of the friction stress over the SMC sample:

$$\Sigma = \tau^\# = H\dot{\varepsilon} \cdot K\varepsilon^\# \quad (4.41)$$

Initially, the material is assumed transverse isotropic, so $\alpha = 1$, and homogenous, so the friction stress is the same everywhere in the SMC material.

It can be noticed that the proposed scalar friction parameter could be tensorized to represent the anisotropy induced by the fibrous network in interactions with the matrix flow. However, in the absence of significant alignment of all the fiber bundles, the friction parameter can be considered as a scalar.

Complete model:

The SMC behavior combines viscous and friction effects. To flow and transport the fiber bundles, the fluid matrix has to impose a shear stress on the fibrous reinforcement which exceeds the friction stress between the fiber bundles. Then, the friction term acts as a plastic additional contribution to the mechanical stress. The resulting compression stress is the sum of both mechanisms, respectively given by Eqs. (4.30) and (4.41):

$$\Sigma = \frac{3}{2} \left(\frac{R}{h} \right)^2 \mu \dot{\varepsilon} + \tau^\# \quad (4.42)$$

During the compression, the mesostructure can evolve according to different transformation mechanisms, changing the value of $\tau^\#$. To simplify this expression, we consider a first order development at the beginning of the flow. The derivative of the compression stress is with respect to the macroscopic compression strain $\varepsilon = -\log\left(\frac{h}{h_0}\right)$:

$$\frac{\partial \tau^\#}{\partial \varepsilon} = HK\varepsilon^\# \left(\frac{\partial \dot{\varepsilon}}{\partial \varepsilon} \right) + HK\dot{\varepsilon} \left(\frac{\partial \varepsilon^\#}{\partial \varepsilon} \right) \quad (4.43)$$

For a constant compression velocity \dot{h} , the derivative of the strain rate $\dot{\varepsilon} = \frac{-\dot{h}}{h}$ is:

$$\frac{\partial \dot{\varepsilon}}{\partial \varepsilon} = \dot{\varepsilon} \quad (4.44)$$

The derivative $\frac{\partial \varepsilon^\#}{\partial \varepsilon}$ expresses the relative evolution of the mesostructure with respect to the deformation of the flow, including all the mesoscale deformation modes which transform the fibrous reinforcement. It is negative for a relaxation of the mesostructure, and positive if it is compacted during the compression.

Using Eq. (4.43) and (4.44), and considering that in the first order $d\varepsilon \simeq \varepsilon$, the compression stress becomes:

$$\Sigma = \frac{3}{2} \left(\frac{R}{h} \right)^2 \mu \dot{\varepsilon} + \tau_0^\# + \underbrace{\left(\tau_0^\# + HK \dot{\varepsilon}_0 \left. \frac{\partial \varepsilon^\#}{\partial \varepsilon} \right|_0 \right)}_{-k_0} \varepsilon \quad (4.45)$$

where k_0 is a stiffness corresponding to the relaxation of the internal friction stress between the fiber bundles.

To simplify the characterization method, the compression stress is reformulated with respect to the quantities directly given by the experimental results as the effective thickness and radius of the charge. Defining a viscosity like quantity $\mu^\#$ as the friction viscosity by:

$$\mu^\# = HK \varepsilon^\# \quad (4.46)$$

the compression stress of Eq. (4.45) is reformulated in:

$$\Sigma = \frac{3}{2} \left(\frac{R}{h} \right)^2 \mu \dot{\varepsilon} + \mu_0^\# \dot{\varepsilon}_0 - k_0 \varepsilon \quad (4.47)$$

where the rheological parameters to identify are μ , $\mu_0^\#$ and k_0 . Thanks to Eq. (4.46), the friction viscosity gives the value of the product HK which characterizes the friction behavior of the fiber bundles.

4.C. Phase averages and averaging theorem

Spatial and phase averaging operators:

The *spatial average* of an arbitrary quantity, for example the stress tensor field $\bar{\bar{\sigma}}$, is defined over a material domain V as:

$$\langle \bar{\bar{\sigma}} \rangle = \frac{1}{V} \int_V \bar{\bar{\sigma}} dV \quad (4.48)$$

In the case of a domain V composed of multiple phases, the averaging operator can be restricted to a single phase using the *phase indicator function* (Torquato, 1991). For example, in the case of a two-phase material, with a matrix phase (m) and a fiber phase (f), the phase indicator function of the matrix is denoted χ_m and is given for any point \vec{x} of the volume V by:

$$\chi_m(\vec{x}) = \begin{cases} 1 & \text{if } \vec{x} \in V_m \\ 0 & \text{otherwise} \end{cases} \quad (4.49)$$

$$\text{and } \chi_m(\vec{x}) + \chi_f(\vec{x}) = 1$$

where V_m is the matrix phase domain inside V .

Then, the average stress of the matrix is:

$$\langle \bar{\bar{\sigma}}^{(m)} \rangle = \frac{1}{V} \int_V \bar{\bar{\sigma}} \chi_m dV = \frac{1}{V} \int_{V_m} \bar{\bar{\sigma}} dV_m \quad (4.50)$$

This average is called the *phase average* of $\bar{\bar{\sigma}}$ over the matrix phase. A special case of the phase average is when the averaged quantity is the phase indicator function:

$$\langle \chi_m \rangle = \frac{V_m}{V} = \phi_m \quad (4.51)$$

The average of the phase indicator function gives the volume fraction of the corresponding phase.

The other way to define an average is to consider the average only over the single phase. This is the *intrinsic phase average*, defined by:

$$\langle \bar{\bar{\sigma}}^{(m)} \rangle_m = \frac{1}{V_m} \int_{V_m} \bar{\bar{\sigma}} \chi_m dV_m = \frac{1}{V_m} \int_{V_m} \bar{\bar{\sigma}} dV \quad (4.52)$$

This second averaging operator describes the average properties of the single phase while the first one considers the global properties of the material domain.

The two phase averages are related by:

$$\langle \bar{\bar{\sigma}}^{(m)} \rangle = \phi_m \langle \bar{\bar{\sigma}}^{(m)} \rangle_m \quad (4.53)$$

and the spatial average is simply given by the sum of the phase averages for all the phases present in the domain:

$$\langle \bar{\bar{\sigma}} \rangle = \langle \bar{\bar{\sigma}}^{(m)} \rangle + \langle \bar{\bar{\sigma}}^{(f)} \rangle \quad (4.54)$$

Averaging theorem:

The establishment of the conservative equations for a multi-phasic material requires to derivate the averaging operators.

Consider a volume V , large enough to contain the moving matrix phase, taking the exterior domain as a third phase if necessary. Then, the volume V is constant and the derivative and the integral can be permuted. The derivation of the phase average with respect to a time or spatial variable s is given by:

$$\frac{d}{ds} \int_V \bar{\bar{\sigma}} \chi_m dV = \frac{1}{V} \int_V \left(\frac{d\bar{\bar{\sigma}}}{ds} \right) \chi_m dV + \frac{1}{V} \int_V \bar{\bar{\sigma}} \left(\frac{d\chi_m}{ds} \right) dV \quad (4.55)$$

The phase indicator function is constant everywhere within each phase. Its derivatives are non-zero only on the boundary of the phase domain. At the matrix phase boundary, the time and spatial derivatives of the matrix phase indicator function are respectively (see Figure 4.34):

$$\frac{\partial \chi_m}{\partial t} dV = \vec{v}^{(m)} \cdot d\vec{S}^{(m \rightarrow *)} \quad \nabla \chi_m dV = -d\vec{S}^{(m \rightarrow *)} \quad (4.56)$$

where $d\vec{S}^{(m \rightarrow *)}$ denotes the surface normal vector pointing outward from the matrix phase.

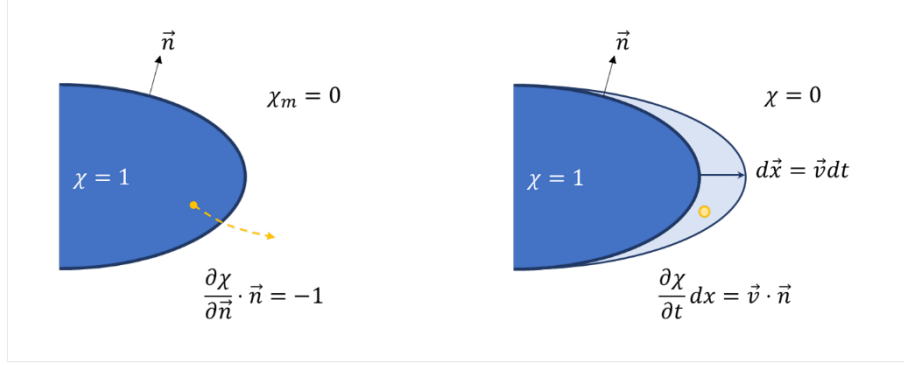


Figure 4.34: Spatial (left) and time (right) derivatives of the phase indicator function.

Using Einstein notation $\bar{\bar{\sigma}} = \sigma_{ij}$, the time derivative of the phase average is:

$$\frac{d}{dt} \langle \sigma_{ij}^{(m)} \rangle = \left\langle \frac{\partial \sigma_{ij}^{(m)}}{\partial t} \right\rangle + \frac{1}{V} \oint \sigma_{ij}^{(m)} v_k^{(m)} dS_k^{(m \rightarrow *)} \quad (4.57)$$

and the spatial derivative of the phase average is:

$$\frac{d}{dx_k} \langle \sigma_{ij}^{(m)} \rangle = \left\langle \frac{\partial \sigma_{ij}^{(m)}}{\partial x_k} \right\rangle - \frac{1}{V} \oint_{S_{m \rightarrow *}} \sigma_{ij}^{(m)} dS_k^{(m \rightarrow *)} \quad (4.58)$$

The application of Eq. (4.58) with the divergence operator gives the average conservation of the momentum for the matrix phase:

$$\underbrace{\nabla \cdot \langle \bar{\bar{\sigma}}^{(m)} \rangle}_{(1)} = \underbrace{\phi_m \nabla \cdot \langle \bar{\bar{\sigma}}^{(m)} \rangle_m}_{(1.1)} + \underbrace{\langle \bar{\bar{\sigma}}^{(m)} \rangle_m \cdot \nabla \phi_m}_{(1.2)} = \underbrace{\langle \nabla \cdot \bar{\bar{\sigma}}^{(m)} \rangle}_{(2)} - \underbrace{\frac{1}{V} \oint_{S_{m \rightarrow f}} \bar{\bar{\sigma}}^{(m)} \cdot d\vec{S}^{(m \rightarrow f)}}_{(3)} \quad (4.59)$$

Term (1) describes the global conservation of momentum, as a flux of stress (1.1) and a term related to the variation of volume fraction of the matrix (1.2). Term (2) is the average of the local momentum equilibria within the matrix phase, and term (3) is the resultant of the stress at the interface between the matrix and the fiber phases (see Figure 4.35).

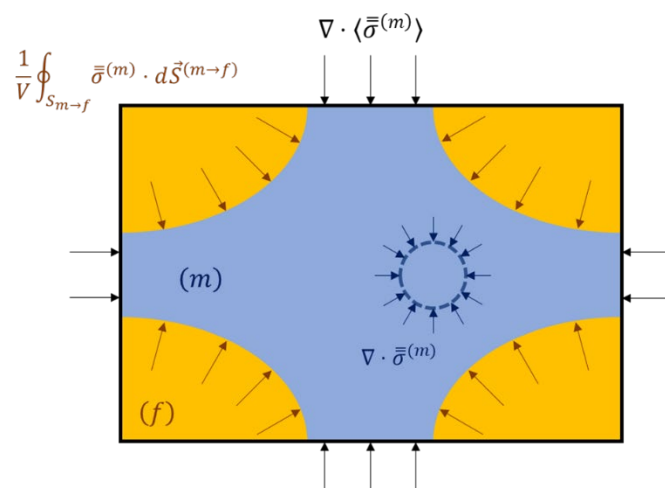


Figure 4.35: Global and local conservations of the momentum.

Bibliography

- [1] Advani, S. G., & Tucker III, C. L. (1987). The use of tensors to describe and predict fiber orientation in short fiber composites. *Journal of rheology*, 31(8), 751-784.
- [2] Advani, S. G., & Tucker III, C. L. (1990). A numerical simulation of short fiber orientation in compression molding. *Polymer composites*, 11(3), 164-173.
- [3] Barone, M. R., & Caulk, D. A. (1985). Kinematics of flow in sheet molding compounds. *Polymer composites*, 6(2), 105-109.
- [4] Barone, M. R., & Caulk, D. A. (1986). A model for the flow of a chopped fiber reinforced polymer compound in compression molding. *Journal of Applied Mechanics*, 53(2), 361-371.
- [5] Boylan, S., & Castro, J. M. (2003). Effect of reinforcement type and length on physical properties, surface quality, and cycle time for sheet molding compound (SMC) compression molded parts. *Journal of applied polymer science*, 90(9), 2557-2571.
- [6] Boylan, S., Abrams, L. M., & Castro, J. M. (2003). Predicting molding forces during sheet molding compounds (SMC) compression molding. II: Effect of SMC composition. *Polymer composites*, 24(6), 731-747.
- [7] Castro, J. M., & Griffith, R. M. (1989). Sheet molding compound compression-molding flow. *Polymer Engineering & Science*, 29(10), 632-638., 29(10), 632-638.
- [8] Chen, Z., Tang, H., Shao, Y., Sun, Q., Zhou, G., Li, Y., . . . Su, X. (2019). Failure of chopped carbon fiber Sheet Molding Compound (SMC) composites under uniaxial tensile loading: Computational prediction and experimental analysis. *Composites Part A: Applied Science and Manufacturing*, 117-130.
- [9] Crowson, R. J., & Folkes, M. J. (1980). Rheology of short glass fiber-reinforced thermoplastics and its application to injection molding. II. The effect of material parameters. *Polymer Engineering & Science*, 20(14), 934-940.
- [10] Dumont, P., Orgéas, L., Favier, D., Pizette, P., & Venet, C. (2007). Compression moulding of SMC: In situ experiments, modelling and simulation. *Composites Part A: Applied Science and Manufacturing*, 38(2), 353-368.
- [11] Dumont, P., Orgéas, L., Le Corre, S., & Favier, D. (2003). Anisotropic viscous behavior of sheet molding compounds (SMC) during compression molding. *International Journal of Plasticity*, 19(5), 625-646.
- [12] Dumont, P., Vassal, J. P., Orgéas, L., Michaud, V., Favier, D., & Manson, J. A. (2007). Processing, characterisation and rheology of transparent concentrated fibre-bundle suspensions. *Rheologica acta*, 46(5), 639-651.
- [13] Engmann, J., Servais, C., & Burbidge, A. S. (2005). Squeeze flow theory and applications to rheometry: A review. *Journal of non-newtonian fluid mechanics*, 132(1-3), 1-27.
- [14] Guiraud, O. (2011). *Rhéologie des suspensions concentrées de fibres: application à la mise en forme des matériaux composites*. Université de Grenoble.

- [15] Han, C. D., & Lem, K. W. (1983). Rheology of unsaturated polyester resins. I. Effects of filler and low-profile additive on the rheological behavior of unsaturated polyester resin. *Journal of Applied Polymer Science*, 28(2), 743-762.
- [16] Hohberg, M., Kärger, L., Henning, F., & Hrymak, A. (2017). Rheological measurements and rheological shell model Considering the compressible behavior of long fiber reinforced sheet molding compound (SMC). *Composites Part A: Applied Science and Manufacturing*, 95, 110-117.
- [17] Huq, A. M., & Azaiez, J. (2005). Effects of length distribution on the steady shear viscosity of semiconcentrated polymer-fiber suspensions. *Polymer Engineering & Science*, 45(10), 1357-1368.
- [18] Jackson, W. C., Advani, S. G., & Tucker, C. L. (1986). Predicting the orientation of short fibers in thin compression moldings. *Journal of composite materials*, 20(6), 539-557.
- [19] Kotsikos, G., & Gibson, A. G. (1998). Investigation of the squeeze flow behaviour of sheet moulding compounds (SMC). *Composites Part A: Applied Science and Manufacturing*, 29(12), 1569-1577.
- [20] Le Corre, S., Dumont, P., Orgéas, L., & Favier, D. (2005). Rheology of highly concentrated planar fiber suspensions. *Journal of Rheology*, 49(5), 1029-1058.
- [21] Lee, C. C., Folgar, F., & Tucker, C. L. (1984). Simulation of compression molding for fiber-reinforced thermosetting polymers. *Journal of Manufacturing Science and Engineering*, 106(2), 114-125.
- [22] Lee, L. J., Marker, L. F., & Griffith, R. M. (1981). The rheology and mold flow of polyester sheet molding compound. *Polymer Composites*, 2(4), 209-218.
- [23] Mahé, F., Binetruy, C., Advani, S., Férec, J., & Eck, B. (2021). A multi-scale statistical description of stacks of non-cohesive thin particles. *Powder Technology*, 399, 116988.
- [24] Merhi, D., Comte, E., Michaud, V., & Månson, J. A. (2004). Effect of glass fiber sizing on Sheet Molding Compounds (SMC) rheology.
- [25] Merhi, D., Comte, E., Michaud, V., & Månson, J. A. (2005). Correlation between sizing formulation and compressive behavior of concentrated glass bundle suspensions. *Polymer composites*, 26(3), 370-376.
- [26] Orgéas, L., & Dumont, P. J. (2011). Sheet molding compounds. *Wiley encyclopedia of composites*, 1-36.
- [27] Oter-Carbonell, L. (2018). *Process-induced microstructure in industrial SMC compression: quantitative descriptive analysis and predictability of a state-of-the-art numerical model*. École centrale de Nantes.
- [28] Romanenko, V. D. (2022). Advanced process simulation of compression molded carbon fiber sheet molding compound (C-SMC) parts in automotive series applications. *Composites Part A: Applied Science and Manufacturing*, 157, 106924.

- [29] Silva-Nieto, R. J., Fisher, B. C., & Birley, A. W. (1981). Rheological characterization of unsaturated polyester resin sheet molding compound. *Polymer Engineering & Science*, 21(8), 21(8), 499-506.
- [30] Torquato, S. (1991). *Random heterogeneous materials: microstructure and macroscopic properties*. Springer.
- [31] Tsai, C. L. (1999). Determination of shear modulus of single fibers. *Experimental mechanics*, 39(4), 284-286.
- [32] Wang, J., O’Gara, J. F., & Tucker III, C. L. (2008). An objective model for slow orientation kinetics in concentrated fiber suspensions: Theory and rheological evidence. *Journal of Rheology*, 52(5), 1179-1200.
- [33] Yang, Y. S., & Suspene, L. (1991). Curing of unsaturated polyester resins: Viscosity studies and simulations in pre-gel state. *Polymer Engineering & Science*, 31(5), 321-332.
- [34] Zeng, H. (2013). *Polymer adhesion, friction, and lubrication*. John Wiley & Sons.

Conclusions and overview on the statistical SMC model

Table of contents

5.1	Summary, conclusions and contributions.....	191
5.2	Discussion about the statistical model.....	194
5.3	Future work and perspectives.....	199
	Bibliography	201

5.1 Summary, conclusions and contributions

In this work, the complex deformation behavior of Sheet Molding Compound materials during the compression molding process is investigated. A statistical framework of discontinuous mechanics is developed to model the effects of the fibrous mesostructure on the rheology of SMC materials. Various aspects of the theoretical work are validated with numerical simulations and experiments for different types of SMC materials. A characterization methodology is proposed to identify the material parameters of the formulated model.

The discontinuous and random nature of the fibrous reinforcement of SMC materials is a major constitutive characteristic of both the process and the material, which limits fundamentally its control and repeatability.

In **Chapter 1**, we presented the main modeling approaches to describe the behavior of SMC materials during the compression molding process, taking into account various physical parameters depending on the model. However, the mechanical contribution of chopped fiber bundles and their random arrangement are generally ignored, even though they seem to significantly affect the way SMC material deform, causing flow irregularities and defects during the industrial molding process.

The objective of this work is to bring new understanding of the material and the process by addressing the following questions:

- How to explain the complex rheology of SMC materials induced by the internal network of chopped fiber bundles?
- What are the principal parameters governing the internal deformation mechanisms of SMC mesostructures?
- How to describe the statistical variability inherent in the nature of the SMC materials?

with the intent of improving the process control and extending it to new applications through a sound and physics-based description of the rheology of SMC materials during the compression molding process.

In **Chapter 2**, an experimental campaign was carried out to highlight the transformation mechanisms involved in the deformation of the discontinuous fibrous reinforcement of SMC materials.

- **The deformation of SMC materials has been found to be strongly dependent on the parameters of the mesostructure, through a combination of fluid and solid deformations leading to complex macroscopic flow patterns.** Fiber bundles are partially reoriented for low fiber contents and relatively short fiber length. For higher fiber contents, the orientation distribution remains isotropic in the plane and the fiber bundles are deformed. For long fiber bundles, they bend in the plane. If these transformation mechanisms occur at the same time, the fiber bundles can partially or fully separate into individual filaments.
- **The manufacturing process of the chopped fiber bundle network is modelled by a new mathematical approach based on integral geometry which allows to describe random planar stacks.** The geometry of the fiber bundles and the parameters are directly related to the geometrical properties of planar stacks using universal relationships. Three mesostructure descriptors provide a complete description of the random stack: the aspect ratio of the fiber bundles, the angular factor and the average number of contacts between two fiber bundles. Through a generalization of this mathematical representation for any shape of stacked thin objects, the validity of this representation has been confirmed and offered new insight about the symmetry and the geometrical properties of any random stacks.
- To confirm this description, **a numerical generator of SMC mesostructures has been implemented.** Chopped fiber bundles are randomly dropped on a flat surface with different distributions of geometry or orientation. They are stacked by creating contacts. Numerical results confirm the mathematical model and validate the proposed parametrization of the mesostructures. A descriptor is introduced to describe the compaction state of the stack. **Before the compression molding process, the SMC materials are compacted by applying a mechanical loading**, which excludes the assumption of dilute media and requires a mechanical model for the compaction of the random stack of chopped fiber bundles.

In **Chapter 3**, the mechanical model of compacted SMC mesostructures is developed through a multi-scale approach, from the fiber scale (microscale), to the scale of the random stacks (mesoscale), to the scale of the process (macroscale). The formulation is divided into three sub-problems, each associated with a material scale:

- **At the microscale, the behavior of fiber bundles is described by a beam model**, depending on an initial kinematic representation of its deformation. Three cases are presented: shear, bending and a mixed kinematics with the Timoshenko beam model. The choice of a given kinematics induces a certain type of mechanical model of the fiber bundle, formulated in the finite element framework.
- **At the mesoscale, the structure made of the stacked fiber bundles is represented by an assembly of the finite element formulations** obtained from the microscopic description. The discontinuous nature of the internal contacts between the fiber bundles is addressed by the use of Lagrangian multipliers, resulting in a non-linear formulation of the mechanical behavior of the stack. This problem is solved by an incremental finite element algorithm, using the linearity of the problem between the creation of two contacts. This procedure has been implemented to complete the generation algorithm of SMC mesostructures for different fiber bundles beam kinematics.
- **At the macroscale, a framework of statistical mechanics is developed to solve large size problem allowing to obtain the full distribution of the contact forces within the fibrous network.** The exponential distribution of the contact forces is parametrized by its average value, deduced from the mesoscopic description. The method is validated by direct mechanical simulation of the compaction of mesostructures.

In **Chapter 4**, a rheological model, based on the formulation of internal friction forces within the fibrous reinforcement, is established and validated with experimental compression tests on various SMC materials.

- **A first campaign of compression experiments with custom-designed SMC materials was conducted to relate the initial compression stress to the mesostructure compaction state.** The lubricated friction law is deduced from the experimental results and the mechanical model of the compacted SMC mesostructures.
- **A new rheological model for SMC materials is derived as a generalized visco-elasto-plastic model.** The fluid behavior of the matrix is captured by a linear viscous model, and the friction contribution, resulting from contacts between fiber bundles and cohesion between matrix and fibers, is formulated as plastic behavior. The friction threshold depends on the mechanical state of the mesostructure. The alignment of the fiber bundles relaxes the internal contact forces, while the friction threshold increases with the mechanical loading of the fiber bundles.
- **A second experimental campaign was carried out in parallel with the model derivation to characterize the rheological parameters of different types of SMC materials.** An analytical solution of the model for a radial squeeze-flow is identified on commercial glass and carbon SMC materials compressed between two large heated platens, under conditions similar to those of the industrial molding process.
- **It is shown that the deformation of the fibrous mesostructure can be directly sensed from the force measurement**, which allows one to characterize its evolution

and find the optimal conditions to compress the SMC materials and limit the deformation of the fiber bundles.

- **The rheological parameters have been directly related to the material properties of the resin and the fiber roving**, and assuming the same friction constant for all the tested material, the shear moduli of the fiber bundles are estimated and are consistent with the literature data.
- **The proposed model generalizes the two main rheological descriptions of SMC materials found in the literature and is consistent with experimental results obtained for different classes of industrial SMC materials.** At low compression strain rates, the solid elasto-plastic behavior is dominant and the material tends to deform as a plastic medium, according to the plug-flow model. At higher compression strain rates, the viscous behavior takes over and the SMC material deforms like a fluid. The fiber bundles can then rotate, but deform if the compression strain rate is too high. The transition between these two rheological behaviors will change during the compression, depending on the mechanical state of the mesostructure.
- **The statistical description of the contact forces applied to the friction model allows one to quantify the variability inherent in SMC materials.** The random nature of the discontinuous mesostructure is reflected in the distribution of the friction forces. According to this description, the friction force distribution can be described by an exponential distribution, with a standard deviation proportional to its mean value. The statistical model therefore explains the irregular fluctuations observed in the flow patterns and could help to optimize the formulation of the SMC materials with respect to the mechanical requirements of the produced parts.

5.2 Discussion about the statistical model

Theoretical arguments, combined with numerical simulations and experimental findings, allow us to derive a constitutive model of SMC materials to describe the internal physical mechanisms involved in the compression molding process. It takes the form of a rheological model shown in Figure 5.1, incorporating the flow of the resin, the mechanical loading of the fibrous mesostructure and their physical coupling.

This model averages the mechanical and frictional behaviors, obtained from the probabilistic description of the material. However, the statistical distribution of friction forces has not yet been studied although it plays an important role in the complex rheology of SMC materials.

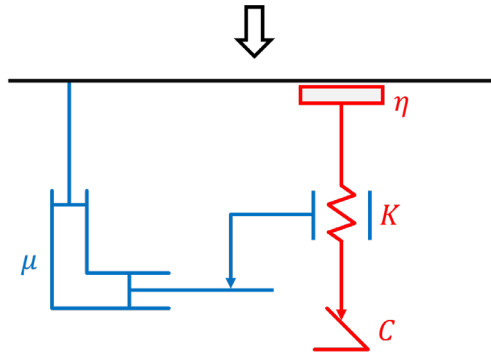


Figure 5.1: SMC rheological model.

According to the proposed model, the SMC material can be in one of these two rheological regimes:

1. **Flow:** the viscous drag forces applied on the fibrous mesostructure are sufficiently high to overcome the friction threshold and allow the transport of the fiber bundles. The material flows and the fibrous reinforcement can deform, relaxing the internal contact forces.
2. **Segregation:** the viscous forces are too small and below the threshold value to transport the fiber bundles. Then, the fluid flows through the fibrous reinforcement which is only compacted in the vertical direction, increasing the contact forces between the fiber bundles.

These regimes are mapped in Figure 5.2 in the fluid versus solid stress coordinate system. The solid behavior is characterized by the mesoscopic compaction stress $\sigma^\#$ and the resulting friction stress $\tau^\# = \eta\sigma^\#$, in which η is the friction coefficient. The fluid behavior is characterized by the compression strain rate $\dot{\epsilon}$ and the viscous stress $\tau = \mu\dot{\epsilon}$, with μ the dynamic viscosity of the SMC material. The boundary separating both regimes is the line $\tau = \tau^\#$.

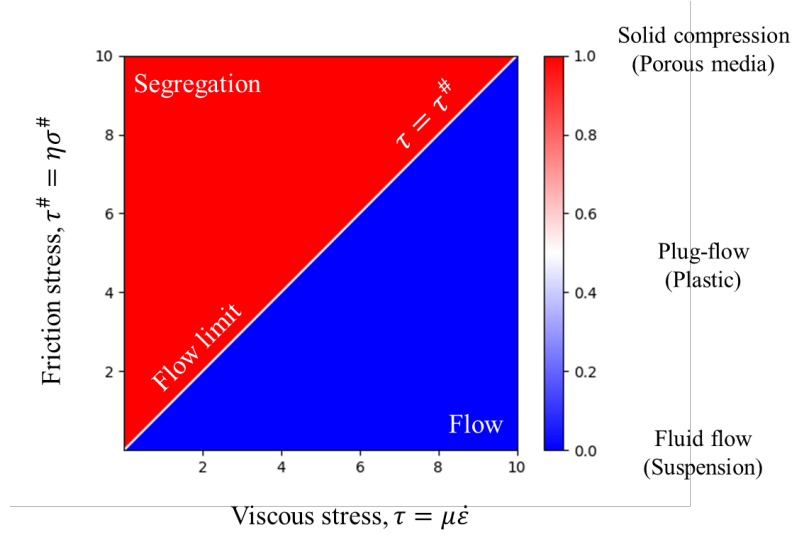


Figure 5.2: Local representation of the two rheological regimes, with the flow limit for $\tau = \tau^\#$.

The non-dimensional number M is defined as the ratio between the viscous over the friction forces:

$$M = \frac{\mu\dot{\epsilon}}{\eta\sigma^\#} \quad (5.1)$$

The friction makes the model non-linear, with a discontinuity induced by the threshold condition at the limit $\tau = \eta\sigma^\#$. From this state, if the material begins to flow ($M > 1$), it will continue in this regime as the fibrous reinforcement gradually relaxes its internal friction forces with the reorientation of the fiber bundles. In contrast, if the composite material cannot flow ($M < 1$), the increasing contact forces will prevent the material from flowing. The friction

threshold separates the material states, which evolve away from this limit and remain in their respective regimes.

The statistical-mechanics framework shows that the contact stress $\sigma^\#$, and hence the friction stress $\tau^\#$, are not constant values, but are statistically described by an exponential distribution, parametrized by its mean value. Here we recall that for an exponential distribution, the mean and median values are related by: $\text{Mean}[\tau^\#] = \ln(2) \text{Median}[\tau^\#]$. In the following, the parametrization using the median value will be more appropriate.

Consider a macroscopic element of SMC material whose state is characterized by its viscous and friction stress as the point $(\tau, \tau^\#)$ in the coordinate system of Figure 5.2. This point represents the median of the set of local states of the macroscopic element. Among these internal states, half of them is below the value $\tau^\#$, and the other half is above $\tau^\#$. As the statistical distribution of the friction stress is known to be exponential, it is possible to calculate, for a given global state, the fraction of its internal states which is above the flow limit ($\tau^\# > \tau$) as a function of M :

$$p(M < 1) = (M + 1)e^{-M} \quad (5.2)$$

Plotting this fraction in the frame of the Figure 5.2 results in Figure 5.3. It represents the probabilistic version of the SMC rheological model, which mixes the two rheological behaviors depending on the median state of the considered macroscopic material point. It can be noted that the representation in Figure 5.3 has radial symmetry, i.e., the rheological behavior of a material point of SMC only depends on the value M related to its median state.

The two representations of the SMC model given in Figure 5.2 and Figure 5.3 represent different aspects of the proposed SMC model. The local representation in two distinct rheological regimes describes the physics involved locally in the SMC material. The probabilistic representation describes the macroscopic behavior of the SMC materials, as a statistical mean between the two rheological behaviors induced by the distribution of its local internal states. At the macroscale, the separation between the two rheological regimes is no longer a sharp limit, but a continuous transition, as a consequence of the statistical description.

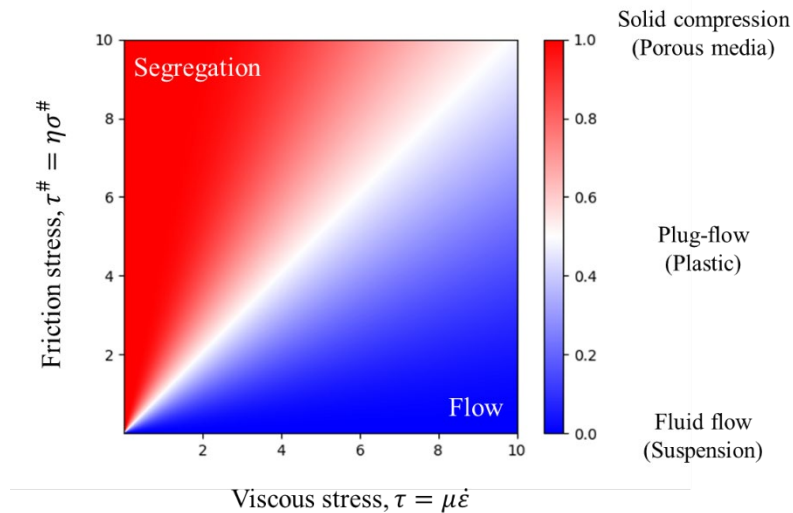


Figure 5.3: Probabilistic representation of the statistical SMC model.

In Figure 5.3, we can find the different states known about SMC materials. Along the horizontal axis ($M \rightarrow +\infty$), the contact stress vanishes. The material state corresponds to a suspension, in that the fiber bundles are suspended in the matrix and do not transfer any mechanical force to each other. As the value of M decreases, the rheological state of the material point approaches the flow limit. The fiber bundles are increasingly in contact. At the flow limit, the SMC material behaves macroscopically like a plastic medium, with one half flowing, and the other half compacted. At the other extreme, when $M \rightarrow 0$, the fibrous reinforcement becomes a porous solid medium, and the resin flows through it, with fiber bundles held stationary by the friction force.

During compression, the material state can change due to the variation of the compression strain rate or the evolution of the mesostructure. Then, the corresponding material point in Figure 5.3 will continue to shift in the graph. In the same way, all the internal local states will shift in the representation of Figure 5.2.

We assume that the evolution of the SMC material has no memory, i.e., the evolution of the SMC mesostructure is only a function of the current state. Furthermore, the compression velocity \dot{h} is considered to evolve slowly during compression. Then, the macroscopic strain rate $\dot{\varepsilon} = -\dot{h}/h$ and the macroscopic compression strain ε are related by the differential equation:

$$d\dot{\varepsilon} = \dot{\varepsilon}d\varepsilon \quad (5.3)$$

Consider an arbitrary set of local states of a given median state as represented in Figure 5.4. The conservation of the median state as the global representation of the set implies that the transformation must be linear, proportional to the radial coordinate $\sqrt{\tau^2 + \tau^{\#2}}$ and homogenous over the state space. Moreover, the separation of the rheological domains explained previously requires that the transformation of material states is symmetrical with respect to the flow limit.

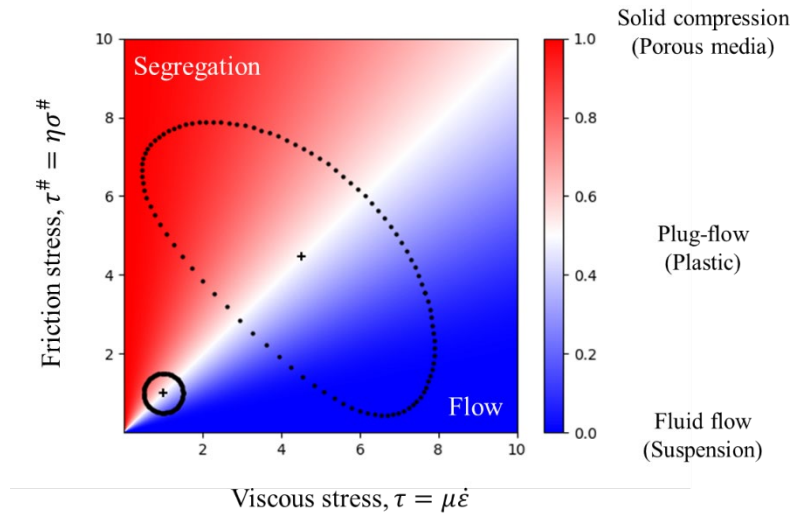


Figure 5.4: Parallel evolution of a set of local states and its global median state.

Under these hypotheses, the transformation of material states is defined as:

$$\begin{cases} d\tau = \mu d\dot{\varepsilon} \\ d\tau^\# = HK \left(\varepsilon^\# - \left| \frac{d\varepsilon^\#}{d\varepsilon} \right| \right) d\dot{\varepsilon} \end{cases} \quad (5.4)$$

where we used the constitutive laws obtained in Chapter 4:

$$\sigma^\# = \frac{K}{\alpha r} \varepsilon^\# \quad \eta = H \cdot \dot{\varepsilon} \cdot \alpha r \quad (5.5)$$

with K the mechanical parameter of the fibrous mesostructure, H the friction parameter, α the angular factor, r the aspect ratio and $\varepsilon^\#$ the mesostructure compaction strain.

If the mesostructure compaction state is constant, $\left| \frac{d\varepsilon^\#}{d\varepsilon} \right| = 0$. The corresponding transformation is the radial transformation represented in Figure 5.5-a. It transforms the set of local states by a homogeneous extension in all directions (in the state space), conserving the relative distribution of material states. It can be noted that the states on the flow limit remains on this limit. At any time, the viscous stress is equal to the friction threshold and the mesostructure remains in the same state. The material points flow as a plug-flow.

At the other extreme, if $\left| \frac{d\varepsilon^\#}{d\varepsilon} \right| = 1$, the transformation is the sum of the radial and transverse transformations, the second one being perpendicular to the flow limit “shears” the set of the local states on either side of the flow limit (see Figure 5.5-b). In the flow domain, the states are transported towards the suspension limit, which reduce the internal friction forces. In the segregation domain, the fibrous mesostructure is compacted while the matrix flows through it.

In general, the transformation of the material state is a linear combination of these two elementary transformations, characterized by the evolution coefficient $0 \leq \left| \frac{d\varepsilon^\#}{d\varepsilon} \right| \leq 1$. This parameter describes the relative deformation between the fibrous mesostructure and the matrix, with a perfect slip for $\left| \frac{d\varepsilon^\#}{d\varepsilon} \right| = 0$ and a perfect adhesion for $\left| \frac{d\varepsilon^\#}{d\varepsilon} \right| = 1$.

The linearity condition on the transformation of material states is important as it corresponds to the ergodicity hypothesis (Torquato, 1991). If the transformation is not linear, the global and local states will evolve differently. However, since at the macroscopic scale the SMC material is always a set of local states, it will result in a chaotic evolution of the material, making any description by a mean field theory wrong.

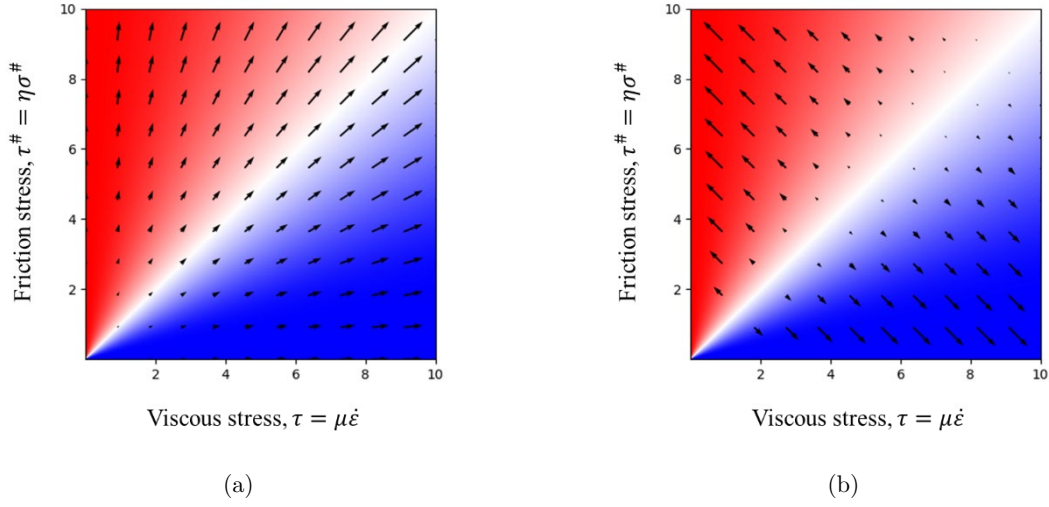


Figure 5.5: Evolution of the material states.

- (a): Radial transformation with a stationary mesostructure, $\left|\frac{d\varepsilon^\#}{d\varepsilon}\right|=0$.
(b): Transverse transformation with an evolving mesostructure, $\left|\frac{d\varepsilon^\#}{d\varepsilon}\right|=1$.

The linearity condition also implies that, according to the form of Eq. (5.4) and the radial symmetry of the transformation field, the evolution coefficient must be a constant parameter, depending only on the material properties. This theoretical argument supports the consistency of the characterization method presented in Chapter 4, with the first order development of the friction stress, in fitting experimental curves over large deformations.

We conclude that, under the assumptions used in this section, the three material parameters identified with the characterization experiment of Chapter 4 are sufficient to characterize the evolving behavior of the SMC materials: the viscosity μ , the friction constant η_{fm} and the evolution constant $C = \left|\frac{d\varepsilon^\#}{d\varepsilon}\right|$.

The proposed model can be extended to non-linear or temperature-dependent viscosities for the matrix, but it requires smooth variations in the mold geometry. In particular, it neglects the presence of thin ribs oriented perpendicular to the flow, which would require a more complex model to capture the complex evolution of the SMC mesostructures in that case.

5.3 Future work and perspectives

The presented work has led to the implementation of the proposed model in a numerical solver based on the library OpenFOAM (Jasak, et al., 2007) to simulate the compression of SMC materials in simple geometries. The purpose of this project is to develop a numerical tool to simulate industrial molding cases, incorporating the mechanical compaction or relaxation of the discontinuous fibrous reinforcement during the process. The evolution model of the SMC mesostructures will be developed and compared to industrial molding parts. A statistical indicator will be estimated from the calculated mean solution to characterize the variability of the solution, which will allow process improvement and reduction of defects.

The geometric description of random mesostructures is found to be more general in its applications than that of fiber bundles. Combined with the general framework of statistical mechanics, it can be used to model other classes of discontinuous composite materials, with direct applications to the recycling of composite materials, which uses similar compression molding processes of shredded composite panels (Henshaw, et al., 1996).

Bibliography

- [1] Henshaw, J. M., Han, W., & Owens, A. D. (1996). An overview of recycling issues for composite materials. *Journal of Thermoplastic Composite Materials*, 9(1), 4-20.
- [2] Jasak, H., Jemcov, A., & Tukovic, Z. (2007). OpenFOAM: A C++ library for complex physics simulations. In *International workshop on coupled methods in numerical dynamics, 1000*, 1-20.
- [3] Mahé, F., Binetruy, C., Advani, S., Férec, J., & Eck, B. (2021). A multi-scale statistical description of stacks of non-cohesive thin particles. *Powder Technology*, 399, 116988.
- [4] Orgéas, L., & Dumont, P. J. (2011). Sheet molding compounds. *Wiley encyclopedia of composites*, 1-36.
- [5] Torquato, S. (1991). *Random heterogeneous materials: microstructure and macroscopic properties*. Springer.

Appendix I

Numerical generator of compacted fibrous mesostructures

I.1 Packages

```
import numpy as np
from matplotlib import pyplot as plt
import pandas as pd
from numba import njit
from sklearn.neighbors import KDTree
from scipy.sparse import dok_matrix, csr_matrix, bmat
from scipy.spatial.distance import pdist
from scipy.sparse.csgraph import reverse_cuthill_mckee
from scipy.sparse.linalg import spsolve
import warnings ; warnings.filterwarnings("ignore")
SMALL = np.random.rand()*1e-12
```

I.2 Inputs

```
NBUNDLES          = 600
PERIODIC           = True
# Geometry
LENGTH            = 25e-3
WIDTH              = 1e-3
THICKNESS          = 0.1e-3
SIZE               = 50e-3
REDUCTION          = 20
# Mechanics
SHEAR_MODULUS     = 1e6
SECTION_AREA      = WIDTH*THICKNESS
# Solver
ITERMAX           = 10000
PHIMAX            = 0.2
```

I.3 Constitutive beam model

```
# Shear
GS = SHEAR_MODULUS*SECTION_AREA
ke = lambda le:\
    [
        GS/le, -GS/le,
        -GS/le, GS/le
    ]

# Interpolation functions
N1 = lambda x, le=LENGTH: 1-x
N2 = lambda x, le=LENGTH: x
SHAPE = [N1, N2]
DOF_NUMBER = int(np.sqrt(len(ke(1)))/2)
```

I.4 Stacking algorithm

```
nbundles = NBUNDLES

# ~~~ Initialize the bundles ~~~
coord = np.random.rand(nbundles, 2)*SIZE
angle = np.random.rand(nbundles)*np.pi
length = np.ones(nbundles)*LENGTH

# ~~~ Periodicity
label = np.arange(nbundles)
ref = np.zeros(nbundles, dtype=int)
l = length.max()
L = SIZE
# Duplicate the bundles for periodic repetitions
if PERIODIC:

    coord = np.vstack([
        coord, # Refs
        coord, # ----
        coord + np.array([ L, 0]), # |_2_|____
        coord + np.array([ 0, L]), # ____|_0_|_1_|
        coord + np.array([-L, -L]), # |_3_|
    ])

    angle = np.hstack([ angle , angle , angle , angle ])
    length = np.hstack([ length, length, length, length ])
    label = np.hstack([ label , label , label , label ])
    ref = np.hstack([ ref , ref+1 , ref+2 , ref+3 ])
```

```

# Keep interior and boundaries
x, y = coord.T
mask = (ref == 0) \
      | (ref == 1) & (x < L+1) \
      | (ref == 2) & (y < L+1) \
      | (ref == 3) & ((x**2 + y**2) < (l**2))
coord = coord[mask]
angle = angle[mask]
length = length[mask]
label = label[mask]
ref = ref[mask]

# ~~~ Find close bundles ~~~
pairwise_dist2 = pdist(coord, 'sqeuclidean')
pairwise_ids = np.vstack(np.triu_indices(len(coord), k=1)).T
diameter2 = np.sum(length[pairwise_ids], axis=1)**2/4
close_ids = pairwise_ids[np.where(pairwise_dist2<diameter2)[0]]

if PERIODIC:
    i, j = close_ids.T
    mask = (ref[i]==0)&(ref[j]==0)|(ref[i]!=ref[j])
    close_ids = close_ids[mask]

# ~~~ Calculate line intersections ~~~
x, y = coord.T
a = np.tan(angle-SMALL)
b = y-a*x
a, b = a[close_ids], b[close_ids]
xint = np.diff(b)/(SMALL-np.diff(a))
yint = np.mean(a*xint+b, axis=1).reshape(-1, 1)

# ~~~ Determine segment intersections ~~~
intersection_dist2 = (x[close_ids]-xint)**2 + (y[close_ids]-yint)**2
intersection_mask = np.multiply(*(intersection_dist2<=length[close_ids]**2/4)
.T)
intersection_ids = close_ids[intersection_mask]
intersection_coord = np.hstack([xint[intersection_mask], yint[intersection_mas
k]])

# ~~~ Compute curvilinear coordinates of the intersections ~~~
vec = np.vstack([np.cos(angle), np.sin(angle)]).T*length.reshape(-1, 1)
x, y = (coord-vec/2)[intersection_ids].T
xint, yint = intersection_coord.T
sint = np.sqrt((x-xint)**2+(y-yint)**2).T

```

```

intersection_ids = label[intersection_ids]%NBUNDLES # Use bundle labels for periodicity

if len(intersection_ids):
    intersection_ids = np.sort(intersection_ids, axis=1) # Reverse if i > j
    sort = pd.DataFrame(intersection_ids) \
        .sort_values(by=[0, 1]).index.values # Sort by (i, j)
    intersection_ids = intersection_ids[sort]
    xint = xint[sort]
    yint = yint[sort]
    sint = sint[sort]

if PERIODIC:
    coord = coord[:nbundles]
    angle = angle[:nbundles]
    length = length[:nbundles]

# ~~~ Make the bundle stack ~~~
@njit
def stack(layer, intersection_ids):
    for i, j in intersection_ids:
        layer[j] = max(layer[j], layer[i]+1)
    return layer

layer = stack(np.zeros(NBUNDLES, dtype=int), intersection_ids)

# ~~~ Reduce the number of intersections ~~~
if REDUCTION>0:
    reduction_mask = (np.diff(layer[intersection_ids]) < REDUCTION).flatten()
    intersection_ids = intersection_ids[reduction_mask]
    xint = xint[reduction_mask]
    yint = yint[reduction_mask]
    sint = sint[reduction_mask]

h = (layer.max()+1)*THICKNESS
phi = np.sum(length)*WIDTH*THICKNESS/SIZE**2/h
alpha = np.pi/2*np.abs(np.sin(angle-angle.reshape(-1, 1))).mean()
print('Initial thickness: {:.1f}mm'.format(h*1e3))
print('TVF : {:.2%}'.format(phi))
print('alpha : {:.3f}'.format(alpha))

```

I.5 Creation of the mesh

```
# ~~~ Create nodes ~~~
label = np.arange(len(intersection_ids)).reshape(-1, 1)
minus = -np.ones((NBUNDLES, 1))
i, j = intersection_ids[None, :, :].T
k = np.arange(NBUNDLES)[: , None]
zeros = np.zeros((NBUNDLES, 1))
block = np.block([
    [minus, k, k, zeros],
    [minus, k, k, length[:, None]],
    [label, i, j, sint[:, [0]]],
    [label, j, i, sint[:, [1]]]
])
nodes = pd.DataFrame(block, columns=['intersection', 'bundle_i', 'bundle_j', 's'])
nodes = nodes.astype({'intersection': int, 'bundle_i': int, 'bundle_j': int})
nodes = nodes.sort_values(by=['bundle_i', 's'], ignore_index=True)

# ~~~ Create vertices (vertical connectivity) ~~~
whr_vertx = nodes['bundle_i'] <= nodes['bundle_j']
whr_cross = nodes['bundle_i'] != nodes['bundle_j']
vertx = nodes[whr_vertx].drop('s', axis=1)
whr_end = vertx['intersection'] == -1
IJ = nodes[whr_cross].sort_values('intersection').index.values.reshape(-1, 2)
IJ = np.sort(IJ, axis=1)
I, J = np.vstack([IJ, [-1, -1]])[vertx['intersection']].T
I[whr_end] = vertx[whr_end].index
J[whr_end] = -1
vertx.insert(1, column='vertx_I', value=I)
vertx.insert(2, column='vertx_J', value=J)

# Find force DoFs (for interpolation)
df = pd.concat([vertx, vertx, vertx[vertx['intersection'] > -1]])
df['force'] = np.hstack([np.zeros(len(vertx)), 2*np.ones(len(vertx)), np.ones(len(vertx[vertx['intersection'] > -1]))]).astype(int)
df['node'] = df.index
df = df.sort_values(by=['node', 'force'])
df.index = np.arange(len(df))
df = df[['node', 'force']]
f0 = -np.ones(len(nodes), dtype=int)
f1 = -np.ones(len(nodes), dtype=int)
f2 = -np.ones(len(nodes), dtype=int)
f0[df[df['force'] == 0]['node']] = df[df['force'] == 0].index
```

```

f1[df[df['force']==1]['node']] = df[df['force']==1].index
f2[df[df['force']==2]['node']] = df[df['force']==2].index
nodes['f0'] = f0
nodes['f1'] = f1
nodes['f2'] = f2

# ~~~ Create elements (in-plane connectivity) ~~~
IDS = np.vstack([np.arange(len(nodes)-1), np.arange(1, len(nodes))]).T
i, j = nodes['bundle_i'].values[IDS].T
IDS = IDS[i==j] # NodeID (nodes.index)
i = nodes['bundle_i'].values[IDS[:, [0]]] # BundleID
lelem = np.diff(nodes['s'].values[IDS]) # Element length
elems = pd.DataFrame(np.hstack([IDS, lelem]), columns=['vertx_I', 'vertx_J', 'length'])
elems[['vertx_I', 'vertx_J']] = elems[['vertx_I', 'vertx_J']].astype(int)

```

I.6 Finite element assembly

```

# ~~~ Build stiffness matrix ~~~
N = DOF_NUMBER*len(nodes)
I, J = elems[['vertx_I', 'vertx_J']].values.T
l = elems['length'].values
rows = np.vstack([[DOF_NUMBER*I+i for _ in range(2*DOF_NUMBER)] for i in range(DOF_NUMBER)] + [[DOF_NUMBER*J+i for _ in range(2*DOF_NUMBER)] for i in range(DOF_NUMBER)]).T.flatten() # [I, I, J, J]
cols = np.vstack([[DOF_NUMBER*I+i for i in range(DOF_NUMBER)] + [DOF_NUMBER*J+i for i in range(DOF_NUMBER)] for _ in range(2*DOF_NUMBER)]).T.flatten() # [I, J, I, J]
Ke = np.vstack(ke(l)).T.flatten()
K = csr_matrix((Ke, (rows, cols)), shape=(N, N))
rows = np.vstack([I, J]).T.flatten()
le = np.vstack([l, l]).T.flatten()
F = np.zeros(N)
F[rows] = 0*le/2

# ~~~ Build contact matrix ~~~
M = len(nodes)+len(vertx)
rows = (np.arange(3*len(vertx))*np.ones((2, 1), dtype=int)).T.reshape(-1, 6)
rows[vertx['intersection']==-1, 1:5] = -1
rows = rows.flatten()
rows = rows[rows>-1]
label = -np.ones(len(rows)+1, dtype=int)
label[np.unique(rows)] = np.arange(M)
rows = label[rows]

```

```

I, J = vertx[['vertx_I', 'vertx_J']].values.T
cols = np.vstack([I, J, I, J, I*(J>-1)-2*(J==-1), J]).T.flatten()
Ce = np.array([1, 0, -1, 1, 0, -1])*np.ones((len(vertx), 1), dtype=int)
Ce = Ce.flatten()[cols>-1]
cols = cols[cols>-1]
cols *= DOF_NUMBER # Vertical displacement must be the first DoF
C = csr_matrix((Ce, (rows, cols)), shape=(M, N))

H = layer.max()+1
i, j = vertx[['bundle_i', 'bundle_j']].values.T
h0 = THICKNESS*np.vstack([layer[i], layer[j]-layer[i]-1, H+1-layer[j]]).T
h1 = np.array([0, 0, 1])*np.ones((len(vertx), 1), dtype=int)
h0[vertx['intersection']==-1, 1] = -1
h1[vertx['intersection']==-1, 1] = -1
h0 = h0.flatten()
h1 = h1.flatten()
h0 = h0[h0>-1]
h1 = h1[h1>-1]

```

I.7 Initialization

```

U = -0
h = H*THICKNESS
phi = np.sum(length)*WIDTH*THICKNESS/SIZE**2/h
u = np.zeros(K.shape[0])
f = np.zeros(C.shape[0])
U_t = [U]
u_t = [u.copy()]
f_t = [f.copy()]
res = []
P0 = bmat([[K, -C.T], [-C, None]], format='csc')
q0 = np.hstack([F*0, -h1])

constr = C@u-(h0+h1*U)
active = np.where(-constr<=SMALL*THICKNESS)[0]
inactive = np.where(-constr>SMALL*THICKNESS)[0]

contacts = np.hstack([np.arange(K.shape[0]), K.shape[0]+active])
P1 = P0[contacts][:, contacts]
renumber = reverse_cuthill_mckee(P1, symmetric_mode=True)
P2 = P1[renumber][:, renumber]

fig, (ax1, ax2, ax3, ax4) = plt.subplots(1, 4, figsize=(20, 6))
ax1.imshow(K[:40, :40].todense())

```

```

ax2.imshow(C[:40, :40].todense())
ax3.imshow(((P2>0)-1*(P2<0))[:80, :80].todense())
ax4.imshow((P2!=0)[:400, :400].todense())
plt.show()

print('Active          : {}'.format(len(active)))
print('Initial thickness: {:.1f}mm'.format(h*1e3))
print('TVF             : {:.2%}'.format(phi))

```

I.8 Solver

```

i = 0
while (i<ITERMAX) and (phi*h/(h+U)<PHIMAX):
    # Contacts
    constr = C@u-(h0+h1*U)
    active = np.where(-constr<=SMALL*THICKNESS)[0]
    inactive = np.where(-constr>SMALL*THICKNESS)[0]
    contacts = np.hstack([np.arange(K.shape[0]), K.shape[0]+active])
    # Solver
    P1 = P0[contacts][:, contacts]
    q1 = q0[contacts]
    renumber = reverse_cuthill_mckee(P1, symmetric_mode=True)
    P2 = P1[renumber][:, renumber]
    q2 = q1[renumber]
    sol0 = np.zeros(P0.shape[0])
    sol1 = np.zeros(P1.shape[0])
    sol2 = spsolve(P2, q2)
    sol1[renumber] = sol2
    sol0[contacts] = sol1
    du_dt = sol0[:K.shape[0]]
    df_dt = sol0[-C.shape[0]:]
    res.append(np.linalg.norm(P2@sol2-q2))
    # Next step
    d = C[inactive]@u-(h0+h1*U)[inactive]
    v = C[inactive]@du_dt-h1[inactive]
    try: t = np.min(d[v<0]/v[v<0])
    except ValueError: break
    # Update
    dU = -t
    du = -du_dt*t
    df = -df_dt*t
    U += dU
    u += du
    f += df

```

```

    # Store
    U_t.append(U)
    u_t.append(u.copy())
    f_t.append(f.copy())
    # Progress
    msg = 'Active = {}, Thickness = {:.2f}mm, TVF = {:.2%}'.format(len(active)
, (h+U)*1e3, phi*h/(h+U))
    i += 1

fig, ax = plt.subplots(1, 2, figsize=(12, 4))
ax[0].semilogy(res)
ax[1].plot(P2@sol2-q2)
plt.show()

```

I.9 Postprocess and plot the distribution of forces

```

fig, ax = plt.subplots()
_, bins, _ = ax.hist(-f[f<0], bins=20, density=True)
ax.set_ylim(ax.get_ylim())
ax.plot(bins, -np.exp(bins/f[f<0].mean())/f[f<0].mean(), 'red')
plt.show()

Phi    = np.array([phi*h/(h+U) for U in U_t])
f0     = np.array([f[f<0].mean() for f in f_t])
F0     = np.array([np.sum(f[nodes['f0']]) for f in f_t])
F2     = np.array([np.sum(f[nodes['f2']]) for f in f_t])

fig, (ax1, ax2) = plt.subplots(1, 2, figsize=(12, 4))
fig.subplots_adjust(wspace=0.2)
ax1.plot(Phi, -f0)
ax1.set_ylim(ax1.get_ylim())
ax1.set_xlabel('Volume fraction')
ax1.set_title('Contact force')
ax2.plot(Phi, -F0, c='tab:blue')
ax2.plot(Phi, -F2, '--', c='tab:blue')
ax2.set_ylim(ax2.get_ylim())
ax2.set_title('Packing force')
ax2.set_xlabel('Volume fraction')
plt.show()

```


Titre : Un cadre de mécanique statistique pour les composites discontinus : application à la modélisation de l'écoulement du moulage par compression de matériaux SMC

Mots clés : SMC, procédé, composite, mécanique statistique, caractérisation, simulation

Résumé : Les Sheet Molding Compounds (SMC) sont des matériaux composites formés de mèches de fibres coupées et d'une résine thermodurcissable. Ils sont mis en forme par moulage par compression et sont connus pour présenter des comportements rhéologiques complexes, difficiles à modéliser et dépendant de l'évolution du renfort fibreux.

Des observations tomographiques, sur une série d'incomplets pour différents matériaux SMC, met en évidence plusieurs mécanismes de transformation du renfort fibreux en fonction de ses caractéristiques. Ces constats soulignent l'implication des contacts et de la friction entre mèches dans la déformation de ces matériaux, mécanismes internes généralement négligés dans les approches de modélisation actuelles.

Un nouveau cadre de mécanique statistique est développé pour modéliser le comportement de milieux fibreux discontinus et aléatoires. Un générateur de mésostructures est implémenté pour étudier les forces de contacts dans un empilement fibreux. A l'échelle macroscopique, le comportement de la mésostructure est décrit analytiquement par une approche probabiliste, en accord avec les résultats des simulations numériques.

Dans le cas de l'écoulement des SMC, cette démarche mène à la formulation d'un modèle de comportement mixte fluide/solide, régi par la distribution des forces de contact à l'intérieur du renfort fibreux. Un protocole expérimental d'identification de ce modèle est développé et appliqué à différents types de matériaux SMC.

Title: Statistical mechanical framework for discontinuous composites: application to the modeling of flow in SMC compression molding

Keywords: SMC, process modeling, composite, statistical mechanics, characterization, simulation

Abstract: Sheet Molding Compounds (SMC) are composite materials made of chopped fiber bundles and a thermosetting resin. They are processed by compression molding and are known to exhibit complex rheological behaviors, difficult to model and coupled to the evolution of the fibrous reinforcement.

Tomographic observations, on a series of short shots of different SMC materials, highlight several transformation mechanisms of the fibrous network according to its characteristics. They reveal the involvement of contacts and friction forces between fiber bundles in the compression deformation of SMC materials. These internal mechanisms are generally neglected in current modeling approaches.

A new framework of statistical mechanics is developed to model the behavior of discontinuous and random fibrous media. A mesostructure generator is implemented to study the contact forces in a fibrous stack. At the macroscopic scale, the behavior of the mesostructure is described analytically by a probabilistic approach, in agreement with the results of numerical simulations.

This framework applied to the flow of SMC materials leads to a mixed fluid/friction model, governed by probabilistic contact forces within the fibrous reinforcement. An experimental characterization protocol is proposed to identify the rheological parameters of this model and applied to different types of SMC materials.